Collapse and post-collapse behavior of steel pipes under external pressure and bending. Application to deep water pipelines

Doctoral Thesis

Facultad de Ingeniería
Universidad de Buenos Aires, Argentina

March 2009

SUBJECT: Collapse and post-collapse behavior of steel pipes under external pressure and bending. Application to deep water pipelines.

DOCTORAL CANDIDATE: Rita G. Toscano

Developed at: Tenaris Siderca S.A. (2003-2007)
SIM & TEC S.A. (2007-2009)

ADVISORS :

Prof. Eduardo N. Dvorkin (Universidad de Buenos Aires, Argentina)
Prof. Andrew Palmer (Cambridge University, U.K.)

Abstract

The production of oil and gas from offshore oil fields is, nowadays, more and more important. As a result of the increasing demand of oil, and being the shallow water reserves not enough, the industry is pushed forward to develop and exploit more difficult fields in deeper waters.

In this Thesis, a methodology for using the finite element method as a robust engineering tool for analyzing the effect of the manufacturing tolerance on the collapse and post collapse behavior of steel pipes was discussed and illustrated with practical examples.

Even though, using a small strain formulation, the matching between numerical and experimental results was excellent, the model results showed high strains in some areas of the collapsed pipes. Therefore, we developed a new shell element, MITC4-3D, incorporating elasto-plastic finite strains, based in the MITC4 formulation. It was implemented for the analyses of elasto-plastic shell structures and the results indicate that it is a very effective element.

Contents

Chapter 1

Introduction

The production of oil and gas from offshore oil fields is, nowadays, more and more important. As a result of the increasing demand of oil, and being the shallow water reserves not enough, the industry is pushed forward to develop and exploit more difficult fields in deeper waters.

Deepwater pipelines are used to carry oil and gas from wellheads and manifolds to platforms or to shore. Figure 1.1 shows a simple representation of a deepwater installation, with the flow lines on the seabed and the risers, a section of pipeline from the seabed to platforms or ships.

Marine pipelines are constructed by different methods [61]. Figures 1.2, 1.3 and 1.4 show some of them: S-lay, J-lay and reeling technique, respectively. S-lay takes its name from the suspended shape of the pipe at the end of the barge, which lays in an elongated "S" from the stringer to the seabed, while for J-lay, the name is taken from the shape of the suspended pipe, which forms a "J" from the vessel to the seabed.

Regarding reel-lay method, the pipe is assembled onshore and wound onto a large reel on the vessel; before to be J-laid on its final location it has to be unwound and straightened.

As a consequence of the extremely severe work conditions, the constructors of deepwater pipelines need tubular products with enhanced resistance to withstand all the loads that will be applied to the pipeline, both during its construction and in operation; among

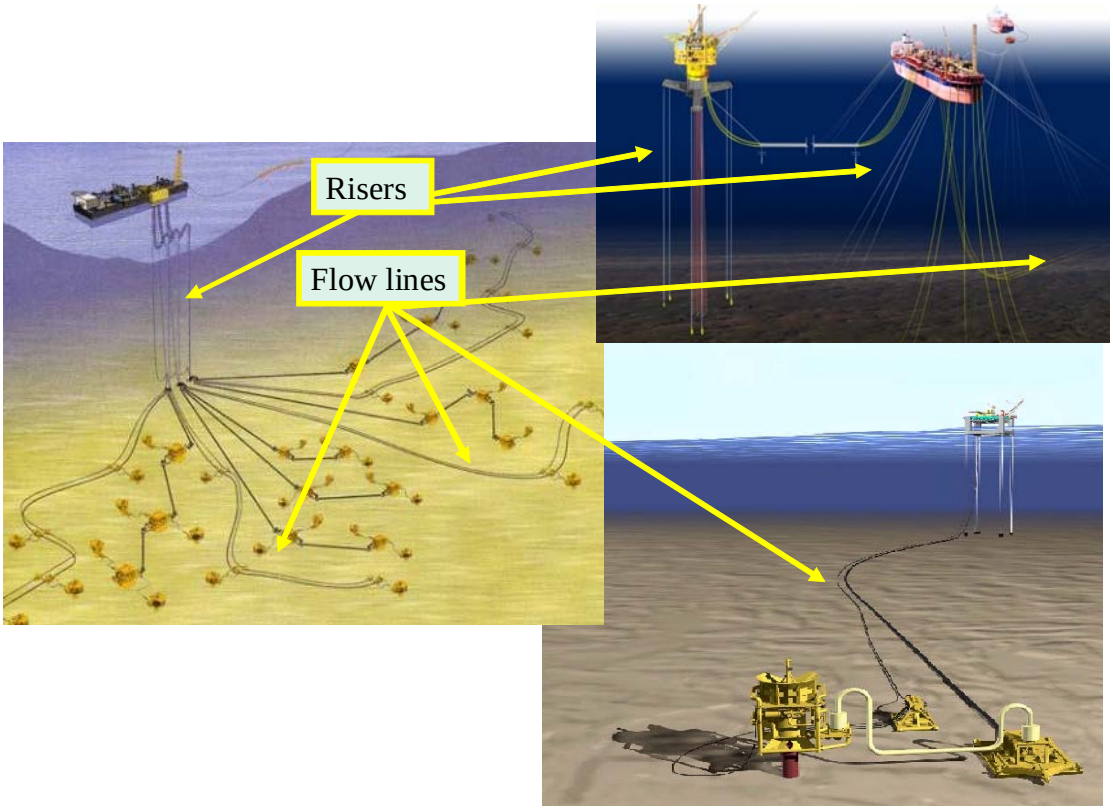

Figure 1.1: Deepwater pipelines.

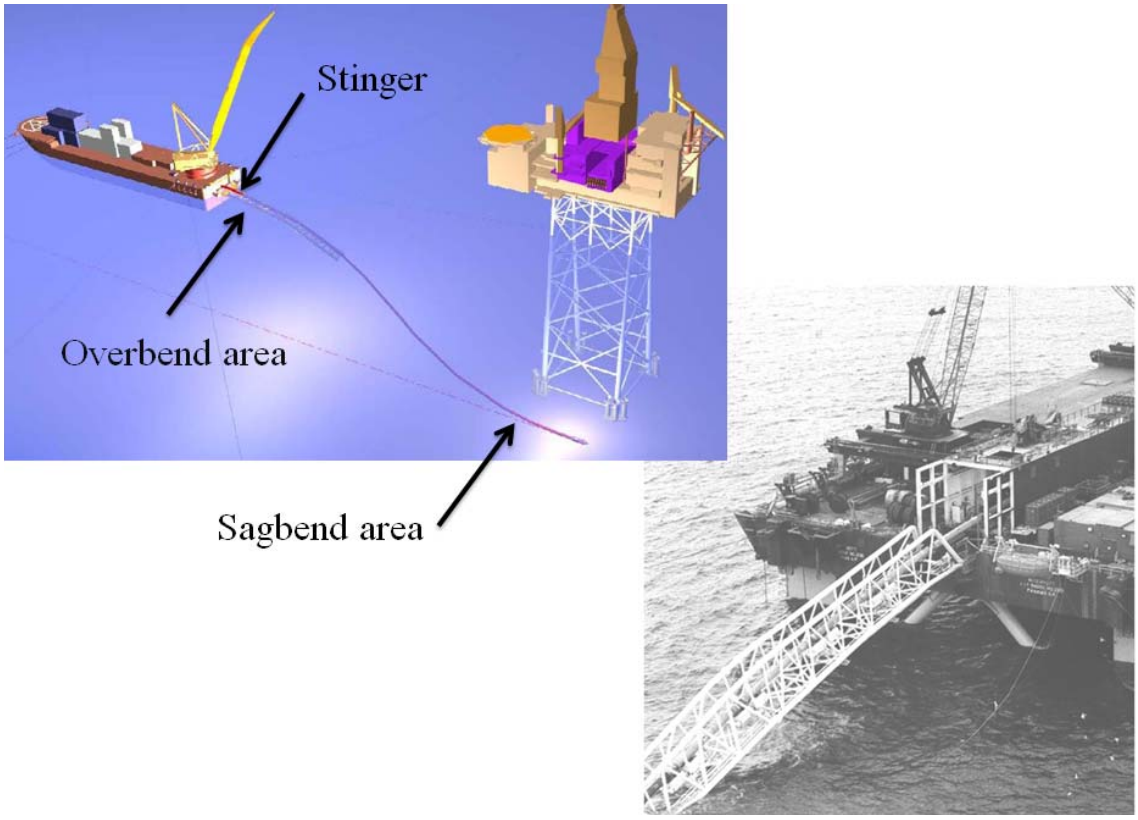

Figure 1.2: S-lay barge pipelaying

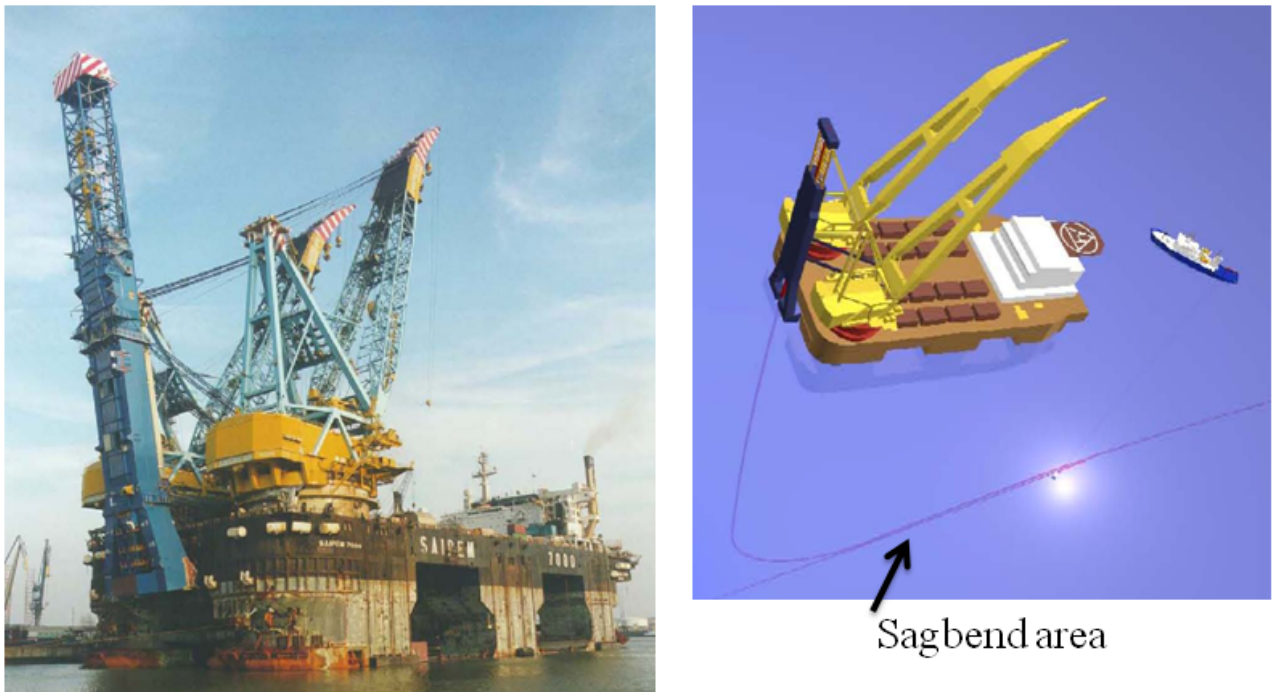

Figure 1.3: J-lay barge pipelaying

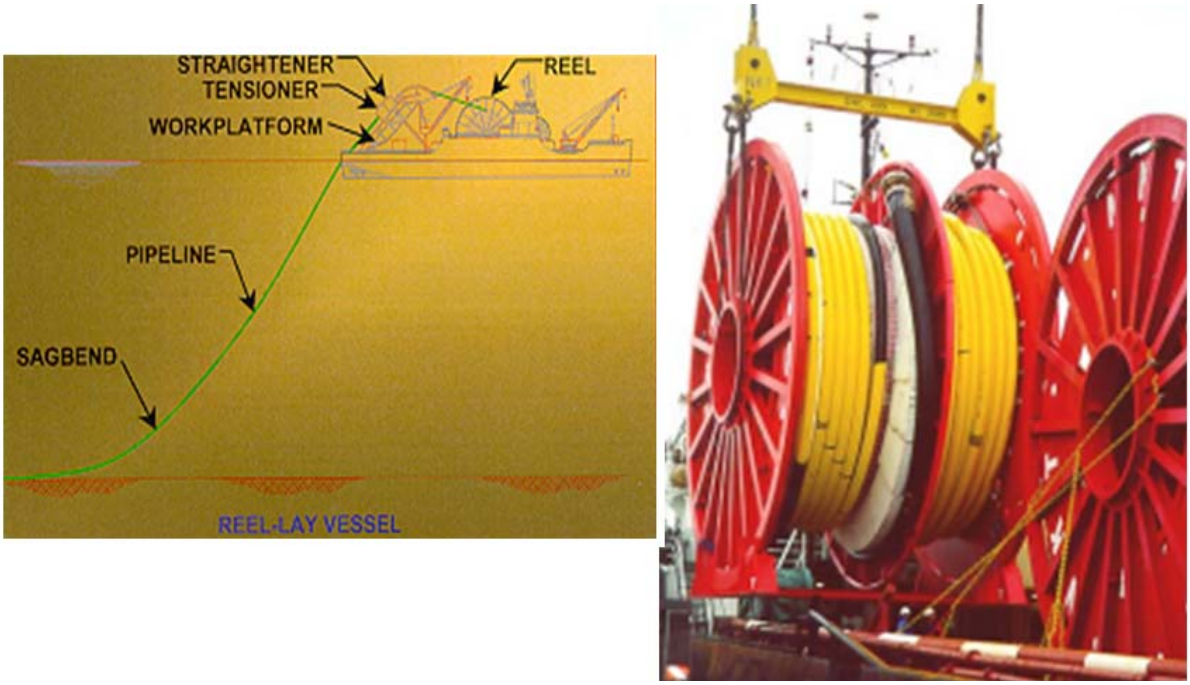

Figure 1.4: Reel-lay barge pipelaying

them: internal and external pressure, bending, fatigue, tension, compression, concentrated loads, impact and thermal load.

A very important issue to take into account is the buckling phenomenon [49] [61]. The pipeline may buckle globally, either downwards (in a free span), horizontally ('snaking' on the seabed), or vertically (as upheaval buckling) (Fig. 1.5); global buckling implies buckling of the pipe as a bar in compression (column mode). If the internal pressure is higher than the external one, it introduces a destabilizing effect. The same problem is encountered in the pipe production process, during the hydrostatic testing, where the pipes are subjected to axial compression and internal pressure. It was demonstrated in [32] and [60] that the pressurized pipe buckling load is lower than the Euler buckling load for the same pipe but under equilibrated internal/external pressures; on the other hand, when the external pressure is higher than the internal one, the resultant pressure has a stabilizing effect.

Figure 1.5: Global buckling

Steel pipes under external pressure may also reach their load carrying capacity due

to a second failure mode: the localized collapse [6] [59]; in this case the pipe structure collapses with its sections loosing their round shape (Fig. 1.6). The local buckle failure mechanism is most common during pipelay, due to excessive bending at the sagbend in conjunction with external overpressure.

Figure 1.6: Local buckling

This thesis is focused on the second failure mode, considering pipes under external pressure only and external pressure plus bending.

In the design of marine pipelines it is very important to be able to determine the collapse pressure of steel pipes subjected to external hydrostatic pressure and bending. It is also required to be able to quantify the effect of shape imperfections, such as ovality and eccentricity, and residual stresses on the collapse strength. The investigation of the post-collapse equilibrium path is also required to assess on the stability of this regime; that is to say, in order to assess if a collapse will be localized in a section or will propagate along the pipeline. Therefore, it is also important to be able to quantify the effect of the geometrical imperfections and of the residual stresses on the post-collapse regime.

The external collapse pressure of very thin pipes is governed by the classical elastic

buckling formulas [19] [77]; however for thicker pipes is necessary to take into account elasto-plastic considerations. The external collapse pressure depends on many factors, among them [22] [38] [40] [45] [47] [54],

- the relation between the outside diameter and the wall thickness ($\frac{OD}{t}$ ratio),
- the yield stress of the pipe (σ_y) and its uniform distribution through the pipe wall,
- the steel work hardening,
- the pipe geometry (outside diameter shape and wall thickness distribution along the pipe),
- the residual stresses (σ_R) locked in the pipe steel during the manufacturing process,
- the localized imperfections in the pipe body.

A pipeline that has been damaged locally or presents some localized imperfections, may fail and, if the hydrostatic pressure is high enough, the collapse may propagate all along the pipeline. The collapse propagation pressure (Pp) is the lowest pressure value that can sustain the collapse propagation [59].

The external collapse propagation pressure is quite lower than the external collapse pressure; hence, in order to avoid the propagation of a collapse buckle and to limit the extent of damage to the pipeline, it is necessary to install buckle arrestors at intervals along the pipeline [44]. Buckle arrestors are devices that locally increase the bending stiffness of the pipe in the circumferential direction. There are many different types of arrestors, as it can be observed in Fig.1.7, but all of them typically take the form of thick-walled rings. The external pressure necessary for propagating the collapse pressure through the buckle arrestors is the collapse cross-over pressure (the minimum pressure value at which the buckle crosses over the arrestor).

Figure 1.8 shows a drawing of the arrestor we are studying: the integral ring buckle arrestor; the curve [*External pressure vs. Internal vol variation*], where we can identify the collapse pressure, the collapse propagation pressure and the cross-over pressure, and

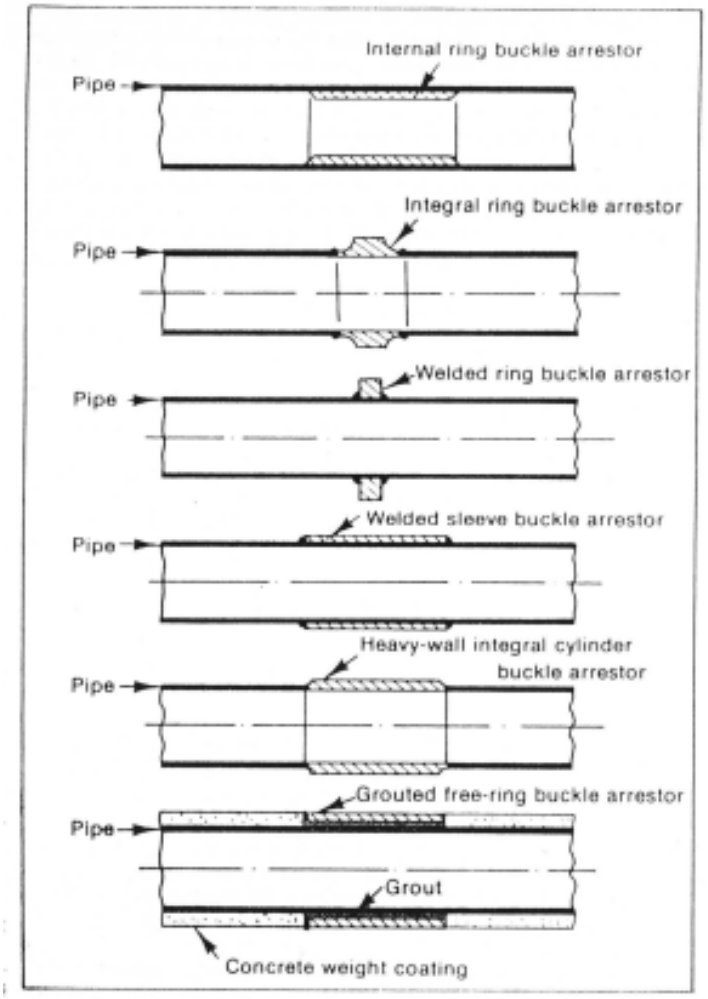

Figure 1.7: Types of buckle arrestors

two arrestors after collapse. In the first case, obviously the external pressure was lower than the cross-over pressure, as the collapse did not cross over the arrestor and the downstream pipe is not collapsed. In the second case, on the contrary, the external pressure was higher than the cross-over pressure, and both, upstream and downstream pipes are collapsed.

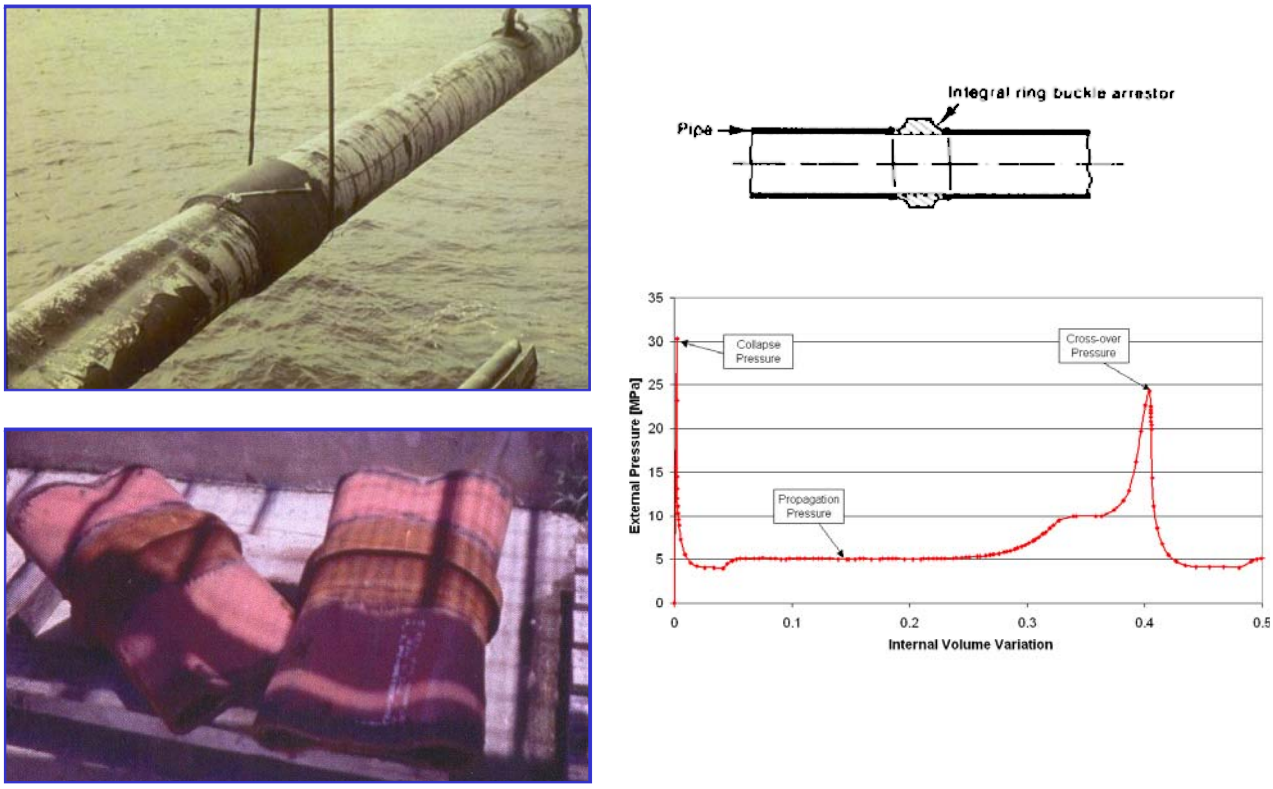

Figure 1.8: Integral ring buckle arrestor

Two different integral buckle arrestor cross-over mechanisms were identified in the literature: flattening and flipping. The occurrence of either cross-over mechanism is determined by the geometry of the pipes and of the arrestors [50] [62]. To validate our numerical results on buckling arresting and cross-over mechanisms, we performed a series of laboratory tests on medium-size carbon steel pipes. Experimental results and numerical analyses are available in the literature for the cross-over of integral ring buckle arrestors under external pressure, on different diameters and materials [44] [51] [55] [56] [57] [62].

From a computational mechanics viewpoint, the topic of tracking the collapse and post-collapse equilibrium path of elasto-plastic structures such as steel pipes, very sensitive to imperfections and that can develop finite strains during its deformation is very challenging. Even tough much research has been dedicated in the last twenty years to this subject there is still ample room for improvement.

Since for the purposes described above numerical models are a fundamental engineering tool, it is of utmost importance to have reliable models that can accurately simulate the pre- and post-collapse behavior of steel pipes under external pressure and bending. In order to assure the reliability of the developed numerical models, it is essential to validate them, by comparing the finite element results with experimental ones.

In Chapter 2 we discuss the determination of the external collapse pressure of steel pipes using finite element models and the effect of some imperfections on the structural behavior of the pipes. We describe some simple 2D finite element models developed as a first approach for the simulation of the external pressure collapse test. We compare the results provided by these 2D models with the experimental results obtained at Tenaris Siderca laboratory; the comparison demonstrates that a 2D geometrical characterization of the pipes does not contain enough information to accurately assess on their collapse strength. However, the 2D models are a useful tool for performing parametric studies on the effects of ovality, eccentricity, residual stresses and work-hardening on the external collapse pressure of the pipes.

To include bending in our analysis, we developed a 3D model of infinite pipes, using MITC4 shell elements that include shear deformation [12] [13] [30]. This model accurately describes the behavior of very long pipes. Considering the pipe dimensions under analysis (in the cases that we analyze $radius/thickness > 8$), the use of shell elements to model the pipes seems to be appropriate as the validations that we performed confirm. We already presented the results and conclusions shown in this Chapter in Refs. [6] [79] [88].

But the pipe shape imperfections and the wall thickness normally change along its length; also localized imperfections can be found in the pipes. Therefore, we also implemented 3D finite element models of finite pipes, developed to overcome the

limitations of the simpler models described previously. The geometrical information on the test samples was acquired using the imperfections measuring system (IMS or "shapemeter") developed at Tenaris Siderca lab, and were used as data for our 3D finite element models [3] [4] [89]. The description of the IMS is included in Appendix A.

In order to build the reliability of the developed numerical models, several tests programs were developed, where we compare the finite element results with the experimental ones obtained at different labs, such as C-FER (Edmonton, Canada) and Tenaris Siderca (Campana, Argentina).

In Chapter 3 we describe the experimental program that we developed to validate the numerical results of the 3D models for external pressure and external pressure plus bending, in the pre and post-collapse regimes [83] [85] [88]. The agreement between the numerical results and the laboratory observations is remarkable good both, in the pre and post-collaspe regimes.

In Chapter 4 we present the analysis of the collapse and post-collapse behavior of pipelines reinforced with buckle arrestors. We developed finite element models to analyze the collapse, collapse propagation and cross-over mechanisms of reinforced pipes under external pressure only and we present an experimental validation of the models. In particular we studied the case of welded integral arrestors [84] [86].

The comparisons between the numerical and experimental results show that the developed finite element models are able to simulate the flattening and the flipping cross-over mechanisms.

The numerical analyzes as well as experimental tests presented in Chapters 3 and 4 refer to seamless pipes. For large diameters, welded pipes are also used. The UOE is one of the available processes for the production of these pipes and it involves the cold forming of long plates. The UOE process is characterized by a forming stage followed by SAW welding and expansion. During the forming stage, the plates are bent into a circular shape by an edge press, and then deformed with the “U” press, and afterwards with the “O” press. Then the formed plate is welded to produce the pipe by SAW process and then expanded with a mechanical expansor to obtain a circular shape. It has been

demonstrated that, for deepwater applications, the cold forming processes involved in UOE pipe manufacturing significantly reduces pipe collapse strength [74].

In Chapter 5 we describe a 2D finite element model of the UOE forming process. The model can simulate the effect of the process parameters corresponding to each forming step on the final geometry and mechanical properties of the pipe, and allow us to evaluate how the different process parameters affect the collapse behavior. A kinematic hardening model is considered in order to incorporate a description of the Bauschinger effect on the final pipe collapse pressures. The results presented in this Chapter were already presented in [87].

Finally, Chapter 6 is devoted to the developement of a new shell element formulation for finite strain analysis.

The shell element MITC4 [12] [13] [30] is nowadays the state-of-the-art element formulation, included under different names in most of the commercial finite element codes. The MITC4 element was developed for material and geometrical nonlinear analyses but small strains.

The infinitesimal strain version of the MITC4 shell element was successfully used for the analysis of deepwater applications of steel marine pipelines. The collapse and post collapse responses were modeled and compared with experimental results, as it was described above. Even though in those verifications the matching between numerical and experimental results was excellent, it was also noticed that in the post–collapse regime very high strains are developed in the steel shell. Therefore, a version of the MITC4 that uses a posteriori updates of the shell thickness was used to incorporate into the model the finite strain behavior. The results indicated that even though the consideration of finite strains improves the solution, the room for improvement - when the overall equilibrium paths are considered - is so small that it hardly justifies the use of a more expensive numerical model. However, if local strains are sought, the finite strain model produces much better approximations to the actual situation. Hence, the motivation for shell element formulations apt for finite strain elasto-plastic analyses is still opened.

A previous attempt to develop the MITC4 formulation valid for large strains elasto-

plastic analyses [36] produced an element which was computationally quite inefficient.

Our new shell element, MITC4-3D, was developed for finite strain analysis [80] [81] [82] using the MITC4 strains interpolation and 3D constitutive relations.

Some of the basic features of our new element are,

- the shell geometry is interpolated using mid-surface nodes and director vectors,
- the node displacements and transverse shear strains are interpolated using the original MITC4 formulation,
- for interpolating the director vectors special care is taken to avoid spurious director vector stretches,
- additional degrees of freedom are considered to include a linear thickness stretching. These thickness-stretching degrees of freedom are condensed at the element level,
- the elasto– plastic formulation is developed following the work of Simo and co-workers, multiplicative decomposition of the deformation gradient tensor and maximum plastic dissipation (associate plasticity),
- we use a general 3D constitutive relation instead of the original laminae plane stress constitutive relation,
- special consideration is given to the formulation efficiency.

As a first stage to test the new formulation, in [81] [82] we considered only hyperelastic material models while in [80] we showed some simple examples considering finite strain elasto–plastic analyses.

In this thesis the new element was implemented for the analyses of elasto-plastic shell structures and the results indicate that it is a very effective element.

Chapter 2

Collapse and post-collapse behavior of steel pipes: Finite Element Models

2.1 Introduction

The main objective of this Chapter is to discuss some basic ideas regarding the behavior of steel pipes under external pressure and bending.

In Section 2.2 we describe some simple 2D finite element models that we developed as a first approach for the simulation of the external pressure collapse test. We compare the results provided by these 2D models with the experimental results obtained at Tenaris Siderca lab. The comparison demonstrates that a 2D geometrical characterization of the pipes does not contain enough information to assess on their collapse strength. However, the 2D models are a useful tool for performing parametric studies on the effects of the ovality, eccentricity, residual stresses and work-hardening of the pipes on the external collapse pressure values.

In section 2.3 we develop a 3D model to describe the behavior of very long pipes. This model can simulate the behavior of the pipes not only under external pressure but also

under bending.

In section 2.4 we present the 3D finite element models of finite pipes, and we use it to study the correct measurement of the residual stresses. In the next Chapter we will incorporate in the model a proper description of the pipe geometry.

2.2 Two dimensional finite element model of very long pipes

In this Section we discuss the 2D finite element models that we implement to simulate the behavior of ideal long specimens in the external pressure collapse test. We also compare experimental results with the predictions of these 2D models.

2.2.1 Formulation of the 2D models

We develop the 2D finite element models using a total Lagrangian formulation [9] that incorporates,

- geometrical nonlinearity due to large displacements/rotations (infinitesimal strains assumption),
- material nonlinearity, an elasto-plastic constitutive relation is used for modeling the steel mechanical behavior (von Mises associated plasticity [42]).

We develop the finite element analyses using a special version of the general purpose finite element code ADINA [76] that incorporates the quadrilateral QMITC element [29] [33] [34].

For modeling the external hydrostatic pressure we use follower loads [19], and we introduce in our models the residual stresses with a linear distribution across the thickness.

When using a 2D model it is important to recognize that the actual collapse test is not modeled exactly neither by plane strain nor by plane stress models because the absence

of longitudinal restraints imposes a plane stress situation at the sample edges and the length L of the samples ($L/D > 10$) approximates a plane strain situation at its center.

In this Section, in order to explore the limitations of the 2D models we analyze the collapse test using both, plane stress and plane strain finite element models.

2.2.2 Two dimensional finite element results vs. experimental results

The 2D finite element models are developed considering an elastic-perfectly plastic material constitutive relation. We will show in Section 2.2.3 that disregarding the steel work-hardening introduces only a negligible error in the calculated collapse pressures.

For standard tests, the laboratory keeps, for each sample, records of the average, maximum and minimum outside diameter (D) at three sections (the central section and the two end sections) and thicknesses (t) at the two end sections (eight points per section).

We construct the geometry of the 2D finite element models using,

- the ovality (Ov) and the average outside diameter of the central section,
- the eccentricity (ε) obtained by averaging the eccentricities of the two end sections and the average thickness obtained by averaging the sixteen thickness determinations.

The ovality and eccentricity are defined as,

$$Ov = \frac{D_{\max} - D_{\min}}{D_{average}} \qquad (2.1)$$

$$\varepsilon = \frac{t_{\max} - t_{\min}}{t_{average}}$$

The residual stresses for each sample are measured using a slit-ring test. The actual transversal yield stress of the sample material is measured and its value is used for the elastic-perfectly plastic material constitutive relation.

To determine the collapse loads of the sample models we calculate the nonlinear load-displacement path and seek for its horizontal tangent.

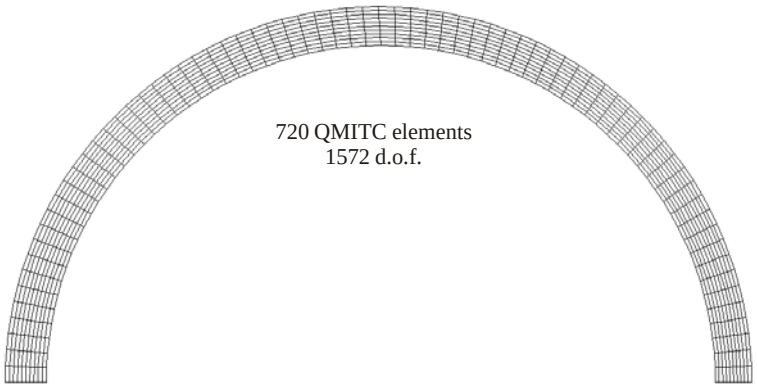

Figure 2.1: 2D finite element mesh

To perform the numerical analyses we use a 2D mesh with 720 QMITC elements (Fig. 2.1) and 1572 d.o.f. Half of the pipe is modeled due to symmetry. To assess on the quality of this mesh we analyze the plane strain collapse of an infinite pipe and we compare our numerical results against the analytical results obtained using the formulas in Ref. [77]. From the results in Table 1 we conclude that the proposed 2D mesh of QMITC elements is accurate enough to represent the collapse of very long specimens.

$Average\ OD\ [mm]$	245.42
$Average\ thickness\ [mm]$	12.61
$\frac{D}{t}$	19.47
$o_v\ [\%]$	0.18
$\sigma_y\ [Mpa]$	890
$\frac{Theoretical\_result}{FE\_result}$	0.992

Table 1. Qualification of the 2D finite element model

From the analyses of different cases we identified two basic types of load /displacement paths. In Fig. 2.2 we present both, direct and inverse collapse behavior of eccentric pipes. The latter case was previously identified in the literature for the case of collapse under external pressure and bending [23] [37].

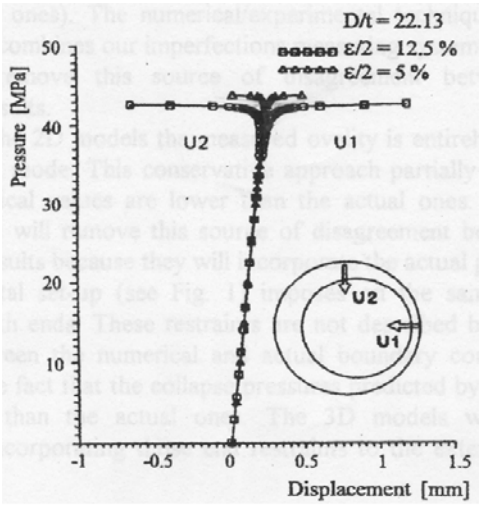

Direct collapse behavior

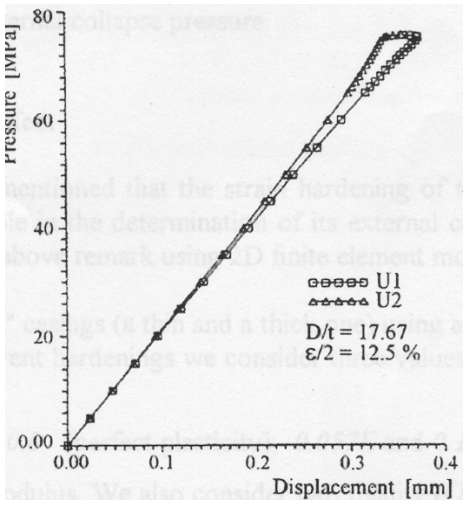

Inverse collapse behavior

Figure 2.2: Eccentric tube: direct collpase behavior (D/t=22.13) and inverse collpase behavior (D/t=17.67)

A total of 32 collapse tests, for casings 9 5/8" OD 47lb/ft and 7" OD 26lb/ft both Grade 95 Ksi, were analyzed using plane stress and plane strain models. The comparisons between the numerical and experimental results are plotted in Fig. 2.3.

It is important to observe that the collapse pressure values determined using the 2D models present a significant deviation from the experimental ones, being in general the former lower than the latter. Some reasons for this behavior are,

- the middle section ovality is not fully representative of the sample geometry,
- in developing the 2D models the measured ovality is entirely assigned to the first elastic buckling mode. This conservative approach partially accounts for the fact that the numerical values are lower than the actual ones,
- the experimental set-up used in these tests (Fig. 2.4) imposes on the samples unilateral radial restraints at both ends. These restraints are not described by the 2D models; the difference between the numerical and actual boundary conditions

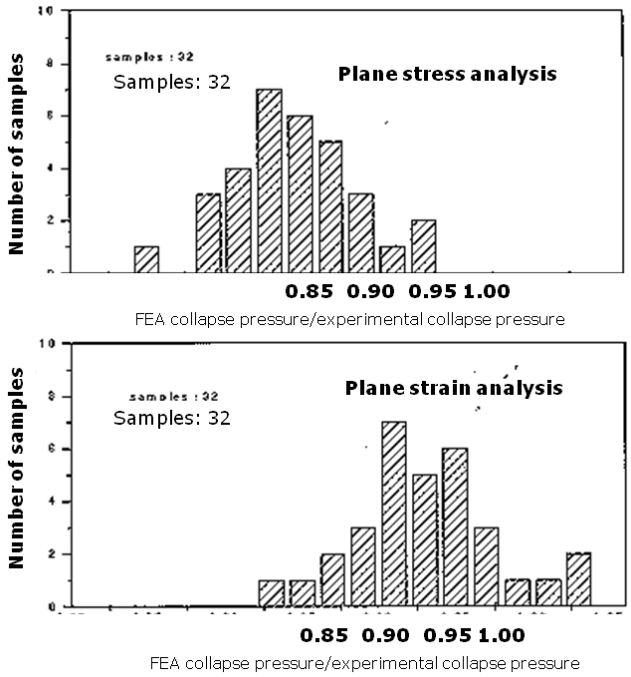

Figure 2.3: Qualification of the 2D models. FEA collapse pressure/experimental collapse pressure. 9 5/8" OD 47# and 7" OD 26# SD95HC

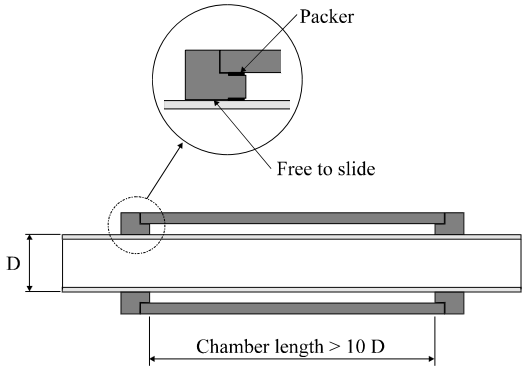

Figure 2.4: Collapse chamber

also partially accounts for the fact that the collapse pressures predicted by the 2D models are in general lower than the actual ones.

It is obvious, from the results in Fig. 2.3, that the 2D geometrical characterization of a pipe is not enough for assessing on its collapse performance. However, the 2D models are very useful for performing parametric studies on the relative weight of different factors that affect the external collapse pressure.

2.2.3 Strain hardening effect

It was already mentioned that the strain hardening of the casing material does not play an important role in the determination of its external collapse pressure. In this Section we examine the above assessment using 2D finite element models.

We analyze two 9 5/8" pipes (a thin and a thick one) using a bilinear material model. In order to explore different hardening values we consider three values for the constant plastic tangential modulus: $E_t = 0.0$ (perfect plasticity), $0.057E$ and $0.10E$, where E is the Young modulus. We also consider two ovality (Ov) values but we do not include in this analysis neither the pipe eccentricity nor its residual stresses. We summarize the numerical results of our analyses in Table 2.

$\frac{D}{t}$	Ov [%]	$E_t = 0.0$	$E_t = 0.057E$	$E_t = 0.1E$
17.66	0.75	59.9	60.2	60.4
17.66	0.35	67.1	67.3	67.5
24.37	0.75	26.7	26.7	26.7
24.37	0.35	29.0	29.1	29.1

Table 2. Analysis of the work-hardening effect on the external collapse pressure [Mpa]

As it can be seen, for all the analyzed cases, the strain hardening has a negligible effect on the external collapse pressure value.

It is important to recognize that in the above analyses we considered σ_y to be independent of E_t. This is not the case if as yield stress we adopt the one corresponding to a relatively large permanent offset [78].

2.2.4 Effect of ovality, eccentricity and residual stresses

Using 2D finite element models we conduct a parametric study aimed at the analysis of the effect, on the casing collapse pressure, of the ovality (Ov), eccentricity (ε) and residual stresses (σ_R).

In the present analyses the ovality is considered to be concentrated in the shape corresponding to the first elastic buckling mode and the eccentricity is modeled considering non-coincident OD and ID centers.

In Fig. 2.5 we plot the results of our parametric study, normalized with the collapse pressure calculated according to API Bulletin 5C3 (1994). It is obvious from these results that the main influence on the external collapse pressure comes from the ovality and from the residual stresses; however, the effect of the residual stresses diminishes when the ratio (D/t) evolves from the plastic collapse range to the elastic collapse range. The eccentricity effect, in the case of the external collapse test with neither axial nor bending loads, is minor.

Most of the literature dealing with casing collapse pressure agrees on the importance of the ovality effect [38] [45] [47] [54] [78].

As a conclusion of the above parametric study we can assess that for producing pipes with enhanced collapse pressure it is very important to have both, a low ovality and low residual stresses.

2.3 Three dimensional finite element model of very long pipes

In the previous Section we presented finite element models developed for studying the collapse behavior of long steel pipes under external pressure; our purpose in the present Section is to extend the study to the post-collapse regime and to loading cases that combine external pressure and bending [79].

We develop a numerical model to simulate the behavior of a very long pipe (infinite pipe) and determine its pre and post-collapse equilibrium path. Using this model we perform parametric studies in order to investigate the significance of the different geometrical imperfections and of the residual stresses on the collapse and collapse propagation pressures.

2.3.1 Formulation of a 3D model for very long pipes

The finite element models were developed using the nonlinear shell elements in the general-purpose finite element code ADINA [76]. The main features of the finite element models are,

- MITC4 shell element (4-node element that includes shear deformations) [12] [13] [30],
- automatic solution of the incremental nonlinear finite element equations [11],
- material non-linearity: elasto-plastic material with multilinear hardening; associated plasticity according with the von Mises yield rule and isotropic or kinematic

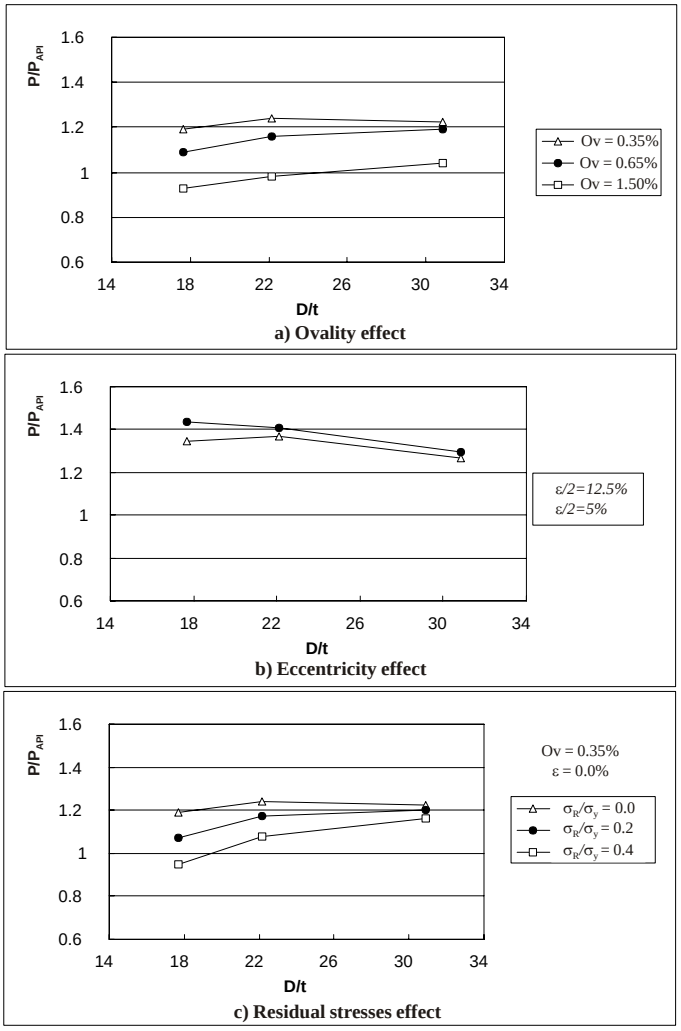

Figure 2.5: Parametric study of the effect of ovality, eccentricity and residual stresses on the casing collpase pressure.

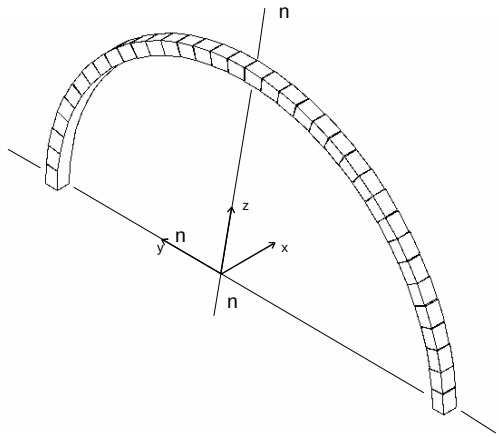

Figure 2.6: Finite element mesh for the analysis of very long pipes

hardening [9],

- geometrical nonlinearity: large displacements / rotations [9].

For the cases with external pressure plus bending we first impose the bending and then the external pressure keeping constant the imposed curvature.

In Fig. 2.6 we present the finite element mesh, which we use for the analysis of very long pipes (the evolution of the cross section shape does not depend on the axial coordinate).

Boundary conditions

- In one of the transverse planes ($x = constant$), both the axial displacements and the rotations respect to $n - n$ axis are restricted.

- The other transverse plane is free to move in the x direction, but is restricted to stay flat (see the constraint equations below). In case it is necessary to model plane strain condition, the movement of this plane is also restricted.

- Rotations are restricted according to the symmetry conditions with respect to the plane $z = 0$.

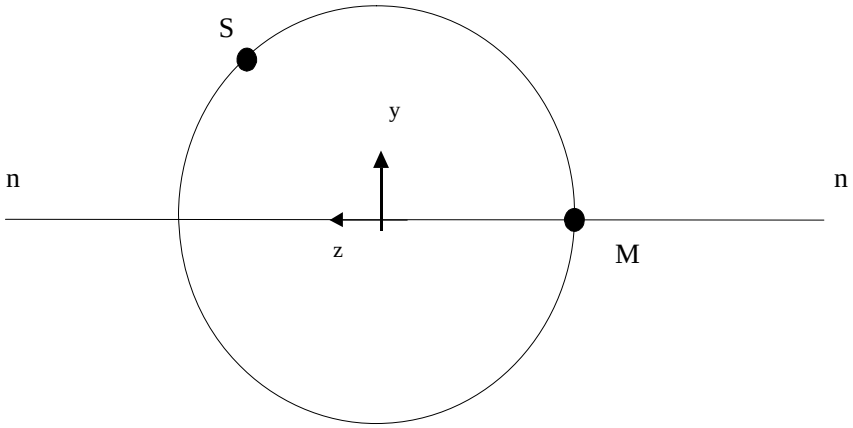

Figure 2.7: Master and slave nodes on the axially unrestricted section

- In order to avoid rigid body displacements, a minimum number of additional constraints is applied.

To be sure that the section keeps plane when bending is applied, we impose constraint equations.

Fig. 2.7 shows, for the nodes on the section with unrestricted axial displacements, the "Master" and "Slave" nodes.

The master node M is one of the two nodes on the intersection between the cross section and the neutral axis corresponding to the applied bending, on the axially unrestricted section. All the other nodes in that section are the slave nodes S.

The constraint equations are,

$$\begin{aligned} u_S &= u_M + \theta_z^M \ (y_S - y_M) + \theta_z^M \ (\nu_S - \nu_M) \\ \theta_z^S &= \theta_z^M \end{aligned}$$

In the above equations,

y : initial y coordinate,

u: displacement along the x axis,

v: displacement along the y axis,

θ_z: rotation with respect to the $n-n$ axis.

It is important to take into account that when the sample is long enough ($L/D > 10$) the end conditions have only a very small influence on the collapse pressure [38].

Following with the example described in Table 1, we compared the results obtained using the two different shell models,

- Short model with no axial displacements (shell under plane strain conditions)
- ($L/D = 10$) model with the ends restrained to remain on a plane (welded end cups)

The results summarized in Table 3 indicate the equivalence of both models. For cases with ($L/D < 10$) we may expect the end conditions to play a more significant role.

Short model under plane strain conditions	$\frac{Theoretical\_result}{FE\_shell\_PS} = 0.980$
Long model; $\frac{L}{D} = 10$	$\frac{Theoretical\_result}{FE\_shell\_long} = 0.978$

Table 3. Long shell model compared with plane strain shell model

2.3.2 Validation of the finite element model

In order to validate the finite element model we introduced, in the present Section we analyze a series of cases presented by S. Kyriakides in [48].

Even tough the pipes analyzed by S. Kyriakides are of smaller outer diameter and different material characteristics (aluminium) than the pipes that we analyze with our model, the mechanism of the collapse behavior is identical; hence, after the validation of the model, we use it on typical seamless pipes.

In the test cases, Kyriakides adopted a bilinear law.

Figure 2.8 shows the curves [*External pressure vs. Radial displ./R*] for a pipe with $D/t = 35$, $D = 1.2522$", $E/\sigma_y = 225$ and $\sigma_y = 31.5\ kg/mm^2$; it can be observed from

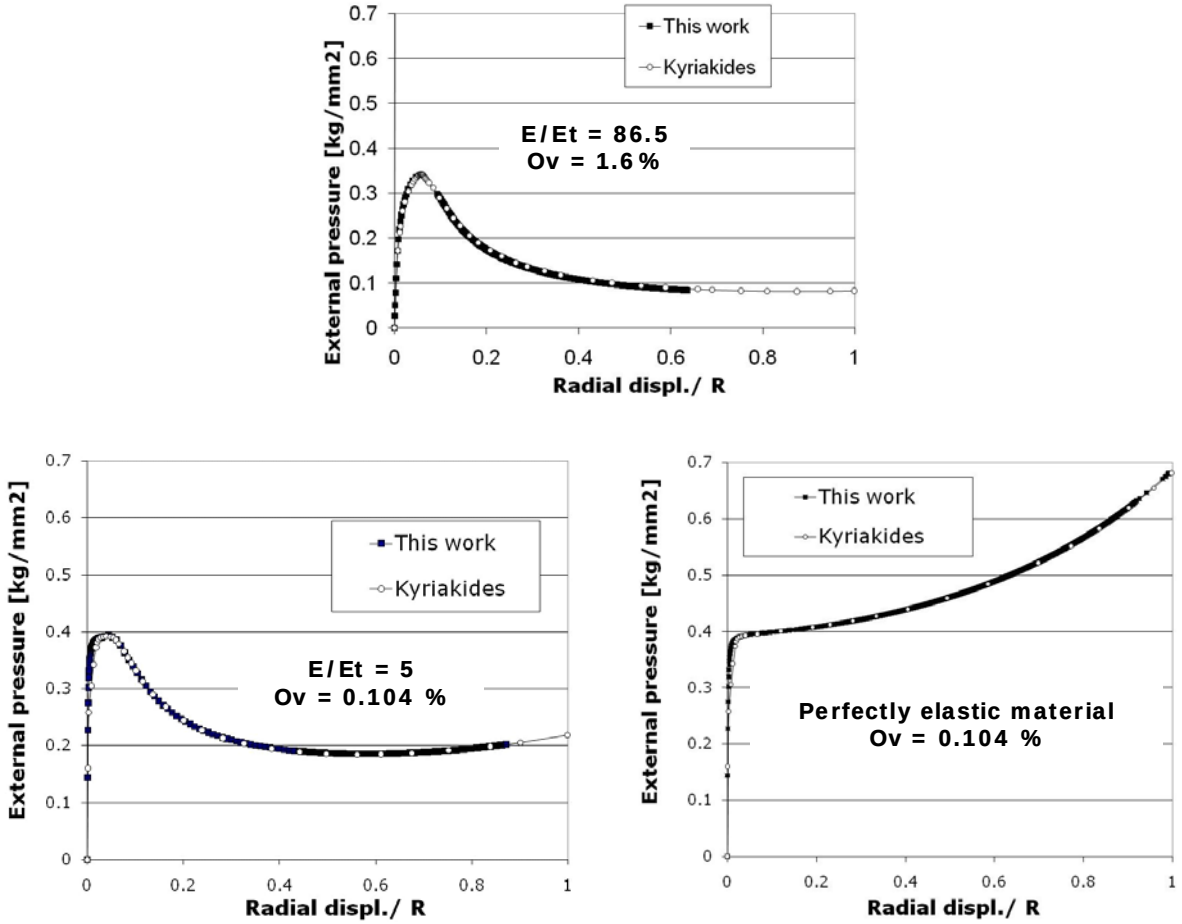

Figure 2.8: Infinite tube. Qualification of the finite element model for the pre and post-collapse equilibrium path

the comparison of those results that our results coincide with the results published by S. Kyriakides, both in the pre critical and post critical regime.

2.3.3 Pipes under bending plus external pressure.

In this section we investigate the pre-collapse, collapse and post-collapse behavior of steel pipes that are first bent and afterwards loaded with an increasing external pressure load up to collapse.

From the finite element results we obtain two important values: the critical external

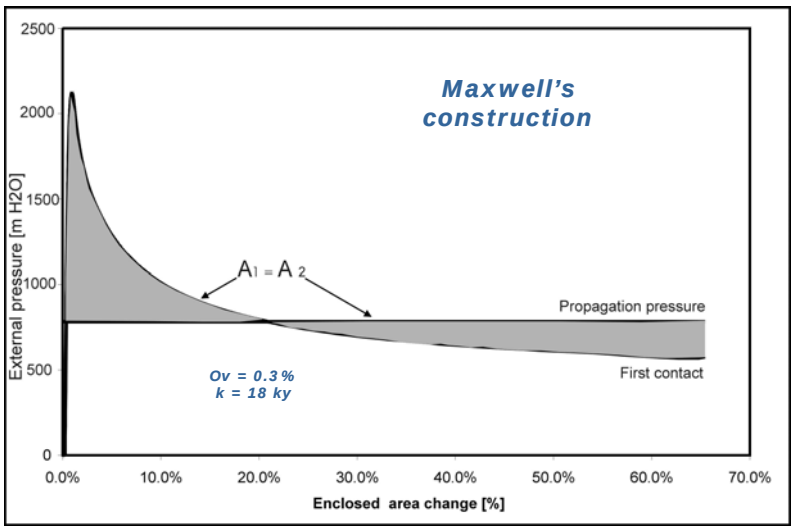

Figure 2.9: Pressure-displacement characteristics of a long pipe under external pressure

pressure (buckling initiation) and the buckling propagation pressure [59]. In order to determine the buckling propagation pressure it is necessary to make the Maxwell construction [48], using the [*Pressure vs. Enclosed area change diagram*] which is post-processed from the finite element results (Fig. 2.9). The propagation pressure is a very important property of the tubular material, since local bumps that drastically diminish the pipes collapse pressure are unavoidable (either during the pipeline construction or during its operation), it is important that the pipeline engineer designs the pipeline buckle arrestors using the proper propagation value.

To illustrate on the actual deformation pattern of the pipe sections, in Fig. 2.10 we show the results of a finite element analysis. In Fig. 2.9 as well as Fig. 2.10 there are some distinct features to be recognized,

- the first stage of the deformation, from $p = 0$ up to the peak pressure is the pre-buckling regime (e.g. point A, Fig. 2.10),

- the peak pressure is the collapse pressure,

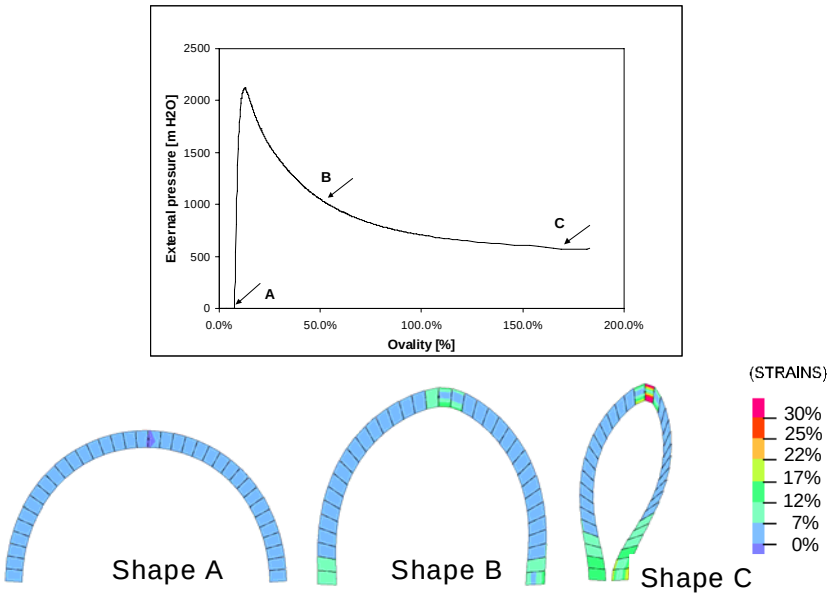

Figure 2.10: Shape of the pipe cross section during the pre-buckling (A) and post-buckling regimes (B and C). 8 5/8" OD 12.7 mm X60 pipe, initial ovality 0.3%

- from the collapse pressure onwards, up to the final stage in which points on the inner surface of the pipe make contact among them, we have the post buckling regime (e.g. point B and C, Fig. 2.10).

Effect of the pipe ovality

In this section we are going to investigate how the pipe bending curvature and its initial ovality influence the pipe critical and buckling propagation pressure.

In what follows we use the notations,

k : constant bending curvature imposed on the pipe, kept constant during the external pressure test.

k_y: value of the constant bending curvature that takes the pipe most stressed point into the plastic regime.

We analyze the behavior of an 8 5/8" OD 12.7 mm WT X60 pipe, with a moderate initial ovality. We represent the external pressure vs. the resulting ovality for each pressure level (we calculate the resulting ovality, adding to the initial values of $D_{\max}$ and $D_{\min}$ the corresponding node displacements). Figure 2.10 shows that the initial ovality is absolutely negligible when compared with the ovality induced by the loading; even the ovality corresponding to point A, that is to say the ovality induced by bending (Brazier effect), is much larger than the initial ovality.

Even tough the initial ovality has a strong influence on the critical collapse pressure when no bending is applied, as it was shown in the previous section, the effect of the initial ovality on the critical collapse pressure diminishes when the imposed curvature is increased. If a perfectly round tube is bent the cross section is ovalized ("Brazier effect"), when the bending increases, the Brazier-ovality grows and therefore the initial ovality becomes less important as compared with this bending-induced ovality.

In Fig. 2.10 we represent the initial shape of the pipe cross section and its shape for the moment at which the inner surface closes onto itself. Please notice the strong asymmetry of the final cross section (point C).

In Fig. 2.11 we measure the applied curvature with the radius "R" and with the maximum bending strain (as a reference we indicate the radius of a typical reel used to lay marine pipelines).

The effect of the pipe initial ovality on their collapse propagation pressure is negligible for any bending situation, as shown in Fig. 2.12.

Effect of the pipe eccentricity

For low values of applied bending the eccentricity effect on the pipes collapse pressure is much lower than the ovality effect, and it is almost independent of the applied bending (Fig. 2.13). The eccentricity effect on the pipes collapse propagation pressure is not very relevant either (Fig. 2.14)

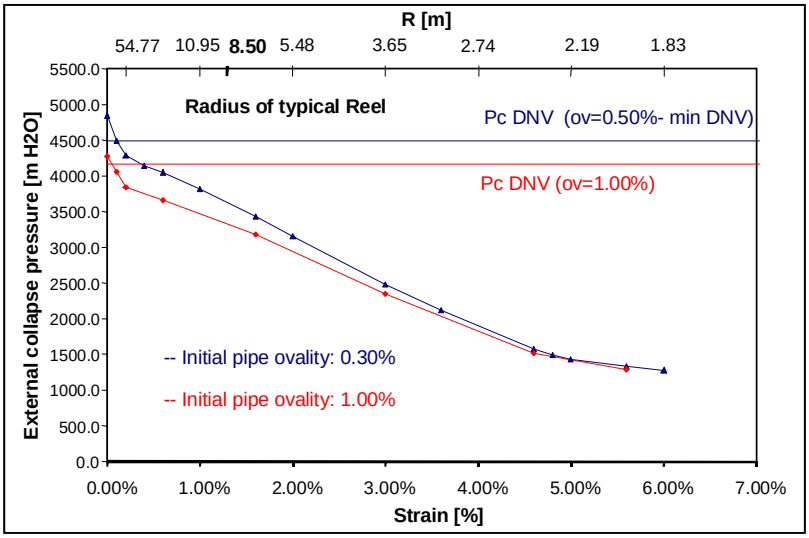

Figure 2.11: Infinite pipe model. Ovality effect on the collapse pressure. 8 5/8" OD 12.7 mm X60 pipe

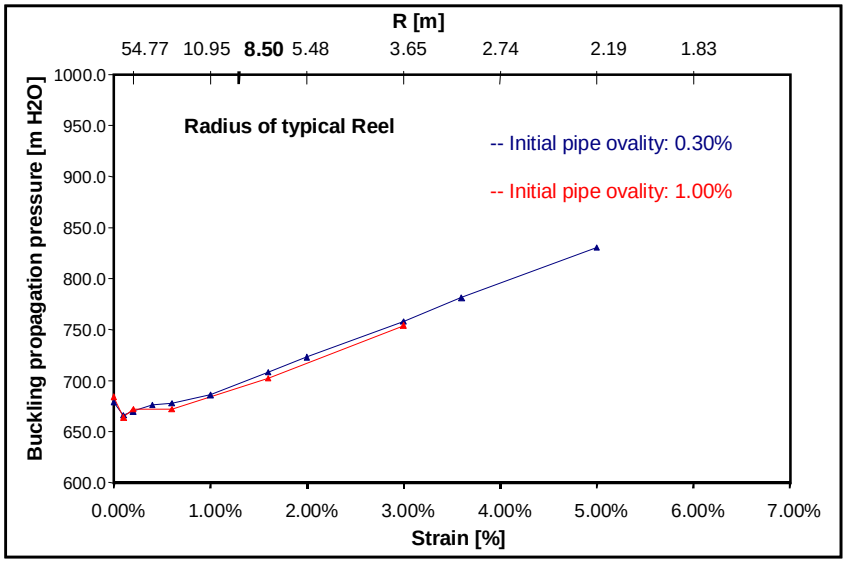

Figure 2.12: Infinite pipe model. Ovality effect on the collapse propagation pressure. 8 5/8" OD 12.7 mm X60 pipe

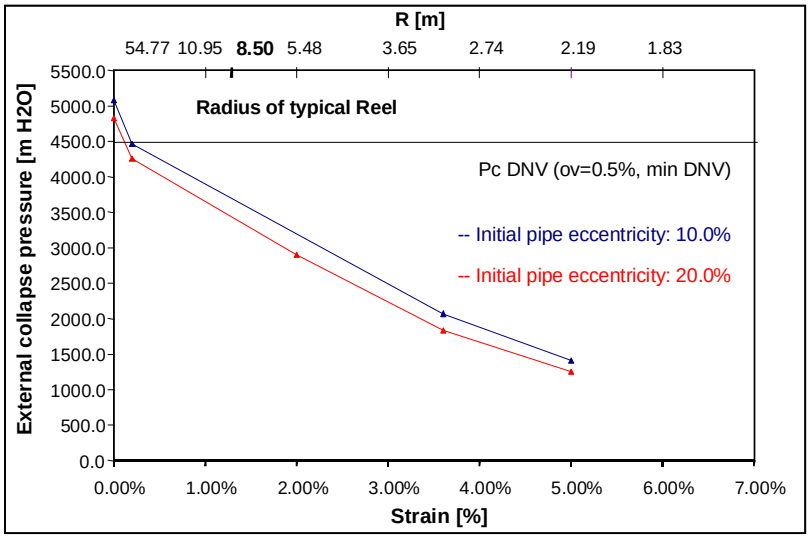

Figure 2.13: Infinite pipe model. Eccentricity effect on the external collapse pressure. 8 5/8" OD 12.7 mm X60 pipe

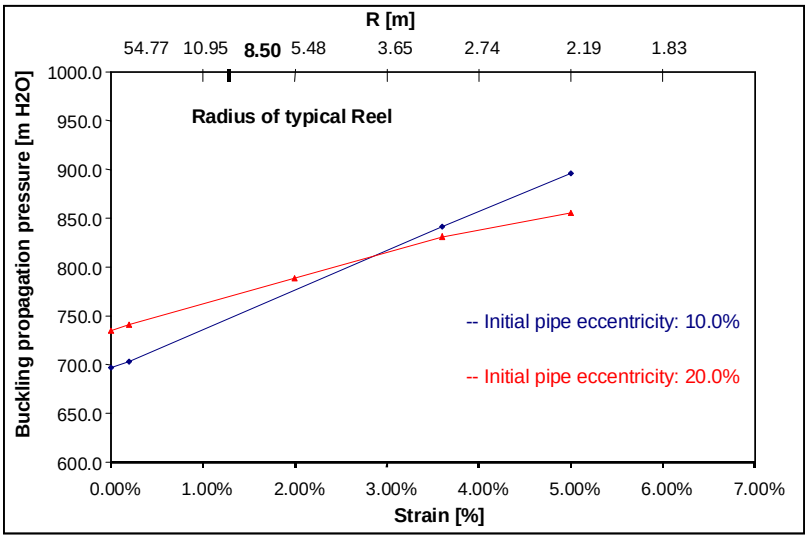

Figure 2.14: Infinite pipe model. Eccentricity effect on the collapse propagation pressure. 8 5/8" OD 12.7 mm X60 pipe

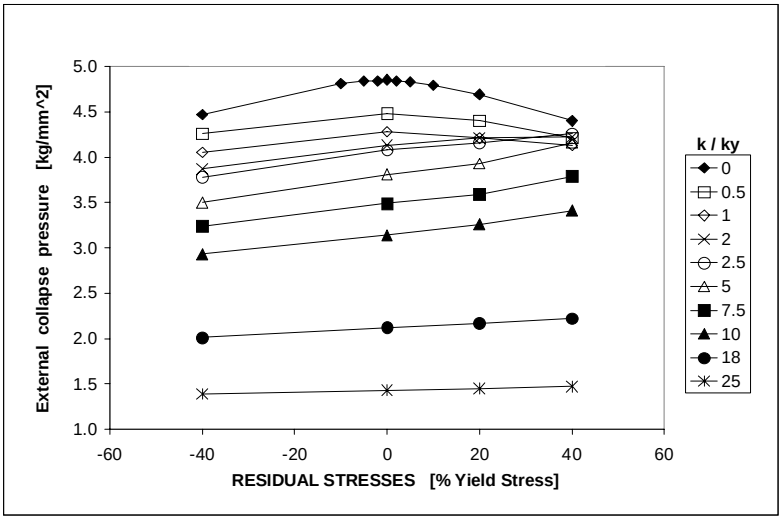

Figure 2.15: Infinite pipe. Residual stresses effect on the external collapse pressure (σ_R>0 indicates compression at the inner radius). 8 5/8" OD 12.7 mm X60 pipe

Effect of the pipe residual stresses

In Figs. 2.15 and 2.16 we present the effect of the residual stresses on the collapse pressure and collapse propagation pressure, for various values of imposed bending (the bending is measured, in these figures, with the relation between the imposed curvature k and the curvature that yields the most strained fiber of the pipe section k_y).

The effect of the residual stresses on the external collapse pressure depends on the applied bending. For the lower values of curvature, the external collapse pressure decreases when the residual stresses absolute value increases, but for higher bending the collapse pressure increases when the residual stresses change from negative to positive values. Anyway, the effect of the residual stresses on the pipe critical collapse pressure is quite low when a strong bending is applied.

The effect of the residual stresses on the collapse propagation pressures is not very important, with or without bending.

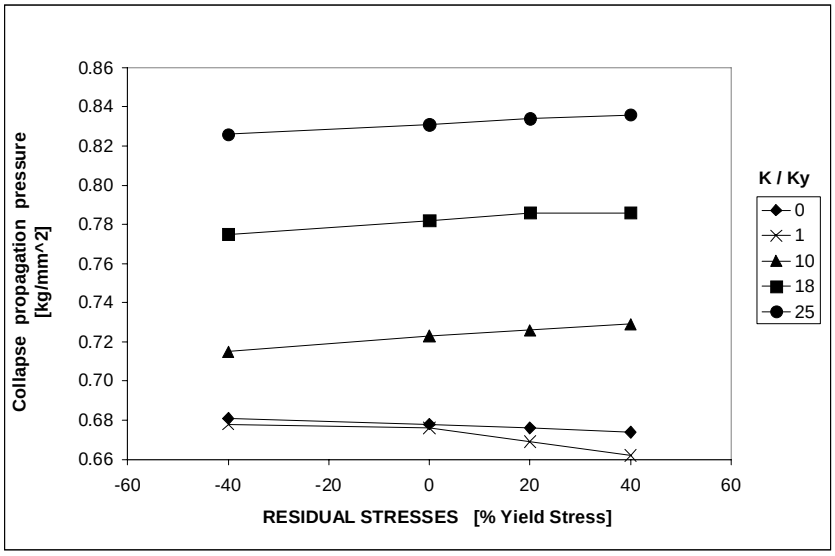

Figure 2.16: Infinite pipe. Residual stresses effect on the collapse propagation pressure. 8 5/8" OD 12.7 mm X60 pipe

Effect of the imposed bending

As it can be seen in the above figures bending diminishes the external collapse pressure of the pipes, due to the fact that it increases its ovality ("Brazier effect").

It is also interesting to observe that bending increases the collapse propagation pressure.

2.4 Three dimensional finite element model of finite pipes

Following what we did above, we use a total Lagrangian formulation that incorporates the geometrical nonlinearity coming from the large displacements /rotations and the material nonlinearity coming from the elasto-plastic constitutive relation. We develop the finite element analyses using the code ADINA [76] and the MITC4 shell element.

As in the previous Section, follower loads are used to model the hydrostatic external

pressure and the residual stresses are modeled with a linear distribution through the thickness.

2.4.1 Residual stresses

We use the slit ring test at our laboratory for measuring the residual stresses in the pipe samples [47] [53] [75]. As we see from Fig. 2.5 the correct measurement of the residual stresses is fundamental for determining the external collapse pressure of a pipe under external pressure only.

When implementing the slit-ring test some laboratories use long slit-ring samples ($L/D > 3$) and other laboratories use short slit-ring samples ($L = 25\ mm$). We prefer to use long samples because they represent the averaged effect of the residual stress distribution.

Slit-ring test: long samples vs. short samples

From a 9.5/8" OD 53.5 lb/ft P110 pipe, 16 long samples ($L = 3D$) and 16 short samples ($L = 25\ mm$) were obtained. The samples were cut and slit open by machining; no torch cutting was used. All the samples were slit open along a generatrix.

To determine the residual stresses the measured openings were post-processed according to the following formula, for long samples (approx. plane strain),

$$\sigma_R = \frac{a\ t\ E}{4\pi R^2\ (1-\nu^2)} \tag{2.2}$$

and for the short ones (approx. plane stress),

$$\sigma_R = \frac{a\ t\ E}{4\pi R^2} \tag{2.3}$$

where,

a: opening of the slit-ring sample,

t: average thickness of the sample (averaged over eight determinations),

E: Young's modulus of the steel,

ν: Poisson ratio of steel,

$R = \frac{D-t}{2}$,

D: outside diameter of the sample before the test (averaged over three determinations).

In Table 4 we summarize the results obtained for the same pipe, with the long and short samples.

Residual stresses	*Long samples*	*Short samples*
Average $[MPa]$	243	217
Standard deviation$[MPa]$	19	39
Maximum $[MPa]$	276	278
Minimum $[MPa]$	217	153

Table 4. Slit-ring tests performed on one pipe

The results obtained with the short samples present a larger dispersion than the results obtained with the long samples. Since the cutting, slitting and measuring techniques employed for both kind of samples are the same, we can correlate the largest dispersion in the short sample results with the physics of our problem: the pipe residual stresses are variable point-to-point and the short samples measure local values while the long samples average the values over a length equal to three diameters.

Since, for determining the casings collapse pressure, the average value of the residual stresses is more significant than local values, we recommend to use slit-ring test samples with $L = 3D$.

Three dimensional simulation of the slit-ring test

To check the capability of our 3D finite element models to simulate different residual stress patterns we consider a 9 5/8" OD 47 lb/ft P110 casing with $\sigma_y = 758MPa$ and $\sigma_R = 0.2\ \sigma_y$.

We calculate the value of the samples opening in a slit-ring-test using the analytical relation (2.3) and (2.2) between residual stresses and sample openings as well as using the 3D finite element model shown in Fig. 2.17, where the residual stresses are simulated with a linear distribution across the thickness and the slit of the cylindrical sample is simulated by removing a row of elements.

The results are shown in Table 5. Hence, our 3D finite element procedure for representing the residual stresses can be considered as realistic enough.

Sample length	$\frac{a_{FEA}}{a_{analytical}}$
25 mm	1.02
$3D$	0.99

Table 5. Validation of the residual stresses simulation using 3D finite element models

2.5 Main observations

It was shown that the models of very long pipes do not contain enough information on the sample geometries to provide accurate predictions on the collapse pressure. However, they are very useful for developing parametric studies.

Using those models, we analyzed the pre and post-collapse regimes of very long pipes, and the effect of the initial ovality, eccentricity and residual stresses on the collapse and collapse propagation pressures.

From our numerical results we draw the following conclusions,

- the initial ovality has very important influence on the pipe collapse pressure when only external pressure is applied, but this influence diminishes as the bending curvature increases,

- the initial ovality has a negligible influence on the collapse propagation pressure under any bending condition,

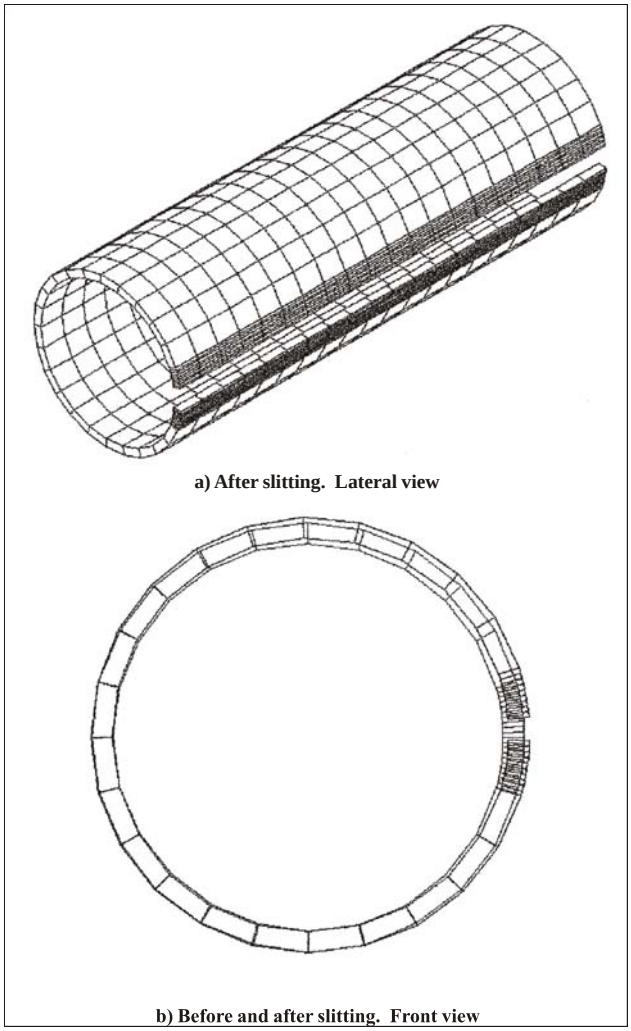

Figure 2.17: Three dimensional finite element simulation of the slit-ring test.

- for low values of applied bending, the eccentricity effect on the collapse pressure is much lower than the ovality effect, and it is almost independent of the applied bending,
- the effect of the residual stresses on the external collapse pressure depends on the applied bending, they are a fundamental ingredient for determining collapse pressures under external pressure only, but it is quite low when a strong bending is applied; however, care should be taken regarding its measurement methodology,
- the effect of the residual stresses on the collapse propagation pressures is not very important, with or without bending,
- bending diminishes the external collapse pressure of the pipes, due to the fact that it increases its ovality.

Chapter 3

Collapse of deepwater pipelines under external pressure plus bending. Validation: numerical vs. experimental results

3.1 Introduction

In this Chapter we present the 3D finite element models of pipes under external pressure and external pressure plus bending; these models incorporate a proper description of the pipe geometries.

We present the results of full-scale test program and finite element analyses performed on seamless steel line pipe samples under external pressure only and external pressure plus bending. These laboratory tests were carried out in order to obtain experimental results to be used in the validation of the numerical models.

In Section 3.2 we describe the experimental program, the laboratory facilities and the experimental tests while in Section 3.3 we describe the finite element models, compare de experimental vs. numerical results and evaluate the sensitivity of the numerical results

to small variations in the model data.

3.2 The experimental validation program

The test objectives were,

- determine the collapse loading and the post-collapse equilibrium path for external pressure loading,

- determine the effect of bending on the collapse strength of the pipe specimens by first applying external pressure then, while maintaining a constant external pressure, increase bending until collapse occurs ($P \rightarrow B$),

- determine the effect of bending on the collapse strength of one pipe specimen by first applying bending then, while maintaining a constant bending strain, increase the external pressure until collapse occurs ($B \rightarrow P$),

- to obtain information for the model, mechanical tests on samples taken in the circumferential direction were made and the hoop residual stresses were measured using slit-ring test.

Therefore, the experimental work involved performing initial geometric measurements, material property tests and full-scale collapse tests (external pressure only), full-scale $P \rightarrow B$ tests and a full-scale $B \rightarrow P$ test. Nine samples were tested, all of them conforming to API 5L grade X65. The nominal dimensions for each sample are indicated in Table 1.

Sample	$OD\ [mm]$	$t\ [mm]$	$\frac{OD}{t}$	*Test tipe*
1	353	22	16.05	*Collapse*
2	353	22	16.05	$P->B$
3	353	22	16.25	$P->B$
4	323.85	17.65	18.35	*Collapse*
5	323.85	17.65	18.35	$P->B$
6	323.85	17.65	18.35	$P->B$
7	323.85	20.30	15.95	*Collapse*
8	323.85	20.30	15.95	$P->B$
9	323.85	20.30	15.95	$B->P$

Table 1. Test Specimens

Geometrical characterization of the samples

The outer surface of the nine samples was mapped using the IMS or "shapemeter" while the thickness of the samples was mapped, using a standard ultrasonic gauge. The mode distributions and the thickness maps are presented in Appendix A.

A few comments can be made about these geometric imperfections,

- the imperfection that controls the value of the buckling pressure is the second mode of the shape Fourier decomposition, which is coincident with the first buckling mode [6],
- the value of that second mode is quite different (lower) from the ovality measured with a standard API ovalimeter [5].

Mechanical characterization of the samples

Coupon tests For each pipe sample the following determinations of the yield stress were made,

- coupons in the circumferential direction, tension and compression tests,

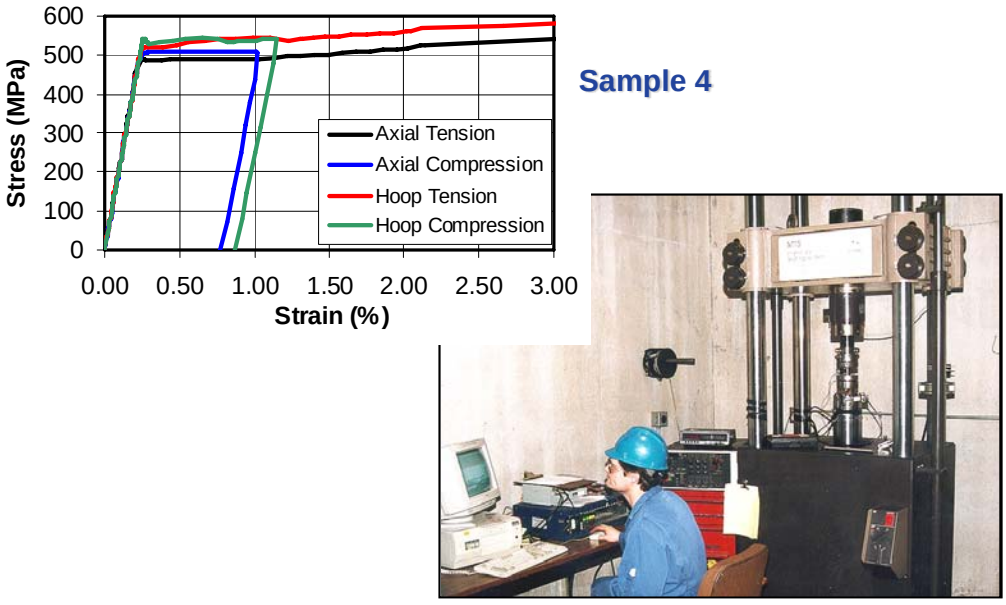

Figure 3.1: Testing Coupons at C-FER and Stress Strain Curves for Sample 4

- coupons in the axial direction, tension and compression tests.

All tension and compression coupon tests were conducted using C-FER's material testing machine shown in Figure 3.1; it also shows some sample stress strain curves from Specimen 4.

The grip assembly used in the set-up is designed to prevent the ends of the specimen from rotating. Complete specimen end fixity was designed in order to prevent specimen buckling and to achieve 1% strain in the compression tests.

Measured yield strengths, based on 0.5% strain, ranged from 427 to 551 MPa for the tensile tests and 452 to 648 MPa for the compression tests.

Ring Splitting Tests

Six ring splitting tests were conducted to determine pipe cross-sectional circumferential residual stresses.

Ring splitting tests were performed for each supplied pipe to measure the opening displacement of the ring sections, from which residual stress estimations were made. Residual stresses were calculated assuming a linear-elastic bending stress distribution through the wall thickness. Table 2 summarizes the hoop compressive yield strengths and hoop residual stresses for each specimen.

$Sample$	σ_y^- $(hoop)$ $[MPa]$	$\frac{\sigma_R(hoop)}{\sigma_y^-(hoop)}$ [%]
1	589.58	4.98
2	587.62	4.99
3	580.26	7.94
4	537.00	36.90
5	536.51	36.90
6	498.64	40.71
7	501.98	18.10
8	501.49	10.03
9	492.46	16.40

Table 2. Circumferential compression yield stress and circumferential residual stresses.

3.2.1 Full-scale Tests

C-FER's Deepwater Experimental Chamber was used for the full-scale tests [92]. The chamber, shown in Figure 3.2, has a tested pressure capacity of 62 MPa, with an inside diameter of 1.22 m and an overall inside length of 10.3 m.

Collapse and Buckle Propagation Tests

Three collapse and buckle propagation tests were conducted. Two of the collapse tests required pressures in excess of 62 MPa. To achieve higher pressures, a secondary pressure vessel was used inside of the Deepwater Experimental Chamber, allowing pressures up to 80 MPa (Fig. 3.3). After initial collapse, they continue pumping water into the pressure

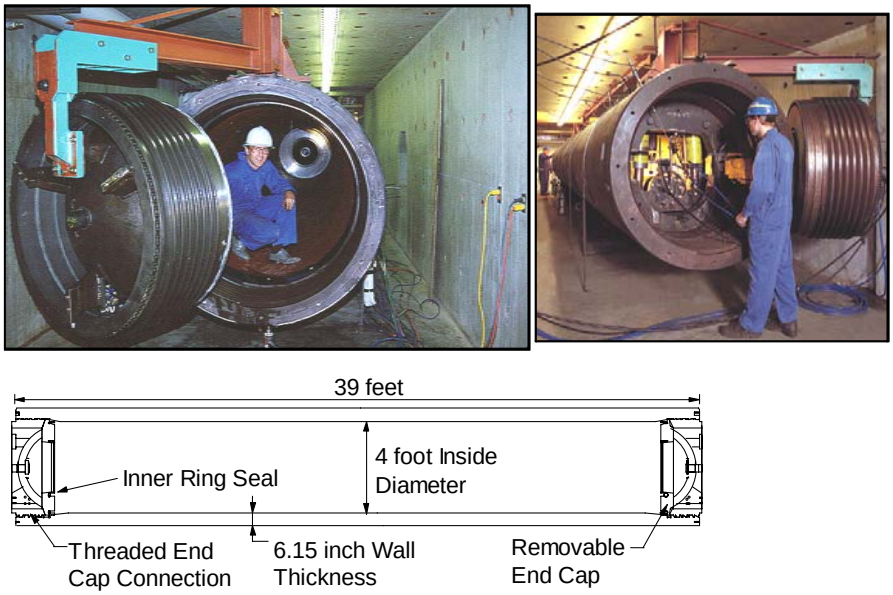

Figure 3.2: C-FER's Deepwater Experimental Chamber

vessel to propagate the buckle. The propagation pressure for the three tests averaged 24% of collapse pressure.

Measurements taken during the test included primary and secondary chamber pressures, specimen internal pressure (which was maintained near atmospheric pressure), the volume of water being pumped into the chamber and the volume of water coming out of the specimen.

P→B Tests

Five $P \rightarrow B$ tests were performed. To perform these tests, a custom-built pipe bending system was installed inside the Deepwater Experimental Chamber (maximum bending strain of 1.5% for a 353 mm OD pipe). The bending system applied equal and opposite end moments to the specimen ends using concentrated loads from hydraulic rams (Fig. 3.4).

Measurements for the tests included chamber pressure (specimen external pressure), specimen internal pressure, hydraulic actuator pressure, strains from four strain gauges

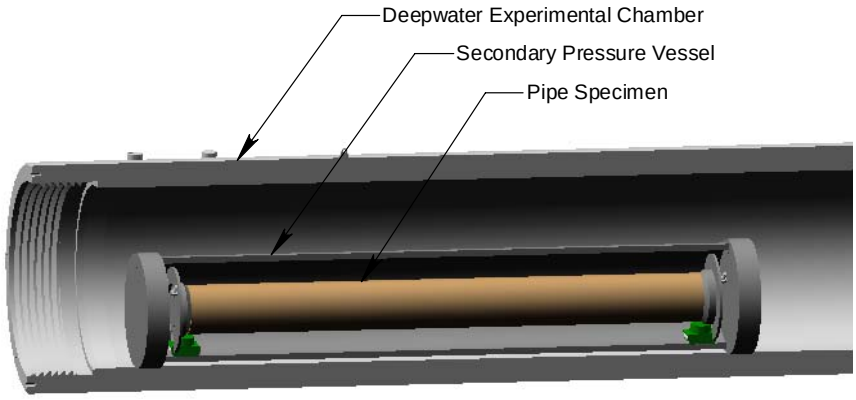

Figure 3.3: Pipe-in-pipe Set-up for High Pressure Tests

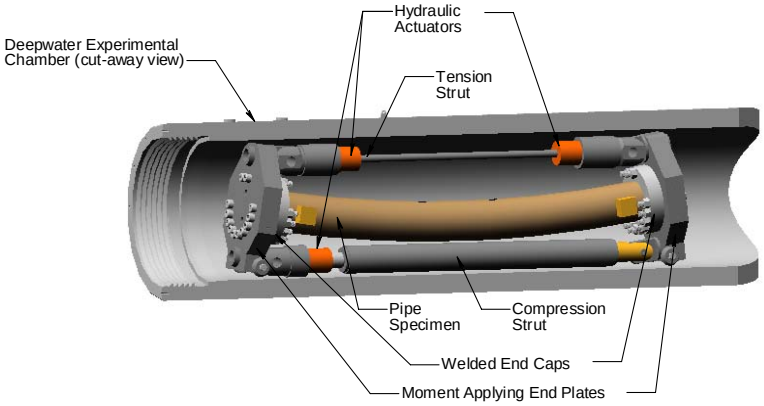

Figure 3.4: Combined Pressure and Bending Set-up

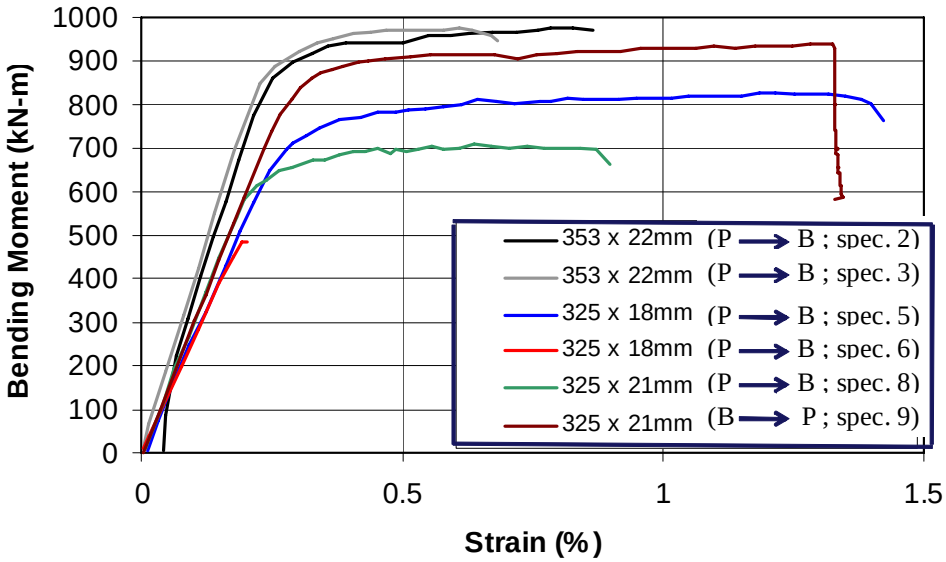

Figure 3.5: Bending Moment – Strain Plots

on the test specimen, and specimen end rotation. Global bending strain was calculated based on the end rotation measurements.

Collapse of many of the specimens was characterized by an audible "bong", a sudden decrease in external pressure and a sudden increase in specimen internal pressure.

B→P Test

A single $B \rightarrow P$ test was performed. Test set-up and measurements for this test were identical to the $P \rightarrow B$ tests described in the previous section.

Moment-strain plots for each of the bend tests are shown in Figure 3.5. The relation between increasing applied bending and decreasing collapse pressure agrees with the same tendency reported in Chapter 2 as a result of finite element simulations of $B \rightarrow P$ tests.

Results of the full-scale tests are shown graphically in Figure 3.6.

The tests successfully demonstrated the influence of bending on collapse strength for the specimens tested. Bending diminishes the external collapse pressure of the pipes, due to the fact that it increases its ovality ("Brazier effect") and introduces a biaxial state

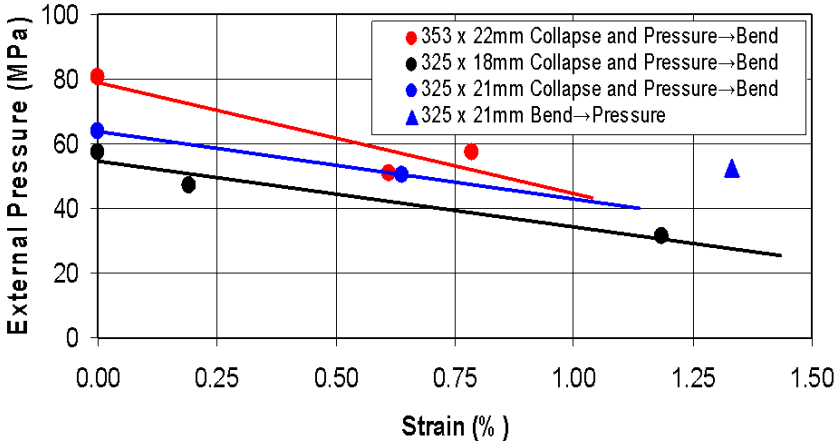

Figure 3.6: Full-scale Test Results

of stress (although present, radial stresses are ignored in this discussion). In addition, the stability of the pipe cross-section is dependent on the sequence of load application, as evidenced by the single $B \rightarrow P$ test result, which was approximately 50% higher than would have been expected for a test conducted with a $P \rightarrow B$ load path. The dependency of collapse on the sequence of loading is related to the loading/unloading sequences (and resulting material stiffness changes) that arise around the circumference of the pipe cross section. The dependency of collapse on the load path is also discussed in [24] for $B \rightarrow P$ and $P \rightarrow B$.

All the collapsed samples were visually inspected for cracks and despite the very large strains that were developed in the post-collapse regime [79], no cracks were found. This demonstrates the high ductility of the steel pipes. One advantage of this ductility is that, in the unlikely event a buckle is formed, the chance of a wet-buckle [48] is greatly reduced.

3.3 Validation of the finite element results

The 3D finite element models of pipes were developed using a material and geometrical nonlinear formulation [9] and they incorporate the following features,

- geometry, as described by the OD mapping and by the thickness distribution, reported in Appendix A for each sample,
- MITC4 shell element [12] [13] [30],
- von Mises elastic - perfectly plastic material model with the yield stress corresponding to the sample's hoop yield stress in compression. In this model, the plastic anisotropy of the material was neglected,
- circumferential residual stresses (experimentally measured),
- contact elements on the pipe inner surface [9] in order to prevent its inter-penetration in the post collapse regime,
- the nonlinear equilibrium path was tracked using the algorithm described in Ref. [11],
- the boundary conditions depend on the collapse chamber used in each case.

3.3.1 Numerical results

Because the characteristics of the collapse chambers used in these tests, shown in Figs. 3.3 and 3.4, the external pressure acts on the lateral surface of the pipes and also it introduces an axial compression on them.

In what follows, in order to validate the numerical models, for the nine tests described in Table 1 we compare the finite element results with the full-scale results.

Sensitivity of the numerical results

It is important to realize that the laboratory determined diameter and wall thickness of the pipe samples, performed at Tenaris Siderca, is subjected to the normal indeterminations of lab measurements.

We also characterize the mechanical properties, such as the yield stress and the residual stresses, with a constant value although they have a degree of variability inside the sample.

Hence, we need to be able to evaluate the sensitivity of the numerical results to small changes in the data.

The sensitivity of the collapse pressure to the yield stress value can be written as,

$$\frac{\partial p_{\text{col}}}{\partial \sigma_y} = \frac{p_{\text{col}}(\sigma_y^0 + \Delta\sigma_y;\ \sigma_{\text{Res}}^{Hoop};\ \sigma_{\text{Res}}^{Axial}) \ -\ p_{\text{col}}(\sigma_y^0;\ \sigma_{\text{Res}}^{Hoop};\ \sigma_{\text{Res}}^{Axial})}{\Delta\sigma_y}$$

In the above equation,

σ_y^0: base value for the yield stress.

$\Delta\sigma_y$: admissible variation for the yield stress.

$\sigma_{\text{Res}}^{Hoop}$: residual stress value in the hoop direction.

$\sigma_{\text{Res}}^{Axial}$: residual stress value in the axial direction.

Initial baseline analyses were performed using the above-discussed geometrical and mechanical properties. Axial residual stresses were not measured in the test program and were assumed to be zero for this baseline case. However, to estimate the sensitivity of collapse pressure to axial residual stresses, we assumed the axial residual stresses to have a linear distribution through the pipe wall thickness. A maximum value was assumed when the residual stress equaled the absolute value of the measured hoop residual stresses and they were tensile on the outer fibers. A minimum value was assumed when they were equal to the absolute value of the hoop residual stresses and they were compressive on the outer fibers. A variation of $\pm 10\%$ was also assumed in the values of yield stress and hoop residual stress to estimate the sensitivity of collapse to changes in their values.

The sensitivity of the collapse pressure to the value of the hoop residual stresses is,

$$\frac{\partial p_{\text{col}}}{\partial \sigma_{\text{Res}}^{Hoop}} = \frac{p_{\text{col}}(\sigma_y^0;\ \sigma_{\text{Res}}^{Hoop} + \Delta\sigma_{\text{Res}}^{Hoop};\ \sigma_{\text{Res}}^{Axial}) \ -\ p_{\text{col}}(\sigma_y^0;\ \sigma_{\text{Res}}^{Hoop};\ \sigma_{\text{Res}}^{Axial})}{\Delta\sigma_{\text{Res}}^{Hoop}}$$

The sensitivity of the collapse pressure to the value of the axial residual stresses can be calculated using a similar procedure.

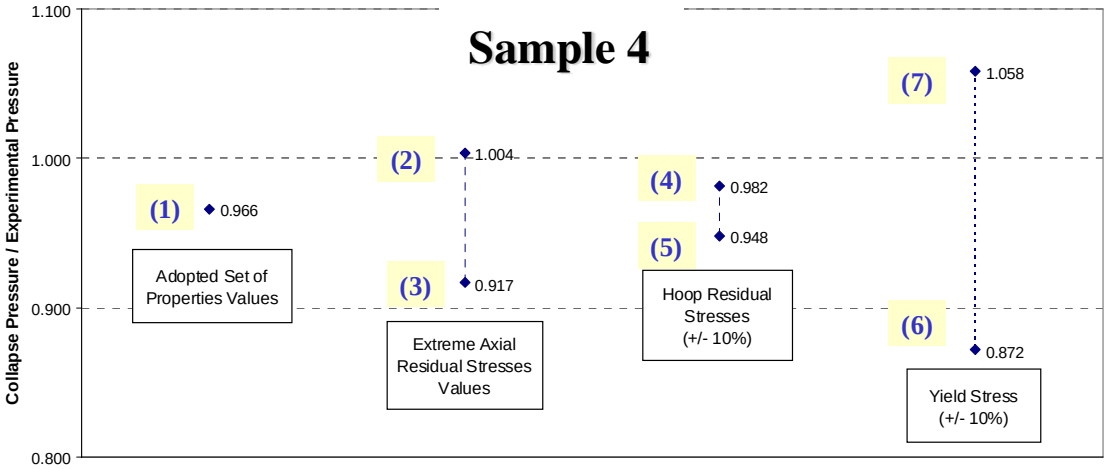

(1) Baseline case: the results were obtained using the measured data with no axial residual stresses
(2) Axial residual stresses equal to – (measured hoop residual stresses)
(3) Axial residual stresses equal to (measured hoop residual stresses)
(4) Hoop residual stresses = 0.9 baseline residual stresses
(5) Hoop residual stresses = 1.1*baseline residual stresses
(6) Yield stress= 0.9*baseline yield stress
(7) Yield stress= 1.1*baseline yield stress

Figure 3.7: Sample 4: sensitivity analysis for the external collapse pressure

External pressure only (samples 4, 1 and 7)

Sample 4. The numerical results compared with the experimental ones are shown in Fig. 3.7.

The baseline finite element result presents an excellent agreement with the experimental result.

The difference of 3.4% between the finite element predicted and the experimentally determined collapse pressures can be attributed to the non-homogeneous yield stress and to the indetermination in the value of the axial residual stresses, as can be seen in Fig. 3.7.

In Fig 3.8 we compare the experimentally and numerically determined [*External Pressure vs. Internal Volume Reduction*] diagrams. In this Figure we also compare the deformed meshes corresponding to the post-collapse regime with the

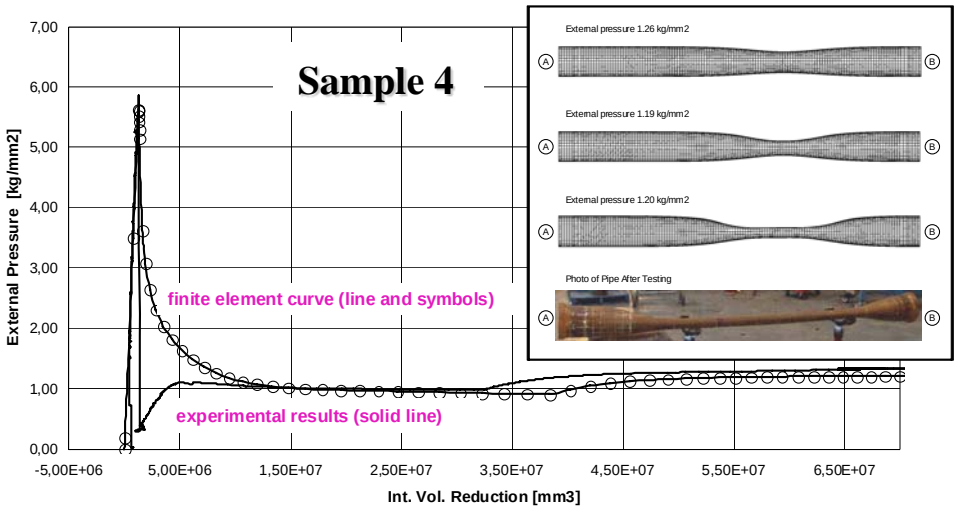

Figure 3.8: Sample 4. External pressure vs. internal volume reduction; finite element curve and experimental results

collapsed pipe profile. It is important to realize that the numerical analysis was halted before the collapse could propagate through the entire sample.

Both diagrams are practically coincident, except in the interval that goes from immediately after the pipe collapse to the point at which the experimentally and numerically determined curves merge again. In the experimental test, after collapse the chamber is abruptly depressurized and water must be pumped to regain pressure. Hence, the [*External Pressure vs.Internal Volume Reduction*] experimental path is different from the numerical one, which better represents the undersea conditions.

Figure 3.9 present the deformed finite element mesh corresponding to a certain point of collapse propagation.

Hence, we can assess that the post-collapse response of the finite element model, specifically the path in which the collapse propagates, has an excellent match with the experimental results.

In the post-collapse regime the pressure raises from 1 kg/mm^2 to approximately

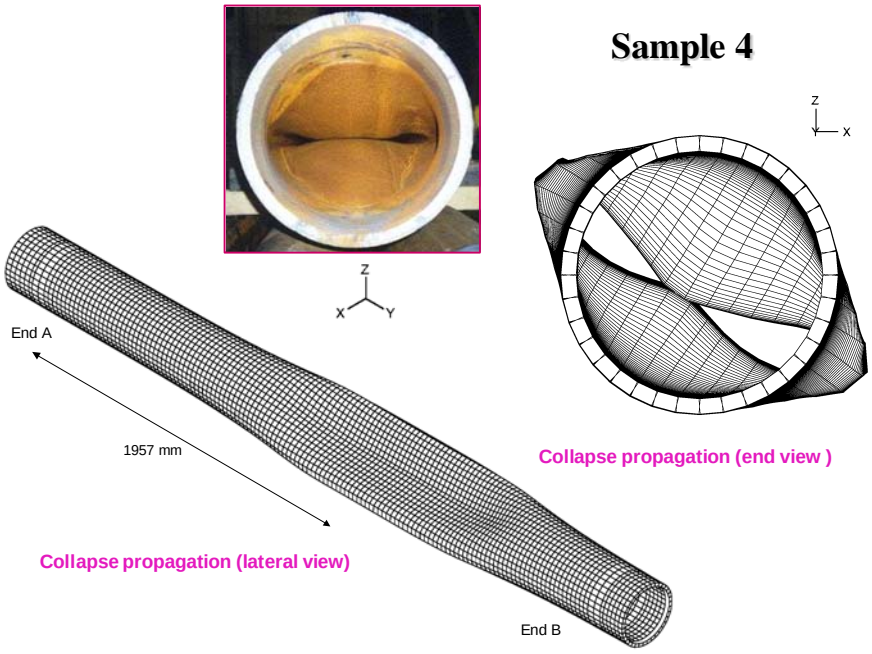

Figure 3.9: Sample 4. Post-collapse: isometric and end view

1.22 kg/mm^2 (propagation pressure) due to the stiffening effect of the contact between opposite points on the inner pipe surface. The ratio between the numerical collapse propagation pressure and the experimental one is 0.89.

In Fig 3.10 we can observe the propagation of the contact pressure along the contact line in the raising part of the equilibrium path.

It is important to note that the sensitivity of the propagation pressure to the yield stress value is quite low: in the analyzed case it is ten times lower than the sensitivity of the collapse pressure to the yield stress value.

With the finite element model, for sample 4, we obtained,

$$\frac{\partial p_{\text{col}}}{\partial \sigma_y^0} = 0.100$$

$$\frac{\partial p_{prop}}{\partial \sigma_y^0} = 0.013$$

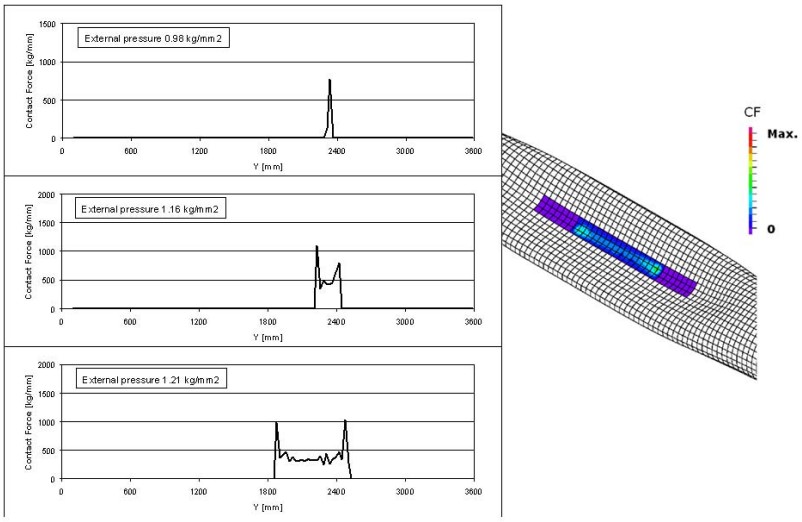

Figure 3.10: Sample 4. Propagation of the contact pressure along the contact line

Samples 7 and 1. Figs. 3.11 and 3.12 summarize the comparison between the finite element and experimental results for samples 7 and 1, respectively, while Figs. 3.13 and 3.14 present the external collapse pressure sensitivity analyses performed on both samples. For sample 7 we have also analyzed the sensitivity of the collapse pressure to the measured thickness. Since we measured the wall thickness using a manual ultrasonic device, errors in this measurement due to a wrong positioning of the ultrasonic gauge are very easy to have.

Regarding the collapse propagation pressure, the ratio between the numerical result and the experimental one is 0.99 for sample 7 and 0.87 for sample 1.

In Fig. 3.15 we map the equivalent logarithmic plastic strains. As we discussed above these strains are rather large, however these samples did not present any crack when it was visually inspected at C-FER after the collapse test.

FEA for the $B \rightarrow P$ Test

In this test, the post-collapse regime was not investigated; hence, only the collapse external pressure could be compared.

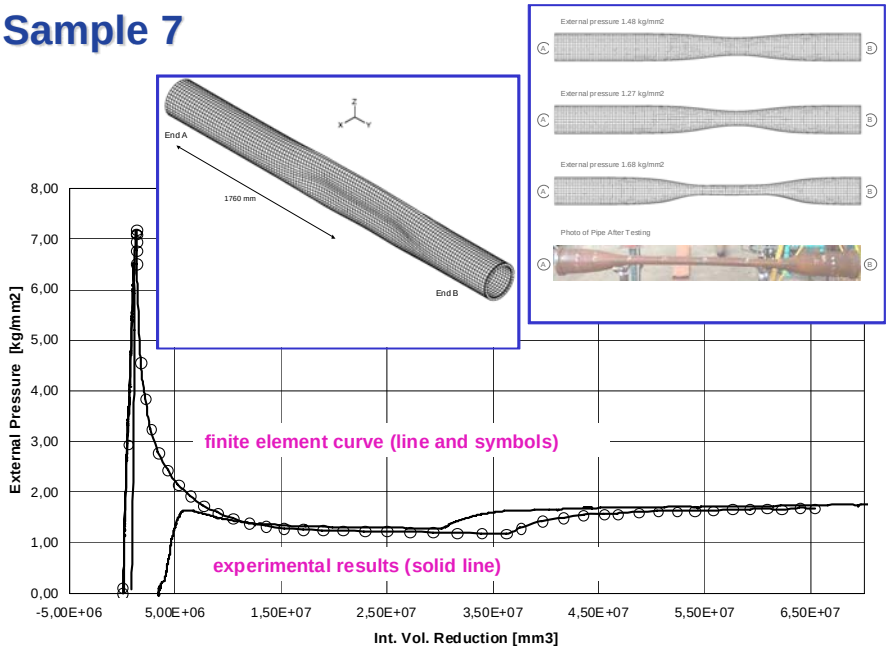

Figure 3.11: Sample 7. External pressure vs. internal volume reduction: finite element curve and experimental results

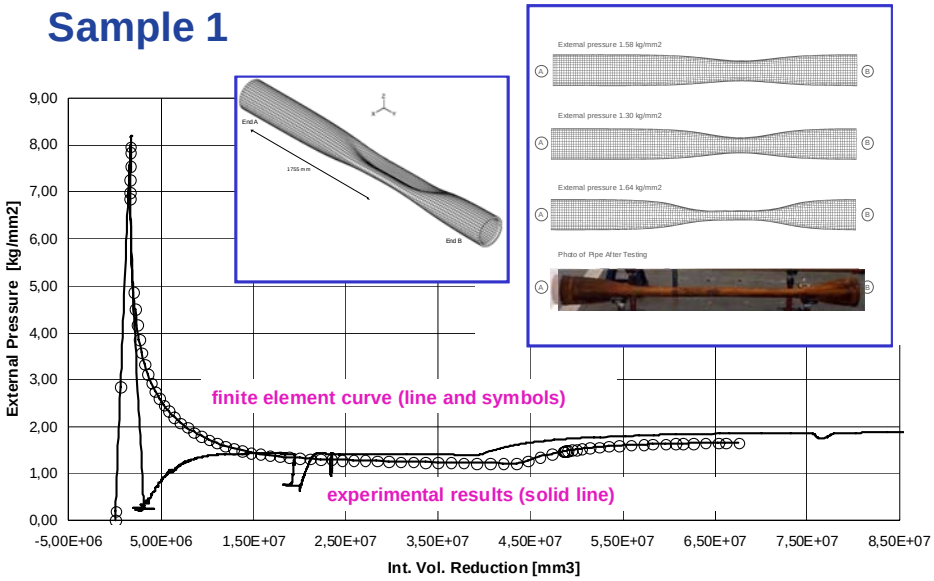

Figure 3.12: Sample 1. External pressure vs. internal volume reduction: finite element curve and experimental results

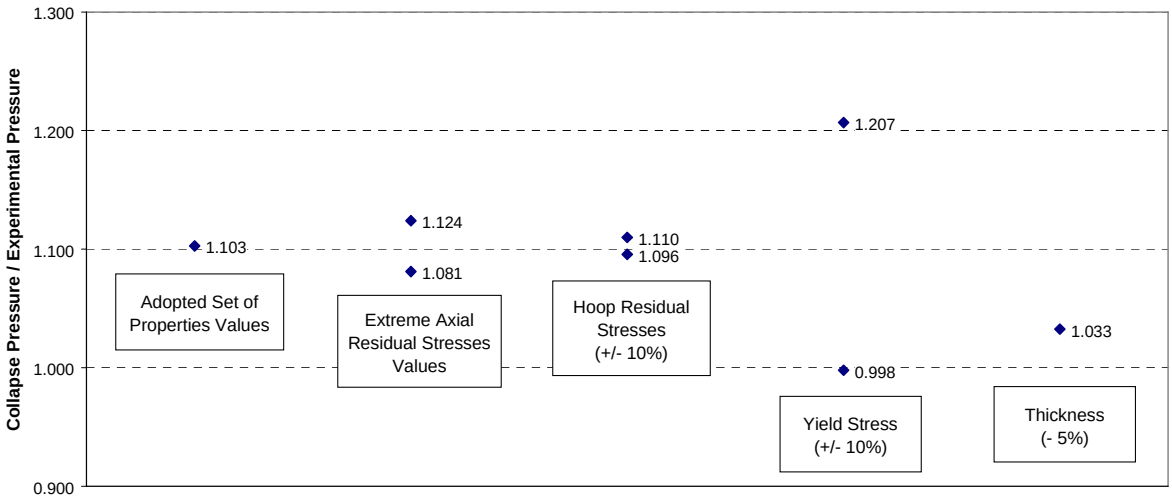

Figure 3.13: Sample 7. Sensitivity analysis for the external collapse pressure

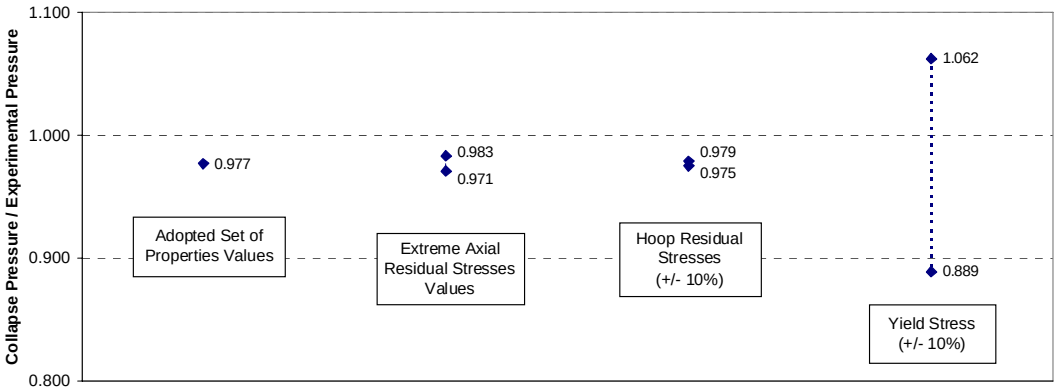

Figure 3.14: Sample 1. Sensitivity analysis for the external collapse pressure

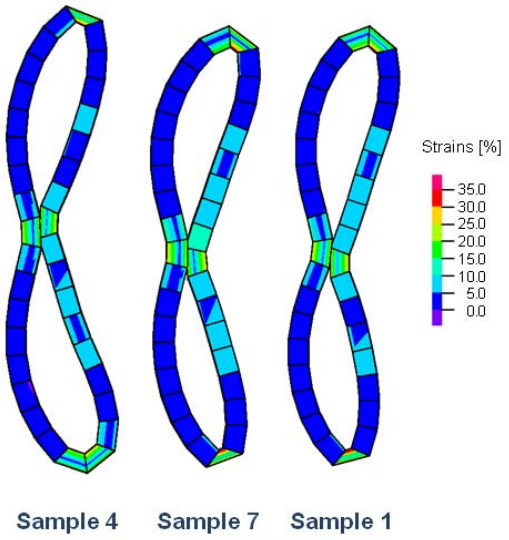

Figure 3.15: Sample 4, 7 and 1. Hencky equivalent plastic strains

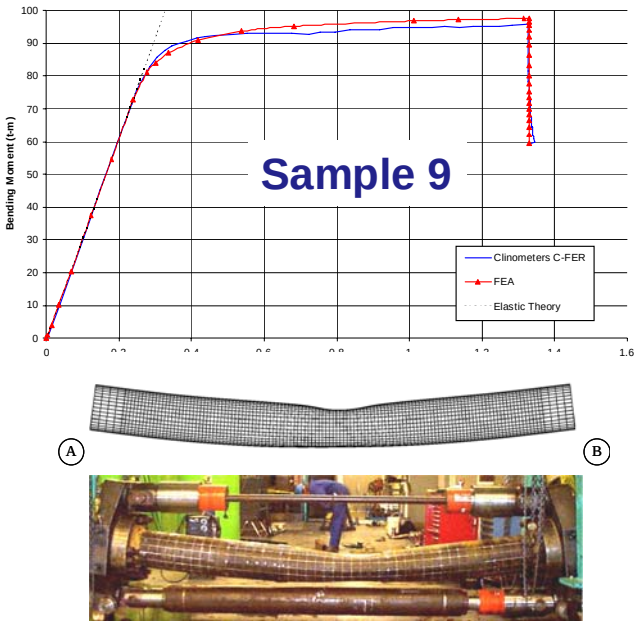

Figure 3.16: Sample 9. Bending moment vs. average bending strain

The finite element result presents an excellent agreement with the experimental result: a difference of only 3.6% between the FEA prediction and the experimentally determined collapse pressures. This can be attributed to the non-homogeneous yield stress and to the uncertainty of the value of the axial residual stresses.

Figure 3.16 presents the curve [*Bending moment vs. average bending strain*] for sample 9.

FEA for the P→B test

In this experimental test, the post-collapse regime was not investigated; hence, only the collapse bending moment could be compared. Five samples were first loaded with external pressure and afterwards, maintaining constant the external pressure, they were bent up to collapse. The following table summarizes the comparison between the numerical and experimental results.

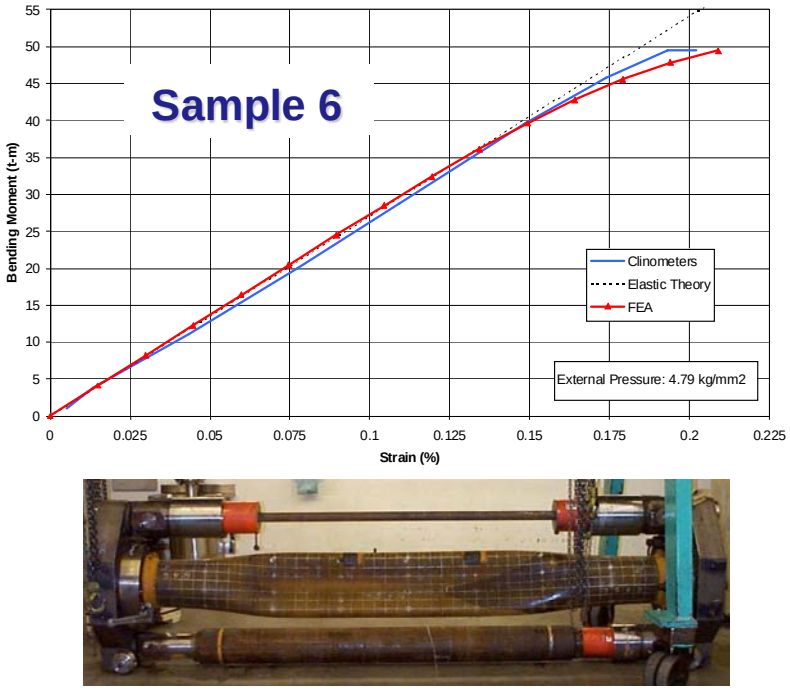

Figure 3.17: Sample 6. Bending moment vs.average bending strain and pipe after collapse

Sample	$\frac{Mc_{numerical}}{Mc_{experimental}}$
2	1.047
3	1.088
5	0.972
6	0.998
8	0.998

Table 3. Results for pressure plus bending

The finite element results are in excellent agreement with the experimental ones. Figures 3.17 and 3.18 present the curves [*Bending moment vs. average bending strain*] and pictures of the pipes after collapse (samples 6 and 8, respectively); Figure 3.18 also shows the equivalent plastic strain distribution.

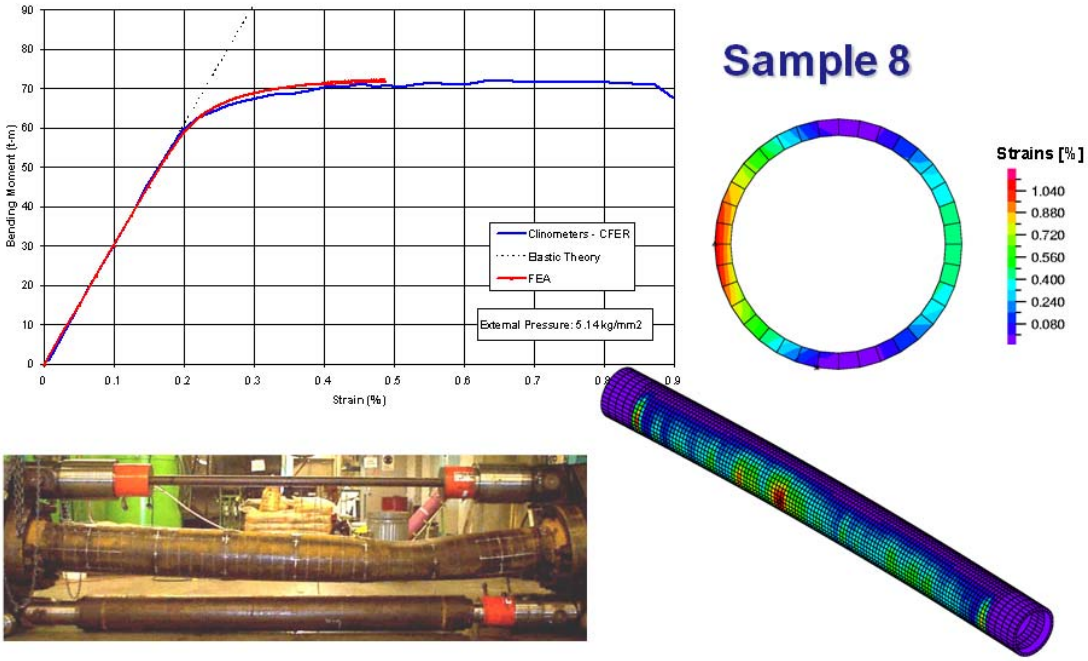

Figure 3.18: Sample 8. Bending moment vs.average bending strain and pipe after collapse. Equivalent plastic strains

Regarding sample 6, the applied external pressure was 91% of the analytically predicted external collapse pressure.

The sensitivity analysis results for all the samples are listed in Table 4.

	$\frac{Pc_{FEA}}{Pc_{\exp}}$	$\frac{Pc_{FEA}}{Pc_{\exp}}$	$\frac{Pc_{FEA}}{Pc_{\exp}}$	$\frac{Pc_{FEA}}{Pc_{\exp}}$	$\frac{Mc_{FEA}}{Mc_{\exp}}$	$\frac{Mc_{FEA}}{Mc_{\exp}}$	$\frac{Mc_{FEA}}{Mc_{\exp}}$	$\frac{Mc_{FEA}}{Mc_{\exp}}$	$\frac{Mc_{FEA}}{Mc_{\exp}}$
Sample	4	7	1	9	6	8	5	2	3
Baseline	0.966	1.103	0.977	0.964	0.998	0.998	0.972	1.047	1.088
Min.axial σ_R	1.004	1.124	0.983	0.956	1.048	0.998	0.972	1.048	1.088
Max.axial σ_R	0.917	1.081	0.971	0.974	0.688	0.998	0.970	1.047	1.088
Min.hoop σ_R	0.982	1.110	0.979	0.962	1.046	0.998	0.972	1.048	1.088
Max.hoop σ_R	0.948	1.096	0.975	0.968	0.902	0.998	0.972	1.047	1.089
Min. σ_y	0.872	0.998	0.889	0.903	0.166	0.827	0.854	0.843	0.919
Max. σ_y	1.058	1.207	1.062	1.022	1.336	1.156	1.088	1.223	1.247

Table 4. Sensitivity Analysis Results

Analysis Predictions

For the pipe specimens subjected to external pressure only, the numerically predicted collapse mode matched the experimentally observed mode in only one case (Fig. 3.19). However, in the cases that included bending, the agreement was excellent (Fig. 3.20).

3.4 Main observations

The agreement between the finite element predictions and the laboratory observations, both in the pre- and post-collapse regimes was very good. Therefore, the finite element models can be used as a reliable engineering tool for analyzing the effect of different imperfections, and of residual stresses, on the collapse and collapse propagation pressure of steel pipes.

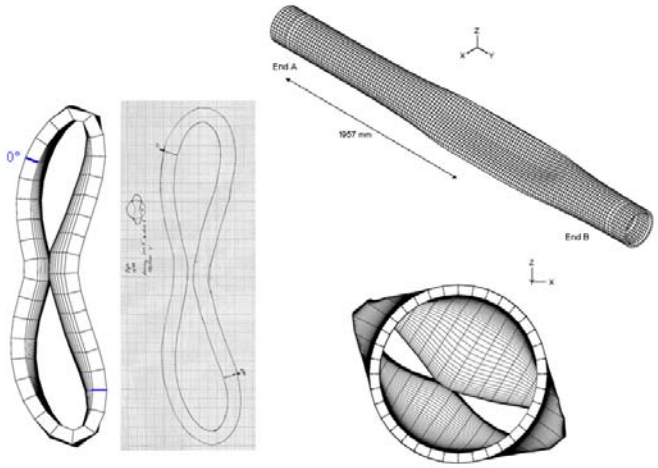

Figure 3.19: Sample 7. FEA and experimental Predictions for the Collapsed Section (External Pressure Only)

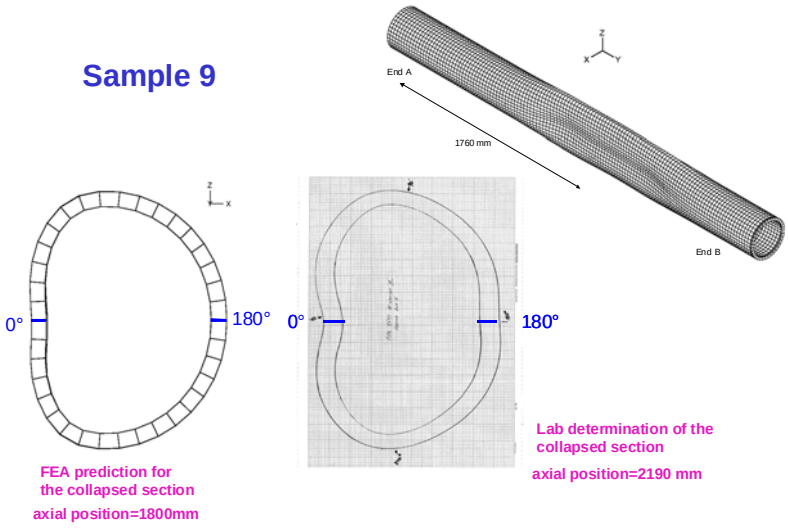

Figure 3.20: Sample 9. Numerically Predicted and Experimentally Observed Collapse Mode for the $B \rightarrow P$ Test

The tests not only confirm the conclusions drawn in the previous Chapter, regarding the detrimental effect of the bending on the collapse pressure of the pipes, but also show the dependency of the collapse on the load path.

Chapter 4

Collapse of deepwater pipelines with buckle arrestors. Validation: numerical vs. experimental results.

4.1 Introduction

In this Chapter we focus on the analysis of the collapse and post-collapse behavior of pipelines reinforced with buckle arrestors; we develop finite element models to analyze the collapse, collapse propagation and cross-over pressures of reinforced pipes and we present an experimental validation of the models. In particular we consider the case of welded integral arrestors.

In Section 4.2 we describe the experimental facilities and the laboratory tests that we performed to determine, for different $[pipe - arrestor]$ geometries, the collapse, propagation and cross-over pressures. In section 4.3 we describe the finite element models that we developed to simulate the collapse tests and finally we compare the experimental results with the finite element ones, in order to validate the model.

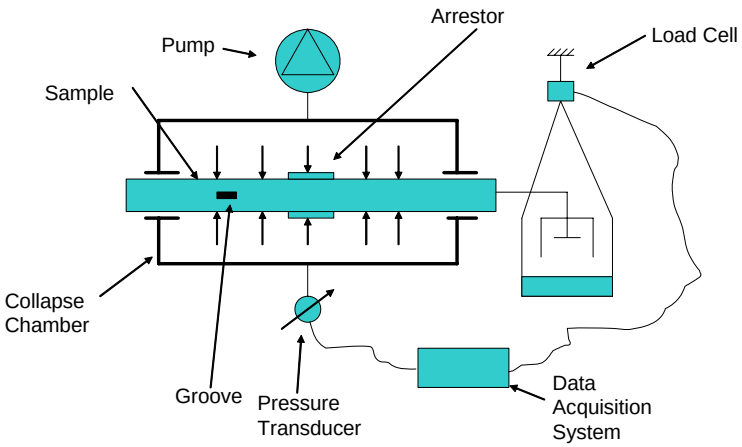

Figure 4.1: Experimental set-up

4.2 Experimental results

4.2.1 Experimental set-up

The purpose of the laboratory tests developed for different combinations [$pipe+arrestor+pipe$] was to track the post-collapse equilibrium path for the assembly under external pressure and to determine from it the collapse and the cross-over pressure. For these tests we used the experimental set-up shown in Fig. 4.1.

Each sample had two pipes, one on each side of the arrestor; Figure 4.2 shows the assembly of one of the samples. For each side, a L/OD ratio greater than 7.5 was used in order to minimize the end - effects on the collapse loads.

Two solid end-caps were welded on each end. The internal section of the end-caps was shaped to avoid localized failure during propagation. The shape of this section was derived from the finite element results of a free propagating buckle 4.13. In Figure 4.3 we compare two samples which were subjected to similar external pressure; sample A, with standard end-caps, was broken while sample B, with the special end-caps, was not.

The biggest chamber at Tenaris Siderca lab facilities was used, which usually tests sample pipes up to OD 10 $\frac{3}{4}$" (273.05 mm) with a maximum length of 4.2 m and a limit

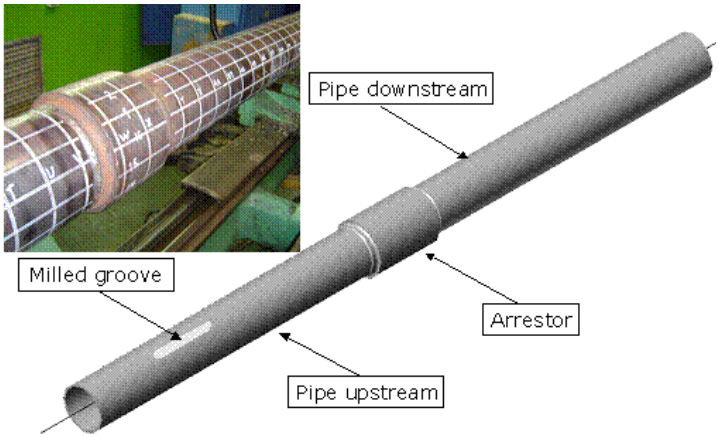

Figure 4.2: Pipes and arrestor assembly

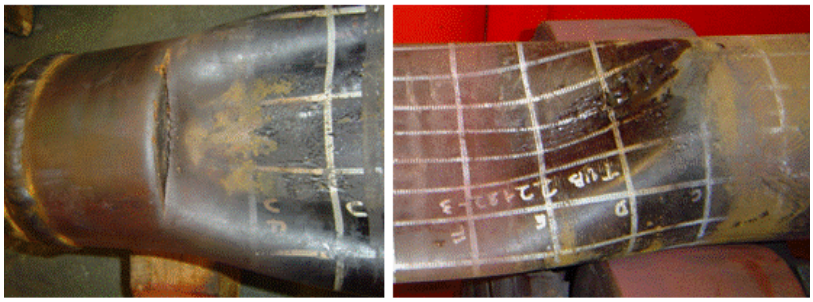

Figure 4.3: Comparison of the critical zone between two samples, with and without end caps.

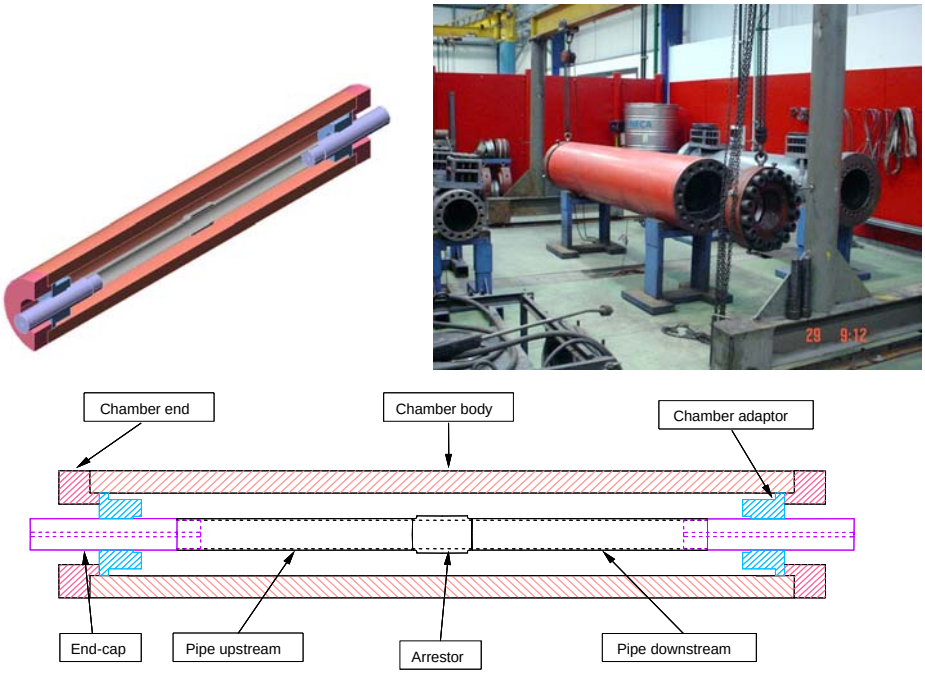

Figure 4.4: Collapse chamber

pressure of 25000 psi. In this opportunity, some modifications had to be made to adapt the chamber ends to the size of the pipe. Figure 4.4 shows a detailed drawing and a photograph of the collapse chamber.

Each specimen was completely filled with water before the beginning of the test. From a 25 mm hole in one of the end-caps (Fig. 4.5) the displaced water was directed to a container connected to a load cell (Fig. 4.6). The load variation in the load cell is proportional to the displaced water and therefore to the variation of the specimen inner volume.

To localize the buckle initiation, we milled a groove on one of the pipes (upstream pipe) as shown in Fig. 4.7.

In Fig. 4.8 we present a detail of the geometry of the arrestor and we define the dimensions and steel grade[1] of the four tested samples.

[1]The steel Grade 6 defined by the standard ASTM A-333 has a minimum yield stress of 240 MPa and a minimum ultimate stress of 414 MPa.

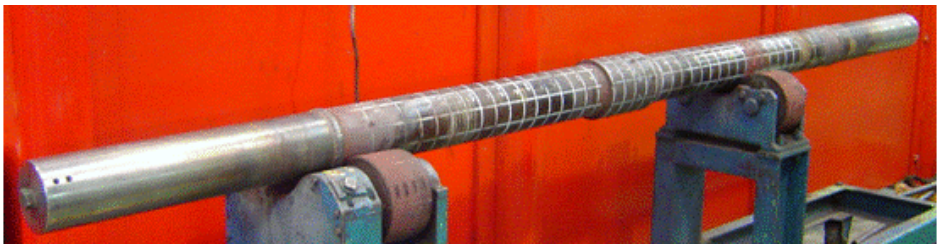

Figure 4.5: End-caps welded to the pipe

Figure 4.6: Internal Volume Variation Measuring System

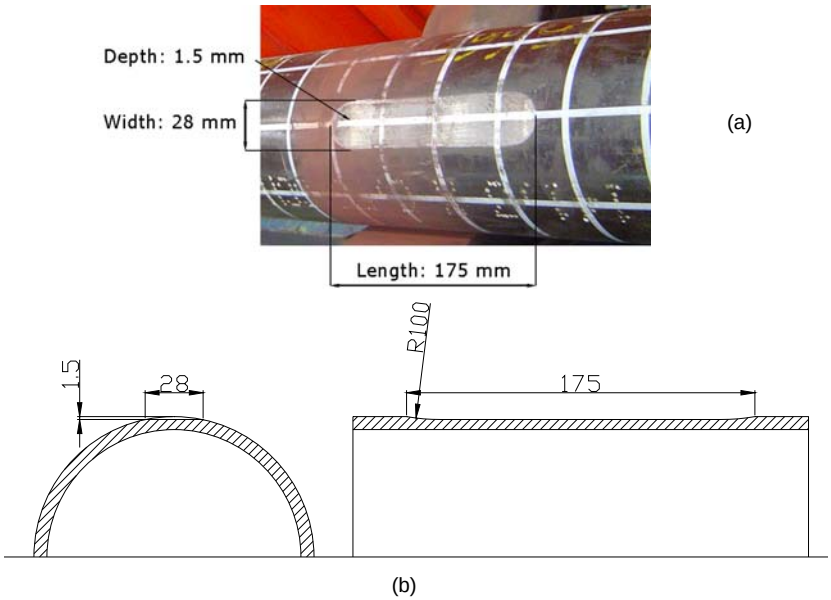

Figure 4.7: Groove machined on the upstream pipe to localize the collapse initiation. (a) General view (b) Detailed sections

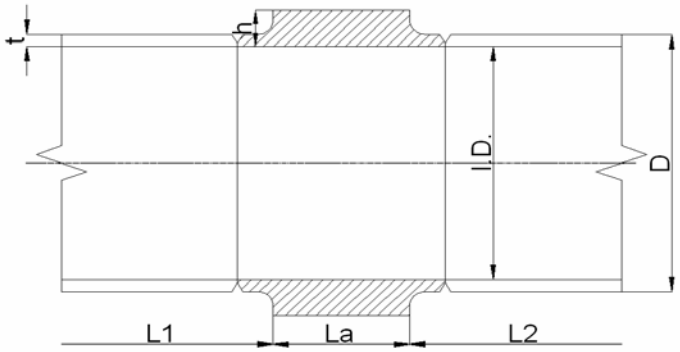

Sample	Pipe OD [mm]	Pipe thickness (t) [mm]	Pipe steel grade	Arrestor (h/t)	Arrestor (La/D)	Arrestor steel grade	Sample length [mm]	Expected cross-over mechanism
1	141.3	6.55	X42	2.0	0.50	6 (ASTM A-333)	2250	Flattening
2	141.3	6.55	X42	2.5	0.50	X42	2250	Flattening
3	141.3	6.55	X42	3.0	0.75	X42	2274	Flipping
4	141.3	6.55	X42	3.0	1.00	X42	2330	Flipping

Figure 4.8: Welded arrestors geometry and materials

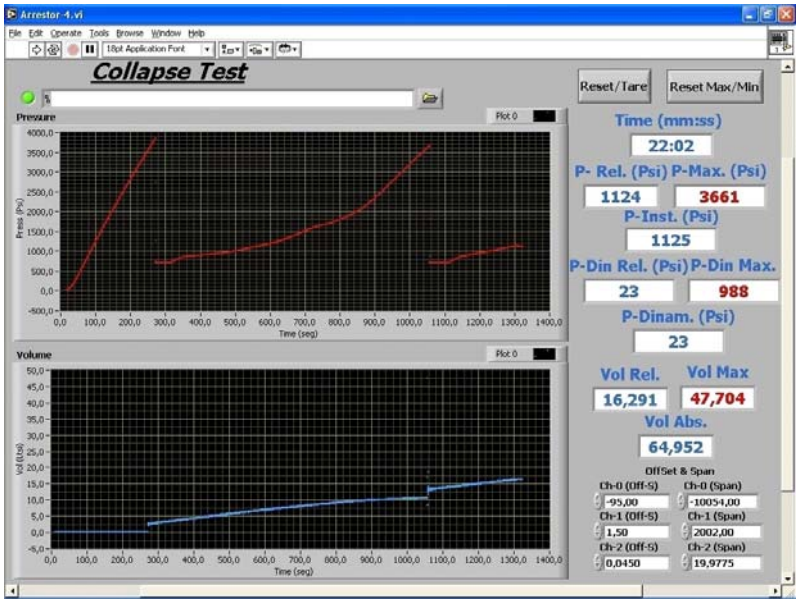

Figure 4.9: Data acquisition during the collapse tests

During the tests, we continuously increased the external pressure as in a standard collapse test; after the collapse the pumping continued through the upstream propagation, cross-over of the arrestor and downstream propagation. All the test data was recorded at an average sampling rate close to 10Hz (Fig. 4.9).

4.2.2 Geometrical characterization of the tested samples

The outer surface of the samples was mapped using the shapemeter [6]. The mode distributions and the thickness maps of the sample 1 are shown in Appendix A.

4.2.3 Mechanical characterization of the tested samples

For all the pipe and arrestor materials we determined,

- stress–strain curves (longitudinal tensile tests since the thickness of the pipes was

The steel Grade X42 defined by the standard API-5L has a minimum yield stress of 290 MPa and a minimum ultimate stress of 414 MPa.

too small for hoop samples),

- hoop residual stresses (evaluated using slit ring tests).

In Table 1 we summarize the residual stress values.

Sample	$\frac{Measured\ \max.\ Residual\ Stresses}{Measured\ Yield\ Stress}$
1	0.39
2	0.47
3	0.47
4	0.49

Table 1. Residual stresses measured using the slit ring test

4.3 The finite element model

As in the models described previously, we simulated the external pressure collapse test using the MITC4 [12] [13] [30] shell element implemented for finite elasto-plastic strains in the ADINA system [76]. The numerical model was developed using a material and geometrical nonlinear formulation, which takes into account large displacements/rotations and finite strains [9], since it was discussed in [83] that even tough the strains during post-collapse regime are rather small, at concentrated locations they can attain quite large values, as shown in Fig. 4.10.

In previous analyses we observed that when using an infinitesimal strains formulation we get results that have an excellent match with the experimental determinations; to confirm this assessment, in this paper we compare the experimental results with the numerical results obtained under the assumption of infinitesimal strains and with the numerical results obtained under the assumption of finite strains.

The model incorporates the following features [9],

- von Mises elasto-plastic material model with isotropic multi-linear hardening. In Figs. 4.11 and 4.12 we show, for one of the tested samples, the experimental stress-strain curves and its fitting using a multilinear hardening model,

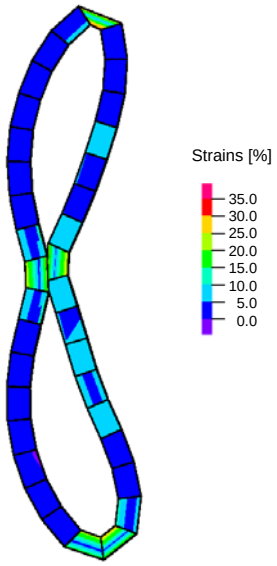

Figure 4.10: Typical post-collpase Hencky strains distribution

- contact elements on the pipe inner surface in order to prevent its inter-penetration in the post-collapse and propagation regimes,
- nonlinear equilibrium path tracing via the algorithm developed in [11],
- hoop residual stresses modeled with the technique discussed in [6].

In Fig. 4.13 we present the finite element mesh, 8500 elements and 42,500 d.o.f, a detail of the mesh in the $[pipes - arrestor]$ transition which was modeled using variable thickness elements [9] and a detail of the end-caps modeling; there are contact elements between the end-caps and the pipes.

Figure 4.14 shows the contact pressure distribution in the third sample, immediately after the cross-over; this Figure includes a detail of the plug cone.

4.4 Validation of the finite element results

In this section we discuss the validation of our finite element results by comparing them with experimental determinations that we obtained using the set-up described above.

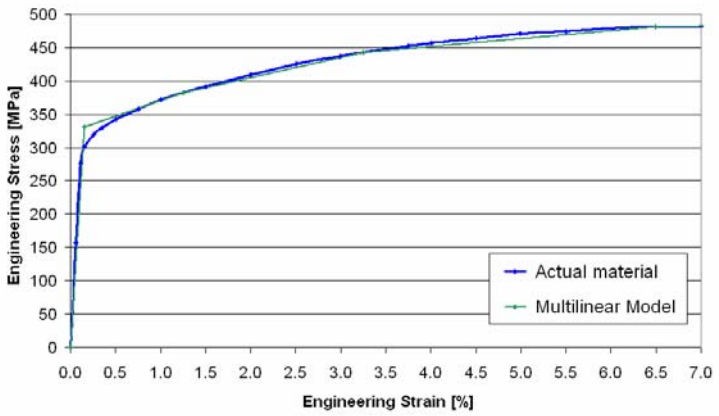

Figure 4.11: Material model for the pipe segments in sample # 1. Experimental and interpolated curves

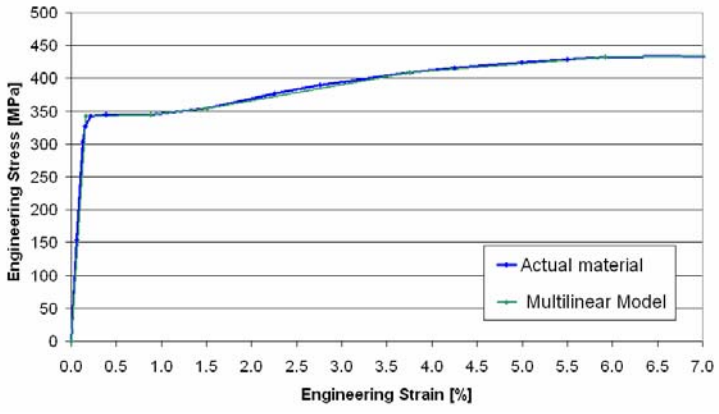

Figure 4.12: Material model for the arrestor in sample # 1. Experimental and interpolated curves

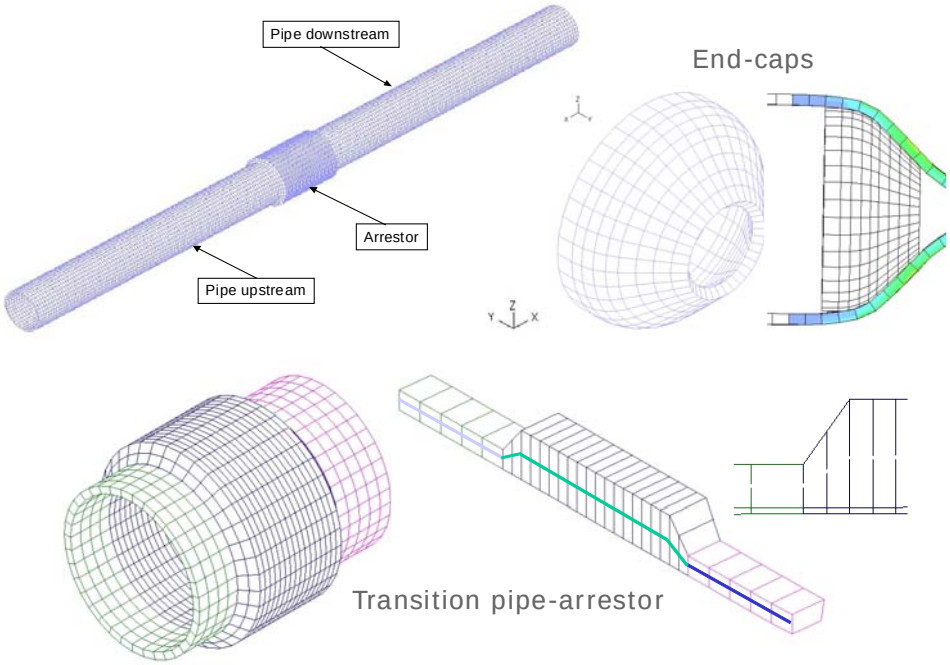

Figure 4.13: Pipe-arrestor finite element mesh

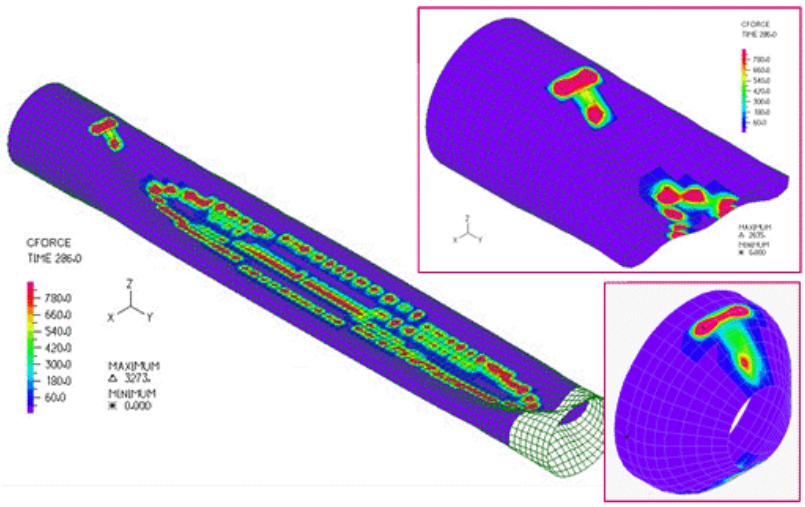

Figure 4.14: Sample 3. Contact forces for the upstream pipe and plug zone

4.4.1 Exploring the finite element model

In order to explore the behavior of our finite element model, first we analyze two perfect samples, without residual stresses. In the first one we expect the collapse buckle to cross the arrestor with a flattening mode while in the second case, because of the higher stiffness of the arrestor, we expect a flipping mode. That supposition is based in previous parametric analyses, where we considered different ratios between the pipe vs. the arrestor stiffness.

In each case we consider an imperfection, centered at a distance of 236.1 mm from the upstream pipe end, with a shape [57],

$$w_o(\theta) = -\Delta_o \left(\frac{OD}{2}\right) \exp\left[-\beta \left(\frac{x}{OD}\right)^2\right] \cos(2\theta) \tag{4.1}$$

where,

w_o : radial displacement,

θ : polar angle,

Δ_o : imperfection amplitude parameter 0.002 mm),

β : parameter that decides the extent of the imperfection, in our case (2.32 OD),

OD : outside diameter;

x : axial coordinate.

In Fig. 4.15 we present the finite element predicted deformed shapes for a $[pipes - arrestor]$ system exhibiting the flattening cross-over mechanism and in Fig. 4.16 we show the predicted deformed shapes for a system presenting the flipping cross-over mechanism.

In both cases we plot the external pressure as a function of the internal volume variation,

$$Vol.\,Variation = \frac{Vol.\,displaced\,water}{Original\,inside\,vol.} \tag{4.2}$$

Considering the $[External\,pressure - volume\,variation]$ diagrams predicted by the finite element models, in each case we observe,

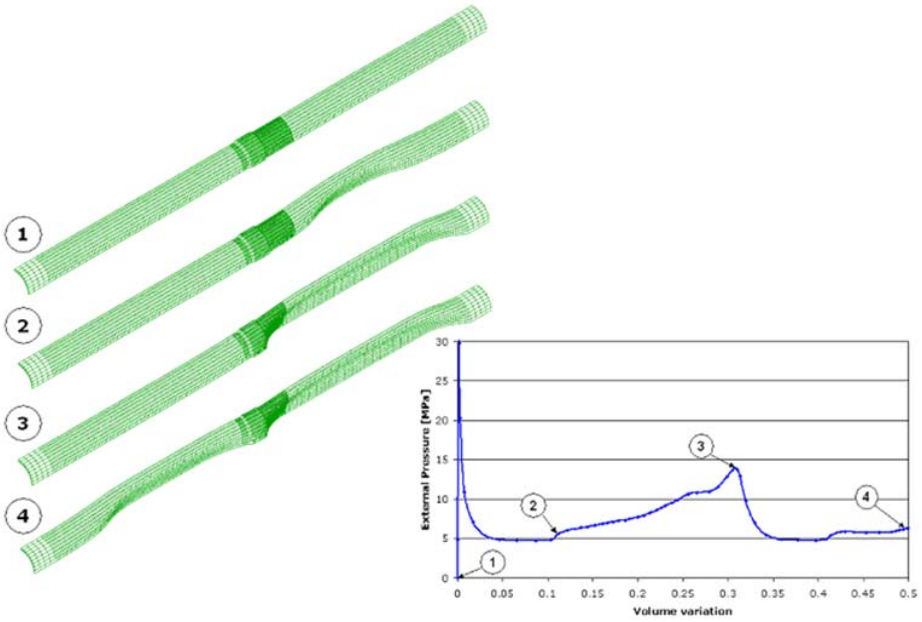

Figure 4.15: Finite element results for the case presenting a flattening cross-over

- the test starts at point "1" and while the external pressure grows the sample maintains its perfect shape and therefore there is a very small internal volume variation. Then the point of maximum pressure is reached ("collapse pressure") and the sample rapidly changes its cross-section shape; while the collapse buckle grows in its amplitude and extension in the upstream pipe axial direction, the external equilibrium pressure drops. At some point the collapse buckle extension starts to grow under constant external pressure ("collapse propagation pressure" [59]),

- at "2" opposite points located on the inner surface of the upstream pipe establish contact and afterwards, while the contact area extends, the external equilibrium pressure increases,

- while the collapse buckle in the upstream pipe approaches the arrestor the external equilibrium pressure keeps increasing but the downstream pipe does not collapse,

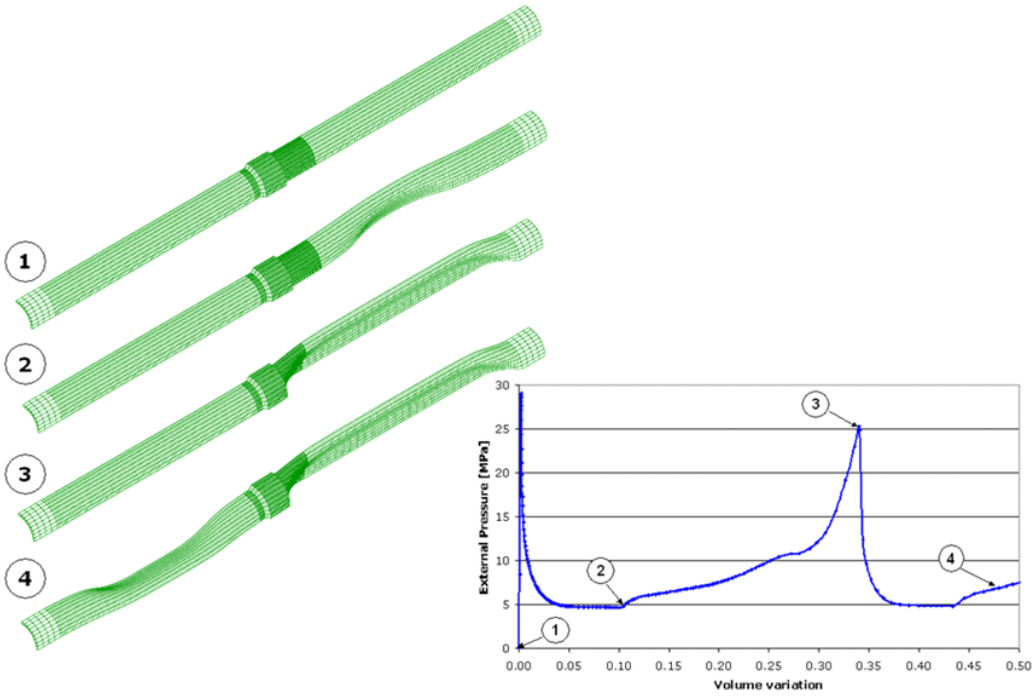

Figure 4.16: Finite element results for the case presenting a flipping cross-over

- at point "3" ("cross-over pressure") the collapse buckle crosses the arrestor and the downstream pipe collapses,
- afterwards the collapse buckle propagates through the downstream pipe.

It is important to notice that in the case with the flattening cross-over mechanism the upstream and downstream pipe have their collapsed sections with the same orientation while in the case with the flipping cross-over mechanism the collapse sections form an angle close to ninety degrees. It is also important to notice that the relation [*cross-over pressure / collapse pressure*] is much higher for the flipping case than for the flattening case.

4.4.2 Comparison between the finite element and experimental results

The four samples tested in the laboratory were modeled and the [*external pressure - volume variation*] equilibrium paths were determined.

In Table 2 we compare the FEM and experimental results.

Sample	$Col\ pres.: \frac{FEM-finite\ strains}{lab}$	$Cross-over\ press.: \frac{FEM-finite\ strains}{lab}$
1	0.924	1.004
2	0.928	0.985
3	0.951	0.926
4	0.852	0.883

Table 2. Validation of the numerical results

It is important to point out that the finite element results indicated in this table were obtained considering that the residual stresses in the two pipe sections are the residual stresses measured in the full length pipe. The modifications in residual stresses induced by the pipe cutting, the welding and groove machining were not introduced in the model. The effect of the residual stresses on the collapse pressure was described in previous

publications [6] [79] [83] [85] [88] as well as in Chapter 2. While this effect is quite important, we found with our numerical experimentation, that the effect of the residual stresses on the cross-over pressure is not so relevant, as shown by the model results that we present in Fig. 4.17.

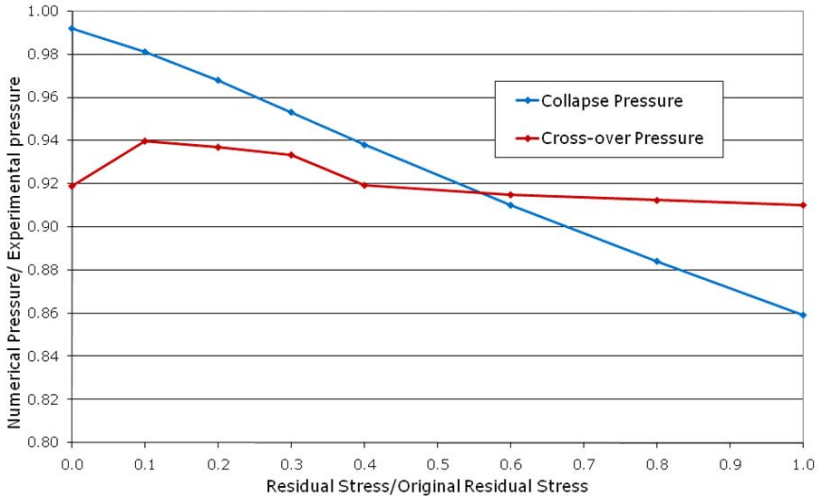

Figure 4.17: Sample 4. Residual stresses effect on the collapse and cross-over pressures

In Figs. 4.18 and 4.19 we compare, for samples 1 and 2 (flattening), the experimentally determined and FEM predicted equilibrium paths under the assumptions of finite strains and infinitesimal strains,

- during the laboratory determination for the first sample some water was spilled out of the measurement system, a fact that explains the shift observed, in the horizontal axis, between the FEM and experimental results,
- for the second sample the agreement between the FEM and experimental results is very good,
- the results obtained using FEM under the assumptions of finite and infinitesimal strains are very close.

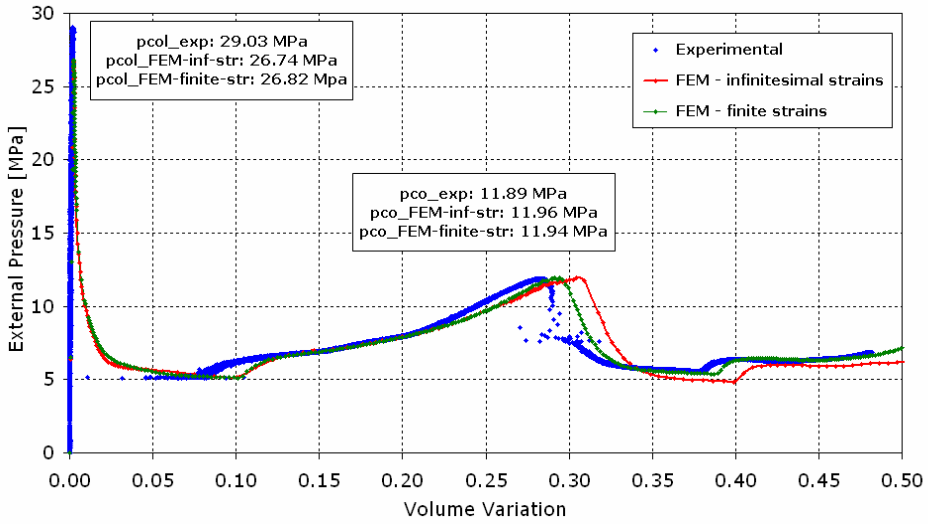

Figure 4.18: Sample 1. FEM vs. experimetal results (flattening cross-over)

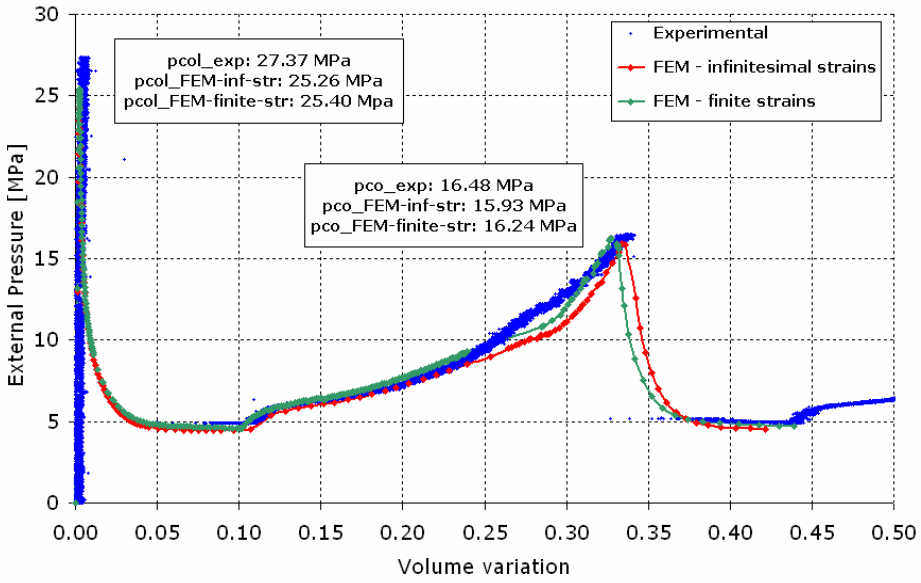

Figure 4.19: Sample 2. FEM vs. experimetal results (flattening cross-over)

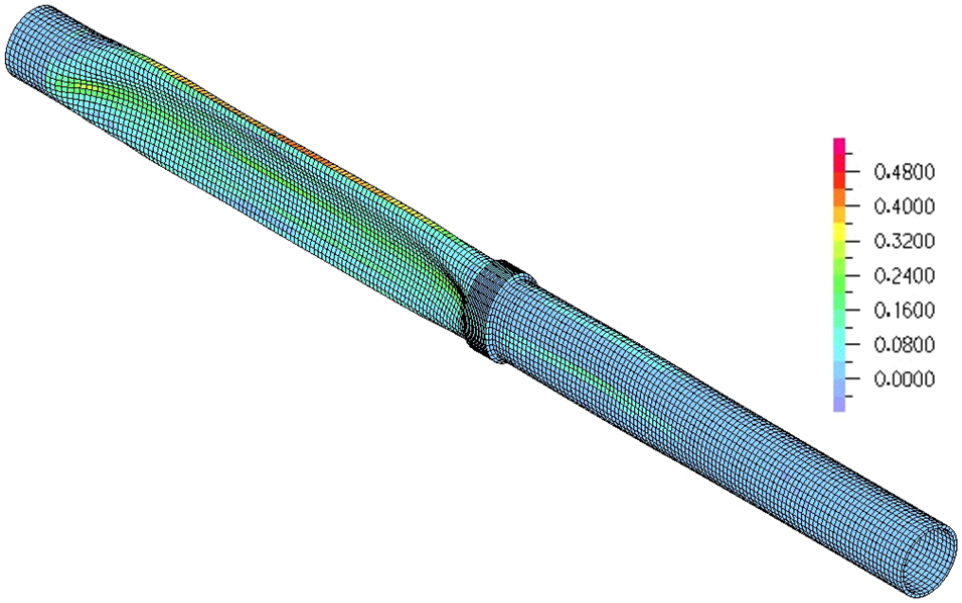

Figure 4.20: Sample 2. Deformed mesh (flattening cross-over). Equivalent plastic strains

In Fig. 4.20 we present, for sample 2, the deformed finite element mesh after cross-over.

In Figs. 4.21 and 4.22 we present the same comparison for samples 3 and 4 (flipping). Again, the agreement between FEM and experimental results is very good and again the results obtained using FEM under the assumptions of finite and infinitesimal strains are very close.

In Fig. 4.23 we present, for sample 4, the deformed finite element mesh after cross-over.

Finally in Fig. 4.24 we compare the experimentally observed and FEM predicted shapes for a case where the cross-over mechanism was flattening. In Fig. 4.25 we make the same comparison for a case in which the cross-over mechanism was flipping.

In both cases the agreement between numerical and experimental results is excellent.

It is interesting to notice that in Samples 2 and 4 the plastic strains in the deformed section knee are very high; in our case the elements were removed when the equivalent

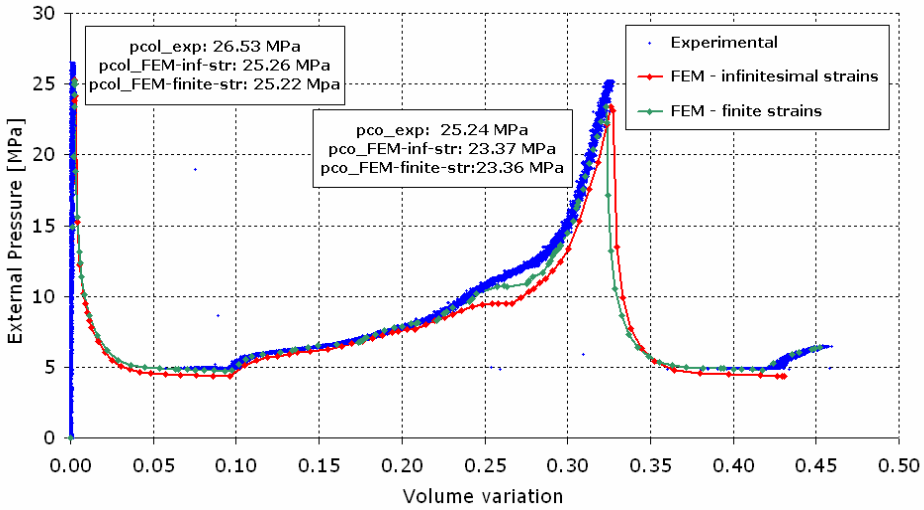

Figure 4.21: Sample 3. FEM vs. experimetal results (flipping cross-over)

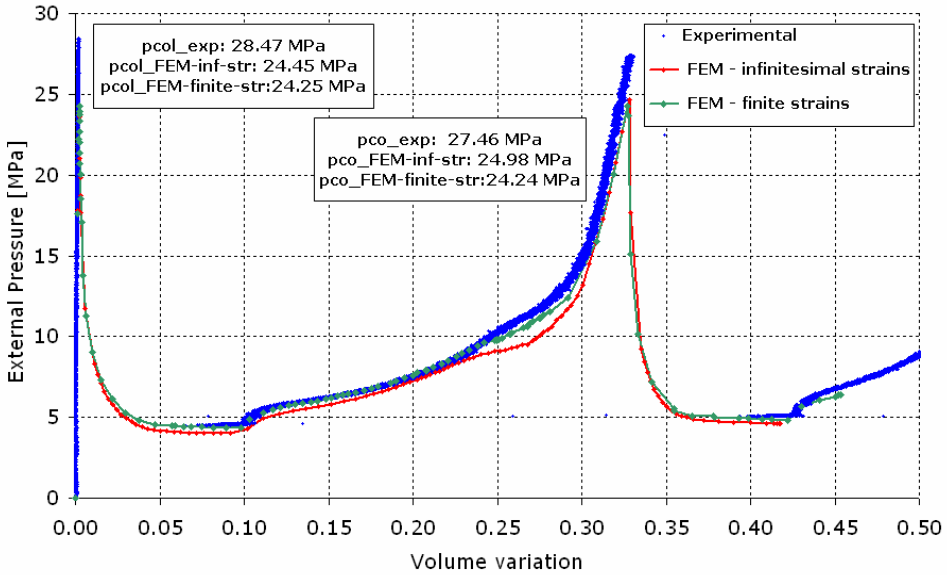

Figure 4.22: Sample 4. FEM vs. experimetal results (flipping cross-over)

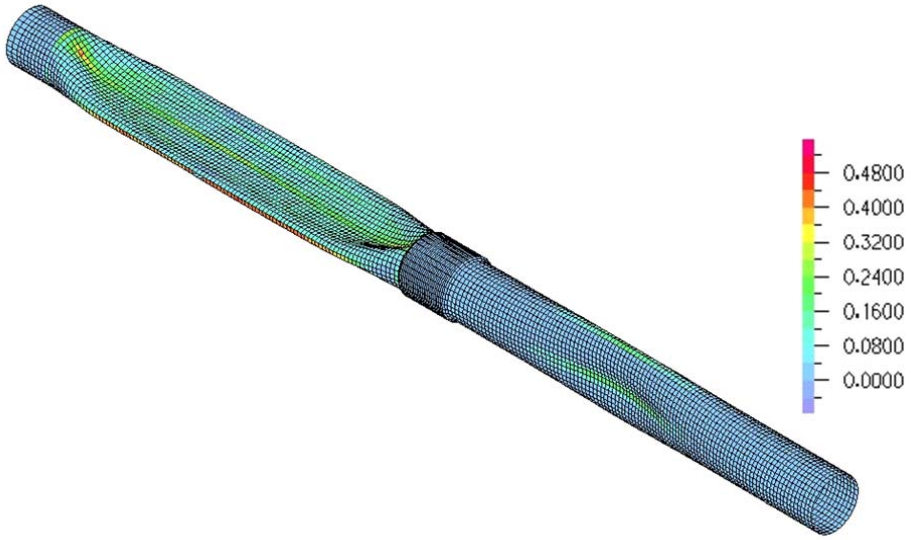

Figure 4.23: Sample 4. Deformed mesh (flipping cross-over). Equivalent plastic strains

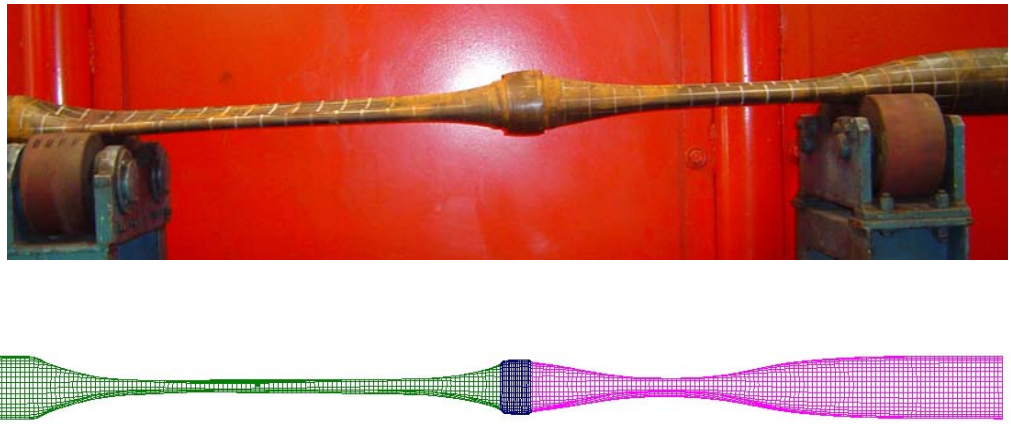

Figure 4.24: Sample 2. Experimentally observed and FEM predicted shapes of collapsed pipes after a flattening cross-over

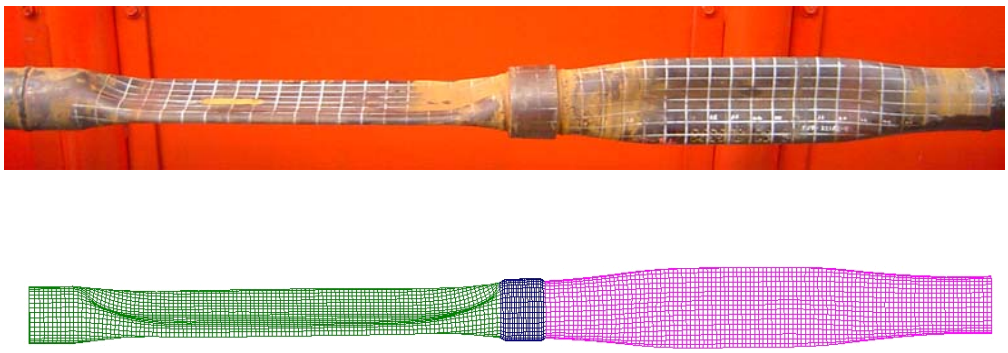

Figure 4.25: Sample 3. Experimentally observed and FEM predicted shapes of collapsed pipes after a flipping cross-over

plastic strain reaches 100%; however more sophisticated criteria for the material damage can be implemented [8].

4.5 Main observations

The two collapse modes reported in the literature, the flattening and the flipping mode, were identified in our simulations.

The agreement between the finite element predictions and the laboratory observations, both for the collapse and cross-over pressure, is very good; hence, finite element models can be used as a reliable engineering tool to assess the performance of integral ring buckle arrestors for steel pipes.

Regarding the use of a finite strain elasto-plastic formulation or of infinitesimal strains, our numerical results consistently show that if the analysis purpose is the determination of the collapse and cross-over pressures, the use of the less expensive infinitesimal strain model is amply justified; however, if detailed information on the strain/ stresses in the collapse buckle is sought, the more resources consuming finite strain models should be used.

Chapter 5

UOE Pipe Manufacturing Process

5.1 Introduction

The UOE process is used in industry for manufacturing steel pipes starting from plates that are cold formed and welded.

In Fig. 5.6 we depict the first step in this process: the edge press where the plate longitudinal sides are bent with a curved shape.

Afterwards, the U-press (Fig. 5.7) and the O-press (Fig. 5.8) are used to complete the preforming of the pipe; this preformed pipe is then welded using an automatic welding process.

To round its shape the pipe is then mechanically expanded to its final dimensions (Fig. 5.9).

The above described cold forming process introduces residual stresses and plastic deformations that, due to the Bauschinger effect [52], will reduce the yielding stress of the steel for compressive loading.

Therefore, for deepwater applications, the cold forming processes involved in UOE pipe manufacturing significantly reduces pipe collapse strength [26].

This Chapter presents a bidimensional finite element model developed to describe the UOE process, following Tenaris CONFAB (Brazil) specifications (process and tooling) [87].

This model was used to analyze the influence of each stage of the process on the material plastic deformations, residual stresses and on the structural behavior of a 12.75" OD 0.5" WT X60 and of an 18.0" OD 1.0" WT X60 UOE welded pipe.

Besides the numerical analysis two samples of each of the following pipes, manufactured at Tenaris CONFAB, were tested at C-FER: 12.75" OD 0.5" WT X60, 16.00" OD 0.5" X60, and 20.00" OD 0.75" WT X80.

The 2D models of the UOE manufacturing process were developed [87] in order to,

- analyze the influence of process variables on the collapse pressure, residual stress and geometry (mode 2 of Fourier decomposition of the pipe external surface),
- correlate the finite element results with the experiemntal ones obtained at C-FER,
- investigate the influence of the material strain hardening.

5.2 Collapse testing

Collapse testing was performed at C-FER's collapse chamber (Fig. 3.2).

Two samples from each of the 12.75", 16" and 20" pipes were tested. Geometric characterization was performed including diameter and wall thickness measurements. Specimens were cut to length and flat end caps were attached by welding.

The testing procedure involved an increase of external pressure until collapse occurred. Table 1 summarizes the specimen average ovality, residual stresses and collapse test results. The ovality was calculated according to Eqn. 2.1, the diameters were measured at C-FER. Collapse and propagation curves for all tested specimens as well as post-test images can be seen in Figures 5.1 through 5.3.

The eccentricity usually is not measured in welded pipes, since they are formed from plates and, therefore, the thickness is almost uniform.

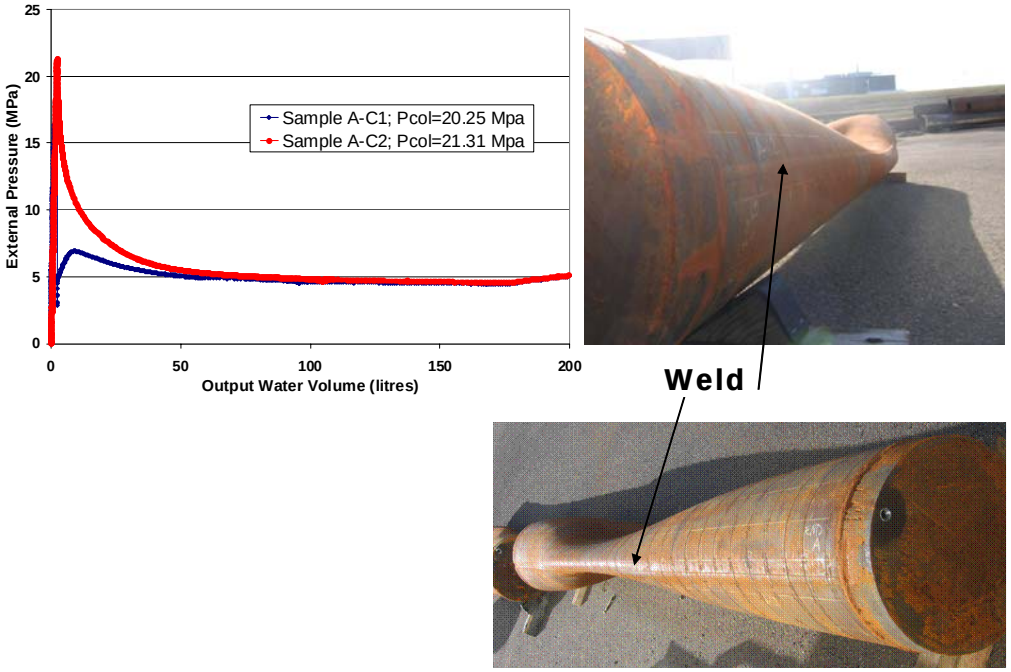

Figure 5.1: 20" OD 0.75" WT X80. Collapse curves and post-collapse samples.

$OD\ [inch]$	$t\ [inch]$	OD/t	$Grade$	$Length\ [inch]$	$Ovality\ [\%]$	$\sigma_R\ [MPa]$	$Pc\ [Mpa]$
20	0.75	26.7	$X80$	378	0.210	34.45	20.25
					0.082		21.31
16	0.50	32	$X60$	368	0.140	26.53	14.18
					0.106		14.78
12.75	0.50	25.5	$X60$	307	0.154	68.90	21.68
					0.204		21.21

Table 1. Collapse testing summary (C-FER lab)

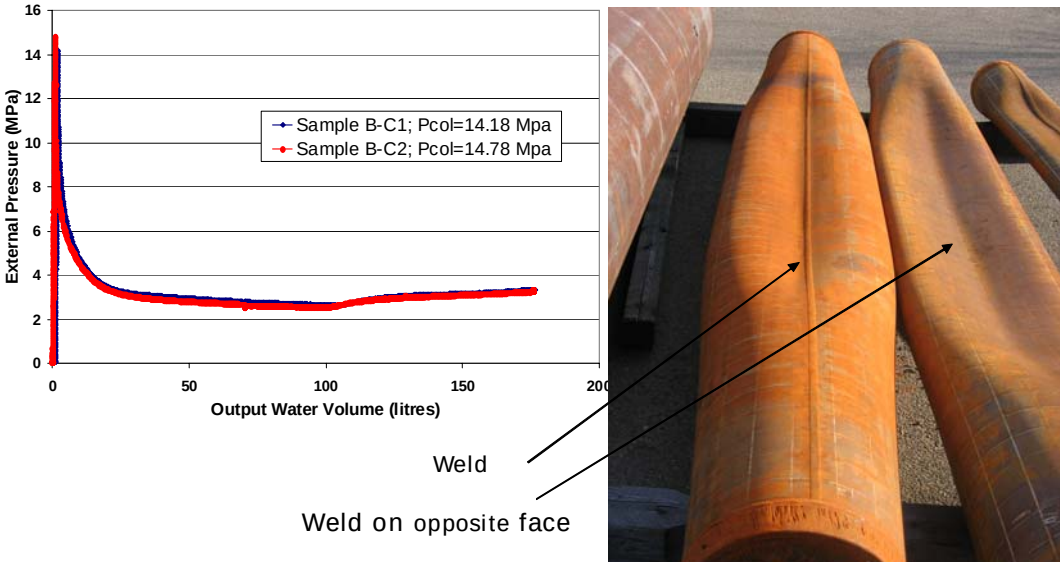

Figure 5.2: 16" OD 0.50" WT X60. Collapse curves and post-collapse samples.

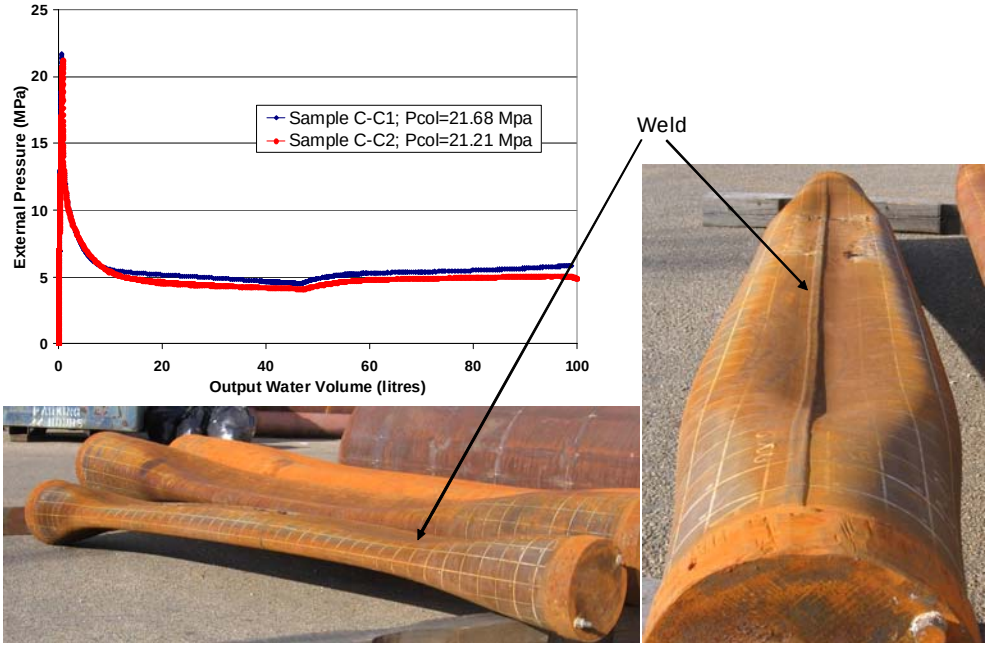

Figure 5.3: 12.75" OD 0.50" WT X60. Collapse curves and post-collapse samples.

5.3 Finite element model

For the numerical simulation of the UOE process, we developed a finite element model using the Q1-P0 plane strain element, in the ADINA general-purpose code [9] [76].

The numerical model was developed using a material and geometrical nonlinear formulation, taking into account large displacements/rotations but small strains [9].

Regarding the material, we use an elasto-plastic bi-linear material model and von Mises associated plasticity with kinematic hardening.

The main characteristics of the material model are,

- Young's modulus : $E = 206010$ MPa,
- Poisson coefficient: $\nu = 0.3$,
- several strain hardening modulus values are considered,

  0.2 % and 1.0 % of the Young's modulus for the 12.75" OD pipe

  1.0 % and 2.0 % of the Young's modulus for the 16.0" OD pipe

  0.2 %, 1.0 % and 2.0 % of the Young's modulus for the 20.0" OD pipe.

During the collapse tests performed at C-FER the tensile / compressive hoop yield stress was determined for fibers located close to the OD and ID respectively.

We use as the yield stress of the unstrained material for each pipe,

$$\sigma_y = \frac{1}{4}\left(\widehat{\sigma}_y^+ + \widetilde{\sigma}_y^+ + \widehat{\sigma}_y^- + \widetilde{\sigma}_y^-\right)$$

Where,

$\widehat{\sigma}_y^+$: tensile test, ID location

$\widehat{\sigma}_y^-$: compressive test, ID location

$\widetilde{\sigma}_y^+$: tensile test, OD location

$\widetilde{\sigma}_y^-$: compressive test, OD location

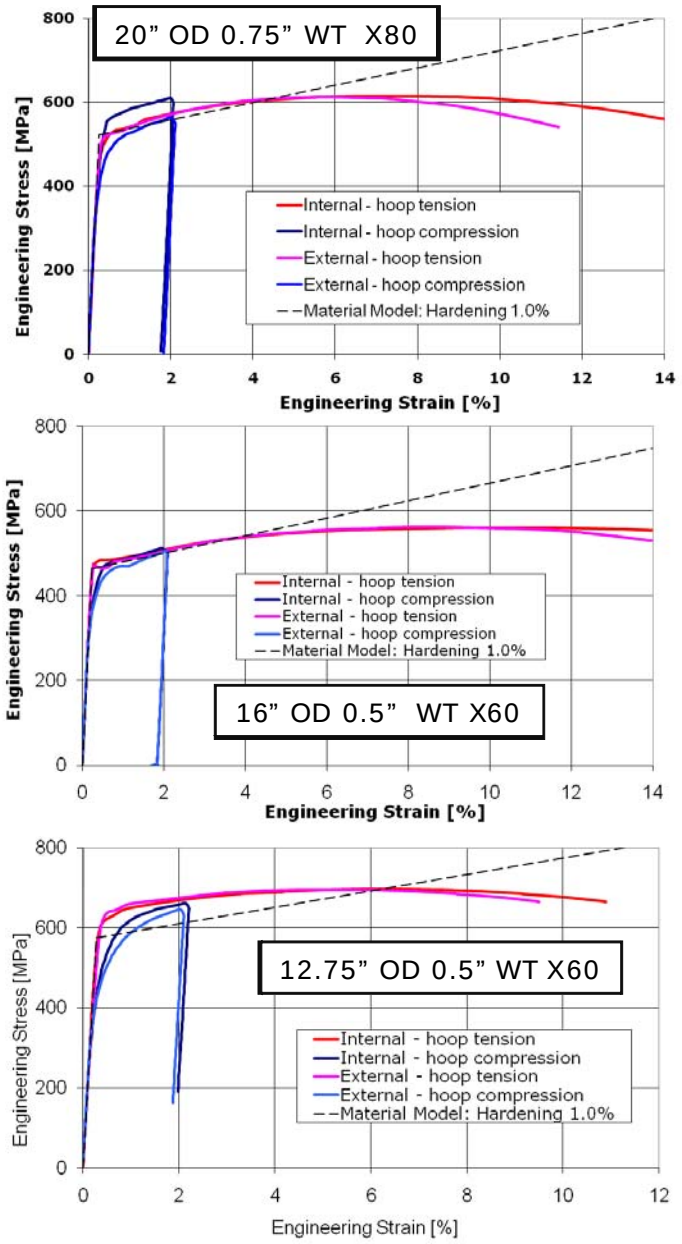

Figure 5.4: C-FER hoop tests and 1.0% strain hardening material model.

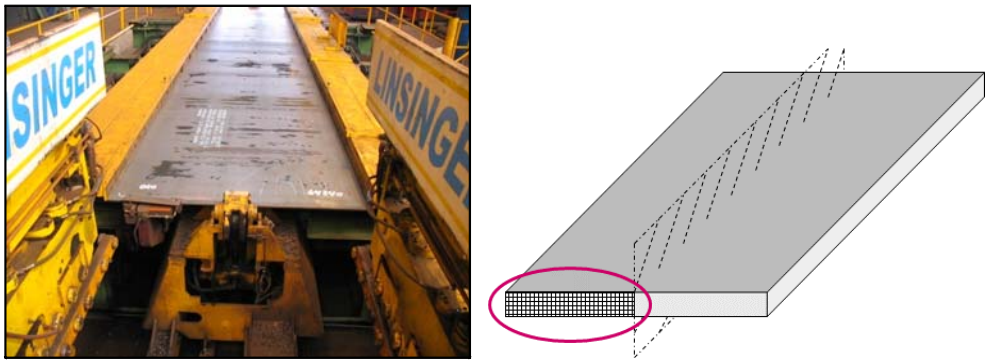

Figure 5.5: Plate: actual process and FE model.

Figure 5.4 shows the stress-strain curves obtained at C-FER and the 1.0 % strain hardening adopted for the numerical model for each pipe.

The forming tools are modeled as rigid bodies and we use a sliding node contact algorithm to simulate the contact between the tools and the plates [76] [87]. Symmetry conditions are considered for the model. Figure 5.5 shows the plate at the beginning of the process and the finite element mesh.

The geometry of the tools was provided by Tenaris CONFAB.

5.3.1 Tooling

The first step of the manufacturing process is the Edge press. During this stage, the upper tool is fixed and the lower tool is moved in the vertical direction. Figure 5.6 shows a picture of the actual process and the finite element model.

Then the manufacturing process continues with the "U" press, where the plate is turned into a “U”. In Figure 5.7 we can observe the following stages,

(a) the upper die ("pear") moves down in the middle of the plate and pushes it to contact the roller,

(b) the pear and the base go down together, keeping a distance of one plate thickness between them,

(c) the roller starts moving to the symmetry axis,

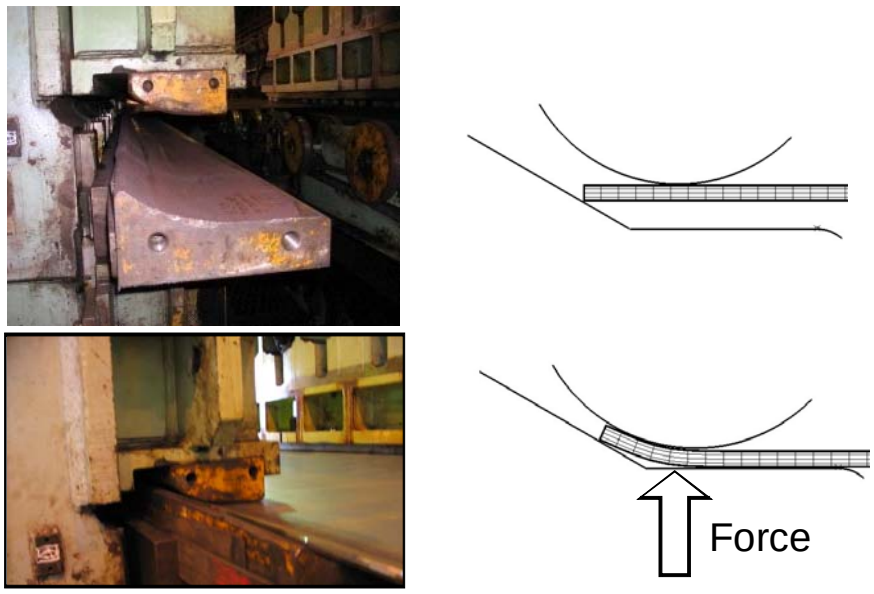

Figure 5.6: Edge press: actual process and FE model

(d) the pear moves to its limit and the load is released; then the plate is formed into an "U" shape.

The "O" press applies a circumferential compression to form an "O" from the "U" obtained in the previous stage (Fig. 5.8). To achieve this, two semi-cylindrical dies press the "U".

To simulate, in the finite element model, the welding at the point of maximum compression, the pipe is fixed at the symmetry axis. Finally, a radial expansion is applied in order to obtain the final shape of the pipe. An internal mandrel with expansion segments is simulated. The segments move in radial direction, and provide the expansion required to obtain the nominal perimeter when the load is released (Fig. 5.9).

Figure 5.10 presents the evolution, along the UOE process, of the accumulated plastic strains for a 16" OD 0.5" WT X60 pipe.

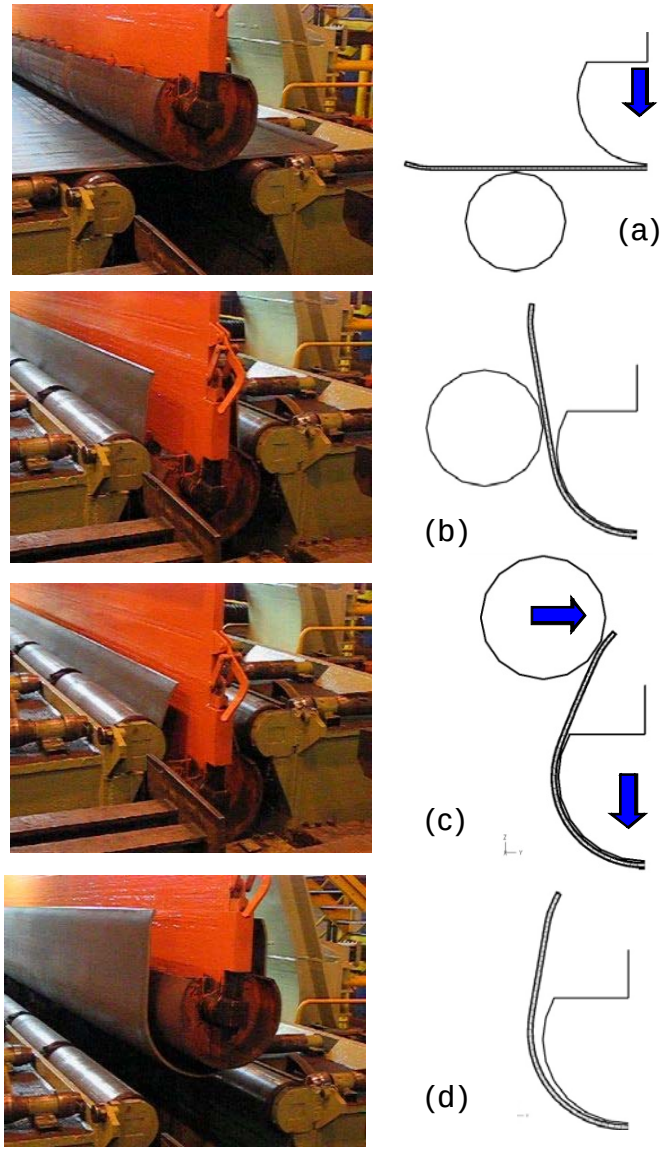

Figure 5.7: U press: actual process and FE model

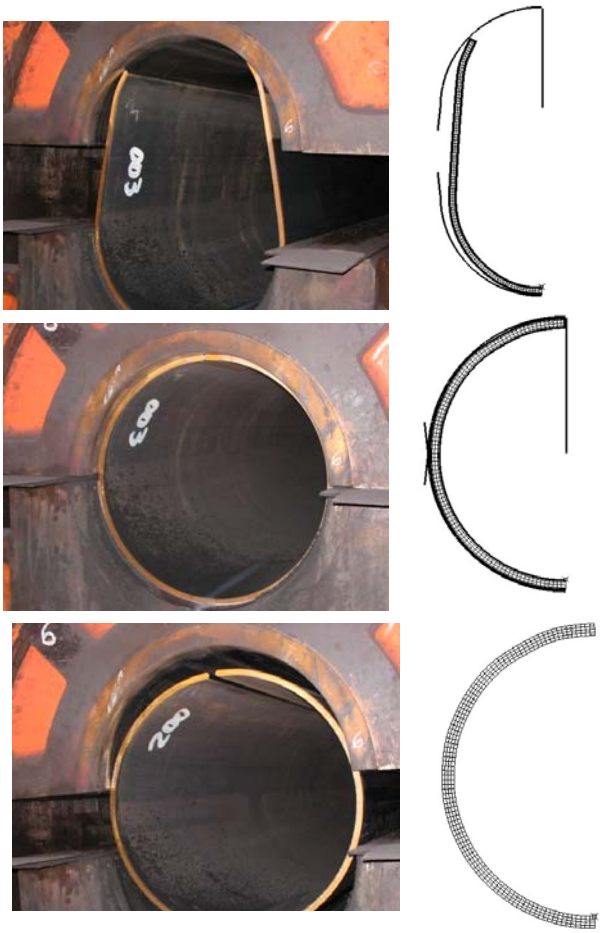

Figure 5.8: O press: actual process and FE model.

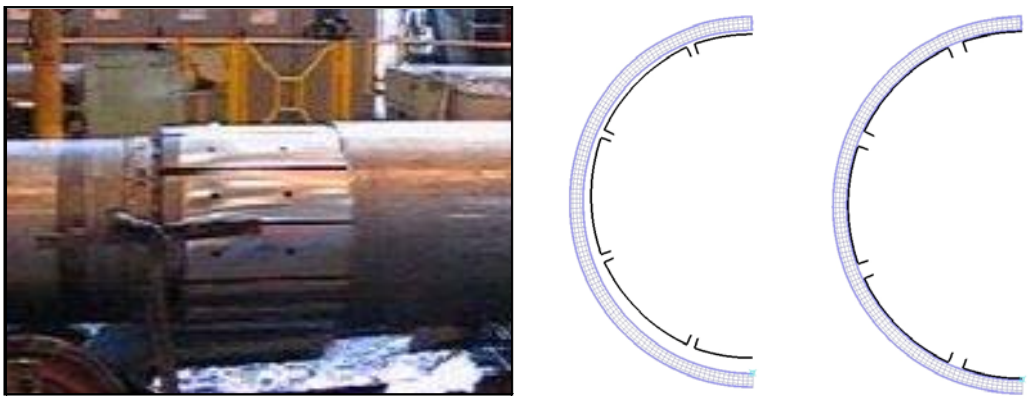

Figure 5.9: Mechanical expansion after welding: actual process and FE model

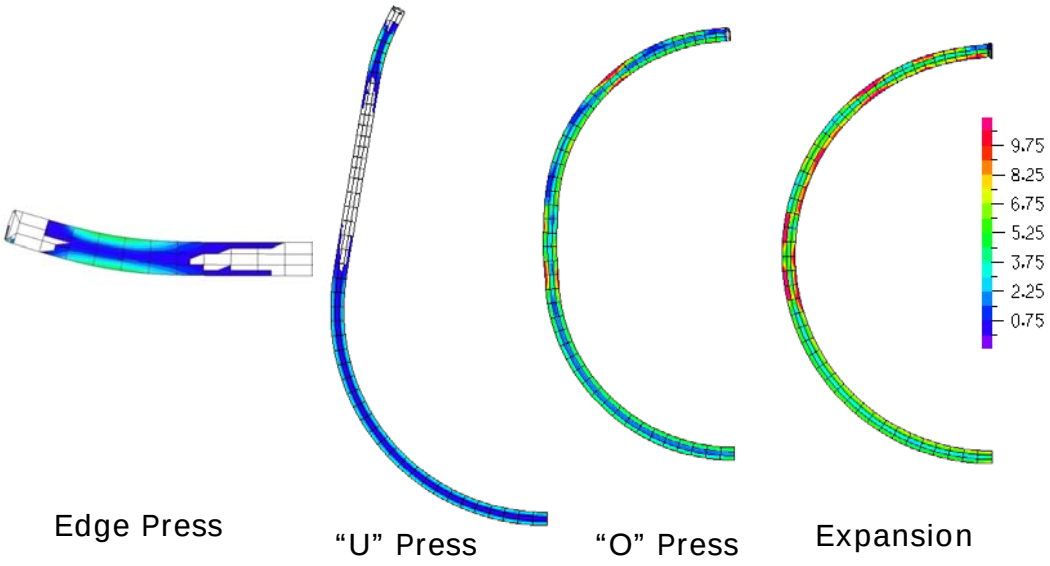

Figure 5.10: 16" OD 0.5" WT X60. Accumulated effective plastic strain evolution [%]

5.4 Description of the evaluated pipe characteristics

The parameters to be analyzed to compare the 2D FEA model with measured results are geometry (mode 2 of Fourier analysis), collapse pressure and residual stresses.

5.4.1 Fourier analysis and determination of mode 2

Fourier analysis of the resulting OD shapes obtained with the numerical simulation of the forming process is performed by using Fourier decomposition, as described in Appendix A. The position of the nodes on the outer surface is used as initial data.

We choose the second mode as geometrical description parameter because, as it was established in Section 3.2, the value of the second mode is quite different (lower) from the ovality measured with a standard API ovalimeter. The imperfection that controls the value of the collapse pressure is the second mode.

Figure 5.11 shows mode 2 distribution along the two samples for each pipe. These mode distributions were obtained from the measurements performed with the "shapemeter" [6] at Tenaris Siderca Full Scale Laboratory.

It can be observed that the distribution is not uniform, therefore it is difficult to compare the actual second mode of the pipes with the value obtained with a bidimensional model. The comparisons are done considering an average value for each sample.

5.4.2 Residual Stresses

A ring splitting test [6] was simulated after the forming process.

The residual stresses are calculated as it was explained in Chapter 2. The ring splitting tests were also performed at C-FER.

5.4.3 Collapse Pressure

A collapse test is now simulated on the result of the UOE forming model. The results of the collapse testing done at C-FER are listed in Table 1. In a second analysis, the

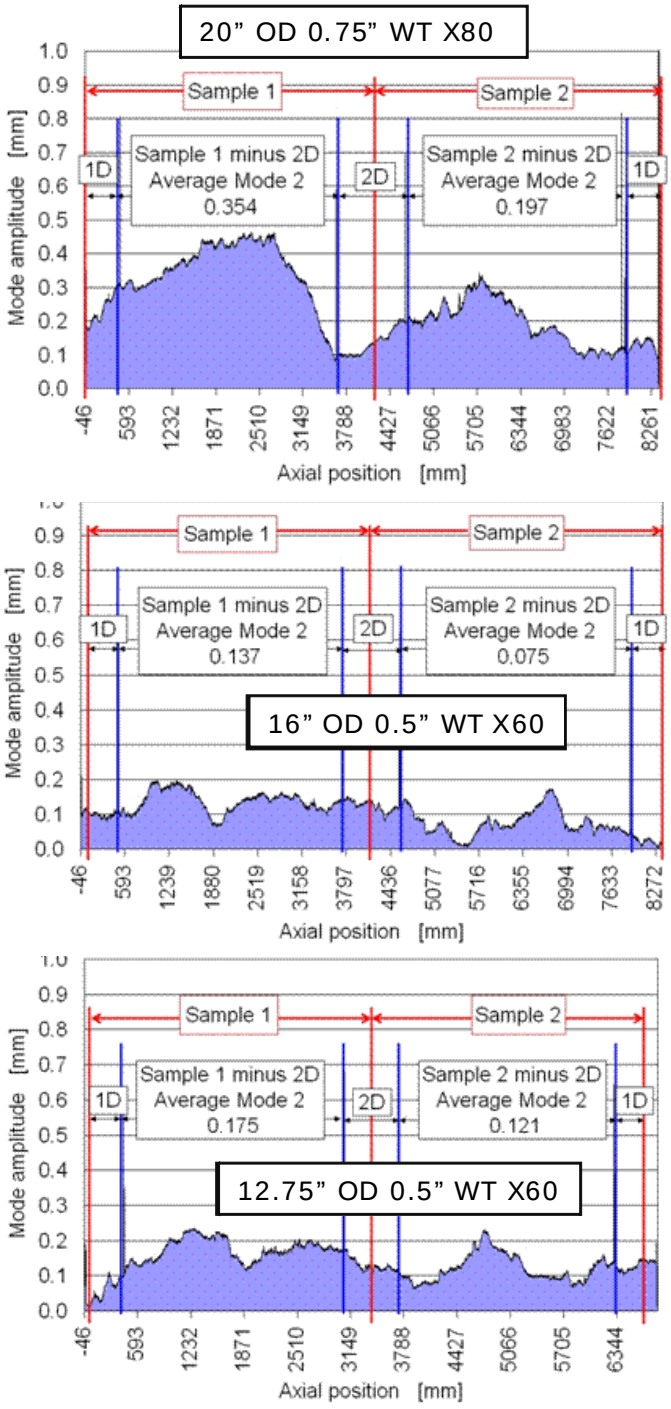

Figure 5.11: Mode 2 distribution along the 2 samples of each pipe

external collapse pressure values are obtained from pipes with the same geometry but without any residual deformation or stresses; these analyses are aimed at the evaluation of the degradation of the external collapse pressure induced by the UOE residual stresses and plastic strains.

An evaluation of the second mode of the Fourier decomposition, residual stresses and collapse pressure is done as a function of the compression strains applied by the "O" press. The applied expansion depends on the applied compression, because the final external tube diameter has to be the nominal one. Taking into account the final shape obtained with the 2D model, the compression rate is calculated with the formula,

$$CR\,[\%] = \frac{OP_A - OP_B}{OP_B} \cdot 100$$

where,

$CR\%$: compression rate [%]

OP_A: outside Perimeter measured as the sum of node to node distances, after O press.

OP_B: outside Perimeter measured as the sum of node to node distances, before O press.

Figures 5.12 to 5.14 show the mode 2, residual stresses and collapse pressure curves for the 20", 16.0" and 12.75" OD pipes, respectively, as a function of the compression rate applied during the "O" press stage. In order to evaluate the detrimental effect of the UOE process on the collapse pressure, it is numerically calculated for pipes with the same external geometry obtained in the numerical analysis but considering the material without any strain history (virgin material). The figures also show the experimental results obtained at C-FER and the average second mode values, as described in the previous section.

As it can be expected from the discussion in Chapter 2, the results of the 2D models do not present an acceptable correlation with the experimental tests; however, these 2D model results can be used to qualitatively explore the effect of the process variables,

The material hardening does not have an important effect on the mode 2 amplitud

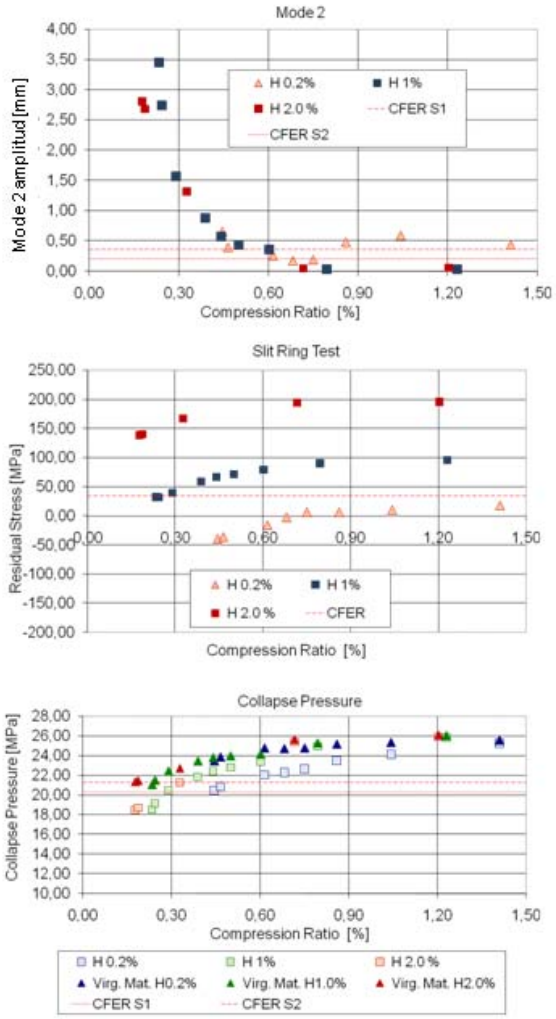

Figure 5.12: 20.0" OD 0.75" WT X80 tube. Mode 2, residual stress, collapse pressure and collapse pressure of the virgin material.

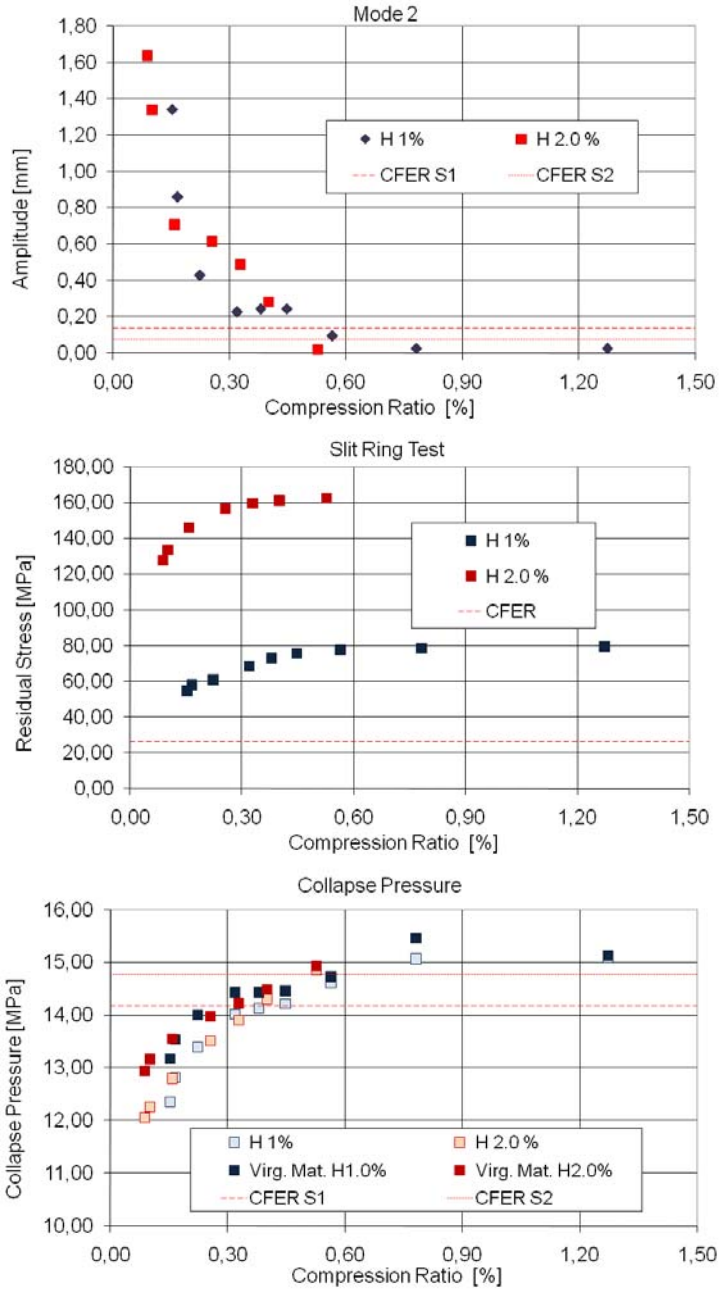

Figure 5.13: 16.0" OD 0.5" WT X60 tube. Mode 2, residual stress, collapse pressure and collapse pressure of the virgin material.

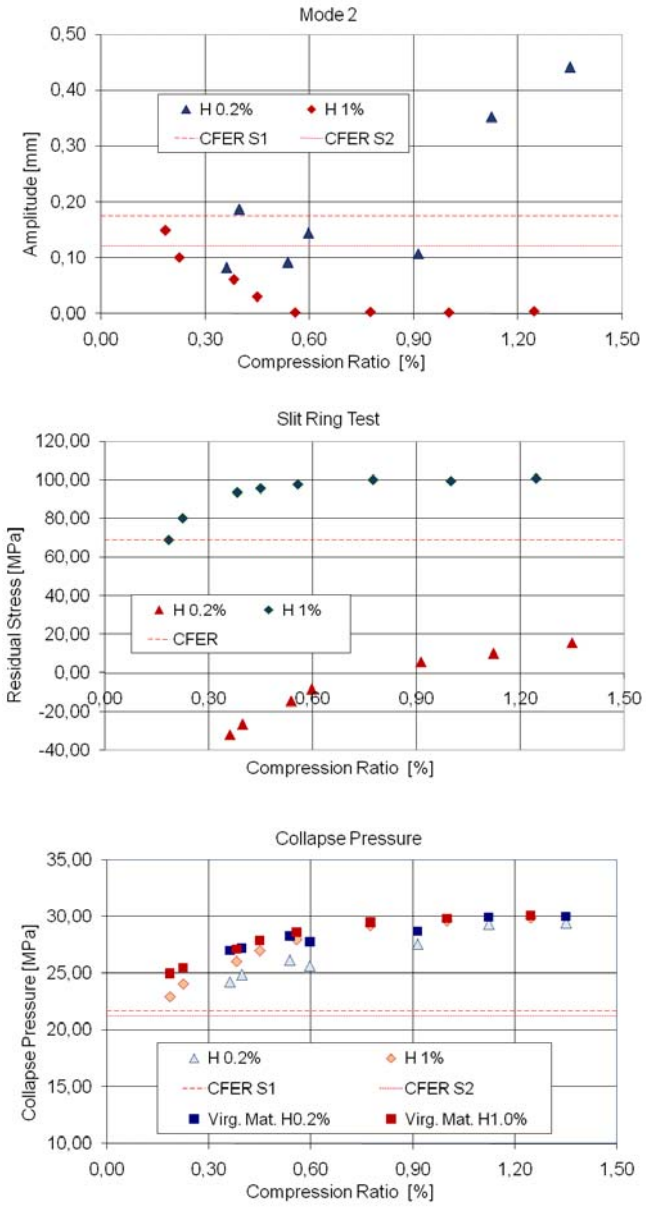

Figure 5.14: 12.75" OD 0.5" WT X60 tube. Mode 2, residual stress, collapse pressure and collapse pressure of the virgin material.

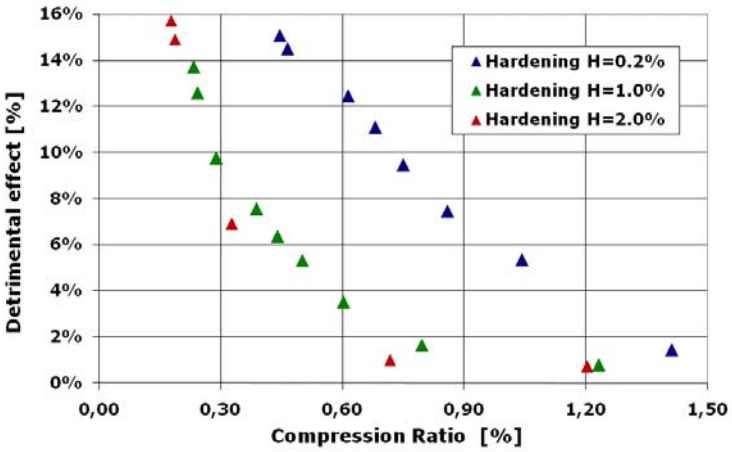

Figure 5.15: 20" OD 0.75" WT X80. Collapse pressure-detrimental effect

nor on the collapse pressure but the residual stresses are quite sensitive to this material parameter. The fact that the sensitivity of the residual stresses is high and the sensitivity of the collapse pressure is low can be explained considering that we are dealing with pipes having a large (OD/t) ratio.

The increase in the compression rate highly improves the shape of the pipes and their collpase pressure.

Also, it can be seen that the difference in the collapse pressure, between the unstrained material model and the 'as built' material model of the tubes, diminishes as the compression rate increases for all cases. This conclusion was also discussed in [41]. Figure 5.15 shows in a more detailed way the detrimental effect of the UOE process on the external collapse pressure, for a 20" OD 0.75" WT X80 pipe and also the benefitial effect of increasing the compression ratio.

Additional analyses were done considering a 16" OD 0.5" X60 UOE pipe and Hardening 1%. Each [*Collapse Pressure vs. Expansion rate*] curve shown in Figure 5.16 was built for a given compression rate value and varying the expansion rate. These analyses are different from the ones shown above because the final diameters are obtained

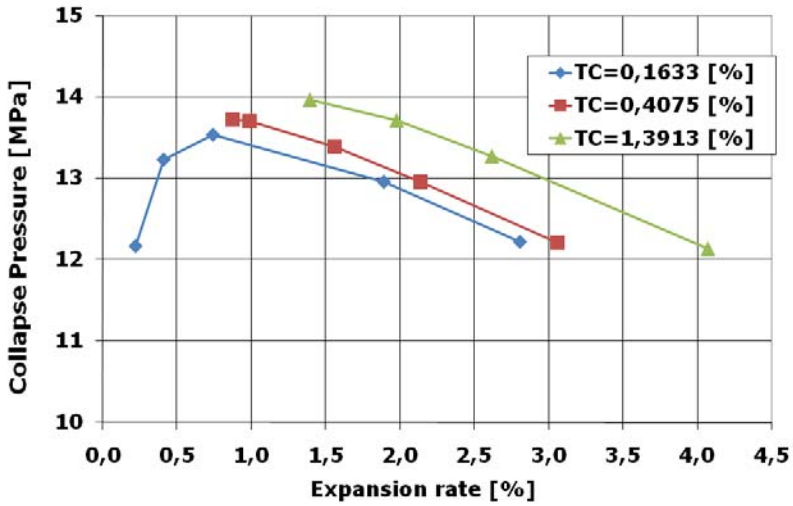

Figure 5.16: Influence of the compression and expansion rates on the collpase pressure

as result of the process.

5.5 Parametric analysis aimed at tooling design

In Figure 5.17 we present the perimeter before the expansion, that we obtained numerically for a 20" OD 1.0" WT X70 pipe, varying the original plate width and L1, which is the length of the rigid tool that separates the superior die from the inferior one, in the "O" press. We can see here not only the influence of the initial plate width in the shape of the pipe but also the influence of L1. When L1 increases, increases also the no bent region; when L1 is higher than a certain value (the maximum of the curves in Fig. 5.17) , the influence of the no stretched fibers is more important than the influence of the stretched ones; therefore, the perimeter decreases.

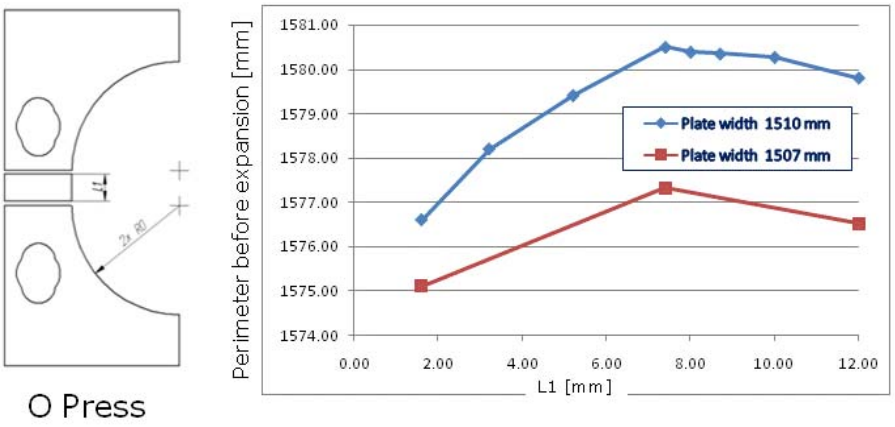

Figure 5.17: 20" OD 1.0" WT X70. Parametric analyses of L1, O Press

5.6 Main observations

We developed a bidimensional model to describe the UOE process, following Tenaris CONFAB specifications (process and tooling). This model is a very useful tool not only to analyze the influence of each stage of the process on the material plastic deformations, residual stresses and on the structural behavior of the pipes but also for tooling design, improvements in the process, etc.

One very important conclusion from this study is that the deterioration of the collapse pressure diminishes as the compression ratio increases, conclusion also presented in [41].

Chapter 6

Large strain shell elements

6.1 Introduction

In 1970, Ahmad, Irons and Zienkiewicz presented a shell element formulation that after many years still constitutes the basis for modern finite element analysis of shell structures [1]. The original formulation was afterwards extended to material and geometric nonlinear analysis under the constraint of the infinitesimal strains assumption, [10] [46] [64].

The fundamental features of the A-I-Z shell element are,

- using isoparametric interpolation functions the displacements inside the shell element are interpolated from three displacement-d.o.f. and two rotation-d.o.f. at each node,
- the interpolated generalized displacement fields present C^o continuity,
- the element is not based on any plate/shell theory but it is a continuum element incorporating several assumptions that we list below (degenerated solid element).

Kinematic and constitutive assumptions,

- a straight line that is initially normal to the mid-surface remains straight after the deformation,

- a straight line that is initially normal to the mid-surface is not stretched during the deformation,

- the through-the-thickness stresses are zero.

It is important to remark that the second assumption precludes the consideration of finite strain deformations.

Even tough the A-I-Z shell element was a breakthrough in the field of finite element analysis of shell structures, it suffers from the locking phenomenon and much research effort has been devoted to the development of A-I-Z type elements that do not present this problem [9] [14] [15] [21] [90] [91].

The MITC4 shell element [12] [13] [30] which was developed to overcome the locking problem of the A-I-Z shell elements has become, since its development in the early eighties, the standard shell element for many finite element codes. However, the limitation of infinitesimal strains is still present in the MITC4 formulation.

Many researchers have developed shell elements that can model finite strain situations, among them,

- an early contribution by Rodal and Witmer [66], where after the displacement calculations the shell element thickness is updated neglecting the elastic strains and invoking the incompressibility of the plastic flow,

- in 1983 Hughes and Carnoy [43] developed a finite strain shell element for the Mooney-Rivlin material model which uses a plane-stress constitutive relation for the laminae and updates afterwards the thickness via a staggered iterative formulation,

- Simo and co-workers [68]- [73] in the period 1988-1992 developed a complete 3D nonlinear shell element formulation,

- Ramm and co-workers [16] [20] developed 3D shell elements considering also through-the-thickness stretching.

In 1995 Dvorkin, Pantuso and Repetto developed the MITC4-TLH element, that based on the original MITC4 formulation can model finite strain elasto-plastic deformations [28] [36]. This element imposes the condition of zero transversal stresses and its computational cost is rather high.

In this thesis we present an element that is also based on the MITC4 formulation and can efficiently model finite strain deformations using a general 3D material model: the MITC4-3D element.

The most relevant differences with the original MITC4 formulation are,

- for each quadrilateral element we have 22 d.o.f.: 5 generalized displacements per node plus 2 extra d.o.f. to incorporate the through-the-thickness stretching,
- we use a general 3D constitutive relation instead of the original laminae plane stress constitutive relation,

  Our objective is to implement the new MITC4-3D element for elasto-plastic finite strain deformations. We achieve this objective in two steps,

- first we explore different hyperelastic formulations for modeling the elastic behavior [82],
- second we implement an elasto-plastic formulation considering metal plasticity.

6.2 The MITC4-3D formulation

Some of the basic features of our MITC4-3D element are,

1. the shell geometry is interpolated using mid-surface nodes and director vectors.
2. the nodal displacements and transverse shear strains are interpolated using the original MITC4 formulation [30],
3. for interpolating the director vectors special care is taken to avoid spurious director vector stretches [39] [68],

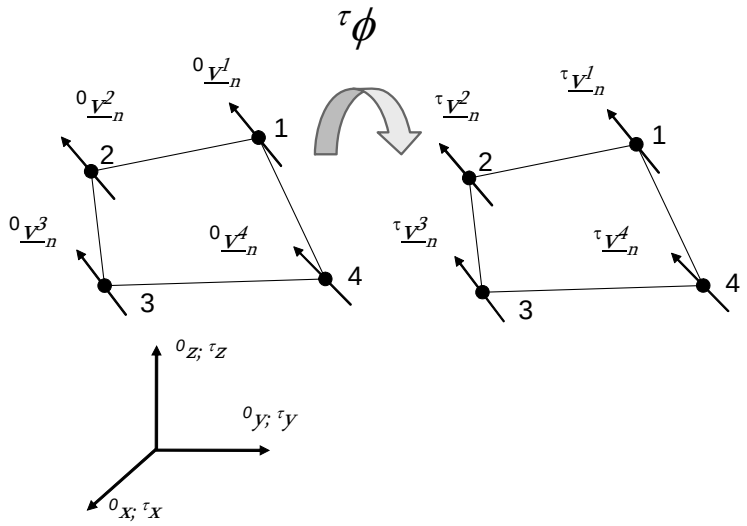

Figure 6.1: Reference ($t = 0$) and spatial ($t = \tau$) configurations

4. two additional degrees of freedom are considered to include a linear thickness stretching. These thickness-stretching degrees of freedom are condensed at the element level,

5. the elasto – plastic formulation is developed following the work of Simo and co-workers [71] : multiplicative decomposition of the deformation gradient tensor and maximum plastic dissipation (associate plasticity),

6. special consideration is given to the formulation efficiency.

6.2.1 Shell element geometry in the reference configuration

Following the MITC4 formulation we define, in the reference configuration, nodes on the shell mid-surface and at each node we define a *director vector* which represents, at that node, an approximation to the shell mid-surface [27].

Therefore, defining inside the element the natural coordinate system (r, s, t) [9], for the element shown in Fig. 6.1 with constant thickness we can write,

$$ {}^{o}\underline{x}(r,s,t) = h_k(r,s)\ {}^{o}\underline{x}_k \ + \ \frac{t}{2}\ {}^{o}\underline{d}\ a \tag{6.1a} $$

where [68] [39],

$$ {}^{o}\underline{d} = \frac{h_k(r,s)\ {}^{o}\underline{V}_n^k}{\left|\left|h_k(r,s)\ {}^{o}\underline{V}_n^k\right|\right|} \tag{6.1b} $$

and,

$h_k(r,s)$: isoparametric 2D interpolation functions [9],

${}^{o}\underline{x}_k$: k-node position vector,

a : constant element thickness.,

${}^{o}\underline{V}_n^k$: k-node director vetor; with $\left|\left|{}^{o}\underline{V}_n^k\right|\right| = 1$.

In the above equations and in what follows we use the summation convention.

6.2.2 Shell geometry in the spatial configuration

For interpolating the spatial geometry in the τ-configuration, Fig. 6.1, we use,

$$ {}^{\tau}\underline{x}(r,s,t) = h_k(r,s)\ {}^{\tau}\underline{x}_k \ + \frac{t}{2}\ ({}^{\tau}\lambda_o + \ {}^{\tau}\lambda_1 t)\ {}^{\tau}\underline{d}\ a \tag{6.2a} $$

$$ {}^{\tau}\underline{d} = \frac{h_k(r,s)\ {}^{\tau}\underline{V}_n^k}{\left|\left|h_k(r,s)\ {}^{\tau}\underline{V}_n^k\right|\right|}\ . \tag{6.2b} $$

For the director vectors in the spatial configuration also $\left|\left|{}^{\tau}\underline{V}_n^k\right|\right| = 1$.

In Eq.(6.2a) ${}^{\tau}\lambda_o$ is a constant thickness stretching and ${}^{\tau}\lambda_1$ is the through-the-thickness stretching gradient.

In our formulation the element d.o.f. ${}^{\tau}\lambda_o$ and ${}^{\tau}\lambda_1$ are discontinuous across element boundaries and they will be condensed at the element level.

6.2.3 Incremental displacements

The incremental displacements to evolve from the τ-configuration to the $\tau + \Delta\tau$-configuration are,

$$\underline{u} = {}^{\tau+\Delta\tau}\underline{x} - {}^{\tau}\underline{x} \tag{6.3a}$$

$$\begin{aligned}\underline{u}(r,s,t) = {} & h_k(r,s)\,\underline{u}_k \\ & + \frac{t}{2}\,a\,\left({}^{\tau}\lambda_o + \Delta\lambda_o + {}^{\tau}\lambda_1\,t + \Delta\lambda_1\,t\right)\,\frac{h_k(r,s)\,{}^{\tau+\Delta\tau}\underline{V}_n^k}{\left|\left|h_k(r,s)\,{}^{\tau+\Delta\tau}\underline{V}_n^k\right|\right|} \\ & - \frac{t}{2}\,a\,\left({}^{\tau}\lambda_o + {}^{\tau}\lambda_1 t\right)\,\frac{h_k(r,s)\,{}^{\tau}\underline{V}_n^k}{\left|\left|h_k(r,s)\,{}^{\tau}\underline{V}_n^k\right|\right|}\,.\end{aligned} \tag{6.3b}$$

In the above, ${}^{\tau+\Delta\tau}\lambda_o = {}^{\tau}\lambda_o + \Delta\lambda_o$ and ${}^{\tau+\Delta\tau}\lambda_1 = {}^{\tau}\lambda_1 + \Delta\lambda_1$.

For the director vector rotations we can write [35],

$${}^{\tau+\Delta\tau}\underline{V}_n^k = {}^{\tau+\Delta\tau}_{\tau}\underline{\underline{R}}\,\cdot\,{}^{\tau}\underline{V}_n^k \tag{6.4}$$

with,

$${}^{\tau+\Delta\tau}_{\tau}\underline{\underline{R}} = \underline{\underline{I}}_3 + \frac{\sin\theta_k}{\theta_k}\,\underline{\underline{\Theta}}^k + \frac{1}{2}\left(\frac{\sin\left(\theta_k/2\right)}{\left(\theta_k/2\right)}\right)^2\,\left(\underline{\underline{\Theta}}^k\right)^2 \tag{6.5}$$

being $\underline{\underline{I}}_3$ is the second order unit tensor.

We use the base vectors $\left({}^{\tau}\underline{V}_1^k;\ {}^{\tau}\underline{V}_2^k;\ {}^{\tau}\underline{V}_n^k\right)$ defined as,

$$\begin{aligned}{}^{\tau}\underline{V}_1^k &= \frac{{}^{\tau}\underline{e}_y \times {}^{\tau}\underline{V}_n^k}{\left|\left|{}^{\tau}\underline{e}_y \times {}^{\tau}\underline{V}_n^k\right|\right|} \\ {}^{\tau}\underline{V}_2^k &= {}^{\tau}\underline{V}_n^k \times {}^{\tau}\underline{V}_1^k\end{aligned}$$

where ${}^{\tau}\underline{e}_y$ is the y base vector at time τ of the fixed cartesian system in Fig. 6.1. For the case ${}^{\tau}\underline{e}_y \times {}^{\tau}\underline{V}_n^k = 0$ [9],

$$\begin{aligned}{}^{\tau}\underline{V}_1^k &= {}^{\tau}\underline{e}_z \\ {}^{\tau}\underline{V}_2^k &= {}^{\tau}\underline{e}_x\ .\end{aligned}$$

Also,

$$\theta_k = \left(\alpha_k^2 + \beta_k^2\right)^{\frac{1}{2}}$$

$$\left[\,\Theta^k\right] = \begin{bmatrix} 0 & 0 & \beta_k \\ 0 & 0 & -\alpha_k \\ -\beta_k & \alpha_k & 0 \end{bmatrix} .$$

From Eqs. (6.4) and (6.5) we get [35],

$$^{\tau+\Delta\tau}\underline{V}_n^k = {}^{\tau}\underline{V}_n^k - \alpha_k\, {}^{\tau}\underline{V}_2^k \;+\; \beta_k\, {}^{\tau}\underline{V}_1^k - \frac{1}{2}\,\left(\alpha_k^2 + \beta_k^2\right)\, {}^{\tau}\underline{V}_n^k \;+\; h.o.t \;\; . \tag{6.6}$$

Hence,

$$\begin{aligned} \underline{u} \;\; = \;\; & h_k\, \underline{u}_k + \frac{t}{2}\,\frac{a}{\left|\left|h_k\, {}^{\tau}\underline{V}_n^k\right|\right|}\,\left({}^{\tau}\lambda_o + {}^{\tau}\,\lambda_1\, t\right)\, h_k\, \left(-\alpha_k\, {}^{\tau}\underline{V}_2^k + \beta_k\, {}^{\tau}\underline{V}_1^k\right) \\ & -\frac{t}{4}\,\frac{a}{\left|\left|h_k\, {}^{\tau}\underline{V}_n^k\right|\right|}\,\left({}^{\tau}\lambda_o + {}^{\tau}\,\lambda_1\, t\right)\, h_k\, \left[(\alpha_k)^2 + (\beta_k)^2\right]\, {}^{\tau}\underline{V}_n^k \\ & +\frac{t}{2}\,\frac{a}{\left|\left|h_k\, {}^{\tau}\underline{V}_n^k\right|\right|}\,\left(\Delta\lambda_o + \Delta\lambda_1\, t\right)\, h_k\, {}^{\tau}\underline{V}_n^k \\ & +\frac{t}{2}\,\frac{a}{\left|\left|h_k\, {}^{\tau}\underline{V}_n^k\right|\right|}\,\left(\Delta\lambda_o + \Delta\lambda_1\, t\right)\, h_k\, \left(-\alpha_k\, {}^{\tau}\underline{V}_2^k + \beta_k\, {}^{\tau}\underline{V}_1^k\right) \\ & -\frac{t}{4}\,\frac{a}{\left|\left|h_k\, {}^{\tau}\underline{V}_n^k\right|\right|}\,\left(\Delta\lambda_o + \Delta\lambda_1\, t\right)\, h_k\, \left[(\alpha_k)^2 + (\beta_k)^2\right]\, {}^{\tau}\underline{V}_n^k \;+\; h.o.t. \end{aligned} \tag{6.7}$$

where, to simplify the previous expression, we made the approximation,

$$\left|\left|h_k\, {}^{\tau+\Delta\tau}\underline{V}_n^k\right|\right| \approx \left|\left|h_k\, {}^{\tau}\underline{V}_n^k\right|\right| \;\; . \tag{6.8}$$

It is important to highlight that the above approximation is only considered in the step linearization; hence it only affects the tangent stiffness matrix and not the calculation of the stresses at $(\tau + \Delta\tau)$.

The terms that include the linear and second order incremental displacements are,

$$\underline{u}_1 = h_k\,\underline{u}_k + \frac{t}{2}\,\frac{a}{\left|\left|h_k\,{}^{\tau}\underline{V}_n^k\right|\right|}\,({}^{\tau}\lambda_o + {}^{\tau}\lambda_1\,t)\,h_k\,(-\alpha_k\,{}^{\tau}\underline{V}_2^k + \beta_k\,{}^{\tau}\underline{V}_1^k) + \frac{t}{2}\,\frac{a}{\left|\left|h_k\,{}^{\tau}\underline{V}_n^k\right|\right|}\,(\Delta\lambda_o + \Delta\lambda_1\,t)\;h_k\,{}^{\tau}\underline{V}_n^k \tag{6.9a}$$

$$\underline{u}_2 = -\frac{t}{4}\,\frac{a}{\left|\left|h_k\,{}^{\tau}\underline{V}_n^k\right|\right|}\,({}^{\tau}\lambda_o + {}^{\tau}\lambda_1\,t)\,h_k\,\left(\alpha_k^2 + \beta_k^2\right)\,{}^{\tau}\underline{V}_n^k \tag{6.9b}$$

$$\underline{u}_3 = \frac{t}{2}\,\frac{a}{\left|\left|h_k\,{}^{\tau}\underline{V}_n^k\right|\right|}\,(\Delta\lambda_o + \Delta\lambda_1\,t)\;h_k\,(-\alpha_k\,{}^{\tau}\underline{V}_2^k + \beta_k\,{}^{\tau}\underline{V}_1^k)\;. \tag{6.9c}$$

6.2.4 Strains interpolation

Depending on the constitutive relation under analysis, we use the Hencky or the Green-Lagrange strain tensor. For both, the transverse shear strains are interpolated using the original MITC4 formulation [30]. The Hencky or logarithmic strain tensor is ${}^{\tau}_{o}\underline{\underline{H}} = \ln {}^{\tau}_{o}\underline{\underline{U}}$ [31] and ${}^{\tau}_{o}\underline{\underline{U}}$ is the right stretch tensor. To interpolate the transverse shear strains they must be expressed in the convective natural coordinate system.

Hencky strain tensor

We can write the Hencky strain tensor as,

$${}^{\tau}_{o}\underline{\underline{H}} = {}^{\tau}_{o}\widetilde{H}_{ij}\;{}^{o}\underline{\widetilde{g}}^{i}\;{}^{o}\underline{\widetilde{g}}^{j} \tag{6.10}$$

where,

${}^{\tau}_{o}\widetilde{H}_{ij}$: covariant components in the element natural (convective) coordinate system,

${}^{o}\underline{\widetilde{g}}^{i}$: contravariant base vectors of the element natural coordinate system in the reference configuration,

${}^{o}\underline{\widetilde{g}}^{i}\;{}^{o}\underline{\widetilde{g}}^{j}$: tensor product of the two contravariant base vectors [31].

We use, following the MITC4 interpolation [30] for the in-layer strain components,

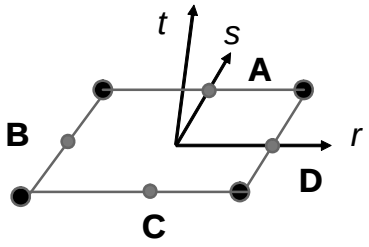

Figure 6.2: Sample points for the MITC4 transverse shear strain interpolations

$$
\begin{aligned}
{}^{\tau}_{o}\widetilde{H}_{rr} &= \left[{}^{\tau}_{o}\widetilde{H}_{rr}\right]^{DI} && \text{(6.11a)}\\
{}^{\tau}_{o}\widetilde{H}_{ss} &= \left[{}^{\tau}_{o}\widetilde{H}_{ss}\right]^{DI} && \text{(6.11b)}\\
{}^{\tau}_{o}\widetilde{H}_{rs} &= \left[{}^{\tau}_{o}\widetilde{H}_{rs}\right]^{DI} \quad . && \text{(6.11c)}
\end{aligned}
$$

In the above equations $\left[{}^{\tau}_{o}\widetilde{H}_{ij}\right]^{DI}$ are the strain components calculated from the displacement interpolation. In the same way, for the through-the-thickness strain component we use,

$$
{}^{\tau}_{o}\widetilde{H}_{tt} = \left[{}^{\tau}_{o}\widetilde{H}_{tt}\right]^{DI} \qquad \text{(6.11d)}
$$

and using the sample points indicated in Fig. 6.2 we interpolate the transverse shear strain components using the standard MITC4 interpolation,

$$
\begin{aligned}
{}^{\tau}_{o}\widetilde{H}_{rt} &= \frac{1}{2}\,(1+s)\,\left[{}^{\tau}_{o}\widetilde{H}_{rt}\right]^{DI}_{A} + \frac{1}{2}\,(1-s)\,\left[{}^{\tau}_{o}\widetilde{H}_{rt}\right]^{DI}_{C} && \text{(6.11e)}\\
{}^{\tau}_{o}\widetilde{H}_{st} &= \frac{1}{2}\,(1+r)\,\left[{}^{\tau}_{o}\widetilde{H}_{st}\right]^{DI}_{D} + \frac{1}{2}\,(1-r)\,\left[{}^{\tau}_{o}\widetilde{H}_{st}\right]^{DI}_{B} \quad . && \text{(6.11f)}
\end{aligned}
$$

$\left[{}^{\tau}_{o}\widetilde{H}_{ij}\right]^{DI}_{SP}$ are the strain components calculated from the displacement interpolation at the *sampling point* " SP ".

Green-Lagrange strain tensor

In the same way, when we use the Green-Lagrange strain tensor,

$$ {}^{\tau}_{o}\underline{\underline{\varepsilon}} = {}^{\tau}_{o}\widetilde{\varepsilon}_{ij}\ {}^{o}\underline{\widetilde{g}}^{i}\ {}^{o}\underline{\widetilde{g}}^{j} \tag{6.12} $$

where ${}^{\tau}_{o}\widetilde{\varepsilon}_{ij}$ are the covariant components in the element natural coordinate system,

$$ {}^{\tau}_{o}\widetilde{\varepsilon}_{rr} = \left[{}^{\tau}_{o}\widetilde{\varepsilon}_{rr}\right]^{DI} \tag{6.13a} $$

$$ {}^{\tau}_{o}\widetilde{\varepsilon}_{ss} = \left[{}^{\tau}_{o}\widetilde{\varepsilon}_{ss}\right]^{DI} \tag{6.13b} $$

$$ {}^{\tau}_{o}\widetilde{\varepsilon}_{rs} = \left[{}^{\tau}_{o}\widetilde{\varepsilon}_{rs}\right]^{DI} \tag{6.13c} $$

$$ {}^{\tau}_{o}\widetilde{\varepsilon}_{tt} = \left[{}^{\tau}_{o}\widetilde{\varepsilon}_{tt}\right]^{DI} \tag{6.13d} $$

and using the MITC4 interpolation we calculate the transverse shear strain components,

$$ {}^{\tau}_{o}\widetilde{\varepsilon}_{rt} = \frac{1}{2}\ (1+s)\ \left[{}^{\tau}_{o}\widetilde{\varepsilon}_{rt}\right]^{DI}_{A} + \frac{1}{2}\ (1-s)\ \left[{}^{\tau}_{o}\widetilde{\varepsilon}_{rt}\right]^{DI}_{C} \tag{6.13e} $$

$$ {}^{\tau}_{o}\widetilde{\varepsilon}_{st} = \frac{1}{2}\ (1+r)\ \left[{}^{\tau}_{o}\widetilde{\varepsilon}_{st}\right]^{DI}_{D} + \frac{1}{2}\ (1-r)\ \left[{}^{\tau}_{o}\widetilde{\varepsilon}_{st}\right]^{DI}_{B}\ . \tag{6.13f} $$

In the above equations $\left[{}^{\tau}_{o}\widetilde{\varepsilon}_{ij}\right]^{DI}_{SP}$ are the strain components calculated from the displacement interpolation at the *sampling point* " SP ".

6.3 Hyperelastic formulation

6.3.1 Constitutive relations

The shell element formulation developed in this thesis is a fully 3D formulation since the in-layer plane stress hypothesis used in the original MITC4 formulation was not invoked.

There are many hyperelastic constitutive models available in the literature [58]. In order to explore the differences in their responses we implemented, for the new MITC4-3D shell element, three hyperelastic isotropic constitutive relations and we analyzed their responses for a number of finite strain cases.

Hooke's law relating 2nd Piola-Kirchhoff stresses and Green-Lagrange strains

In this case the elastic energy per unit volume of the reference ($^{\tau}_{o}\mathcal{U}$) configuration is defined as [31],

$$^{\tau}_{o}\mathcal{U}=\frac{1}{2}\ ^{\tau}_{o}\underline{\underline{\varepsilon}} : \underline{\underline{\underline{\underline{C}}}} :\ ^{\tau}_{o}\underline{\underline{\varepsilon}} \tag{6.14}$$

where $^{\tau}_{o}\underline{\underline{\varepsilon}}$ is the Green-Lagrange strain tensor [31] and $\underline{\underline{\underline{\underline{C}}}}$ is the isotropic Hooke's constitutive fourth order tensor [31].

Using the Doyle-Ericksen formula [31] we get,

$$^{\tau}_{o}\underline{\underline{S}} = \underline{\underline{\underline{\underline{C}}}} :\ ^{\tau}_{o}\underline{\underline{\varepsilon}} \tag{6.15}$$

where $^{\tau}_{o}\underline{\underline{S}}$ is the second Piola-Kirchhoff stress tensor [31].

Hooke's law establishes a linear relation between the deviatoric parts of the stress and strain measures and a linear relation between their hydrostatic parts. It should be noticed that, in this case, since for finite strains the hydrostatic part of the Green-Lagrange strain tensor does not represent the volumetric strain, the physics in Eq. (6.15) is not obvious.

Compressible neo-Hookean model

We use the neo-Hookean model formulated in [71] where the elastic energy is split into a volumetric and a deviatoric part,

$$^{\tau}_{o}\mathcal{U}= {}^{\tau}_{o}\mathcal{U}_v(^{\tau}J) +\ ^{\tau}_{o}\mathcal{U}_D(^{\tau}\overline{\underline{\underline{b}}})\ . \tag{6.16}$$

In the above,

$$^{\tau}J \ = \ \frac{^{o}\rho}{^{\tau}\rho} \tag{6.17}$$

$$^{\tau}\overline{\underline{\underline{b}}} \ = \ (^{\tau}J)^{-\frac{2}{3}}\ ^{\tau}\underline{\underline{b}} \tag{6.18}$$

The second order tensor $^{\tau}_{o}\underline{\underline{X}}$ is the deformation gradient tensor;

${}^{\tau}\underline{\underline{b}} = {}^{\tau}_{o}\underline{\underline{X}} \cdot {}^{\tau}_{o}\underline{\underline{X}}^{T}$ is the Finger strain tensor and $({}^{o}\rho,\ {}^{\tau}\rho)$ are the densities in the reference and spatial configurations respectively. In Cartesian coordinates ${}^{\tau}J = \det\left[{}^{\tau}_{o}\underline{\underline{X}}\right]$ [31].

For the terms in Eq. (6.16) Simo and Hughes use [71],

$$ {}^{\tau}_{o}\mathcal{U}_{v}({}^{\tau}J) = \frac{1}{2}\,\kappa\,\left[\frac{1}{2}\,\left({}^{\tau}J^{2}-1\right) - \ln\left({}^{\tau}J\right)\right] \tag{6.19} $$

$$ {}^{\tau}_{o}\mathcal{U}_{D}({}^{t}\overline{\underline{b}}) = \frac{1}{2}\,G\,\left[tr({}^{\tau}\overline{\underline{b}}) - 3\right] = \frac{1}{2}\,G\,\left[tr(\,{}^{\tau}_{o}\overline{\underline{\underline{C}}}\,) - 3\right] \tag{6.20} $$

where,

$$ {}^{\tau}_{o}\overline{\underline{\underline{C}}} = {}^{\tau}J^{-\frac{2}{3}}\,{}^{\tau}_{o}\underline{\underline{X}}^{T} \cdot {}^{\tau}_{o}\underline{\underline{X}} $$

and,

$$ \kappa = \frac{E}{3\,(1-2\nu)}\ \text{(compressibility modulus)} \tag{6.21a} $$

$$ G = \frac{E}{2\,(1+\nu)}\ \text{(shear modulus)} \tag{6.21b} $$

being E the Young´s modulus and ν the Poisson´s coefficient.

Hence, using the Doyle-Ericksen formula and doing a push-forward [31] we get,

$$ {}^{\tau}\underline{\underline{\tau}} = {}^{\tau}J\,\frac{d\,\mathcal{U}_{v}}{d\,J}|_{0}^{\tau}\,{}^{\tau}\underline{\underline{g}} + 2\,dev\left[{}^{\tau}_{o}\underline{\underline{X}} \cdot \frac{\partial\,\mathcal{U}_{D}}{\partial\,\overline{\underline{\underline{C}}}}|_{0}^{\tau} \cdot {}^{\tau}_{o}\underline{\underline{X}}^{T}\right] \tag{6.22} $$

where ${}^{\tau}\underline{\underline{\tau}}$ is the Kirchhoff stress tensor [31].

In this case the relation between the hydrostatic component of ${}^{\tau}\underline{\underline{\tau}}$ and the volumetric stretch ${}^{\tau}J$ is explicit.

Hooke's law relating the Hencky strain tensor and its energy conjugate stress tensor

In this case the elastic energy per unit volume of the reference configuration is defined as,

$$ {}^{\tau}_{o}\mathcal{U} = \frac{1}{2}\,{}^{\tau}_{o}\underline{\underline{H}} : \underline{\underline{\underline{\underline{C}}}} :{}^{\tau}_{o}\,\underline{\underline{H}} \tag{6.23} $$

where $\underset{\equiv\equiv}{C}$ is the isotropic Hooke's constitutive fourth order tensor.

For an **isotropic** elastic material the stress measure energy-conjugate to the Hencky strain tensor is ${}^{\tau}_{o}\underline{\underline{\Gamma}}$ with,

$$ {}^{\tau}_{o}\Gamma^{IJ} = \left[{}^{\tau}_{o}R^{*}\left(\tau^{ij}\right)\right]^{IJ} \tag{6.24} $$

in the above equation $\left[{}^{\tau}_{o}R^{*}\left(\tau^{ij}\right)\right]^{IJ}$ are the rotational pull-back of the contravariant components of the Kirchhoff stress tensor [31].

Using the Doyle-Ericksen formula we get,

$$ {}^{\tau}_{o}\underline{\underline{\Gamma}} = \underset{\equiv\equiv}{C} : {}^{\tau}_{o}\underline{\underline{H}} \, . \tag{6.25} $$

It is important to notice that the hydrostatic part of the Hencky strain tensor is the logarithmic volumetric strain; hence, in this case the linear relation between the hydrostatic component of ${}^{\tau}_{o}\underline{\underline{\Gamma}}$ and the logarithmic volumetric strain has an obvious physical meaning.

For this constitutive relation we use the interpolations shown in Eqs. (6.11a) - (6.11f).

The behavior of the considered hyperelastic models

In order to explore the response that we can expect from the considered hyperelastic models, in Fig. 6.3 we analyze a simple plane-stress tension test.

It is obvious that except for very small axial displacements (infinitesimal strain situation) the three material models provide different responses, being the response of the first material model the most different while the responses of the other two models are close.

When dealing with a specific material only a laboratory test can indicate which hyperelastic law is the one that best approximates its behavior.

For metals undergoing finite elasto-plastic deformations, laboratory tests performed by Anand [2] indicate that using the standard values of the Young modulus and Poisson

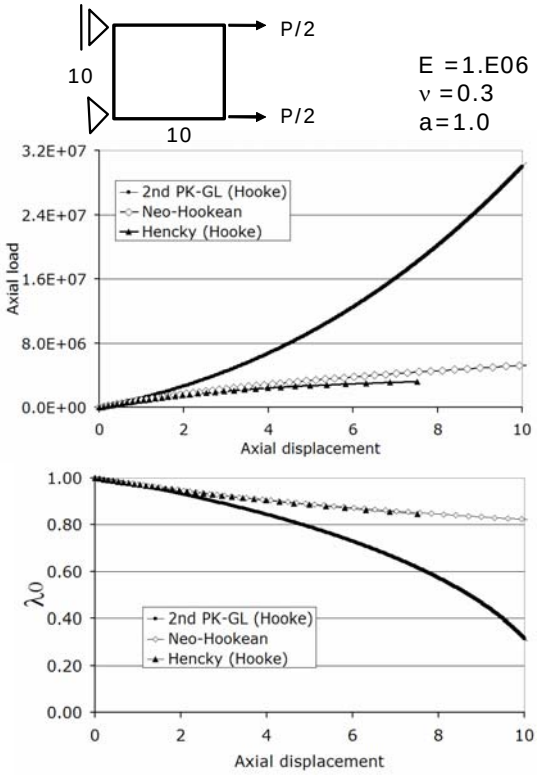

Figure 6.3: Plane stress axial test

coefficient (the ones determined in small strain lab tests), the Hooke's law relating the Hencky strain tensor and its energy conjugate stress tensor provides the results that best approximate the actual material behavior for moderate elastic strains.

6.3.2 The incremental formulation

Using a total Lagrangian formulation we can write the Principle of Virtual Work for the equilibrium configuration at $\tau + \Delta\tau$ [9],

$$\int_{{}^oV} {}^{\tau+\Delta\tau}_{o}S^{IJ}\ \delta\ {}^{\tau+\Delta\tau}_{o}\varepsilon_{IJ}\ {}^{o}dV = {}^{\tau+\Delta\tau}\mathcal{R} \tag{6.26}$$

where ${}^{\tau+\Delta\tau}\mathcal{R}$ is the virtual work of the external loads acting on the solid body in the $\tau + \Delta\tau-$configuration.

Now we can write [9],

$$\begin{aligned} {}^{\tau+\Delta\tau}_{o}S^{IJ} &= {}^{\tau}_{o}S^{IJ} + {}_{o}S^{IJ} && \text{(6.27a)}\\ {}^{\tau+\Delta\tau}_{o}\varepsilon_{IJ} &= {}^{\tau}_{o}\varepsilon_{IJ} + {}_{o}\varepsilon_{IJ} && \text{(6.27b)}\\ {}_{o}\varepsilon_{IJ} &= {}_{o}e_{IJ} + {}_{o}\eta_{IJ}\ . && \text{(6.27c)} \end{aligned}$$

In the above equations ${}_{o}S^{IJ}$ and ${}_{o}\varepsilon_{IJ}$ are incremental quantities; ${}_{o}e_{IJ}$ is the increment in the Green-Lagrange strain tensor, linear in the incremental displacement and ${}_{o}\eta_{IJ}$ is the nonlinear increment.

Using an incremental constitutive equation,

$${}_{o}S^{IJ} = {}_{o}C^{IJKL}\ {}_{o}\varepsilon_{KL} \tag{6.28}$$

we get the linearized incremental equation,

$$\int_{{}^oV} {}_{o}C^{IJKL}\ {}_{o}e_{KL}\ \delta_{o}e_{IJ}\ {}^{o}dV + \int_{{}^oV} {}^{\tau}_{o}S^{IJ}\ \delta\ {}_{o}\eta_{IJ}\ {}^{o}dV = {}^{\tau+\Delta\tau}\mathcal{R} - \int_{{}^oV} {}^{\tau}_{o}S^{IJ}\ \delta\ {}_{o}e_{IJ}\ {}^{o}dV\ . \tag{6.29}$$

In what follows we develop Eq. (6.29) for the three hyperelastic material models considered above.

First case: linear relation between 2^{nd} Piola-Kirchhoff stresses and Green-Lagrange strains

We transform the components of the fourth order Hooke's constitutive tensor from a Cartesian system, with base vectors ${}^{o}\underline{e}_{\alpha}$, to the natural coordinate system, with covariant base vectors ${}^{o}\widetilde{\underline{g}}_{i}$, using,

$$C^{\alpha\beta\gamma\delta}\ {}^{o}\underline{e}_{\alpha}\ {}^{o}\underline{e}_{\beta}\ {}^{o}\underline{e}_{\gamma}\ {}^{o}\underline{e}_{\delta} = \widetilde{C}^{ijkl}\ {}^{o}\widetilde{\underline{g}}_{i}\ {}^{o}\widetilde{\underline{g}}_{j}\ {}^{o}\widetilde{\underline{g}}_{k}\ {}^{o}\widetilde{\underline{g}}_{l}\ . \tag{6.30}$$

Hence,

$${}_{o}\widetilde{S}^{ij} = \widetilde{C}^{ijkl}\ {}_{o}\widetilde{\varepsilon}_{kl} = \widetilde{C}^{ijkl}\ ({}_{o}\widetilde{e}_{kl} + {}_{o}\widetilde{\eta}_{kl}) \tag{6.31}$$

and the linearized incremental equation is,

$$\int_{{}^{o}V} \widetilde{C}^{ijkl}\ {}_{o}\widetilde{e}_{kl}\ \delta_{o}\widetilde{e}_{ij}\ {}^{o}dV + \int_{{}^{o}V} {}^{\tau}_{o}\widetilde{S}^{ij}\ \delta_{o}\widetilde{\eta}_{ij}\ {}^{o}dV = {}^{\tau+\Delta\tau}\mathcal{R} - \int_{{}^{o}V} {}^{\tau}_{o}\widetilde{S}^{ij}\ \delta_{o}\widetilde{e}_{ij}\ {}^{o}dV\ . \tag{6.32}$$

In order to develop the stiffness matrices, we analize the different terms of this expression.

$${}^{\tau}_{o}\widetilde{\varepsilon}_{ij} = \frac{1}{2}\left({}^{\tau}\widetilde{\underline{g}}_{i}\ \cdot\ {}^{\tau}\widetilde{\underline{g}}_{j} - {}^{0}\widetilde{\underline{g}}_{i}\ \cdot\ {}^{0}\widetilde{\underline{g}}_{j}\right) \tag{6.33a}$$

$${}^{\tau+\Delta\tau}_{o}\widetilde{\varepsilon}_{ij} = \frac{1}{2}\left({}^{\tau+\Delta\tau}\widetilde{\underline{g}}_{i}\ \cdot\ {}^{\tau+\Delta\tau}\widetilde{\underline{g}}_{j} - {}^{0}\widetilde{\underline{g}}_{i}\ \cdot\ {}^{0}\widetilde{\underline{g}}_{j}\right) \tag{6.33b}$$

where,

$${}^{\tau+\Delta\tau}\widetilde{\underline{g}}_{i} = \frac{\partial^{\tau+\Delta\tau}\underline{x}}{\partial r_{i}} = \frac{\partial}{\partial r_{i}}\left({}^{0}\underline{x} + {}^{\tau}\underline{u} + \underline{u}\right) = {}^{\tau}\widetilde{\underline{g}}_{i} + \frac{\partial\underline{u}}{\partial r_{i}}\ . \tag{6.34}$$

Replacing (6.34) in (6.33b),

$$ {}^{\tau+\Delta\tau}_{o}\widetilde{\varepsilon}_{ij} = \frac{1}{2}\left({}^{\tau}\underline{\widetilde{g}}_i + \frac{\partial \underline{u}}{\partial r_i}\right) \cdot \left({}^{\tau}\underline{\widetilde{g}}_j + \frac{\partial \underline{u}}{\partial r_j}\right) - {}^{0}\underline{\widetilde{g}}_i \cdot {}^{0}\underline{\widetilde{g}}_j \,. \tag{6.35} $$

From Eq.(6.27b),

$$ {}_{o}\widetilde{\varepsilon}_{ij} = {}^{\tau+\Delta\tau}_{o}\widetilde{\varepsilon}_{ij} - {}^{\tau}_{o}\widetilde{\varepsilon}_{ij} $$

then we get the total increment,

$$ {}_{0}\widetilde{\varepsilon}_{ij} = \frac{1}{2}\left({}^{\tau}\underline{\widetilde{g}}_i \cdot \frac{\partial \underline{u}}{\partial r_j} + {}^{\tau}\underline{\widetilde{g}}_j \cdot \frac{\partial \underline{u}}{\partial r_i} + \frac{\partial \underline{u}}{\partial r_i} \cdot \frac{\partial \underline{u}}{\partial r_j}\right) \,. \tag{6.37} $$

Refering to Eqs.(6.9a)-(6.9c), we can calculate the linear increment ${}_{0}\widetilde{e}_{ij}$ and the non-linear increments ${}_{0}\widetilde{\eta}_{ij}$,

$$ {}_{0}\widetilde{e}_{ij} = \frac{1}{2}\left({}^{\tau}\underline{\widetilde{g}}_i \cdot \frac{\partial \underline{u}_1}{\partial r_j} + {}^{\tau}\underline{\widetilde{g}}_j \cdot \frac{\partial \underline{u}_1}{\partial r_i}\right) \tag{6.38} $$

$$ {}_{0}\widetilde{\eta}_{1,ij} = \frac{1}{2}\frac{\partial \underline{u}_1}{\partial r_j} \cdot \frac{\partial \underline{u}_1}{\partial r_i} \tag{6.39a} $$

$$ {}_{0}\widetilde{\eta}_{2,ij} = \frac{1}{2}\left({}^{\tau}\underline{\widetilde{g}}_i \cdot \frac{\partial \underline{u}_2}{\partial r_j} + {}^{\tau}\underline{\widetilde{g}}_j \cdot \frac{\partial \underline{u}_2}{\partial r_i}\right) \tag{6.39b} $$

$$ {}_{0}\widetilde{\eta}_{3,ij} = \frac{1}{2}\left({}^{\tau}\underline{\widetilde{g}}_i \cdot \frac{\partial \underline{u}_3}{\partial r_j} + {}^{\tau}\underline{\widetilde{g}}_j \cdot \frac{\partial \underline{u}_3}{\partial r_i}\right) \,. \tag{6.39c} $$

Therefore, the total non-linear increment and its variation are,

$$ \begin{aligned} {}_{0}\widetilde{\eta}_{ij} &= {}_{0}\widetilde{\eta}_{1,ij} + {}_{0}\widetilde{\eta}_{2,ij} + {}_{0}\widetilde{\eta}_{3,ij} \\ \delta_0\widetilde{\eta}_{ij} &= \delta_0\widetilde{\eta}_{1,ij} + \delta_0\widetilde{\eta}_{2,ij} + \delta_0\widetilde{\eta}_{3,ij} \,. \end{aligned} $$

The equilibrium equation for the linearized incremental step, from time τ to $\tau+\Delta\tau$, and considering Total Lagrangian Formulation, is formulated as,

$$ ({}^{\tau}_{0}\underline{K}_{NL} + {}^{\tau}_{0}\underline{K}_{L})\,\underline{U} = {}^{\tau+\Delta\tau}\underline{\mathcal{R}} - {}^{\tau}\underline{F} \,. $$

We calculate each matrix and the nodal equivalent force vector in the following apparts.

Linear matrix ${}^{\tau}_{0}\underline{K}_L$ and the vector of nodal equivalent forces ${}^{\tau}\underline{F}$ Defining ${}^{\tau}_{0}\underline{B}$ as the strain-displacement matrix, the linear increment results,

$$ {}_0\widetilde{e}_{vw} = {}^{\tau}_{0}\widetilde{B}_{(vw)y}\, U^y \tag{6.41} $$

where the matricial form is,

$$ {}_0\underline{\widetilde{e}} = {}^{\tau}_{0}\underline{\widetilde{B}}\, \underline{U} \tag{6.42} $$

with ${}^{\tau}_{0}\underline{\widetilde{B}}$ a (6x22) matrix.

Being ${}_0\widetilde{\gamma}_{IJ} = 2\ {}_0\widetilde{e}_{ij}$, the linear increment array is,

$$ {}_0\underline{\widetilde{e}}^T = [{}_0\widetilde{e};\ {}_0\widetilde{e}_{ss};\ {}_0\widetilde{e}_{tt};\ {}_0\widetilde{\gamma}_{rs};\ {}_0\widetilde{\gamma}_{rt};\ {}_0\widetilde{\gamma}_{st}]\ . $$

The total amount of the elemental unknowns is 22.

$$ \underline{U}^T = \left[u_1;\ v_1;\ w_1;\ \alpha_1;\ \beta_{1;}\ u_2;\ v_2;\ w_2;\ \alpha_2;\ \beta_{2;}\ u_3;\ v_3;\ w_3;\ \alpha_3;\ \beta_{3;}\ u_4;\ v_4;\ w_4;\ \alpha_4;\ \beta_{4;}\ \Delta\lambda_o;\ \Delta\lambda_1\right] $$

We define 3 matrices: $\underline{H}_0$, $\underline{V}_{12}$, $\underline{MV}_n$ and $\underline{MV}_{n\_t}$, whose expressions are developed in Appendix B.

Therefore, considering Eq. (6.9a) and the matrices mentioned above, we get the following expression to calculate $\underline{u}_1$,

$$ \underline{u}_1 = \underline{H}_0 \left[\underline{I} + \frac{t}{2}\, \frac{a}{\left|\left|h_k\ {}^{\tau}\underline{V}^k_n\right|\right|}\ \left[({}^{\tau}\lambda_o + {}^{\tau}\lambda_1\ t)\ \underline{V}_{12} + \underline{MV}n\right]\right] \underline{U} \tag{6.43} $$

where $\underline{I}$ is the unit matrix of (22x22).

In order to simplify the algebra, we call,

$$ f = \frac{1}{\left|\left|h_k\ {}^{\tau}\underline{V}^k_n\right|\right|} = \frac{1}{\sqrt{{}^{\tau}\underline{V}_n\ \cdot\ {}^{\tau}\underline{V}_n}} \tag{6.44} $$

and calculate its derivatives,

$$\begin{aligned}
\frac{\partial f}{\partial r} &= -\frac{1}{2}\ ({}^{\tau}\underline{V}_n\ \cdot\ {}^{\tau}\underline{V}_n)^{-\frac{3}{2}}\ \left[{}^{\tau}\underline{V}_{n,r}\ \cdot\ {}^{\tau}\underline{V}_n\right]\ 2 \\
\frac{\partial f}{\partial r} &= -\left({}^{\tau}\underline{V}_n\ \cdot\ {}^{\tau}\underline{V}_n\right)^{-\frac{3}{2}}\ \left[\left(h_{k,r}\ {}^{\tau}\underline{V}_n^k\right)\ \cdot\ {}^{\tau}\underline{V}_n\right] \\
\frac{\partial f}{\partial r} &= -\frac{1}{\left|\left|h_k\ {}^{\tau}\underline{V}_n^k\right|\right|^3}\ \left(h_{k,r}\ {}^{\tau}\underline{V}_n^k\right)\ \cdot\ {}^{\tau}\underline{V}_n
\end{aligned} \tag{6.45}$$

$$\frac{\partial f}{\partial s} = -\frac{1}{\left|\left|h_k\ {}^{\tau}\underline{V}_n^k\right|\right|^3}\ \left(h_{k,s}\ {}^{\tau}\underline{V}_n^k\right)\ \cdot\ {}^{\tau}\underline{V}_n\ . \tag{6.46}$$

We rewrite Eq. (6.43),

$$\underline{u}_1 = \underline{H}_0\ \left[\underline{I} + \frac{t}{2}\ a\ f\ \left[({}^{\tau}\lambda_o + {}^{\tau}\lambda_1\ t)\ \underline{V}_{12} + \underline{MV}_n\right]\right]\ \underline{U} \tag{6.47}$$

$$\begin{aligned}
\frac{\partial \underline{u}_1}{\partial r} &= \left\{\begin{array}{c} \underline{H}_{0,r}\ \left[\underline{I} + \frac{t}{2}\ a\ f\ \left[({}^{\tau}\lambda_o + {}^{\tau}\lambda_1\ t)\ \underline{V}_{12} + \underline{MV}_n\right]\right] + \\ \underline{H}_0\ \left[\frac{t}{2}\ a\ \frac{\partial f}{\partial r}\ \left[({}^{\tau}\lambda_o + {}^{\tau}\lambda_1\ t)\ \underline{V}_{12} + \underline{MV}_n\right]\right] \end{array}\right\}\ \underline{U} \\
\frac{\partial \underline{u}_1}{\partial r} &= \widetilde{\underline{M}}_r\ \underline{U}
\end{aligned} \tag{6.48a}$$

$$\begin{aligned}
\frac{\partial \underline{u}_1}{\partial s} &= \left\{\begin{array}{c} \underline{H}_{0,s}\ \left[\underline{I} + \frac{t}{2}\ a\ f\ \left[({}^{\tau}\lambda_o + {}^{\tau}\lambda_1\ t)\ \underline{V}_{12} + \underline{MV}_n\right]\right] + \\ \underline{H}_0\ \left[\frac{t}{2}\ a\ \frac{\partial f}{\partial s}\ \left[({}^{\tau}\lambda_o + {}^{\tau}\lambda_1\ t)\ \underline{V}_{12} + \underline{MV}_n\right]\right] \end{array}\right\}\ \underline{U} \\
\frac{\partial \underline{u}_1}{\partial s} &= \widetilde{\underline{M}}_s\ \underline{U}
\end{aligned} \tag{6.48b}$$

$$\begin{aligned}
\frac{\partial \underline{u}_1}{\partial t} &= \underline{H}_0\ \frac{1}{2}\ a\ f\ \left[({}^{\tau}\lambda_o + 2\ {}^{\tau}\lambda_1\ t)\ \underline{V}_{12} + \underline{MV}_{n_t}\right]\ \underline{U} \\
\frac{\partial \underline{u}_1}{\partial t} &= \widetilde{\underline{M}}_t\ \underline{U}\ .
\end{aligned} \tag{6.48c}$$

From Eq. (6.42) and (6.48a) to (6.48c),

$$
\begin{aligned}
{}_0\widetilde{e}_{rr} &= {}^{\tau}\widetilde{\underline{g}}_r\ \widetilde{\underline{M}}_r\ \underline{U} = {}^{\tau}_0\widetilde{\underline{B}}_{rr}\ \underline{U} && (6.49a)\\
{}_0\widetilde{e}_{ss} &= {}^{\tau}\widetilde{\underline{g}}_s\ \widetilde{\underline{M}}_s\ \underline{U} = {}^{\tau}_0\widetilde{\underline{B}}_{ss}\ \underline{U} && (6.49b)\\
{}_0\widetilde{e}_{tt} &= {}^{\tau}\widetilde{\underline{g}}_t\ \widetilde{\underline{M}}_t\ \underline{U} = {}^{\tau}_0\widetilde{\underline{B}}_{tt}\ \underline{U} && (6.49c)\\
{}_0\widetilde{\gamma}_{rs} &= 2\ {}_0\widetilde{e}_{rs} = \left({}^{\tau}\widetilde{\underline{g}}_s\ \widetilde{\underline{M}}_r + {}^{\tau}\widetilde{\underline{g}}_r\ \widetilde{\underline{M}}_s\right)\ \underline{U} = {}^{\tau}_0\widetilde{\underline{B}}_{rs}\ \underline{U} && (6.49d)\\
{}_0\widetilde{\gamma}_{rt} &= 2\ {}_0\widetilde{e}_{rt} = \left({}^{\tau}\widetilde{\underline{g}}_t\ \widetilde{\underline{M}}_r + {}^{\tau}\widetilde{\underline{g}}_r\ \widetilde{\underline{M}}_t\right)\ \underline{U} = {}^{\tau}_0\widetilde{\underline{B}}_{rt}\ \underline{U} && (6.49e)\\
{}_0\widetilde{\gamma}_{st} &= 2\ {}_0\widetilde{e}_{st} = \left({}^{\tau}\widetilde{\underline{g}}_s\ \widetilde{\underline{M}}_t + {}^{\tau}\widetilde{\underline{g}}_t\ \widetilde{\underline{M}}_s\right)\ \underline{U} = {}^{\tau}_0\widetilde{\underline{B}}_{st}\ \underline{U}\,. && (6.49f)
\end{aligned}
$$

The dimension of the matrices ${}^{\tau}_0\widetilde{\underline{B}}_{ij}$ is (1x22).

In each Gauss point, the shear strain components ${}_0\widetilde{\varepsilon}rt$ and ${}_0\widetilde{\varepsilon}_{st}$ are interpolated according to,

$$
\begin{aligned}
{}^{\tau}_o\widetilde{\varepsilon}_{rt} &= \frac{1}{2}(1+s)\ \left[{}^{\tau}_o\widetilde{\varepsilon}_{rt}\right]^{DI}_A + \frac{1}{2}(1-s)\ \left[{}^{\tau}_o\widetilde{\varepsilon}_{rt}\right]^{DI}_C && (6.50a)\\
{}^{\tau}_o\widetilde{\varepsilon}_{st} &= \frac{1}{2}(1+r)\ \left[{}^{\tau}_o\widetilde{\varepsilon}_{st}\right]^{DI}_C + \frac{1}{2}(1-r)\ \left[{}^{\tau}_o\widetilde{\varepsilon}_{st}\right]^{DI}_B\,. && (6.50b)
\end{aligned}
$$

Therefore,

$$
\begin{aligned}
{}^{\tau}_0\widetilde{\underline{B}}_{rt} &= \frac{1}{2}(1+s)\ \left[{}^{\tau}_0\widetilde{\underline{B}}_{rt}\right]^{DI}_A + \frac{1}{2}(1-s)\ \left[{}^{\tau}_0\widetilde{\underline{B}}_{rt}\right]^{DI}_C && (6.51a)\\
{}^{\tau}_0\widetilde{\underline{B}}_{st} &= \frac{1}{2}(1+r)\ \left[{}^{\tau}_0\widetilde{\underline{B}}_{st}\right]^{DI}_D + \frac{1}{2}(1-r)\ \left[{}^{\tau}_0\widetilde{\underline{B}}_{st}\right]^{DI}_B\,. && (6.51b)
\end{aligned}
$$

From Eq. (6.49a) to (6.49d), (6.51a) and (6.51b) we get the linear (6x22) matrix ${}^{\tau}_0\widetilde{\underline{B}}$.

$$
{}^{\tau}_0\widetilde{\underline{B}} = \begin{bmatrix}
{}^{\tau}_0\widetilde{\underline{B}}_{rr}\\
{}^{\tau}_0\widetilde{\underline{B}}_{ss}\\
{}^{\tau}_0\widetilde{\underline{B}}_{tt}\\
{}^{\tau}_0\widetilde{\underline{B}}_{rs}\\
{}^{\tau}_0\widetilde{\underline{B}}_{rt}\\
{}^{\tau}_0\widetilde{\underline{B}}_{st}
\end{bmatrix} \qquad (6.52)
$$

Finally, we get the following expressions for the linear stiffness matrix ${}^{\tau}_{0}\underline{K}_L$ and the force vector ${}^{\tau}\underline{F}$,

$$ {}^{\tau}_{0}\underline{K}_L = \int_{{}^{o}V} {}^{\tau}_{0}\widetilde{\underline{B}}^T \ \widetilde{\underline{C}} \ {}^{\tau}_{0}\widetilde{\underline{B}} \ {}^{0}dV \tag{6.53} $$

$$ {}^{\tau}\underline{F} = \int_{{}^{o}V} {}^{\tau}_{0}\widetilde{\underline{B}} \ {}^{\tau}_{0}\widetilde{\underline{S}} \ {}^{0}dV \ . \tag{6.54} $$

Non-linear matrix ${}^{\tau}_{0}\underline{K}_{NL,1}$ The non-linear increments ${}_{0}\widetilde{\eta}_{rs}$ are calculated taking into account the matrices obtained in.(6.49a) to (6.49f),

$$ \begin{aligned} {}_{0}\widetilde{\eta}_{1,ij} &= \frac{1}{2} \ \frac{\partial \underline{u}_1}{\partial r_j} \ \cdot \ \frac{\partial \underline{u}_1}{\partial r_i} \\ {}_{0}\widetilde{\eta}_{1,ij} &= \frac{1}{2} \ \underline{U}^T \ \widetilde{\underline{M}}_i^T \ \widetilde{\underline{M}}_j \ \underline{U} = \frac{1}{2} \ \underline{U}^T \ \widetilde{\underline{A}}_{ij} \ \underline{U} \\ \delta_0\widetilde{\eta}_{1,ij} &= \frac{1}{2} \ \left(\underline{\delta U}^T \ \widetilde{\underline{A}}_{ij} \ \underline{U} + \underline{U}^T \ \widetilde{\underline{A}}_{ij} \ \underline{\delta U} \right) \\ \delta_0\widetilde{\eta}_{1,ij} &= \frac{1}{2} \ \underline{\delta U}^T \ \left(\widetilde{\underline{A}}_{ij} + \widetilde{\underline{A}}_{ij}^T \right) \ \underline{U} \\ \delta_0\widetilde{\eta}_{1,ij} &= \frac{1}{2} \ \underline{\delta U}^T \ \widetilde{\underline{M}}_{ij} \ \underline{U} = \underline{\delta U}^T \ \frac{1}{2} \ \widetilde{\underline{M}}_{ij} \ \underline{U} \end{aligned} $$

where $\widetilde{\underline{M}}_{ij} = \widetilde{\underline{A}}_{ij} + \widetilde{\underline{A}}_{ij}^T$. Please note that, in a general case, $\widetilde{\underline{A}}_{ij} \neq \widetilde{\underline{A}}_{ji}$.

We call,

$$ {}^{\tau}_{0}\widetilde{\underline{B}}_{ij}^{NL,1} = \frac{1}{2} \ \widetilde{\underline{M}}_{ij} \tag{6.55} $$

Taking into account that, in each Gauss Point, $\widetilde{\eta}_{1,rt}$ and $\widetilde{\eta}_{1,st}$ must be interpolated, we have,

$$ {}^{\tau}_{0}\widetilde{\underline{B}}_{rt}^{NL,1} = \frac{1}{2} \ \left[{}^{\tau}_{0}\widetilde{\underline{B}}_{rt,A}^{NL,1} \ (1+s) \ + \ {}^{\tau}_{0}\widetilde{\underline{B}}_{rt,C}^{NL,1} \ (1-s) \right] \tag{6.56a} $$

$$ {}^{\tau}_{0}\widetilde{\underline{B}}_{tr}^{NL,1} = \frac{1}{2} \ \left[{}^{\tau}_{0}\widetilde{\underline{B}}_{tr,A}^{NL,1} \ (1+s) \ + \ {}^{\tau}_{0}\widetilde{\underline{B}}_{tr,C}^{NL,1} \ (1-s) \right] \tag{6.56b} $$

$$ {}^{\tau}_{0}\widetilde{\underline{B}}_{st}^{NL,1} = \frac{1}{2} \ \left[{}^{\tau}_{0}\widetilde{\underline{B}}_{st,D}^{NL,1} \ (1+r) \ + \ {}^{\tau}_{0}\widetilde{\underline{B}}_{st,B}^{NL,1} \ (1-r) \right] \tag{6.56c} $$

$$ {}^{\tau}_{0}\widetilde{\underline{B}}_{ts}^{NL,1} = \frac{1}{2} \ \left[{}^{\tau}_{0}\widetilde{\underline{B}}_{ts,D}^{NL,1} \ (1+r) \ + \ {}^{\tau}_{0}\widetilde{\underline{B}}_{ts,B}^{NL,1} \ (1-r) \right] \tag{6.56d} $$

Finally, we get the non-linear matrix ${}^{\tau}_{0}\underline{K}_{NL,1}$,

$$
\begin{aligned}
{}^{\tau}_{0}\underline{K}_{NL,1} \;=\; \int_{{}^{o}V} \; & [\,{}^{\tau}_{o}\widetilde{S}^{rr}\;{}^{\tau}_{0}\widetilde{\underline{B}}^{NL,1}_{rr} \;+\; {}^{\tau}_{o}\widetilde{S}^{ss}\;{}^{\tau}_{0}\widetilde{\underline{B}}^{NL,1}_{ss} \;+\; {}^{\tau}_{o}\widetilde{S}^{33}\;{}^{\tau}_{0}\widetilde{\underline{B}}^{NL,1}_{tt} \;+\; {}^{\tau}_{o}\widetilde{S}^{rs}\;({}^{\tau}_{0}\widetilde{\underline{B}}^{NL,1}_{rs} \;+\; {}^{\tau}_{0}\widetilde{\underline{B}}^{NL,1}_{sr}) \;+ \\
& {}^{\tau}_{o}\widetilde{S}^{rt}\;({}^{\tau}_{0}\widetilde{\underline{B}}^{NL,1}_{rt} \;+\; {}^{\tau}_{0}\widetilde{\underline{B}}^{NL,1}_{tr}) \;+\; {}^{\tau}_{o}\widetilde{S}^{st}\;({}^{\tau}_{0}\widetilde{\underline{B}}^{NL,1}_{st} \;+\; {}^{\tau}_{0}\widetilde{\underline{B}}^{NL,1}_{ts})]\;{}^{0}dV. \qquad (6.57)
\end{aligned}
$$

Non-linear matrix ${}^{\tau}_{0}\underline{K}_{NL,2}$ From Eq. 6.9b and 6.44,

$$
\underline{u}_2 = -\frac{t}{4}\; a\; f\; ({}^{\tau}\lambda_o + {}^{\tau}\lambda_1\; t)\; h_k\; \left(\alpha_k^2 + \beta_k^2\right)\; {}^{\tau}\underline{V}^k_n\;.
$$

We can write,

$$
\alpha_k^2 + \beta_k^2 = \left[\begin{array}{cc} \alpha_k & \beta_k \end{array}\right] \;\cdot\; \left[\begin{array}{c} \alpha_k \\ \beta_k \end{array}\right]\;.
$$

Hence, the displacement derivatives are,

$$
\begin{aligned}
\frac{\partial \underline{u}_2}{\partial r} &= \left[\begin{array}{cc} \alpha_k & \beta_k \end{array}\right] \left(-\frac{t}{4}\right)\; a\; ({}^{\tau}\lambda_o + {}^{\tau}\lambda_1\; t)\; \left(h_{k,r}\; f + \frac{\partial f}{\partial r}\; h_k\right)\; {}^{\tau}\underline{V}^k_n \left[\begin{array}{c} \alpha_k \\ \beta_k \end{array}\right] \\
\frac{\partial \underline{u}_2}{\partial s} &= \left[\begin{array}{cc} \alpha_k & \beta_k \end{array}\right] \left(-\frac{t}{4}\right)\; a\; ({}^{\tau}\lambda_o + {}^{\tau}\lambda_1\; t)\; \left(h_{k,s}\; f + \frac{\partial f}{\partial s}\; h_k\right)\; {}^{\tau}\underline{V}^k_n \left[\begin{array}{c} \alpha_k \\ \beta_k \end{array}\right] \\
\frac{\partial \underline{u}_2}{\partial t} &= \left[\begin{array}{cc} \alpha_k & \beta_k \end{array}\right] \left(-\frac{1}{4}\right)\; a\; f\; ({}^{\tau}\lambda_o + 2\;{}^{\tau}\lambda_1\; t)\; h_k\; {}^{\tau}\underline{V}^k_n \left[\begin{array}{c} \alpha_k \\ \beta_k \end{array}\right]\;.
\end{aligned}
$$

We build (22x22) matrices ${}^{\tau}_{0}\widetilde{\underline{B}}^{2}_{ij}$ with rows and columns according to the previous formulas, and taking into account Eq.(6.39b). Please note that these matrices have non zero numbers only in correspondance with the degrees of freedom α_k and β_k,

$$
\begin{aligned}
{}_0\widetilde{\eta}_{2,rr} &= \underline{U}^T\ {}^{\tau}_{0}\widetilde{\underline{B}}^2_{rr}\ \underline{U} \\
{}_0\widetilde{\eta}_{2,ss} &= \underline{U}^T\ {}^{\tau}_{0}\widetilde{\underline{B}}^2_{ss}\ \underline{U} \\
{}_0\widetilde{\eta}_{2,tt} &= \underline{U}^T\ {}^{\tau}_{0}\widetilde{\underline{B}}^2_{tt}\ \underline{U} \\
{}_0\widetilde{\eta}_{2,rs} &= \underline{U}^T\ {}^{\tau}_{0}\widetilde{\underline{B}}^2_{rs}\ \underline{U} \\
{}_0\widetilde{\eta}_{2,rt} &= \underline{U}^T\ {}^{\tau}_{0}\widetilde{\underline{B}}^2_{rt}\ \underline{U} \\
{}_0\widetilde{\eta}_{2,st} &= \underline{U}^T\ {}^{\tau}_{0}\widetilde{\underline{B}}^2_{st}\ \underline{U}\ .
\end{aligned}
$$

We calculate the variations,

$$
\begin{aligned}
\delta_0\widetilde{\eta}_{2,ij} &= \underline{\delta U}^T\ {}^{\tau}_{0}\widetilde{\underline{B}}^2_{ij}\ \underline{U} + \underline{U}^T\ {}^{\tau}_{0}\widetilde{\underline{B}}^2_{ij}\ \underline{\delta U} = \underline{\delta U}^T\ \left({}^{\tau}_{0}\widetilde{\underline{B}}^2_{ij} + {}^{\tau}_{0}\ \widetilde{\underline{B}}^{2,T}_{ij}\right)\ \underline{U} \\
\delta_0\widetilde{\eta}_{2,ij} &= \underline{\delta U}^T\ {}^{\tau}_{0}\widetilde{\underline{B}}^{NL,2}_{ij}\ \underline{U}
\end{aligned}
$$

being ${}^{\tau}_{0}\widetilde{\underline{B}}^{NL,2}_{ij} = {}^{\tau}_{0}\ \widetilde{\underline{B}}^{NL,2}_{ji}$.

For the interpolation of the transverse shear strain components the calculations are similar to those shown in Eqs. (6.56a) to (6.56d).

Finally, the matrix ${}^{\tau}_{0}\underline{K}_{NL,2}$ is,

$$
\begin{aligned}
{}^{\tau}_{0}\underline{K}_{NL,2} = \int_{{}^{o}V} [\ & {}^{\tau}_{o}\widetilde{S}^{rr}\ {}^{\tau}_{0}\widetilde{\underline{B}}^{NL,2}_{rr} + {}^{\tau}_{o}\ \widetilde{S}^{ss}\ {}^{\tau}_{0}\widetilde{\underline{B}}^{NL,2}_{ss} + {}^{\tau}_{o}\ \widetilde{S}^{tt}\ {}^{\tau}_{0}\widetilde{\underline{B}}^{NL,2}_{tt} + {}^{\tau}_{o}\ \widetilde{S}^{rs}\ ({}^{\tau}_{0}\widetilde{\underline{B}}^{NL,2}_{rs} + {}^{\tau}_{0}\ \widetilde{\underline{B}}^{NL,2}_{sr}) + \\
& {}^{\tau}_{o}\widetilde{S}^{rt}\ ({}^{\tau}_{0}\widetilde{\underline{B}}^{NL,2}_{rt} + {}^{\tau}_{0}\ \widetilde{\underline{B}}^{NL,2}_{tr}) + {}^{\tau}_{o}\ \widetilde{S}^{st}\ ({}^{\tau}_{0}\widetilde{\underline{B}}^{NL,2}_{st} + {}^{\tau}_{0}\ \widetilde{\underline{B}}^{NL,2}_{ts})]\ {}^{0}dV\ . \qquad (6.58)
\end{aligned}
$$

Non-linear matrix ${}^{\tau}_{0}\underline{K}_{NL,3}$ From Eq. (6.9c) and (6.44), we get,

$$
\underline{u}_3 = \frac{t}{2}\ a\ f\ \ (\Delta\lambda_o + \Delta\lambda_1\ t)\ \ h_k\ (-\alpha_k\ {}^{\tau}\underline{V}^k_2 + \beta_k\ {}^{\tau}\underline{V}^k_1)
$$

$$
\begin{aligned}
\frac{\partial \underline{u}_3}{\partial r} &= \frac{t}{2}\, a\, (\Delta\lambda_o + \Delta\lambda_1\, t) \left(\frac{\partial f}{\partial r}\, h_k + f\, h_{k,r}\right) (-\alpha_k\, {}^{\tau}\underline{V}_2^k + \beta_k\, {}^{\tau}\underline{V}_1^k) \\
\frac{\partial \underline{u}_3}{\partial s} &= \frac{t}{2}\, a\, (\Delta\lambda_o + \Delta\lambda_1\, t) \left(\frac{\partial f}{\partial s}\, h_k + f\, h_{k,s}\right) (-\alpha_k\, {}^{\tau}\underline{V}_2^k + \beta_k\, {}^{\tau}\underline{V}_1^k) \\
\frac{\partial \underline{u}_3}{\partial t} &= \frac{1}{2}\, a\, f\, (\Delta\lambda_o + 2\, \Delta\lambda_1\, t)\, h_k\, (-\alpha_k\, {}^{\tau}\underline{V}_2^k + \beta_k\, {}^{\tau}\underline{V}_1^k)\,.
\end{aligned}
$$

To simplify, we define the following expressions,

$$
\begin{aligned}
\widetilde{A}_{rr} &= \frac{t}{2}\, a \left(\frac{\partial f}{\partial r}\, h_k + f\, h_{k,r}\right) \\
\widetilde{A}_{ss} &= \frac{t}{2}\, a \left(\frac{\partial f}{\partial s}\, h_k + f\, h_{k,s}\right) \\
\widetilde{A}_{tt} &= \frac{1}{2}\, a\, f\, h_k\,.
\end{aligned}
$$

We rewrite the derivative expressions,

$$
\begin{aligned}
\frac{\partial \underline{u}_3}{\partial r} &= (\Delta\lambda_o + \Delta\lambda_1\, t)\; \widetilde{A}_{rr}\, (-\alpha_k\, {}^{\tau}\underline{V}_2^k + \beta_k\, {}^{\tau}\underline{V}_1^k) \\
\frac{\partial \underline{u}_3}{\partial s} &= (\Delta\lambda_o + \Delta\lambda_1\, t)\; \widetilde{A}_{ss}\, (-\alpha_k\, {}^{\tau}\underline{V}_2^k + \beta_k\, {}^{\tau}\underline{V}_1^k) \\
\frac{\partial \underline{u}_3}{\partial t} &= (\Delta\lambda_o + 2\, \Delta\lambda_1\, t)\; \widetilde{A}_{tt}\, (-\alpha_k\, {}^{\tau}\underline{V}_2^k + \beta_k\, {}^{\tau}\underline{V}_1^k)\,.
\end{aligned}
$$

We proceed now in a similar way as we did to calculate ${}^{\tau}_{0}\underline{K}_{NL,2}$. We build (22x22) matrices ${}^{\tau}_{0}\widetilde{\underline{B}}^{3}_{ij}$ with rows and columns according to the previous formulas, and taking into account Eq.(6.39c) Please note that this matrices have non zero numbers only in correspondance with the degrees of freedom α_k, β_k, $\Delta\lambda_o$ and $\Delta\lambda_1$.

$$
\begin{aligned}
{}_0\widetilde{\eta}_{3,rr} &= \underline{U}^T \, {}^{\tau}_{0}\widetilde{\underline{B}}^{3}_{rr} \, \underline{U} \\
{}_0\widetilde{\eta}_{3,ss} &= \underline{U}^T \, {}^{\tau}_{0}\widetilde{\underline{B}}^{3}_{ss} \, \underline{U} \\
{}_0\widetilde{\eta}_{3,tt} &= \underline{U}^T \, {}^{\tau}_{0}\widetilde{\underline{B}}^{3}_{tt} \, \underline{U} \\
{}_0\widetilde{\eta}_{3,rs} &= \underline{U}^T \, {}^{\tau}_{0}\widetilde{\underline{B}}^{3}_{rs} \, \underline{U} \\
{}_0\widetilde{\eta}_{3,rt} &= \underline{U}^T \, {}^{\tau}_{0}\widetilde{\underline{B}}^{3}_{rt} \, \underline{U} \\
{}_0\widetilde{\eta}_{3,st} &= \underline{U}^T \, {}^{\tau}_{0}\widetilde{\underline{B}}^{3}_{st} \, \underline{U} \, .
\end{aligned}
$$

We calculate the variations,

$$
\begin{aligned}
\delta_0\widetilde{\eta}_{3,ij} &= \underline{\delta U}^T \, {}^{\tau}_{0}\widetilde{\underline{B}}^{3}_{ij} \, \underline{U} + \underline{U}^T \, {}^{\tau}_{0}\widetilde{\underline{B}}^{3}_{ij} \, \underline{\delta U} = \underline{\delta U}^T \, \left({}^{\tau}_{0}\widetilde{\underline{B}}^{3}_{ij} + {}^{\tau}_{0}\widetilde{\underline{B}}^{3,T}_{ij} \right) \, \underline{U} \\
\delta_0\widetilde{\eta}_{3,ij} &= \underline{\delta U}^T \, {}^{\tau}_{0}\widetilde{\underline{B}}^{NL,3}_{ij} \, \underline{U}
\end{aligned}
$$

being ${}^{\tau}_{0}\widetilde{\underline{B}}^{NL,3}_{ij} = {}^{\tau}_{0}\widetilde{\underline{B}}^{NL,3}_{ji}$.

For the interpolation of the transverse shear strain components the calculations are similar to those shown in (6.56a) to (6.56d).

Finally, the matrix ${}^{\tau}_{0}\underline{K}_{NL,3}$ is,

$$
\begin{aligned}
{}^{\tau}_{0}\underline{K}_{NL,3} = \int_{{}_oV} [\, & {}^{\tau}_{o}\widetilde{S}^{rr} \, {}^{\tau}_{0}\widetilde{\underline{B}}^{NL,3}_{rr} + {}^{\tau}_{o}\widetilde{S}^{ss} \, {}^{\tau}_{0}\widetilde{\underline{B}}^{NL,3}_{ss} + {}^{\tau}_{o}\widetilde{S}^{tt} \, {}^{\tau}_{0}\widetilde{\underline{B}}^{NL,3}_{tt} + {}^{\tau}_{o}\widetilde{S}^{rs} \, ({}^{\tau}_{0}\widetilde{\underline{B}}^{NL,3}_{rs} + {}^{\tau}_{0}\widetilde{\underline{B}}^{NL,3}_{sr}) + \\
& {}^{\tau}_{o}\widetilde{S}^{rt} \, ({}^{\tau}_{0}\widetilde{\underline{B}}^{NL,3}_{rt} + {}^{\tau}_{0}\widetilde{\underline{B}}^{NL,3}_{tr}) + {}^{\tau}_{o}\widetilde{S}^{st} \, ({}^{\tau}_{0}\widetilde{\underline{B}}^{NL,3}_{st} + {}^{\tau}_{0}\widetilde{\underline{B}}^{NL,3}_{ts})] \, {}^{0}dV \, .
\end{aligned} \tag{6.59}
$$

Second case: compressible neo-Hookean model

We have to find the incremental constitutive relation between the components of the Second Piola Kirchhoff and Green Lagrange strain tensors,

$$
{}_oS^{IJ} = {}_oC^{IJKL} \, {}_o\varepsilon_{KL} \tag{6.60}
$$

The Green Lagrange strain second order tensor is defined in the reference configuration as [31],

$$ {}^{\tau}_{o}\underline{\underline{\epsilon}} = \frac{1}{2}\left({}^{\tau}_{o}\underline{\underline{C}} - {}^{0}\underline{\underline{g}} \right) \tag{6.61} $$

where ${}^{\tau}_{o}\underline{\underline{C}} = {}^{\tau}_{o}\underline{\underline{X}}^{T} \cdot {}^{\tau}_{o}\underline{\underline{X}}$ is the Green strain tensor and ${}^{0}\underline{\underline{g}}$ is the reference configuration metric tensor.

From Eq. (6.61),

$$ \frac{\partial\, C_{PQ}}{\partial\, \varepsilon_{PQ}} \,|^{\tau}_{0} = 2\ . \tag{6.62} $$

Therefore, the components of the incremental constitutive tensor can be calculated from,

$$ {}_{o}C^{LMPQ} \;=\; \frac{\partial S^{LM}}{\partial \varepsilon_{PQ}} \,|^{\tau}_{0} = \frac{\partial S^{LM}}{\partial C_{PQ}} \,|^{\tau}_{0}\; \frac{\partial C_{PQ}}{\partial \varepsilon_{PQ}} \,|^{\tau}_{0} $$

with no addition in repeated indices.

$$ {}_{o}C^{LMPQ} \;=\; 2\,\frac{\partial S^{LM}}{\partial C_{PQ}} \tag{6.63} $$

The above derivative is calculated using Serrin formula [31],

$$ \underline{\Phi}_A\underline{\Phi}_A = \; {}^{\tau}\lambda_A^2\; \frac{{}^{\tau}_{o}\underline{\underline{C}} - \left({}^{\tau}I_1^C \;-\; {}^{\tau}\lambda_A^2 \right)\; {}^{o}\underline{\underline{g}} + \; {}^{\tau}I_3^C\; {}^{\tau}\lambda_A^{-2}\; {}^{\tau}_{o}\underline{\underline{C}}^{-1}}{2\; {}^{\tau}\lambda_A^4 \;-\; {}^{\tau}I_1^C\; \lambda_A^2 \;+\; {}^{\tau}I_3^C\; {}^{\tau}\lambda_A^{-2}} \tag{6.64} $$

being $\underline{\Phi}_A$ the eigenvectors of the second order Green tensor ${}^{\tau}_{o}\underline{\underline{C}}$ and ${}^{\tau}\lambda_A^2$ its eigenvalues, with no addition in A.

The igenvalues ${}^{\tau}\lambda_A^2$ are the roots of the following polynomial [31],

$$ p({}^{\tau}\lambda_I^2) = \; -{}^{\tau}\lambda_I^6 \;+\; {}^{\tau}I_1^C\; {}^{\tau}\lambda_I^4 \;-\; {}^{\tau}I_2^C\; {}^{\tau}\lambda_I^2 \;+\; {}^{\tau}I_3^C \quad . \tag{6.65} $$

Taking into account that, for the case of isotropic elasticity, ${}^{\tau}_{o}\underline{\underline{S}}$ and ${}^{\tau}_{o}\underline{\underline{C}}$ are colinear tensors, ${}^{\tau}_{o}\underline{\underline{S}}$ can be written as,

$$ {}^{\tau}_{o}\underline{\underline{S}} = \; {}^{\tau}_{0}S^{I}\; \underline{\Phi}_I\underline{\Phi}_I \tag{6.66} $$

$$ {}^{\tau}_{o}S^{LM} = {}^{\tau}_{0}S^{I} \left[{}^{\tau}\lambda_I^2 \, \frac{{}^{\tau}_{o}C_{lm} - \left({}^{\tau}I_1^C - {}^{\tau}\lambda_I^2 \right) \, {}^{o}g_{lm} + {}^{\tau}I_3^C \, {}^{\tau}\lambda_I^{-2} \, {}^{\tau}_{o}C^{-1}_{lm}}{2 \, {}^{\tau}\lambda_I^4 - {}^{\tau}I_1^C \, \lambda_I^2 + {}^{\tau}I_3^C \, {}^{\tau}\lambda_I^{-2}} \right] \tag{6.67} $$

in the above,

$$ {}^{\tau}_{o}S^{I} = \frac{1}{{}^{\tau}\lambda_I^2} \left[\frac{\kappa}{2} \left({}^{\tau}J^{\,2} - 1 \right) + G \, ({}^{\tau}J)^{-2/3} \left(\frac{2 \, {}^{\tau}\lambda_I^2 - {}^{\tau}\lambda_{II}^2 - {}^{\tau}\lambda_{III}^2}{3} \right) \right] \tag{6.68a} $$

$$ {}^{\tau}_{o}S^{II} = \frac{1}{{}^{\tau}\lambda_{II}^2} \left[\frac{\kappa}{2} \left({}^{\tau}J^{\,2} - 1 \right) + G \, ({}^{\tau}J)^{-2/3} \left(\frac{2 \, {}^{\tau}\lambda_{II}^2 - {}^{\tau}\lambda_I^2 - {}^{\tau}\lambda_{III}^2}{3} \right) \right] \tag{6.68b} $$

$$ {}^{\tau}_{o}S^{III} = \frac{1}{{}^{\tau}\lambda_{III}^2} \left[\frac{\kappa}{2} \left({}^{\tau}J^{\,2} - 1 \right) + G \, ({}^{\tau}J)^{-2/3} \left(\frac{2 \, {}^{\tau}\lambda_{III}^2 - {}^{\tau}\lambda_I^2 - {}^{\tau}\lambda_{II}^2}{3} \right) \right] \tag{6.68c} $$

where ${}^{\tau}_{o}S^{I}$ are the eigenvalues of ${}^{\tau}_{o}\underline{\underline{S}}$ calculated using Eq. (6.22) and doing a pull-back [31], while ${}^{\tau}I_1^C$; ${}^{\tau}I_2^C$; ${}^{\tau}I_3^C$ are the invariants of ${}^{\tau}_{o}\underline{\underline{C}}$,

$$ {}^{\tau}I_1^C = tr \left({}^{\tau}_{o}\underline{\underline{C}} \right) \tag{6.69} $$

$$ {}^{\tau}I_2^C = \frac{1}{2} \left[\left({}^{\tau}I_1^C \right)^2 - tr \left({}^{\tau}_{o}\underline{\underline{C}}^2 \right) \right] \tag{6.70} $$

$$ {}^{\tau}I_3^C = \det \left({}^{\tau}_{o}\underline{\underline{C}} \right) \tag{6.71} $$

${}^{\tau}J = \det \left({}^{\tau}_{o}\underline{\underline{X}} \right)$ gives the local volume change. Provided that ${}^{\tau}\lambda_I$ are the eigenvalues of ${}^{\tau}_{o}\underline{\underline{X}}$, it is ${}^{\tau}J = {}^{\tau}\lambda_I \, {}^{\tau}\lambda_{II} \, {}^{\tau}\lambda_{III}$.

From Eq. (6.67), and to simplify the algebra, we call,

$$ f({}^{\tau}_{o}C_{LM}, {}^{\tau}\lambda_I) = \frac{{}^{\tau}_{o}C_{LM} - \left({}^{\tau}I_1^C - {}^{\tau}\lambda_I^2 \right) \, {}^{o}g_{LM} + {}^{\tau}I_3^C \, {}^{\tau}\lambda_I^{-2} \, {}^{\tau}_{o}C^{-1}_{LM}}{2 \, {}^{\tau}\lambda_I^4 - {}^{\tau}I_1^C \, \lambda_I^2 + {}^{\tau}I_3^C \, {}^{\tau}\lambda_I^{-2}} \, . \tag{6.72} $$

So,

$$ {}^{\tau}_{o}S^{LM} = {}^{\tau}_{0}S^{I} \, {}^{\tau}\lambda_I^2 \, f({}^{\tau}_{o}C_{LM}, {}^{\tau}\lambda_I) \tag{6.73} $$

$$ \begin{aligned} \frac{\partial S^{LM}}{\partial C_{PQ}}\Big|_0^{\tau} = {} & \frac{\partial S^I}{\partial C_{PQ}}\Big|_0^{\tau} \, {}^{\tau}\lambda_I^2 \, f({}^{\tau}_{o}C_{LM}, {}^{\tau}\lambda_I) + {}^{\tau}_{0}S^I \, 2 \, {}^{\tau}\lambda_I \, \frac{\partial \lambda_I}{\partial C_{PQ}}\Big|_0^{\tau} \, f({}^{\tau}_{o}C_{lm}, {}^{\tau}\lambda_I) + \\ & {}^{\tau}_{0}S^I \, {}^{\tau}\lambda_I^2 \, \frac{\partial f(C_{LM}, \lambda_I)}{\partial C_{PQ}}\Big|_0^{\tau} \, . \end{aligned} \tag{6.74} $$

In Appendix B we calculate each term of the last expression: $\frac{\partial \lambda_I}{\partial C_{PQ}}|_0^\tau$, $\frac{\partial S^I}{\partial C_{PQ}}|_0^\tau$ and $\frac{\partial f(C_{LM},\lambda_I)}{\partial C_{PQ}}|_0^\tau$.

After the above calculations we use the neo-Hookean incremental constitutive tensor in Eqs.(6.29).

Of course we do not loose the hyperelastic symmetry, that is to say,

$$ {}_oC^{LMPQ} = {}_oC^{PQLM} \quad . \tag{6.75}$$

Third case: linear relation between the Hencky strain tensor and its energy conjugate stress tensor

For an isotropic elastic material [7],

$$ {}^{\tau+\Delta\tau}_{o}S^{IJ} \; \delta \, {}^{\tau+\Delta\tau}_{o}\varepsilon_{IJ} = {}^{\tau+\Delta\tau}_{o} \; \Gamma^{IJ} \; \delta \, {}^{\tau+\Delta\tau}_{o}H_{IJ} \tag{6.76}$$

Therefore, we can write the Principle of Virtual Work for the equilibrium configuration at $\tau + \Delta\tau$ [9],

$$ \int_{{}^oV} {}^{\tau+\Delta\tau}_{o}\Gamma^{IJ} \; \delta \, {}^{\tau+\Delta\tau}_{o}H_{IJ} \; {}^odV = \; {}^{\tau+\Delta\tau}\mathcal{R} \; . $$

The stresses and strains are decomposed into the known quantities ${}^\tau_0\Gamma^{IJ}$ and ${}^\tau_oH_{IJ}$, and the unknown increments ${}_o\Gamma^{IJ}$ and ${}_oH_{IJ}$, so,

$$ \begin{aligned} {}^{\tau+\Delta\tau}_{0}\Gamma^{IJ} &= {}^\tau_0\Gamma^{IJ} + {}_o\,\Gamma^{IJ} \\ {}^{\tau+\Delta\tau}_{o}H_{IJ} &= {}^\tau_oH_{IJ} + {}_o\,H_{IJ} \end{aligned} $$

$$ \int_{{}^oV} \left({}^\tau_0\Gamma^{IJ} + {}_o\,\Gamma^{IJ}\right) \; \delta \; \left({}^\tau_oH_{IJ} + {}_o\,H_{IJ}\right) \; {}^odV = \; {}^{\tau+\Delta\tau}\mathcal{R} \quad . $$

Being $\delta \, {}^\tau_oH_{IJ} = 0$,

$$\int_{{}^oV} \left({}^{\tau}_{0}\Gamma^{IJ} \; + \; {}_o\Gamma^{IJ}\right) \; \delta_o H_{IJ} \; {}^o dV = \; {}^{\tau+\Delta\tau}\mathcal{R} \; .$$

It is necessary to put the strain increments in terms of the displacement increments. To do that, we take into account (6.61),

$${}_oH_{IJ} = \; \frac{\partial H_{IJ}}{\partial C_{MN}}|^{\tau}_0 \; {}_oC_{MN} \; = \; 2 \; \frac{\partial H_{IJ}}{\partial C_{MN}}|^{\tau}_0 \; {}_o\varepsilon_{MN} \; .$$

We define the fourth order tensor,

$${}^{\tau}_{o}\lambda^{MN}_{IJ} = \; 2 \; \frac{\partial H_{IJ}}{\partial C_{MN}}|^{\tau}_0 \tag{6.78}$$

hence,

$${}_oH_{IJ} = \; {}^{\tau}_{o}\lambda^{MN}_{IJ} \; {}_o\varepsilon_{MN} \; . \tag{6.79}$$

To calculate the above defined tensor components we use again the Serrin formula. Using the tensor ${}^{\tau}_{o}\underline{\underline{\underline{\lambda}}}$ and Eq. (6.25), we can calculate the increment ${}_o\widetilde{\Gamma}^{ij}$ as,

$${}_o\Gamma^{IJ} = \; {}_oC^{IJKL} \; {}_oH_{KL} = \; {}_oC^{IJKL} \; {}^{\tau}_{o}\lambda^{MN}_{IJ} \; \left({}_oe_{MN} \; + \; {}_o\eta_{MN}\right) \; . \tag{6.80}$$

Hence, the linearized incremental equation (6.29) can be written, in the element natural system, as,

$$\int_{{}_oV} \widetilde{C}^{ijkl} \; {}^{\tau}_{o}\widetilde{\lambda}^{pq}_{ij} \; {}^{\tau}_{o}\widetilde{\lambda}^{rs}_{kl} \; {}_o\widetilde{e}_{pq} \; \delta_o\widetilde{e}_{rs} \; {}^o dV + \int_{{}_oV} {}^{\tau}_{o}\widetilde{\Gamma}^{ij} \; {}^{\tau}_{o}\widetilde{\lambda}^{mn}_{ij} \; \delta_o\widetilde{\eta}_{mn} \; {}^o dV = {}^{\tau+\Delta\tau}\mathcal{R} - \int_{{}_oV} {}^{\tau}_{o}\widetilde{\Gamma}^{ij} \; {}^{\tau}_{o}\widetilde{\lambda}^{mn}_{ij} \; \delta_o\widetilde{e}_{mn} \; {}^o dV \; . \tag{6.81}$$

Matrices ${}^{\tau}_{0}\underline{\widetilde{B}}$, ${}^{\tau}_{0}\underline{\widetilde{B}}^{NL,1}_{ij}$, ${}^{\tau}_{0}\underline{\widetilde{B}}^{NL,2}_{ij}$ and ${}^{\tau}_{0}\underline{\widetilde{B}}^{NL,3}_{ij}$ are those calculated for the first case, therefore the linear stiffness matrix and the vector of nodal equivalent forces are,

$${}^{\tau}_{0}\underline{K}_L = \int_{{}_oV} {}^{\tau}_{0}\underline{B}^T \; {}^{\tau}_{0}\underline{\widetilde{\lambda}}^T \; \underline{\widetilde{C}} \; {}^{\tau}_{0}\underline{\widetilde{\lambda}} \; {}^{\tau}_{0}\underline{B} \; {}^0 dV$$

$$ {}^{\tau}\underline{F} = \int_{{}^{o}V} {}^{\tau}_{0}\underline{B}^{T}\ {}^{\tau}_{0}\widetilde{\underline{\lambda}}^{T}\ {}^{\tau}_{0}\underline{\Gamma}\ {}^{0}dV\ . $$

We define a new vector (6x1) vector ${}^{\tau}_{o}\widetilde{\underline{G}}$. The expressions of the nonlinear matrices are similar to the Eqs. (6.57), (6.58) and (6.59), but replacing the components of the second order Piola Kirchhoff tensor ${}^{\tau}_{o}\widetilde{S}^{ij}$ with the components ${}^{\tau}_{o}\widetilde{G}^{ij}$.

$$ {}^{\tau}_{o}\widetilde{\underline{G}} = {}^{\tau}_{0}\widetilde{\underline{\Gamma}}^{T}\ {}^{\tau}_{0}\widetilde{\underline{\lambda}} \tag{6.82} $$

In the last equation, the second Piola Kirchhoff tensor ${}^{\tau}_{0}\widetilde{\underline{\underline{\Gamma}}}$ is written as a (6x1) array while the fourth order tensor ${}^{\tau}_{o}\widetilde{\underline{\underline{\underline{\lambda}}}}$ is a (6x6) matrix.

$$ \begin{aligned} {}^{\tau}_{0}\underline{K}_{NL,1} = \int_{{}^{o}V} [\ & {}^{\tau}_{o}\widetilde{G}^{rr}\ {}^{\tau}_{0}\widetilde{\underline{B}}^{NL,1}_{rr} + {}^{\tau}_{o}\widetilde{G}^{ss}\ {}^{\tau}_{0}\widetilde{\underline{B}}^{NL,1}_{ss} + {}^{\tau}_{o}\widetilde{G}^{tt}\ {}^{\tau}_{0}\widetilde{\underline{B}}^{NL,1}_{tt} + \\ & {}^{\tau}_{o}\widetilde{G}^{rs}\ ({}^{\tau}_{0}\widetilde{\underline{B}}^{NL,1}_{rs} + {}^{\tau}_{0}\widetilde{\underline{B}}^{NL,1}_{sr}) + {}^{\tau}_{o}\widetilde{G}^{rt}\ ({}^{\tau}_{0}\widetilde{\underline{B}}^{NL,1}_{rt} + {}^{\tau}_{0}\widetilde{\underline{B}}^{NL,1}_{tr}) + \\ & {}^{\tau}_{o}\widetilde{G}^{st}\ ({}^{\tau}_{0}\widetilde{\underline{B}}^{NL,1}_{st} + {}^{\tau}_{0}\widetilde{\underline{B}}^{NL,1}_{ts})]\ {}^{0}dV \end{aligned} \tag{6.83} $$

$$ \begin{aligned} {}^{\tau}_{0}\underline{K}_{NL,2} = \int_{{}^{o}V} [\ & {}^{\tau}_{o}\widetilde{G}^{rr}\ {}^{\tau}_{0}\widetilde{\underline{B}}^{NL,2}_{rr} + {}^{\tau}_{o}\widetilde{G}^{ss}\ {}^{\tau}_{0}\widetilde{\underline{B}}^{NL,2}_{ss} + {}^{\tau}_{o}\widetilde{G}^{tt}\ {}^{\tau}_{0}\widetilde{\underline{B}}^{NL,2}_{tt} + \\ & {}^{\tau}_{o}\widetilde{G}^{rs}\ ({}^{\tau}_{0}\widetilde{\underline{B}}^{NL,2}_{rs} + {}^{\tau}_{0}\widetilde{\underline{B}}^{NL,2}_{sr}) + {}^{\tau}_{o}\widetilde{G}^{rt}\ ({}^{\tau}_{0}\widetilde{\underline{B}}^{NL,2}_{rt} + {}^{\tau}_{0}\widetilde{\underline{B}}^{NL,2}_{tr}) + \\ & {}^{\tau}_{o}\widetilde{G}^{st}\ ({}^{\tau}_{0}\widetilde{\underline{B}}^{NL,2}_{st} + {}^{\tau}_{0}\widetilde{\underline{B}}^{NL,2}_{ts})]\ {}^{0}dV \end{aligned} \tag{6.84} $$

$$ \begin{aligned} {}^{\tau}_{0}\underline{K}_{NL,3} = \int_{{}^{o}V} [\ & {}^{\tau}_{o}\widetilde{G}^{rr}\ {}^{\tau}_{0}\widetilde{\underline{B}}^{NL,3}_{rr} + {}^{\tau}_{o}\widetilde{G}^{ss}\ {}^{\tau}_{0}\widetilde{\underline{B}}^{NL,3}_{ss} + {}^{\tau}_{o}\widetilde{G}^{tt}\ {}^{\tau}_{0}\widetilde{\underline{B}}^{NL,3}_{tt} + \\ & {}^{\tau}_{o}\widetilde{G}^{rs}\ ({}^{\tau}_{0}\widetilde{\underline{B}}^{NL,3}_{rs} + {}^{\tau}_{0}\widetilde{\underline{B}}^{NL,3}_{sr}) + {}^{\tau}_{o}\widetilde{G}^{rt}\ ({}^{\tau}_{0}\widetilde{\underline{B}}^{NL,3}_{rt} + {}^{\tau}_{0}\widetilde{\underline{B}}^{NL,3}_{tr}) + \\ & {}^{\tau}_{o}\widetilde{G}^{st}\ ({}^{\tau}_{0}\widetilde{\underline{B}}^{NL,3}_{st} + {}^{\tau}_{0}\widetilde{\underline{B}}^{NL,3}_{ts})]\ {}^{0}dV\ . \end{aligned} \tag{6.85} $$

The resulting stiffness matrices are, of course, also symmetric.

During the calculation, the first step is to calculate the components of the second order Hencky tensor, ${}^{\tau}_{o}H_{ij}$, and interpolate the transversal shear components according

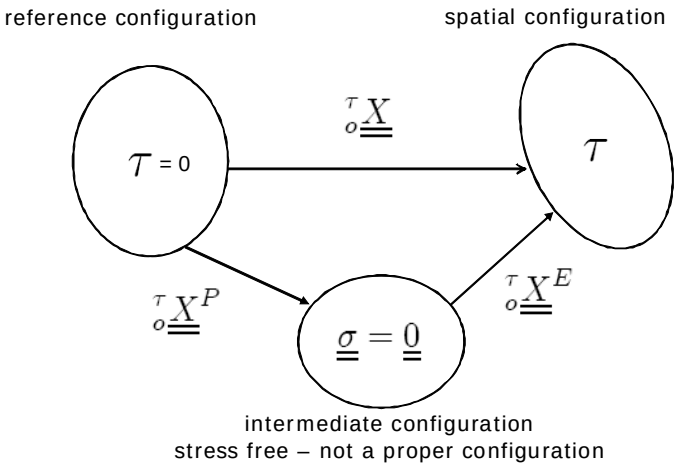

Figure 6.4: Lee's multiplicative decomposition

to Eqs. (6.11a) to (6.11f). With the interpolated Hencky strain values we calculate the interpolated second order Green tensor, and with the latest we calculate ${}^{\tau}_{o}\lambda^{MN}_{IJ}$.

The terms ${}^{\tau}_{o}\lambda^{MN}_{IJ}$ are calculated in Appendix B.

6.4 Elasto-plastic formulation

6.4.1 Constitutive relation

This full 3D constitutive relation is based on,

- Lee´s multiplicative decomposition of the deformation gradient (Fig. 6.4),
- maximum plastic dissipation,
- for the elastic part an hyperelastic relation using Hooke with Hencky strains Eq.(6.25).

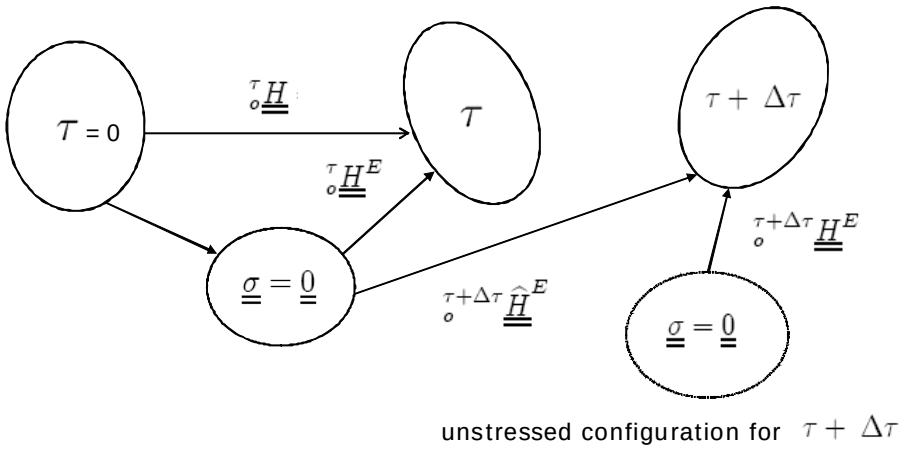

Figure 6.5: Incremental step

6.4.2 The incremental formulation

Using a total Lagrangian formulation, we can write the Principle of Virtual Work for the equilibrium configuration at $\tau + \Delta\tau$ [9],

$$\int_{{}^{o}V} {}^{\tau+\Delta\tau}\Gamma^{IJ}\ \delta\ {}^{\tau+\Delta\tau}_{o}H^{E}_{IJ}\ {}^{o}dV = {}^{\tau+\Delta\tau}\mathcal{R} \tag{6.86}$$

where ${}^{\tau+\Delta\tau}\mathcal{R}$ is the virtual work of the external loads acting on the solid body in the $\tau + \Delta\tau$ configuration and ${}^{\tau}_{o}\underline{\underline{H}}^{E}$ is the elastic Hencky strain tensor. From Fig.(6.4) it is clear that the stresses in the multiplicative decomposition scheme are developed during the elastic process and, therefore, the stresses develop virtual work with the variations of the elastic strains.

To perform the step from τ to $\tau + \Delta\tau$ we first consider an "elastic predictor" phase, that is to say, we assume that the intermediate configuration is locked; then we consider a "plastic corrector" phase to update the intermediate configuration. In Fig. (6.5) we schematize this procedure.

For the elastic predictor phase,

$$\int_{{}^oV} {}^{\tau+\Delta\tau}\Gamma^{IJ}\ \delta\widehat{H}^E_{IJ}\ {}^o dV = {}^{\tau+\Delta\tau}\mathcal{R}\ . \tag{6.87}$$

During an iterative process we linearize the steps around the previous iteration $(k-1)$ results, therefore,

$${}^{\tau+\Delta\tau}\Gamma^{IJ}|^k = {}^{\tau+\Delta\tau}\Gamma^{IJ}|^{(k-1)} + {}_o\Gamma^{IJ}\ . \tag{6.88}$$

Replacing the last expression in Eq. (6.87), we get,

$$\int_{{}^oV} \left({}^{\tau+\Delta\tau}\Gamma^{IJ}|^{(k-1)} + {}_o\Gamma^{IJ}\right)\ \delta\widehat{H}^E_{IJ}\ {}^o dV = {}^{\tau+\Delta\tau}\mathcal{R}\ . \tag{6.89}$$

Since we are interpolating the total components of ${}^\tau_o\underline{\underline{H}}$, not only the elastic part, we must calculate,

$$\begin{aligned} \delta\ \widehat{H}^E_{IJ} &= \frac{\partial \widehat{H}^E_{IJ}}{\partial H_{LM}}|^{(k-1)}\ \delta H_{LM} \\ \frac{\partial \widehat{H}^E_{IJ}}{\partial H_{LM}}|^k &= \frac{\partial \widehat{H}^E_{IJ}}{\partial H_{LM}}|^{(k-1)} + \frac{\partial^2 \widehat{H}^E_{IJ}}{\partial H_{RS}\,\partial H_{LM}}|^{(k-1)}\ {}_0H_{RS} \end{aligned} \tag{6.90}$$

hence,

$$\delta\widehat{H}^E_{IJ} = \left(\frac{\partial \widehat{H}^E_{IJ}}{\partial H_{LM}}|^{(k-1)} + \frac{\partial^2 \widehat{H}^E_{IJ}}{\partial H_{RS}\,\partial H_{LM}}|^{(k-1)}\ {}_0H_{RS}\right)\ \delta H_{LM}\ . \tag{6.91}$$

Regarding the increment ${}_o\Gamma^{IJ}$,

$${}_o\Gamma^{IJ} = \frac{\partial \Gamma^{IJ}}{\partial \widehat{H}^E_{PQ}}|^{(k-1)}\ \frac{\partial \widehat{H}^E_{PQ}}{\partial H_{RS}}|^{(k-1)}\ {}_0H_{RS}\ . \tag{6.92a}$$

Replacing Eqs.(6.91) and (6.92a) into Eq.(6.86) and neglecting the product of increments we get,

$$\int_{{}^oV} {}^{\tau+\Delta\tau}\Gamma^{IJ}|^{(k-1)} \; \frac{\partial \widehat{H}^E_{IJ}}{\partial H_{LM}}|^{(k-1)} \; \delta H_{LM} \; {}^odV \; +$$

$$\int_{{}^oV} \frac{\partial \Gamma^{IJ}}{\partial \widehat{H}^E_{PQ}}|^{(k-1)} \; \frac{\partial \widehat{H}^E_{PQ}}{\partial H_{RS}}|^{(k-1)} \; {}_0H_{RS} \; \frac{\partial \widehat{H}^E_{IJ}}{\partial H_{LM}}|^{(k-1)} \; \delta H^o_{LM} \; {}^odV \; +$$

$$\int_{{}^oV} {}^{\tau+\Delta\tau}\Gamma^{IJ}|^{(k-1)} \; \frac{\partial^2 \widehat{H}^E_{IJ}}{\partial H_{RS} \, \partial H_{LM}}|^{(k-1)} \; {}_0H_{RS} \; \delta H_{LM} \; {}^odV \; = \; {}^{\tau+\Delta\tau}\mathcal{R}|^{(k)} \; . \tag{6.93}$$

Now we define the following tensors,

$${}_0C^{IJPQ}_{EP}|^{(k-1)} \; = \; \frac{\partial \Gamma^{IJ}}{\partial \widehat{H}^E_{PQ}}|^{(k-1)} \tag{6.94}$$

$${}^{\tau+\Delta\tau}_0\widehat{D}^{RS}_{PQ}|^{(k-1)} \; = \; \frac{\partial \widehat{H}^E_{PQ}}{\partial H_{RS}}|^{(k-1)} \tag{6.95}$$

$${}^{\tau+\Delta\tau}_0\widehat{DD}^{RSLM}_{IJ}|^{(k-1)} \; = \; \frac{\partial^2 \widehat{H}_{IJ}}{\partial H_{RS} \, \partial H_{LM}}|^{(k-1)} \; . \tag{6.96}$$

The fourth order tensor ${}_0\underset{\equiv\equiv}{C}_{EP}$ is the tangent constitutive elato-plastic tensor.

Regarding the fourth order tensor ${}^{\tau+\Delta\tau}_0\underset{\equiv\equiv}{\widehat{D}}$, obviously it is ${}^{\tau+\Delta\tau}_0\underset{\equiv\equiv}{\widehat{D}} = \underset{\equiv\equiv}{I}$ when there is not plastic deformation.

The derivation of the tensors ${}^{\tau+\Delta\tau}_0\underset{\equiv\equiv}{\widehat{D}}$ and ${}^{\tau+\Delta\tau}_0\underset{\equiv\equiv\equiv\equiv}{\widehat{DD}}$ is presented in Appendix C.

The tensors defined in Eqs.(6.94)-(6.96) are calculated at each Gauss point. They cannot be calculated at the sampling points, because the deformation gradient tensor ${}^{\tau+\Delta\tau}_0\underset{\equiv\equiv}{X}$ is only known at Gauss points [28]. Replacing into Eqn (6.93),

$$\int_{{}^oV} \delta H_{LM} \; {}^{\tau+\Delta\tau}\Gamma^{IJ}|^{(k-1)} \; {}^{\tau+\Delta\tau}_0\widehat{D}^{LM}_{IJ}|^{(k-1)} \; {}^odV +$$

$$\int_{{}^oV} \delta H_{LM} \; {}^{\tau+\Delta\tau}_0\widehat{D}^{LM}_{IJ}|^{(k-1)} \; {}_0C^{IJPQ}_{EP} \; {}^{\tau+\Delta\tau}_0\widehat{D}^{RS}_{PQ}|^{(k-1)} \; {}_0H_{RS} \; {}^odV +$$

$$\int_{{}^oV} \delta H_{LM} \; {}^{\tau+\Delta\tau}\Gamma^{IJ}|^{(k-1)} \; {}^{\tau+\Delta\tau}_0\widehat{DD}^{RSLM}_{IJ}|^{(k-1)} \; {}_0H_{RS} \; {}^odV = \; {}^{\tau+\Delta\tau}\mathcal{R} \; . \tag{6.97}$$

Replacing Eq. (6.78) into Eq.(6.79) we get,

$$
\begin{aligned}
{}_0H_{RS} &= {}^{\tau+\Delta\tau}_{\ 0}\lambda^{VW}_{RS}\big|^{(k-1)}\ {}_0\varepsilon_{VW} \\
\delta H_{LM} &= {}^{\tau+\Delta\tau}_{\ 0}\lambda^{XT}_{LM}\big|^{(k-1)}\ \delta\varepsilon_{XT}\ .
\end{aligned}
$$

The strain increment ${}_0\varepsilon_{MN}$ can be decomposed into a linear part in incremental displacements, ${}_0e_{MN}$, and a non-linear part in incremental displacements, ${}_0\eta_{MN}$,

$$
{}_0\varepsilon_{MN} = {}_0e_{MN} + {}_0\eta_{MN}\ .
$$

Linearizing,

$$
{}_0\varepsilon_{VW}\ \delta\varepsilon_{XT} = {}_0e_{MN}\ \delta e_{XT}\ .
$$

Substituting in Eq. (6.97),

$$
\begin{aligned}
&\int_{{}^oV} \delta\eta_{XT}\ {}^{\tau+\Delta\tau}_{\ 0}\lambda^{XT}_{LM}\big|^{(k-1)}\ {}^{\tau+\Delta\tau}\Gamma^{IJ}\big|^{(k-1)}\ {}^{\tau+\Delta\tau}_{\ 0}\widehat{D}^{LM}_{IJ}\big|^{(k-1)}\ {}^oV + \\
&\int_{{}^oV} \delta e_{XT}\ {}^{\tau+\Delta\tau}_{\ 0}\lambda^{XT}_{LM}\big|^{(k-1)}\ {}^{\tau+\Delta\tau}_{\ 0}\widehat{D}^{LM}_{IJ}\big|^{(k-1)}\ {}_0C^{IJPQ}_{EP}\ {}^{\tau+\Delta\tau}_{\ 0}\widehat{D}^{RS}_{PQ}\big|^{(k-1)}\ {}^{\tau+\Delta\tau}_{\ 0}\lambda^{VW}_{RS}\big|^{(k-1)}\ {}_0e_{VW}\ {}^oV + \\
&\int_{{}^oV} \delta e_{XT}\ {}^{\tau+\Delta\tau}_{\ 0}\lambda^{XT}_{LM}\big|^{(k-1)}\ {}^{\tau+\Delta\tau}\Gamma^{IJ}\big|^{(k-1)}\ {}^{\tau}_{0}\widehat{DD}^{RSLM}_{IJ}\big|^{(k-1)}\ {}^{\tau}_{0}\lambda^{VW}_{RS}\big|^{(k-1)}\ {}_0e_{VW}\ {}^oV = \\
&\qquad {}^{\tau+\Delta\tau}\mathcal{R} - \int_{{}^oV} \delta e_{XT}\ {}^{\tau+\Delta\tau}_{\ 0}\lambda^{XT}_{LM}\big|^{(k-1)}\ {}^{\tau+\Delta\tau}\Gamma^{IJ}\big|^{(k-1)}\ {}^{\tau+\Delta\tau}_{\ 0}\widehat{D}^{LM}_{IJ}\big|^{(k-1)}\ {}^oV\ . \qquad (6.98)
\end{aligned}
$$

Linear matrix ${}^{\tau+\Delta\tau}_{\ 0}\underline{K}_L\big|^{(k-1)}$ and the vector of nodal equivalent forces ${}^{\tau+\Delta\tau}\underline{F}\big|^{(k-1)}$.

The Eqs.(6.41) is substituted into Eq. (6.98), getting 2 lineal stiffness matrices ${}^{\tau+\Delta\tau}_{\ 0}\underline{K}_L$ and ${}^{\tau+\Delta\tau}_{\ 0}\underline{K}_{L2}$,

$$
\begin{aligned}
{}^{\tau+\Delta\tau}_{\ 0}K_{L,\,ZY}\big|^{(k-1)} &= \int_{{}^oV} {}^{\tau+\Delta\tau}_{\ 0}B_{(XT)Z}\big|^{(k-1)}\ {}^{\tau+\Delta\tau}_{\ 0}\lambda^{XT}_{LM}\big|^{(k-1)}\ {}^{\tau+\Delta\tau}_{\ 0}\widehat{D}^{LM}_{IJ}\big|^{(k-1)}\ . \qquad (6.99a) \\
&\quad {}_0C^{IJPQ}_{EP}\ {}^{\tau+\Delta\tau}_{\ 0}\widehat{D}^{RS}_{PQ}\big|^{(k-1)}\ {}^{\tau+\Delta\tau}_{\ 0}\lambda^{VW}_{RS}\big|^{(k-1)}\ {}^{\tau+\Delta\tau}_{\ 0}B_{(VW)Y}\ {}^oV
\end{aligned}
$$

$$
{}^{\tau+\Delta\tau}_{0}\underline{K}_{L}|^{(k-1)} = \int_{{}^{o}V} {}^{\tau+\Delta\tau}_{0}\underline{B}^{T}|^{(k-1)}\ {}^{\tau+\Delta\tau}_{0}\underline{\lambda}^{T}|^{(k-1)}\ {}^{\tau+\Delta\tau}_{0}\widehat{\underline{D}}^{T}|^{(k-1)} \cdot \qquad (6.100a)
$$
$$
{}_{0}\underline{C}_{EP}\ {}^{\tau+\Delta\tau}_{0}\underline{\widehat{D}}|^{(k-1)}\ {}^{\tau+\Delta\tau}_{0}\underline{\lambda}|^{(k-1)}\ {}^{\tau+\Delta\tau}_{0}\underline{B}|^{(k-1)}\ {}^{o}dV
$$

$$
{}^{\tau+\Delta\tau}_{0}K_{L2,ZY}|^{(k-1)} = \int_{{}^{o}V} {}^{\tau+\Delta\tau}_{0}B_{XTZ}|^{(k-1)}\ {}^{\tau+\Delta\tau}_{0}\lambda^{XT}_{LM}|^{(k-1)}\ {}^{\tau+\Delta\tau}\Gamma^{IJ}|^{(k-1)} \qquad (6.101a)
$$
$$
{}^{\tau}_{0}\widehat{DD}^{RSLM}_{IJ}|^{(k-1)}\ {}^{\tau+\Delta\tau}_{0}\lambda^{VW}_{RS}|^{(k-1)}\ {}^{\tau+\Delta\tau}_{0}B_{VWY}|^{(k-1)}\ {}^{o}dV\ .
$$

As the influence of ${}^{\tau+\Delta\tau}_{0}\underline{K}_{L2}$ is not very significant in the iterative process, we do not consider this matrix in the equation system.

The vector of nodal equivalent forces is,

$$
{}^{\tau+\Delta\tau}F_{z}|^{(k-1)} = \int_{{}^{o}V} {}^{\tau+\Delta\tau}_{0}B_{(XT)Z}|^{(k-1)}\ {}^{\tau+\Delta\tau}_{0}\lambda^{XT}_{LM}|^{(k-1)}\ {}^{\tau+\Delta\tau}\Gamma^{IJ}|^{(k-1)}\ {}^{\tau+\Delta\tau}_{0}\widehat{D}^{LM}_{IJ}|^{(k-1)}\ {}^{o}dV
$$

$$
{}^{\tau+\Delta\tau}\underline{F}|^{(k-1)} = \int_{{}^{o}V} {}^{\tau+\Delta\tau}_{0}\underline{B}^{T}\ {}^{\tau+\Delta\tau}_{0}\underline{\lambda}^{T}|^{(k-1)}\ {}^{\tau+\Delta\tau}_{0}\underline{\widehat{D}}|^{(k-1)}\ {}^{\tau+\Delta\tau}\underline{\Gamma}|^{(k-1)}\ {}^{0}dV\ . \qquad (6.102)
$$

Non-linear matrix ${}^{\tau+\Delta\tau}_{0}\underline{K}_{NL}|^{(k-1)}$

From 6.98 we also get ${}^{\tau+\Delta\tau}_{0}\underline{K}_{NL}|^{(k-1)}$,

$$
{}^{\tau+\Delta\tau}_{0}\underline{K}_{NL}|^{(k-1)} = \int_{{}^{o}V} \delta\eta_{XT}\ {}^{\tau+\Delta\tau}_{0}\lambda^{XT}_{LM}|^{(k-1)}\ {}^{\tau+\Delta\tau}\Gamma^{IJ}|^{(k-1)}\ {}^{\tau+\Delta\tau}_{0}\widehat{D}^{LM}_{IJ}|^{(k-1)}\ {}^{o}dV\ .
$$

Matrices ${}^{\tau}_{0}\widetilde{\underline{B}}^{NL,1}_{ij}$, ${}^{\tau}_{0}\widetilde{\underline{B}}^{NL,2}_{ij}$ and ${}^{\tau}_{0}\widetilde{\underline{B}}^{NL,3}_{ij}$ are those calculated for the linear relation between 2^{nd} Piola-Kirchhoff and Green Lagrange

We define a new (6x1) vector ${}^{\tau}_{0}\underline{G}_{P}$. The expressions of the stifness matrices are similar to Eqs. (6.83) to (6.85), but replacing the components of the vector ${}^{\tau}_{0}\underline{G}$ for the components of the new vector ${}^{\tau}_{0}\underline{G}_{P}$,

$$ {}^{\tau+\Delta\tau}_{0}G_P^{XT}|^{(k-1)} = {}^{\tau+\Delta\tau}\Gamma^{IJ}|^{(k-1)}\ {}^{\tau+\Delta\tau}_{0}\widehat{D}_{IJ}^{LM}|^{(k-1)}\ {}^{\tau+\Delta\tau}_{0}\lambda_{LM}^{XT}|^{(k-1)} $$

$$ {}^{\tau}_{0}G_P\,(i)\,|^{(k-1)} = {}^{\tau+\Delta\tau}\underline{\Gamma}^{T}|^{(k-1)}\ {}^{\tau+\Delta\tau}_{0}\underline{\widehat{D}}|^{(k-1)}\ {}^{\tau+\Delta\tau}_{0}\underline{\lambda}|^{(k-1)}\,(:,i) $$

where ${}^{\tau+\Delta\tau}_{0}\lambda|^{(k-1)}\,(:,i)$ is the i column of the fourth order tensor ${}^{\tau+\Delta\tau}_{0}\underline{\underline{\underline{\underline{\lambda}}}}|^{(k-1)}$expressed as a (6x6) matrix.

Provided that the second order tensor ${}^{\tau+\Delta\tau}\underline{\underline{\Gamma}}|^{(k-1)}$ is defined in the intermediate configuration, it remains in cartesian coordinates. Therefore, for the elasto-plastic formulation, we do not calculate the stifness matrices in convective coordiantes but in the cartesian coordiante system. Regarding the integration volume, as the step between the reference configuration and the intermediate configuration is totally plastic, there is not volume variation between them, therefore we can integrate in the reference volume.

Finally we get the following nonlinear finite element equations,

$$ ({}^{\tau+\Delta\tau}_{0}\underline{K}_L|^{(k-1)} + {}^{\tau+\Delta\tau}_{0}\underline{K}_{NL}|^{(k-1)})\ \underline{U} = {}^{\tau+\Delta\tau}\underline{\mathcal{R}}|^{(k)} - {}^{\tau+\Delta\tau}\underline{F}|^{(k-1)}\ . $$

6.4.3 Calculation of stresses (Radial Return algorithm)

This algorithm was already presented in [36] and [28].

Elastic predictor The trial values $\underline{\underline{\widehat{X}}}_p$ and $\widehat{\sigma}_y$ are those calculated at last converged step τ.

$$ \underline{\underline{\widehat{X}}}_p = {}^{\tau}_{0}\underline{\underline{X}}_p $$

$$ \widehat{\sigma}_y = {}^{\tau}_{0}\sigma_y $$

$$ \underline{\underline{\widehat{C}}}_E = (\underline{\underline{\widehat{X}}}_p)^{-T}\ \cdot\ {}^{\tau+\Delta\tau}_{0}\underline{\underline{C}}\ \cdot\ (\underline{\underline{\widehat{X}}}_p)^{-1} $$

${}^{\tau+\Delta\tau}_{0}\underline{\underline{C}}$ was calculated taking into account the transverse shear strain interpolation.

$$\widehat{\underline{\underline{H}}}_E = \ln\left[\left(\widehat{\underline{\underline{C}}}_E\right)^{-\frac{1}{2}}\right]$$

$$\widehat{\underline{\underline{\Gamma}}} = \underline{\underline{\underline{\underline{C}}}} : \widehat{\underline{\underline{H}}}_E$$

where $\underline{\underline{\underline{\underline{C}}}}$ is an isotropic and constant fourth order tensor (Hooke's law).

$$\widehat{\underline{\underline{\Gamma}}}_D = \widehat{\underline{\underline{\Gamma}}} - \frac{1}{3}\,\widehat{\underline{\underline{\Gamma}}}_V\ {}^{0}\underline{\underline{g}}$$

and,

$$\widehat{\Gamma}_V = \widehat{\Gamma}^{II}$$

$$\widehat{\Phi} = \left(\frac{3}{2}\,\widehat{\underline{\underline{\Gamma}}}_D : \widehat{\underline{\underline{\Gamma}}}_D\right)^{\frac{1}{2}} - \widehat{\sigma}_y\ .$$

IF($\widehat{\Phi} \leq 0$) then,

$${}^{\tau+\Delta\tau}_{0}\underline{\underline{X}}_p = \widehat{\underline{\underline{X}}}_p$$

$${}^{\tau+\Delta\tau}_{0}\sigma_y = \widehat{\sigma}_y$$

$${}^{\tau+\Delta\tau}\underline{\underline{\Gamma}}_D = \widehat{\underline{\underline{\Gamma}}}_D$$

$${}^{\tau+\Delta\tau}\underline{\underline{\Gamma}} = \widehat{\underline{\underline{\Gamma}}}$$

$${}^{\tau+\Delta\tau}\underline{\underline{H}}_E = \widehat{\underline{\underline{H}}}_E$$

ELSE

go to plastic corrector

Plastic corrector Being E the elastic modulus, E_t the tangent modulus after plasticity, G the shear modulus of the elastic law, μ the Poisson coeficient and κ the compressibility modulus, and considering a bilinear elasto-plastic model, the hardening modulus h is,

$$h = \frac{E\ E_t}{E - E_t}\ .$$

$\Delta\overline{e}_p$ is the equivalent plastic strain increment,

$$\Delta\overline{e}_p = \frac{\widehat{\Phi}}{3\ G\ +\ h}$$

and,

$$^{\tau+\Delta\tau}_{0}\sigma_y = \ ^{t}\sigma_y\ +\ h\ \Delta\overline{e}_p$$

$$^{\tau+\Delta\tau}\underline{\underline{\Gamma}}_D = \ \widehat{\underline{\underline{\Gamma}}}_D - \sqrt{6}\ G\ \Delta\overline{e}_p\ \frac{\widehat{\underline{\underline{\Gamma}}}_D}{\sqrt{\widehat{\underline{\underline{\Gamma}}}_D : \widehat{\underline{\underline{\Gamma}}}_D}}$$

$$^{\tau+\Delta\tau}_{0}\underline{\underline{X}}_p = \left(e^{\sqrt{\frac{3}{2}}\ \Delta\overline{e}_p\ \frac{\hat{\underline{\underline{\Gamma}}}_D}{\sqrt{\hat{\underline{\underline{\Gamma}}}_D : \hat{\underline{\underline{\Gamma}}}_D}}} \right)\ ^{\tau}_{0}\underline{\underline{X}}_p$$

$$^{\tau+\Delta\tau}_{0}\underline{\underline{C}}_E = (^{\tau+\Delta\tau}_{0}\underline{\underline{X}}_p)^{-T}\ \cdot\ ^{\tau+\Delta\tau}_{0}\underline{\underline{C}}\ \cdot\ (^{\tau+\Delta\tau}_{0}\underline{\underline{X}}_p)^{-1}$$

$$^{\tau+\Delta\tau}_{0}\underline{\underline{U}}_E = \left(^{\tau+\Delta\tau}_{0}\underline{\underline{C}}_E\right)^{\frac{1}{2}}$$

$$^{\tau+\Delta\tau}_{0}\underline{\underline{H}}_E = \ln\left(^{\tau+\Delta\tau}_{0}\underline{\underline{U}}_E\right)$$

We calculate $^{\tau+\Delta\tau}\Gamma^{IJ}$ remembering that in case of asociated von Mises flow rule the hidrostatic stress is only related to the elastic deformations.

$$^{\tau+\Delta\tau}\Gamma^{IJ} = ^{\tau+\Delta\tau}\ \Gamma^{IJ}_{D}\ +\ \kappa\ \ ^{\tau+\Delta\tau}_{0}H_{E,V}\ \ \delta_{IJ}\ \ .$$

6.4.4 Algorithmic consistent tangent constitutive tensor

The fourth order tensor ${}_0\underset{\equiv\equiv\equiv}{C}_{EP}$ is the material elastic consitutive tensor, it is constant for linear elastic behavior and it is a function of the total elastic strain for nonlinear elastic behavior [31].

This algorithm was already presented in [36] and [28], where was derived a tangent constitutive tensor consistent with the radial return algorithm.

$$ {}^{\tau+\Delta\tau}\lambda_{EP} = \frac{3}{2}\,\frac{\Delta\overline{e}_p}{{}^{\tau}_{0}\sigma_y} $$

$$ {}^{\tau+\Delta\tau}\chi_3 = \frac{9\,G\,(1-\frac{2}{3}\,h\,{}^{\tau+\Delta\tau}\lambda_{EP})}{2\,{}^{\tau}_{0}\sigma_y^2\;(3\,G+h)} $$

$$ {}_0\underset{\equiv\equiv\equiv}{C}_{EP}\,|^{(k-1)} = \frac{2\,G}{1+2\,G\,{}^{+\Delta\tau}\lambda_{EP}}\left[\underset{\equiv\equiv\equiv}{I}^{DEV} - {}^{\tau+\Delta\tau}\chi_3\;{}^{\tau+\Delta\tau}\underset{\equiv}{\Gamma}_D|^{(k-1)}\;{}^{\tau+\Delta\tau}\underset{\equiv}{\Gamma}_D|^{(k-1)}\right] + \frac{E}{3\,(1-2\,\upsilon)}\;{}^0\underset{\equiv}{g}\,{}^0\underset{\equiv}{g} \tag{6.103} $$

in the above $\underset{\equiv\equiv\equiv}{I}$ is the fourth order unit tensor,

$$ \underset{\equiv\equiv\equiv}{I} = I_{KLRS}\;\underline{e}_K\underline{e}_L\underline{e}_R\underline{e}_S \quad . $$

The Eq. 6.103 represents the continuum tangential elasto-plastic constitutive tensor. Therefore,

$$ {}_0\underset{\equiv}{\Gamma}^{IJ} = {}_0\underset{\equiv\equiv\equiv}{C}_{EP}\,|^{(k-1)} \;:\; {}_0\underset{\equiv\equiv}{\widehat{H}}^{E}\,|^{(k-1)} \quad . $$

To find the unit tensor components we apply its definition, that is, if we multiply a tensor A by the unit tensor, we obtain the same tensor A.

$$ a_{IJ}\;\underline{e}_I\underline{e}_J = \; I_{KLRS}\;\underline{e}_K\underline{e}_L\underline{e}_R\underline{e}_S\;a_{PQ}\;\underline{e}_P\underline{e}_Q $$

$$ a_{IJ}\;\underline{e}_I\underline{e}_J = \; I_{KLRS}\;a_{PQ}\;\delta_{RP}\;\delta_{SQ}\;\underline{e}_K\underline{e}_L $$

$$a_{IJ}\ \underline{e}_I\underline{e}_J = I_{KLRS}\ a_{RS}\ \underline{e}_K\underline{e}_L$$

$$a_{KL} = I_{KLRS}\ a_{RS}$$

hence,

$$I_{KLRS} = \delta_{KR}\ \delta_{LS}$$

The deviatoric part of the fourth order unit tensor $\underline{\underline{\underline{\underline{I}}}}$ is,

$$\underline{\underline{\underline{\underline{I}}}}^{DEV} = \underline{\underline{\underline{\underline{I}}}} - \frac{1}{3}\ {}^0\underline{\underline{g}}\,{}^0\underline{\underline{g}}$$

$${}^0\underline{\underline{g}}\,{}^0\underline{\underline{g}} = \delta_{KL}\ \underline{e}_K\underline{e}_L\ \delta_{RS}\ \underline{e}_R\underline{e}_S$$

$${}^0\underline{\underline{g}}\,{}^0\underline{\underline{g}} = \delta_{KL}\ \delta_{RS}\ \underline{e}_K\underline{e}_L\underline{e}_R\underline{e}_S$$

$$I^{DEV}_{KLRS} = \delta_{KR}\ \delta_{LS} - \frac{1}{3}\ \delta_{KL}\ \delta_{RS}$$

6.5 Numerical studies

The d.o.f. $(\Delta\lambda_o, \Delta\lambda_1)$ are condensed at the element level and (20x20) element stiffness matrices are obtained and assembled into the global stiffness matrices.

6.5.1 Basic numerical studies

Convergence

The MITC4-3D shell element inherits from the MITC4 element the following properties,

- it does not contain spurious rigid body modes,
- it satisfies Irons' Patch Test.

Conditioning

In order to investigate the conditioning of the MITC4-3D element in Fig. 6.6 we compare, for a very thin element, the conditioning number of the stiffness matrices corresponding to a standard MITC4 element and to the new element. We use the conditioning number defined as [9],

$$cond\ (\underline{K}) = \log_{10} \frac{\Lambda_{\max}}{\Lambda_{\min}} . \tag{6.104}$$

In the above equation,

$\Lambda_{\max}$: maximum eigenvalue of the stiffness matrix,

$\Lambda_{\min}$: minimum non-zero eigenvalue of the stiffness matrix.

The comparison was performed considering the three defined hyperelastic constitutive relations and three different values of the Poisson coefficient. In the case of the MITC4-3D element the eigenvalues correspond to the condensed (20x20) stiffness matrix.

We see that the conditioning number of the MITC4-3D element is only slightly deteriorated in the case of an extreme value of the Poisson coefficient, as compared with the conditioning number of the standard MITC4 element.

6.5.2 Finite strain analyses

Hyperelastic materials

In this subsection we are going to analyze several cases of hyperelastic shells deforming into the finite strain regime.

For each case we consider the three hyperelastic constitutive models described above; hence, the purpose of this section is twofold: the investigation of the numerical performance of the MITC4-3D element formulation and the investigation of the differences in the shell structural responses corresponding to the three material models.

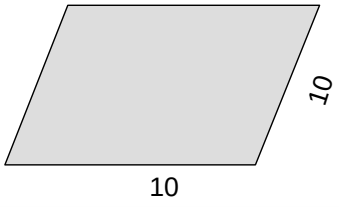

		cond(K)		
		ν=0.0	ν=0.3	ν=0.499
MITC4		7.3	7.3	7.3
MITC4-3D	2nd PK-GL (Hooke)	7.3	7.3	8.1
	Neo-Hookean	7.3	7.3	8.1
	Hencky (Hooke)	7.3	7.3	8.1

Figure 6.6: Conditioning of the MITC4-3D element compared with the conditioning of the MITC4 element

Cantilever under constant moment In Fig. 6.7 we present the results for an elastic cantilever with $(L/a) = 100$, $E = 1.2E^{07}$ and $\nu = 0.0$.

We get the same result for the three considered material models because the strains developed in the cantilever beam are only moderately high.

Cantilever under tip load In Fig. 6.8 we present the results for the tip vertical displacement of an elastic cantilever with $(L/a) = 10$, $E = 1.2E^{07}$ and $\nu = 0.3$.

Regarding the equilibrium path we get the same result for the three material models considered. In Fig. 6.9 we present the results for $({}^{\tau}\lambda_o,\ {}^{\tau}\lambda_1)$ and in this case the results corresponding to the first constitutive relation are only slightly different from the results corresponding to the other two constitutive relations.

Again the reason for these very similar responses lies in the fact that the strains developed in the cantilever beam are only moderately high.

Infinitely long cylinder under internal pressure We consider the infinite cylinder represented in Fig. 6.10 under internal pressure. In the same figure we represent

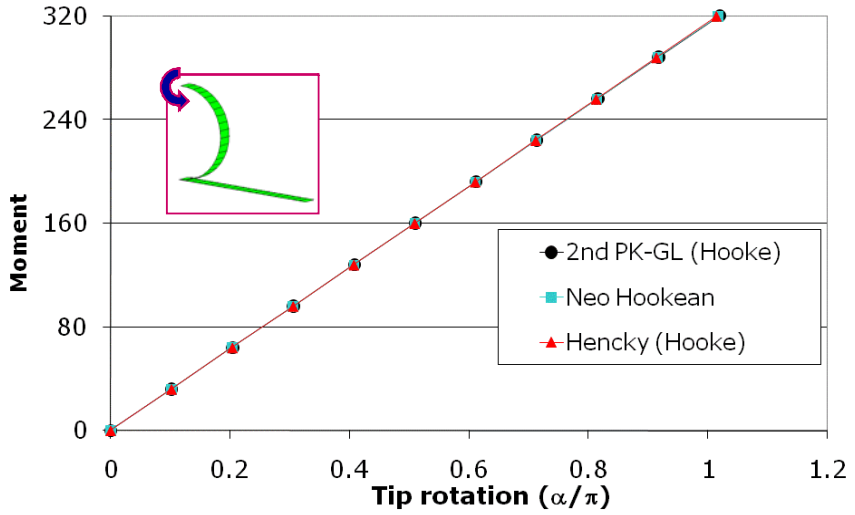

Figure 6.7: Elastic cantilever under constant moment $(L/a) = 100$

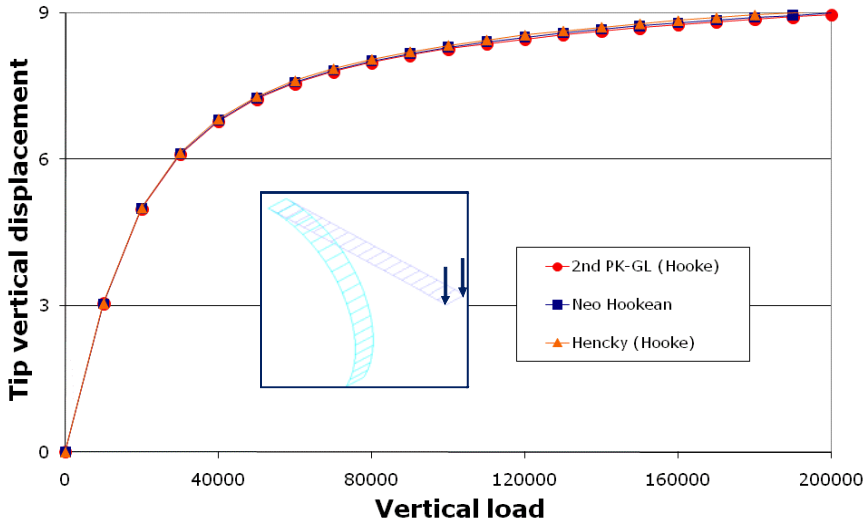

Figure 6.8: Vertical displacement of a cantilever under tip load $(L/a) = 10$

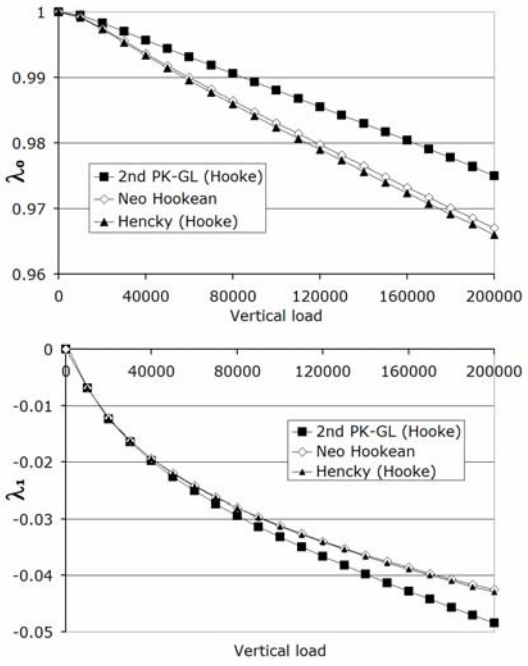

Figure 6.9: Cantilever under tip load $(L/a) = 10$. Through-the-thickness stretching in the element at the fixed boundary

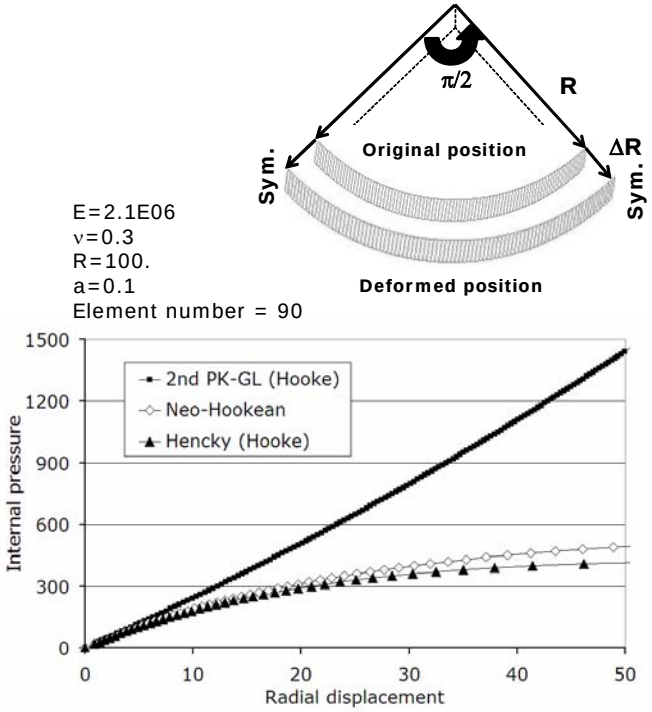

Figure 6.10: Infinite cylinder under internal pressure

the equilibrium paths obtained for the infinitely long cylinder considering the three hyperelastic constitutive models discussed above. The strains developed in the cylinder wall are quite high; hence, the equilibrium paths are quite different, in particular the one corresponding to the first hyperelastic model.

Finally in Fig. 6.11 we present the predictions of the through-the-thickness stretching obtained with the three models considering two different values of the Poisson coefficient. Again the higher the strains the larger the difference between the structural responses predicted using the first constitutive model and the structural response predicted using any of the other two models.

Sphere under internal pressure For the analysis of a sphere under internal pressure we consider two cases; a thick and a thin sphere, as it is shown in Fig. 6.12. For symmetry reasons only one eight of the shell is modeled.

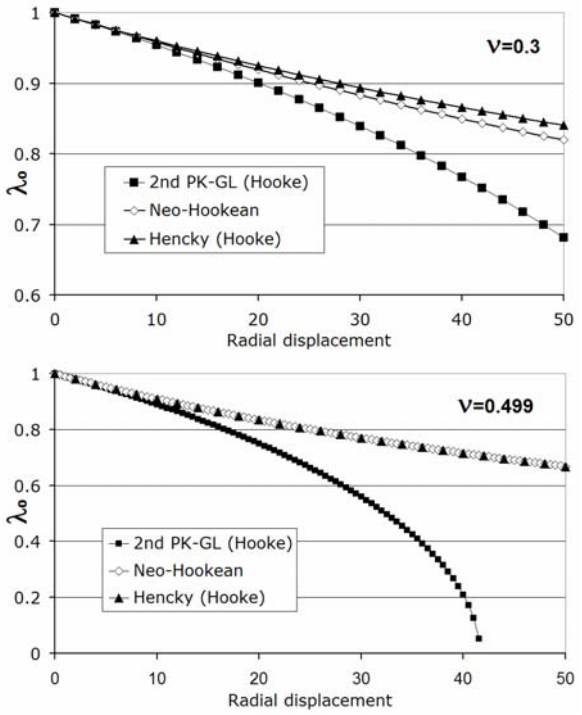

Figure 6.11: Infinitely long cylinder. Through-the-thickness stretching

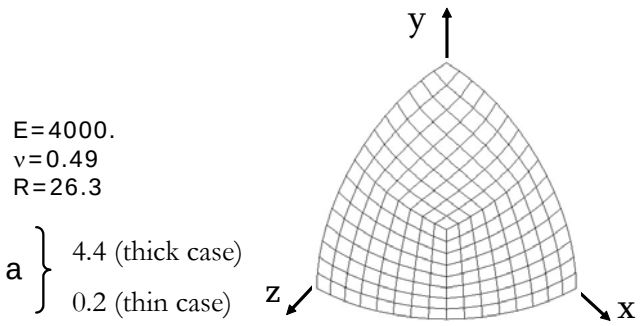

Figure 6.12: Sphere under internal pressure

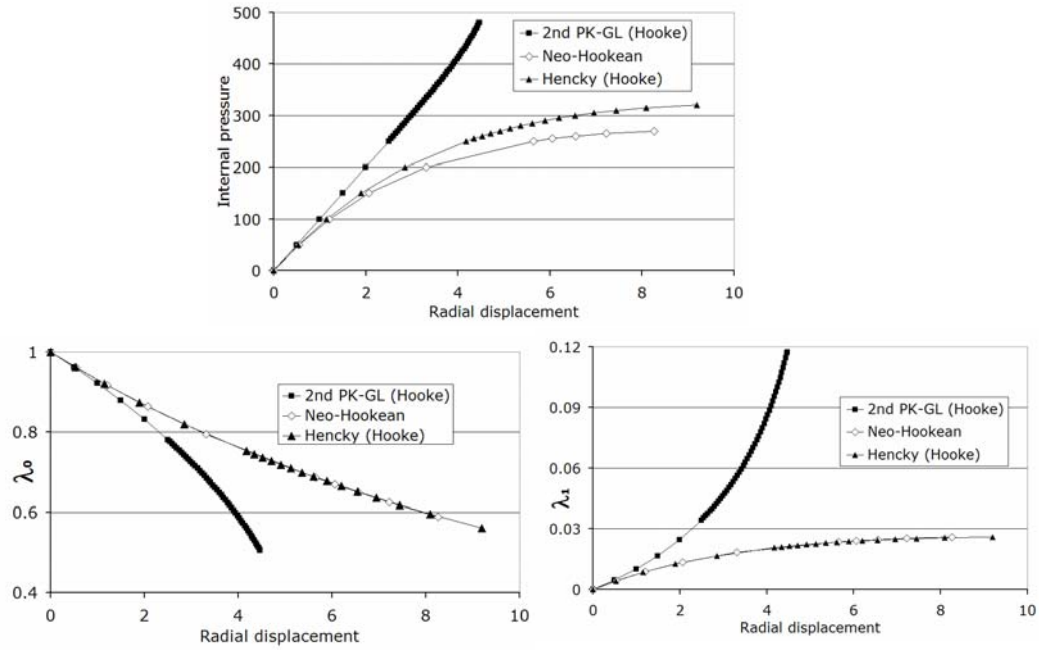

Figure 6.13: Sphere under internal pressure - thick case

In Fig. 6.13 we present the results corresponding to the thick case; again, the first material model provides results that are quite different from the results provided by the other two material models.

In Fig. 6.14 we present the results corresponding to the thin case and the comment related to the behavior of the material constitutive models is again the same.

Notice that, as we should expect, when the thickness decreases $\lambda_1 \to 0$.

Twisted ribbon For the two load cases represented in Fig. 6.15, in which the resulting strains are only moderate, the load displacements are identical considering the three material models.

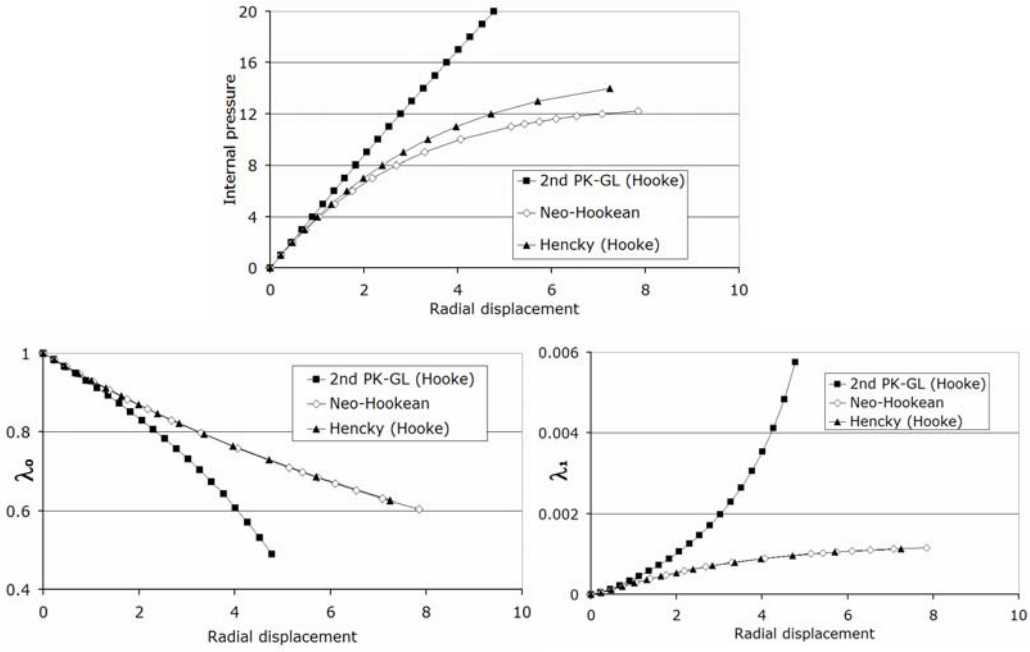

Figure 6.14: Sphere under internal pressure - thin case

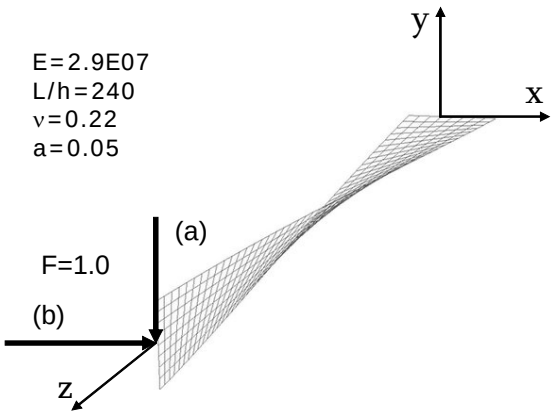

Case	Hooke w/ G.L.	Neo-Hookean	Hooke w/ Hencky
(a)	1.3675	1.3675	1.3675
(b)	0.3428	0.3428	0.3428

Figure 6.15: Twisted ribbon considering two load cases. Loaded point displacements

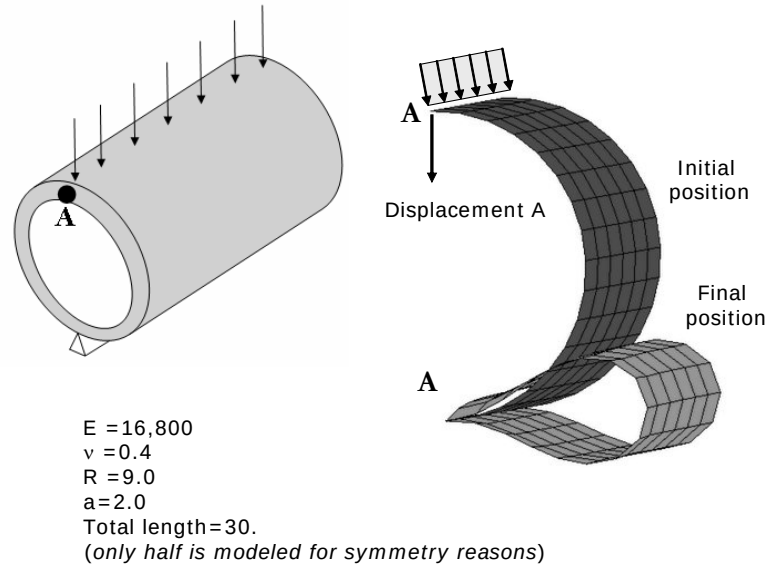

Figure 6.16: Cylinder under line load

Cylinder under line load In Fig. 6.16 we describe the analyzed case.

In Figs. 6.17 and 6.18 we present the results obtained, for the three different hyperelastic constitutive relations.

Pinched hemispherical shell This case, depicted in Fig. 6.19, was used as a test case in many previous publications (e.g. [69]). It is a shell element with two opposite polar holes spanning a latitude of 18° each; for symmetry reasons only one eight of the shell is modeled.

The results obtained with the MITC4-3D element and the above described constitutive relations, using two different meshes, are presented in Fig. 6.20.

In this case the results corresponding to the three constitutive models converge to almost the same result when the mesh is refined.

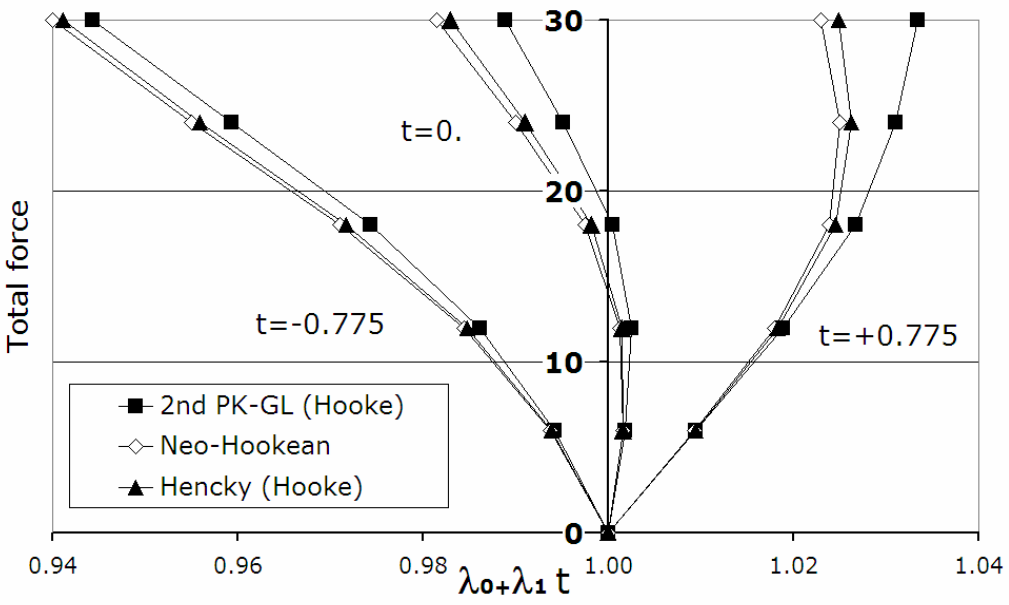

Figure 6.17: Thickness stretching at different depths for the element containing node A

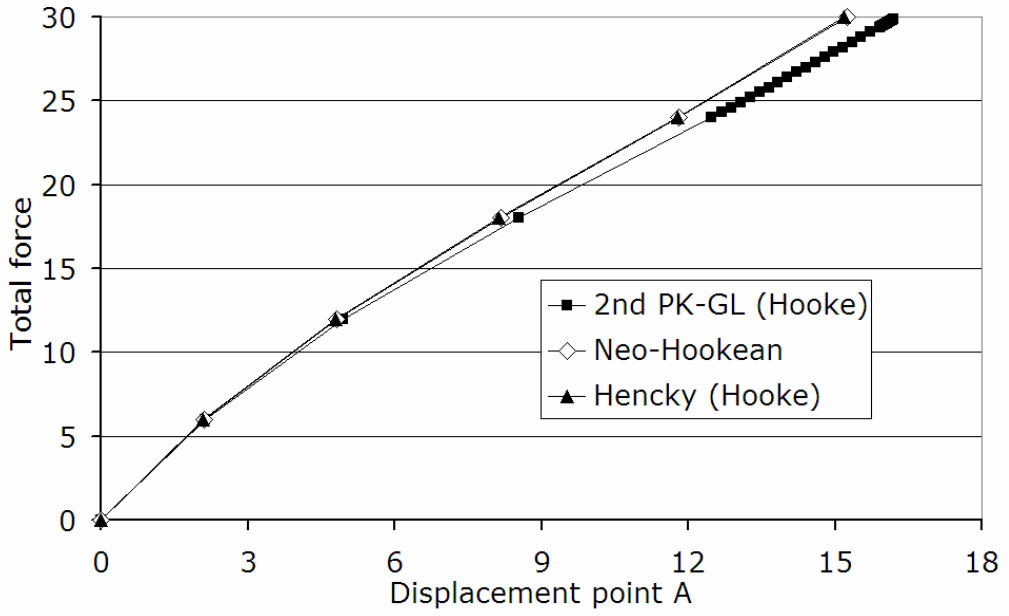

Figure 6.18: Load - displacement curves for the cylinder under line load

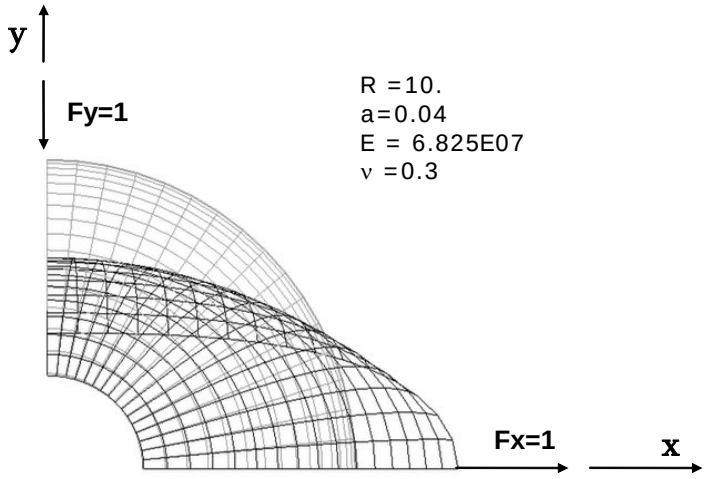

Figure 6.19: Pinched spherical shell with a 18° top hole

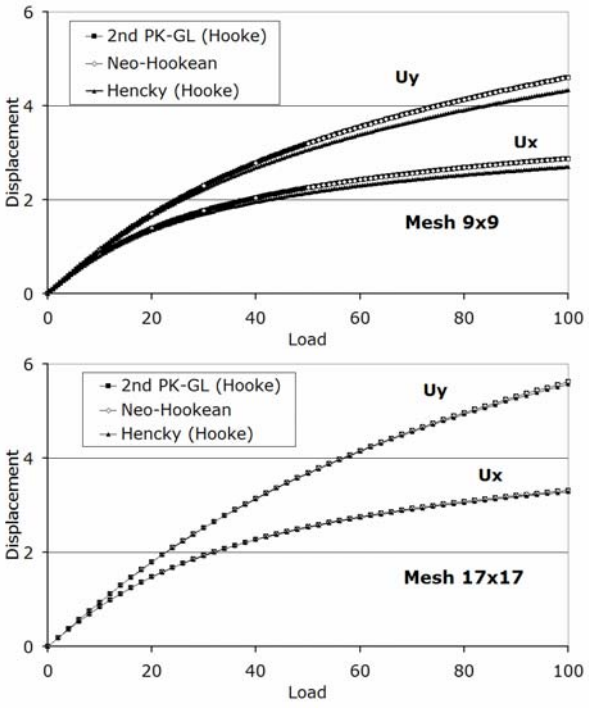

Figure 6.20: Pinched spherical shell results

Elasto-plastic material

In this subsection we are going to analyze several cases of elasto-plastic shells deforming into the finite strain regime [80].

We have validated the new MITC4-3D element comparing its results and iterative behavior with an implementation of the MITC4 element in which the thickness is updated a posteriori of each iteration.

Large membrane strains in an elasto-plastic panel In Fig. 6.21 we present a case of large membrane strains. For this problem $E = 2.1\ 10^{+06}$, $E_t = 2100$, $\nu = 0.3$, $a = 0.1$, $\sigma_y = 2100$.

Imposed displacements were applied. The Figure shows the mesh, the load P and the thickness stretching. We compare the results obtained with MITC4-3D with those obtained with the MITC4 element with a posteriori thickness update. The coincidence in the results is perfect.

Inflation of an infinitely long elasto-plastic cylinder under internal pressure We consider the infinite cylinder represented in Fig. 6.22 under internal pressure. For this problem $E = 2.1\ 10^{+06}$, $E_t = 2100$, $\nu = 0.3$, $a = 0.1$, $\sigma_y = 2100$,and the cylinder radious is 100. Radial displacements were applied. The Figure shows the equilibrium path calculated with both elements, MITC4-3D and MITC4 with a posteriori thickness update, and the thickness stretching vs radial displacement curve. Regarding the equilibrium path, the coincidence is perfect.

Elasto-plastic cantilever beam under tip load In Fig. 6.23 we show the results for the tip vertical displacement of an elasto-plastic cantilever with $(L/a) = 100$, $E = 1.2\ 10^{+07}$, $E = 1.2\ 10^{+05}$, $\nu = 0.3$ and $\sigma_y = 2.4\ 10^{+04}$.

Regarding the equilibrium path we obtained similar results for both formulations, MITC4-3D and MITC4 with a posteriori thickness update.

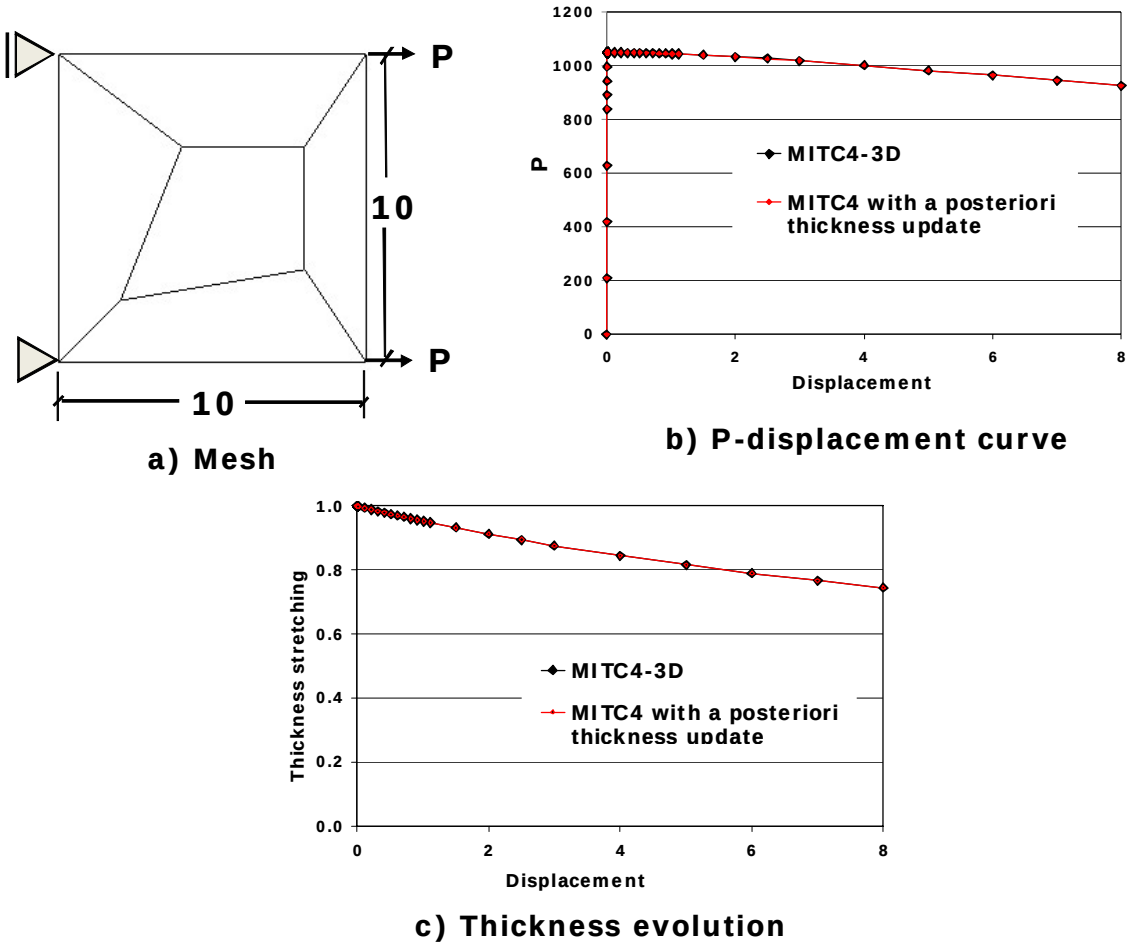

Figure 6.21: Elasto-plastic panel.

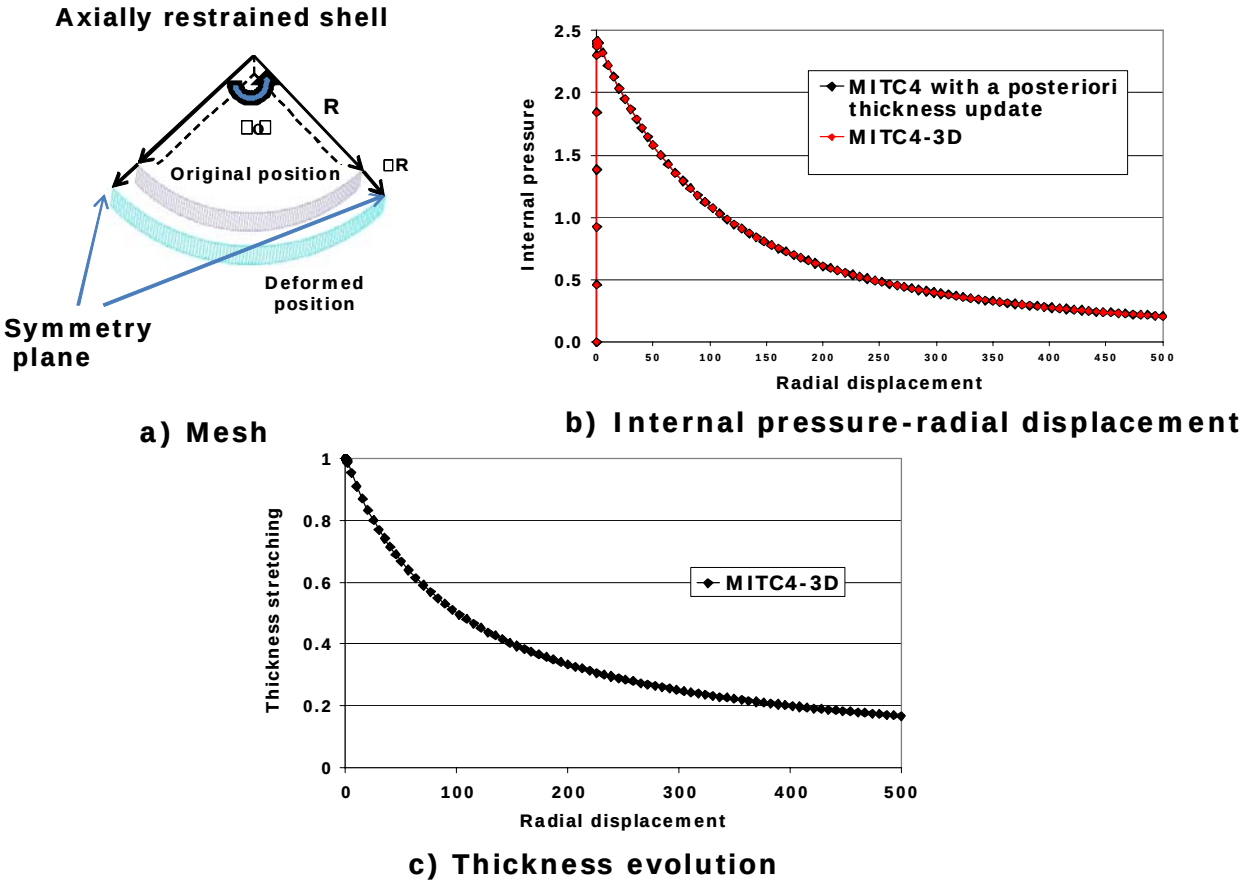

Figure 6.22: Inflation of an infinitely long elasto-plastic cylinder

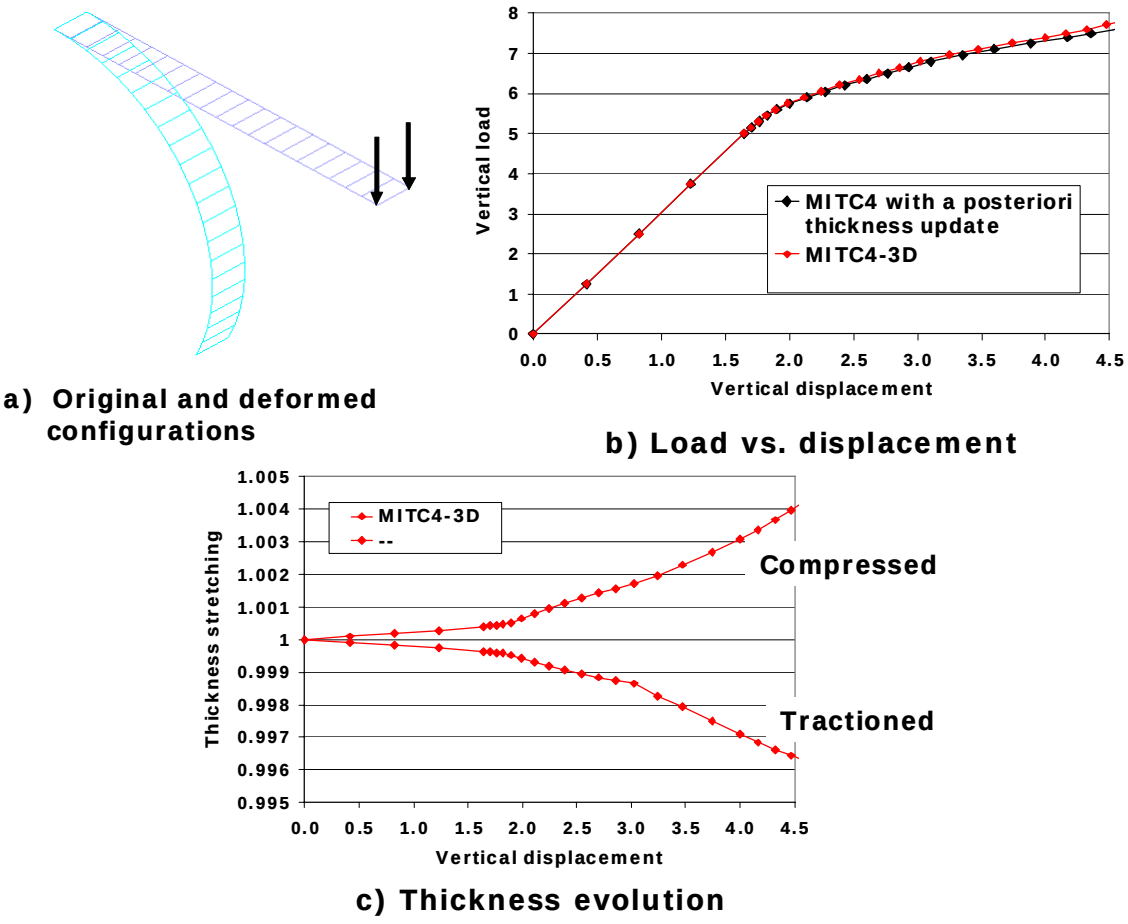

Figure 6.23: Elasto-plastic cantilever beam under tip load

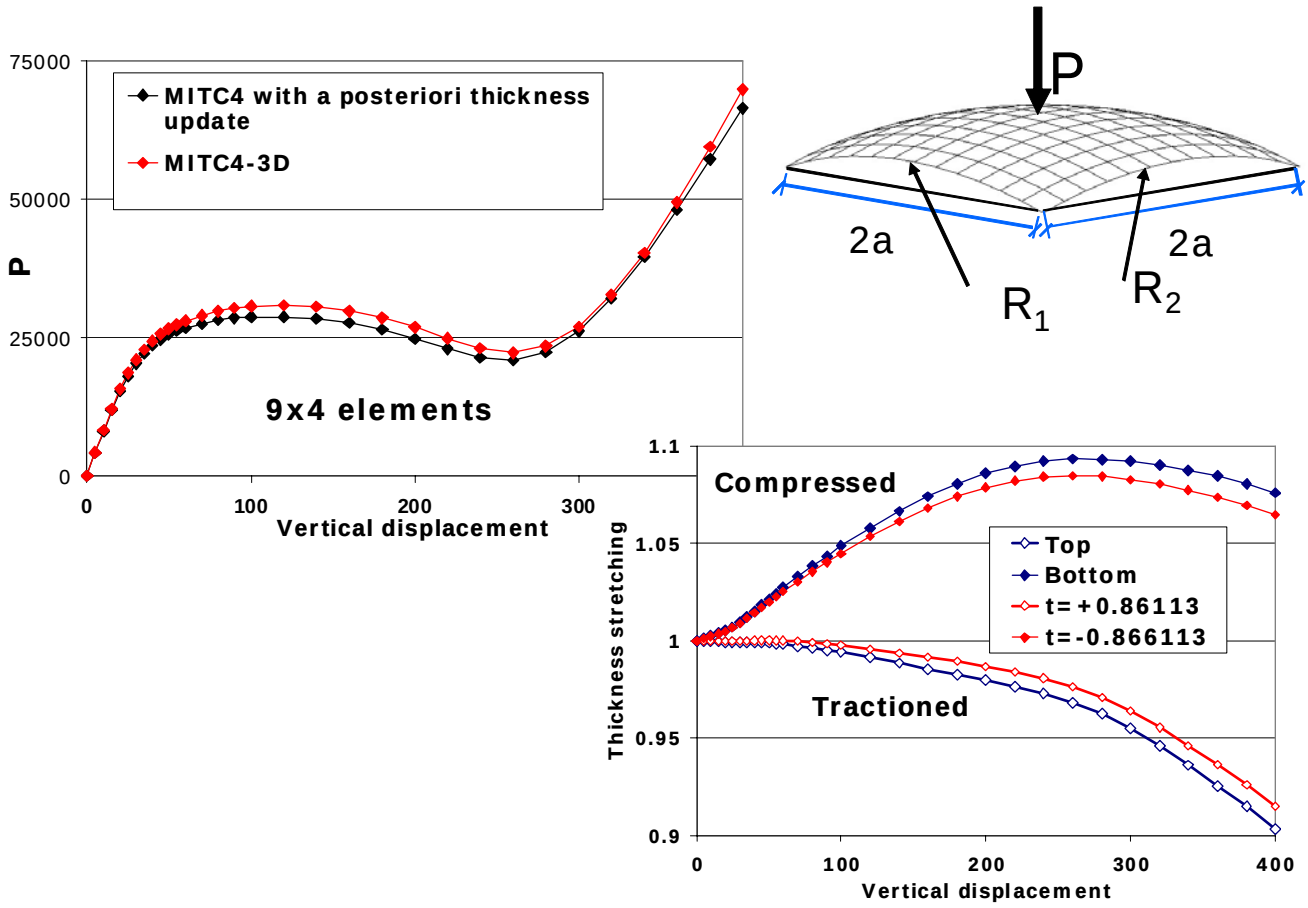

Figure 6.24: Spherical shell, vertical load vs. vertical displacement, and through the thickness stretching at the element closest to the center.

Spherical shell For the analysis of a sphere under a concentrated load we use a 3x3 mesh for one quarter of the shell, as it is shown in Fig.6.24 The main characteristics of the shell are: $E = 68,95$, $E_t = 6$, $\nu = 0.3$, $\sigma_y = 0,9$, $R1 = R2 = 2540$ and $a = 784,9$. The same figure shows the curve Vertical load vs Vertical displacement at the center of the shell and the through the thickness stretching vs. vertical displacement at the element closest to the center, at top and bottom, and at coordiante t=$\pm$0.86113.

In Fig. 6.25 we compare the numerical efficiency of the MITC4-3D with that of the MITC4 with a posteriori thickness update element. We can observe that the iterations

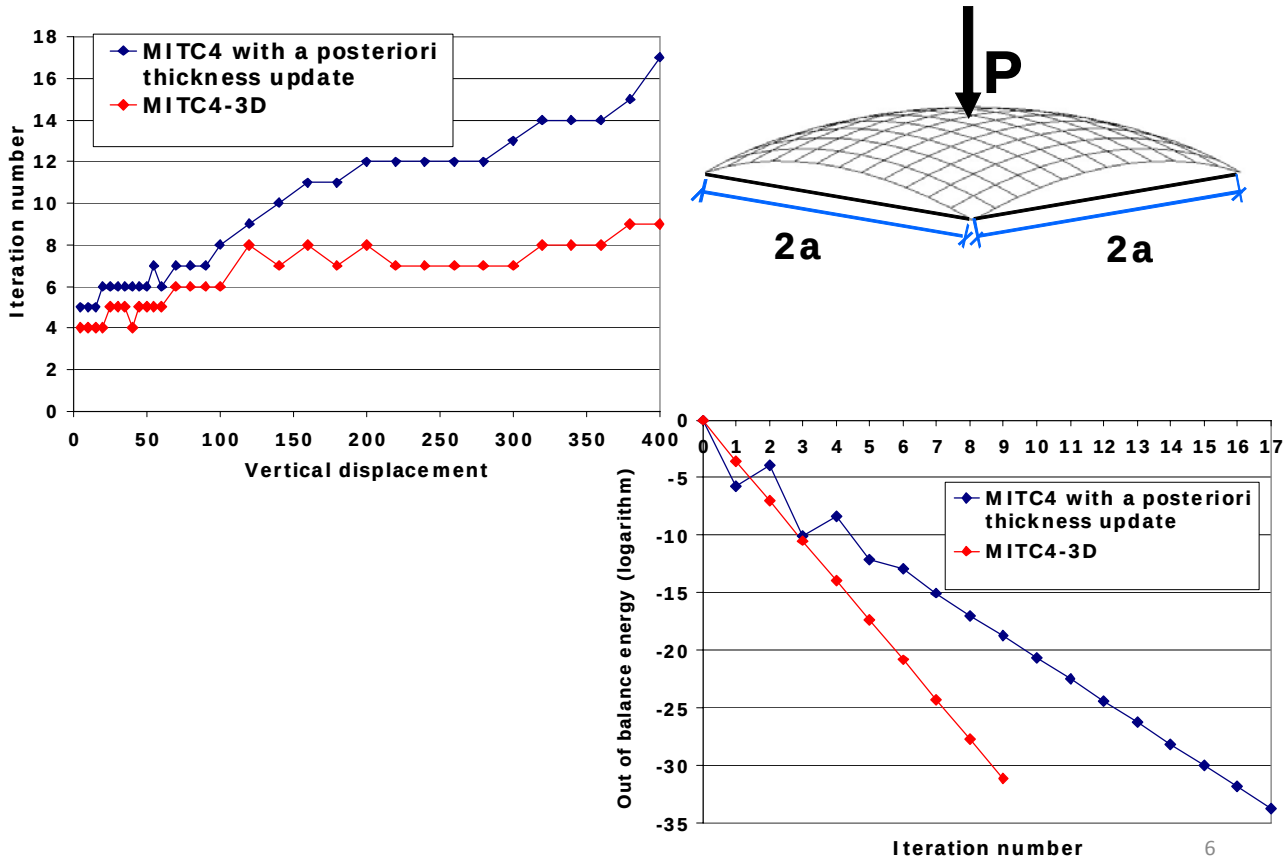

Figure 6.25: Spherical shell: numerical efficiency study

number for the new element is much lower than for the previous one. The second graph shows the logarithmic values of the out of balance energy for each iteration of the last step for both elements. For the MITC4-3D the out of balance energy decreases more abruptly than for the other element. From those graphs it can be drawn thet the new element is more efficient, and this was our main objetive to develop it.

Pipe: external collapse pressure In this case, we analyze the behavior of a pipe under external pressure. The material properties are: $E = 21000kg/mm^2$, $E_t = 86kg/mm^2$, $\nu = 0.3$ and $\sigma_y = 54,75kg/mm^2$. Regarding the geometry of the pipe, the external diameter is $341,5mm$, the thicknes $a = 17,65mm$ and the ovality $\frac{D_{\max}-D_{\min}}{D_{average}} = 0,47\%$. Figure 6.26 shows the pipe after some collapse propagation; the red

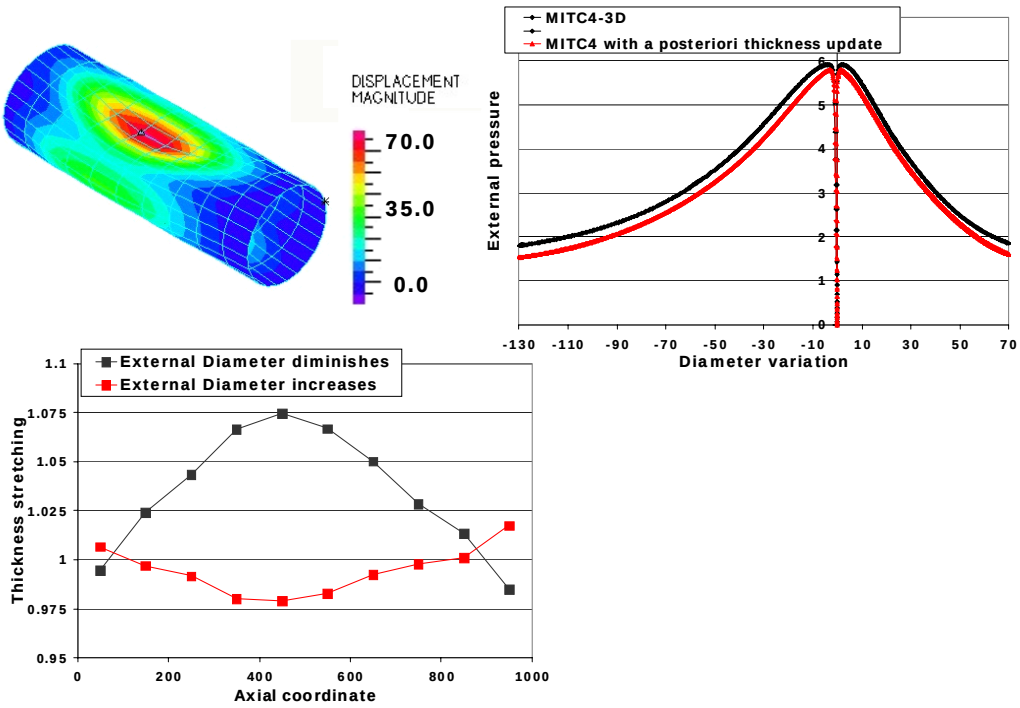

Figure 6.26: Pipe: external collapse pressure

area corresponds to diameter diminish while the lateral green area correponds to diameter increase. The Figure also shows the curves External pressure vs. diameter variation, for both elements. It can be observed that the results are very similar. The curves Thickness stretching vs. Axial coordinates for element lines corresponding to diameters that increase and to diameters that decrease are also presented.

The Figure 6.27 compares the *iterations number vs. diameter variation* for MITC4-3D vs MITC4 with a posteriori thickness update. As we observed in the previos example, the new element shows a much better efficiency.

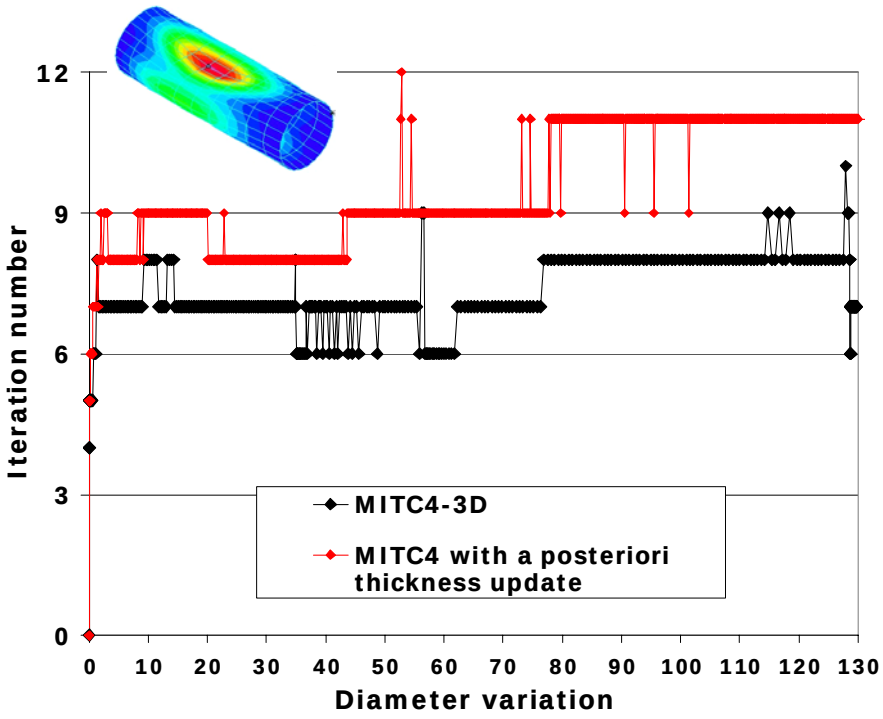

Figure 6.27: Pipe: efficiency analysis

6.6 Main observations

A new shell element, MITC4-3D, with elasto-plastic finite strains and based in the MITC4 formulation was implemented for the analyses of elasto-plastic shell structures. The results indicate that it is a very effective element.

Chapter 7

Conclusions

Establishing manufacturing tolerances for steel pipes to be used in pipelines, such as amplitude of the out-of-roundness specially its second mode in a Fourier decomposition, eccentricity, residual stresses, etc. is an involved issue that should balance production cost with expected performance.

Finite element models are nowadays a relevant tool for exploring the effect of those tolerances on the collapse and propagation pressure of tubular goods and to study the technological windows (the locus in the space of the process control variables that defines a given process set-up) of the production process of the pipes that will render products within the expected tolerances.

Since technological decisions, with high influence on the ecological impact of industrial facilities and pipeline installations, on labor conditions and on revenues, are reached based on the results provided by numerical models, it is evident that these models have to be highly reliable. Therefore, it is of the utmost importance that sound computational mechanics formulations are used and that the model results are subjected to experimental validation.

In this thesis we proposed some guidelines for the development of finite element models that provide the link between manufacturing tolerances and performance predictions.

Some of the aspects that we discussed are,

- the usage of 2D and 3D models,
- the usage of shell elements,
- long vs. short models,
- nonlinearities to be included in the models,
- follower loads,
- material modeling,
- modeling of residual stresses,
- code verification and validation of the results.

Regarding the link between production process and manufacturing tolerances, we discussed some results that we obtained for the UOE process.

7.1 Model definitions

We discussed which model is the most adequate to investigate the effect of manufacturing tolerances on the collapse and post-collapse behavior of steel pipes.

7.1.1 The usage of 2D and 3D models

Material properties, residual stresses and pipe dimensions like eccentricity, out-of roundness, thickness, etc. vary along the length of a given pipe.

When the collapse behavior of a specific pipe is investigated, a 3D model that incorporates a detailed geometrical and material description needs to be developed.

However, we may also need to perform parametric studies to investigate the effect of manufacturing tolerances on the collapse and propagation pressures; in these cases we consider an infinite pipe with uniform properties along its length and we use a 2D

plane strain model built using continuum elements or 3D short shell models, if we need to include bending in the analysis.

In Section 2.2 we described the model we developed using 2D continuum elements QMITC. This model was very useful to study the effect of ovality, eccentricity and residual stresses on the external collapse pressure. To assess on the quality of the mesh we analyzed the plane strain collapse of an infinite pipe and we compared our numerical results with the analytical results obtained using the theoretical formulas. The comparison showed that the proposed 2D mesh of QMITC elements is accurate enough to represent the collapse of very long specimens.

The ovality is considered to be concentrated in the shape corresponding to the first elastic buckling mode and the eccentricity is modeled considering non-coincident OD and ID centers.

For the range of (D/t) values that are relevant for pipelines, we can model the collapse and post-collapse behavior of the pipes using shell elements. In particular we selected a shell element that is free from the locking problem: the MITC4 element. In the code ADINA this element was implemented improving its in-surface behavior via incompatible modes.

In Section 2.3, to include bending in the analyses, we developed a numerical model to simulate the behavior of a very long tube (infinite tube) and determine its pre and post-collapse equilibrium path. Using this model we performed parametric studies in order to investigate the significance of the different geometrical imperfections and of the residual stresses on the collapse and collapse propagation pressures.

For the cases with external pressure plus bending we first imposed the bending and then the external pressure keeping constant the imposed curvature.

The 3D finite element models of finite pipes were developed to overcome the limitations of the simpler models described previously.

It is important to take into account that when the sample is long enough $(L/D > 10)$ the end conditions have only a very small influence on the collapse pressure.

7.1.2 Nonlinearities

It is also necessary to decide on the nonlinearities that we must include in our finite element models to be able to predict the collapse of steel pipes under external pressure and to track their post-collapse behavior.

Since we need to predict collapse, we have to use a geometrically nonlinear analysis considering large displacements/rotations, that is to say we have to fulfill the equilibrium equations in the deformed configuration. As it was demonstrated in Section 4.4, even if very high strains are developed at localized points, the general behavior of the post-collapse response can be determined without including in the analyses finite strain models.

In the range of (OD/t) values that are within our scope, the collapse is an elastic-plastic collapse, that is to say plasticity is developed before and after collapse; hence the material nonlinearity has to be included in the analysis.

To track the collapse and post-collapse response of the pipes we use an algorithm that iterates in the load-displacement space.

7.1.3 Follower loads

It is important to consider follower loads to model the effect of the external hydrostatic pressure, since the consideration of fixed-direction loads results in important errors when predicting collapse pressures.

7.1.4 Material modeling

In our models we use von Mises associated elasto-plastic material models with isotropic hardening. We model the hardening using bilinear or multi-lineal models. Even though it is clear that more sophisticated hardening models can be used, this very simple model has been very successful in the prediction of collapse and post collapse pipe behaviors, as it was shown in Chapters 3 and 4.

7.1.5 Modeling of residual stresses

In most of our analyses we considered a linear residual stresses distribution across the pipe wall thickness. In Section 2.4 we checked the modeling of the residual stresses distribution by modeling a slit ring test using the ADINA "element birth and death" feature.

7.1.6 Code verification and model validation

In the verification process we have to prove that we are solving the equations right, and therefore this is a mathematical step [65]. In this step we have to show that our numerical scheme is convergent and stable.

It is important to notice that the verification process is not only related to a numerical procedure but also to its actual implementation in software (either commercial software or an in-house one) [65].

In the validation process we have to prove that we are solving the right equations, and therefore it is an engineering step [65].

We do validate neither a formulation nor software: we validate the usage of verified software when used by a design analyst in the simulation of a specific process. We have to validate the complete procedure.

In Chapter 3 we developed a complete validation of the collapse and post-collapse analyses of pipes under external pressure plus bending while in Chapter 4 we validated the analysis of pipes with collapse arrestors under external pressure only. Regarding the latter case, the numerical results not only match the experimental values of collapse pressure, collapse propagation pressure and cross-over pressure but also the cross-over collapse modes, flattening and flipping.

7.2 The UOE process

In Chapter 5 we simulated the UOE forming process of the pipes using a 2D finite element model, developed with ADINA.

The UOE process introduces accumulated plastic strains and residual stresses; to evaluate their effect on the result of the forming model we modeled a collapse test. We also performed parametric analyses, in order to study the influence of the tooling on the final shape and strength of the welded pipes.

Summarizing, a methodology for using the finite element method as a robust engineering tool for analyzing the effect of the manufacturing tolerance on the collapse and post collapse behavior of steel pipes was discussed and illustrated with practical examples.

7.3 New shell finite strain element MITC4-3D

Even though the matching between numerical and experimental results was excellent, the model results showed high strains in some areas of the collapsed pipes. Therefore, we developed a new shell element, MITC4-3D, with elasto-plastic finite strains, based in the MITC4 formulation. It was implemented for the analyses of elasto-plastic shell structures and the results indicate that it is a very effective element.

Appendix A

Imperfections Measuring System

The Imperfections Measuring System (IMS) or shapemeter (Fig. A.1), developed at Tenaris Siderca lab on the basis of previous publications by Arbocz and co-workers [3] [4] [89], has been used to survey pipe geometry and then analyze their collapse pressure. The information provided by the IMS proved to be very valuable to assess on the collapse resistance of pipes.

A.1 Mapping of the sample's external surface

To map the external surface of a sample we rotate it in a lathe and at regular intervals of time, radial and angular positions are sent to an acquisition system (Fig. A.1). The position of the pipe surface is recorded from a linear variable displacement transducer (LVDT). A rotary encoder placed on the rotation axis provides the angular position.

We developed an algorithm to transform the acquired data into the Fourier series description of the samples external surface [6].

Figure A.1: The IMS (or shapemeter)

A.1.1 Algorithm to process the data acquired with the imperfections measuring system

The data are acquired along a spiral path; however, in subsequent analyses we will consider that the points corresponding to a turn are located on a planar section, at an axial distance z_k from an arbitrary origin. As the pitch of the spiral is less than half of the typical wall thickness under analysis, this assumption is valid for the purpose of modelling the collapse test.

The data are fitted to a perfect circle (of unknown center and radius) through a least squares method [89]. This approach is consistent with the subsequent Fourier decomposition (see Fig. A.2).

Input data r_j: radial distance from the rotation axis to the external surface, j^{th} data point.

q_j: total turns corresponding to the j^{th} data point, measured from an arbitrary defined zero.

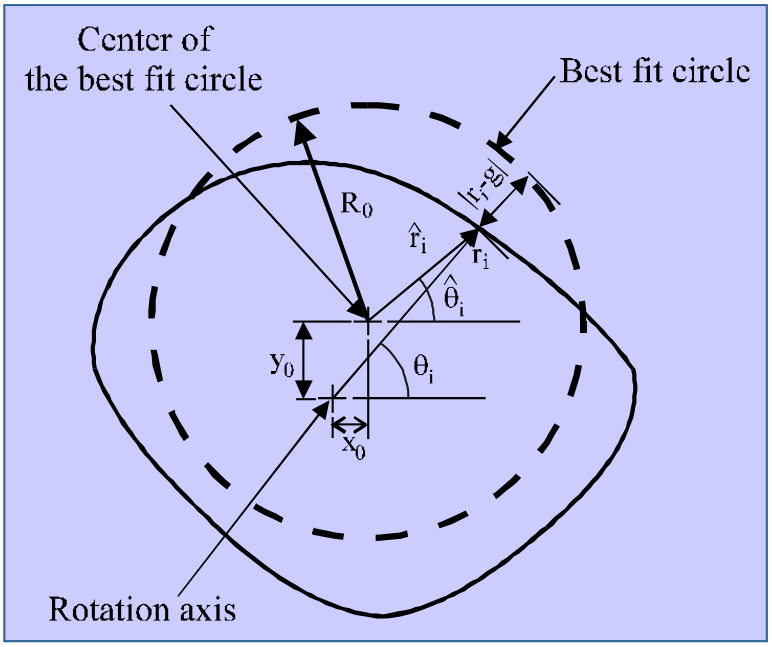

Figure A.2: Algorithm to process the data acquired with the LVDT

Algorithm

Initial data reduction We can define,

$$k = int(q_j) \tag{A.1}$$

the k^{th} turn. For this turn we have,

$$\begin{aligned} z_k &= \Delta z \; int(q_j) \\ \theta_i^k &= 2\pi \; (q_j - int(q_j)) \\ r_i^k &= r_j \end{aligned} \tag{A.2}$$

where $i = 1$ for the first j which satisfies $(q_j - int(q_j)) > 0$ (indication of a new turn). Δz indicates the axial advance per turn. The number of data points per turn is not constant.

Fit to best circle For the k^{th} section we can define a "best-fit circle", with radius R_0 and with its center located at (xo, yo) in a Cartesian system, contained in the section plane and with its origin at the section rotation center [89]. The superindex k in θ_i^k and r_i^k is omitted.

For determining R_0, x_0 and y_0 we solve the following minimization problem,

$$\begin{aligned} (R_0, x_0, y_0) &= arg[minE_2(R_0, x_0, y_0)] \\ E_2 &= \sum_i \left[r_i - g\left(\theta_i, R_0, x_0, y_0\right)\right]^2 \\ g\left(\theta_i, R_0, x_0, y_0\right) &= \left(x_0\ \cos\theta_i\ +\ y_0\ \sin\theta_i\right)\ +\ \sqrt{R_0^2 - \left(x_0\ \sin\theta_i\ -\ y_0\ \cos\theta_i\right)^2} \end{aligned} \tag{A.3}$$

To solve the above nonlinear minimization problem we apply the Levemberg-Marquard method [63], using as first trial a simplified (linearized) solution in which the expression for g reduces to [67],

$$g_{lin}\left(\theta_i, R_0, x_0, y_0\right) = \left(x_0\ \cos\theta_i\ +\ y_0\ \sin\theta_i\right)\ +\ R_0 \tag{A.4}$$

Data reduction to new center Once the center of the "best-fit circle" is determined we reduce the acquired data to it,

$$\begin{aligned} \widehat{x}_i &= r_i\ \cos\theta_i\ -\ x_0 \\ \widehat{y}_i &= r_i\ \sin\theta_i\ -\ y_0 \\ \widehat{r}_i &= \sqrt{\widehat{x}_i^2 + \widehat{y}_i^2} \\ \widehat{\theta}_i &= \tan^{-1}\left(\frac{\widehat{y}_i}{\widehat{x}_i}\right) \end{aligned} \tag{A.5}$$

Fourier transform We expand using a discrete Fourier transform,

$$\widehat{a}_j = \frac{1}{\pi} \sum_{k=1}^{M} \left[\widehat{r}_k \cos\left(j\, \widehat{\theta}_k\right) \Delta\widehat{\theta}_k \right] \tag{A.6}$$

$$\widehat{b}_j = \frac{1}{\pi} \sum_{k=1}^{M} \left[\widehat{r}_k \sin\left(j\, \widehat{\theta}_k\right) \Delta\widehat{\theta}_k \right]$$

where M is the number of samples taken in each turn (360 on average).

Shape reconstruction

$$\widehat{r}\,(\theta) = R_0 + \sum_{j=1}^{N} \left[\widehat{a}_j \cos(j\,\theta) + \widehat{b}_j \sin(j\,\theta) \right] \tag{A.7}$$

where N is the number of modes used in the reconstruction of the shape.

Sampling theorems [17] put a limit on the maximum value of N that can be used (in our case $N < \frac{M}{2} \simeq 180$, tipically 50). For practical purposes we define the amplitude of the j mode of the Fourier decomposition as,

$$A_j = \sqrt{\widehat{a}_j^2 + \widehat{b}_j^2}. \tag{A.8}$$

A.2 Deepwater pipelines. Measurements.

The scope of this Section is the geometrical survey of the 9 samples of the tests described in Chapter 3. The geometrical survey is composed by the mapping of the external surface and the measurement of the wall thicknesses.

The results of the topography mapping of the external surface, the modal analysis of the circular deviations and the wall thicknes are analyzed. The samples belong to two different mills.

The results of the geometrical mapping of 9 samples of Tenaris pipes are presented. Each group of 3 samples was obtained from 2 pipes (Figure A.3).

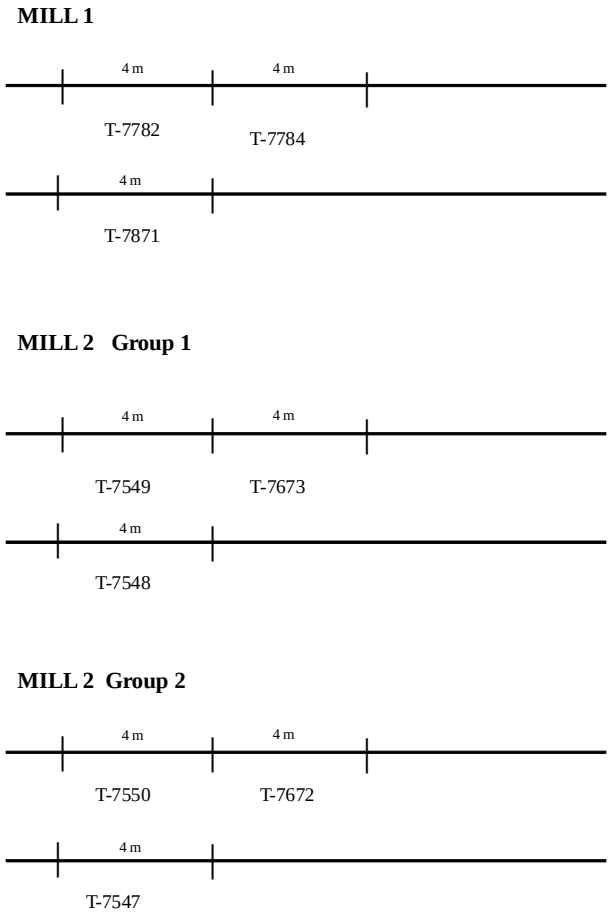

Figure A.3: Sample distribution

A.2.1 Pipe data

Table 1 summarizes the main characteristics of the samples.

Sample	*Mill*	*OD*	*t*	*Position*	*Grade*	*Tenaris_ID*
		[*mm*]	[*mm*]			
1	*MILL*1	353.00	22.00	*extreme*	*X*65	$T-7782$
2	*MILL*1	353.00	22.00	*middle*	*X*65	$T-7784$
3	*MILL*1	353.00	22.00	*alone*	*X*65	$T-7871$
4	*MILL*2	323.85	17.65	*extreme*	*X*65	$T-7549$
5	*MILL*2	323.85	17.65	*middle*	*X*65	$T-7673$
6	*MILL*2	323.85	17.65	*alone*	*X*65	$T-7548$
7	*MILL*2	323.85	20.30	*extreme*	*X*65	$T-7550$
8	*MILL*2	323.85	20.30	*middle*	*X*65	$T-7672$
9	*MILL*2	323.85	20.30	*alone*	*X*65	$T-7547$

Table 1. Samples description

A.2.2 Pipe Survey

Fourier analysis of the circular deviations Figure A.4 shows, for Mill 1's samples, the Fourier series decomposition of the deviations with respect to the average diameter.

Wall thickness

The specimens are 4 meters long. The grid has 48 longitudinal sections with a 75 mm spacing, and 16 circumferential generatrices, giving 768 grid points.

The pipe wall thicknesses have been obtained with a manual ultrasonic gage at each grid point. Figure A.5 shows the 3-D representation for the Mill 1's samples.

A brief statistic calculation is synthesized in Table 2.

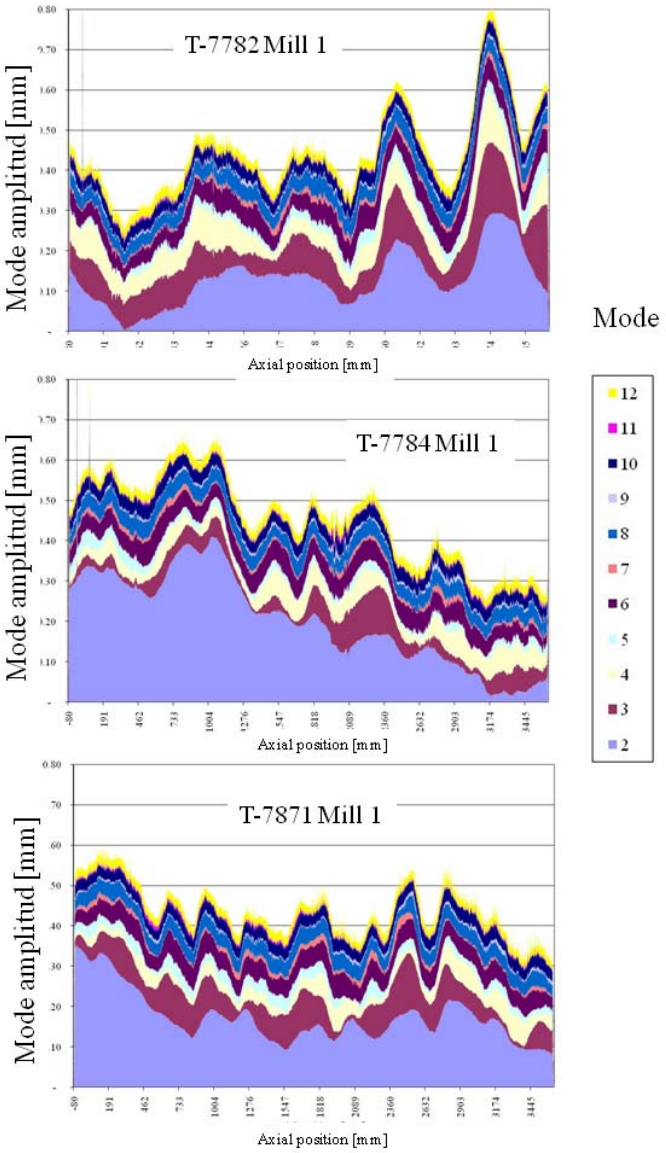

Figure A.4: Mill 1: Modal analysis: mode amplitude distribution along the sample

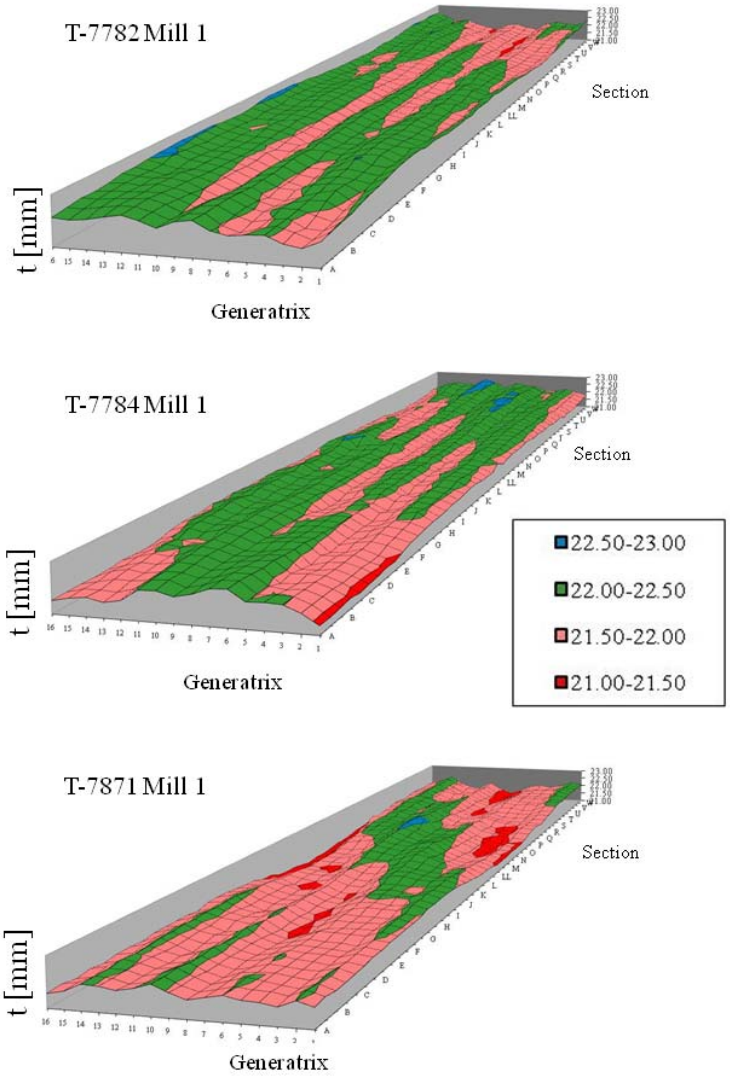

Figure A.5: Mill 1, wall thickness distribution

Sample	*Mill*	*LabID*	t_{nom}	$t_{average}$	*t std dev*	$\varepsilon_{\max}$	*Section*
			$[mm]$	$[mm]$	$[mm]$	$[\%]$	
1	$Mill1$	$T-7782$	22.00	22.07	0.24	5.32	ST
2	$Mill1$	$T-7784$	22.00	22.04	0.24	5.05	AB
3	$Mill1$	$T-7871$	22.00	21.84	0.26	6.86	O
4	$Mill2$	$T-7549$	17.65	18.37	0.36	9.75	R
5	$Mill2$	$T-7673$	17.65	18.32	0.23	6.74	F
6	$Mill2$	$T-7548$	17.65	18.18	0.19	5.10	VW
7	$Mill2$	$T-7550$	20.30	21.17	0.36	6.60	WX
8	$Mill2$	$T-7672$	20.30	21.11	0.37	8.82	W
9	$Mill2$	$T-7547$	20.30	21.14	0.40	8.14	IJ

Table 2. Statistic calculation

A.3 Deepwater pipelines with buckle arrestors. Measurements.

In this Section we present the results of the geometrical mapping of one of the samples used in the tests described in Chapter 4.

The Fourier decomposition of the outside surface of that sample is shown in Fig. (A.6). The zone with high amplitude corresponds to the milled groove, whereas the zone with low amplitude corresponds to the arrestor, which was machined in a lathe.

The thickness of the samples was also mapped using a standard ultrasonic gauge; the thickness map for the first sample is shown in Fig. (A.7).

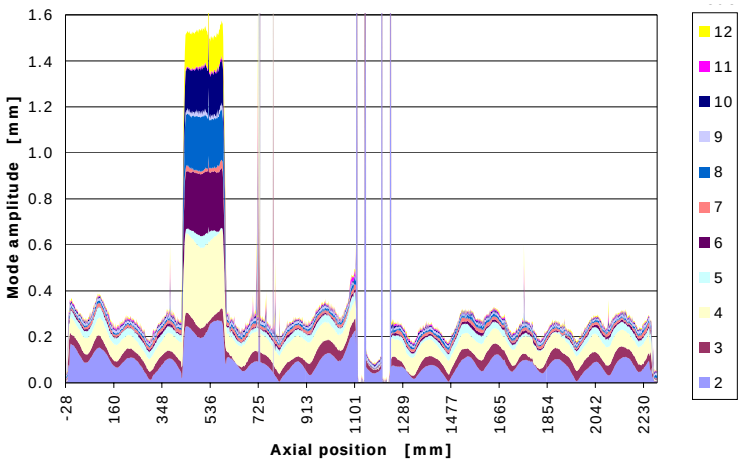

Figure A.6: Outside surface Fourier decomposition of Sample #1

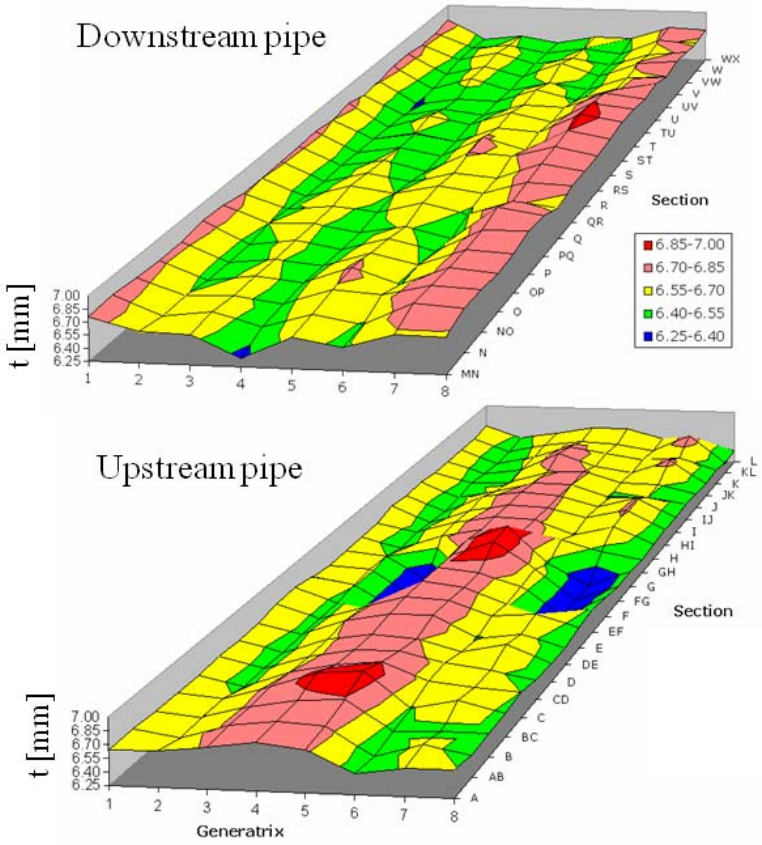

Figure A.7: Sample #1 - 5 9/16" OD 6.55 mm WT AST A-333. Thickness distribution

Appendix B

Hyper-elastic material

B.1 First case: linear relation between 2^{nd} Piola-Kirchhoff stresses and Green-Lagrange strains

B.1.1 Matrices $\underline{H}_0, \underline{V}_{12}$, $\underline{MV}n$ and $\underline{MV}_{n\_t}$

In this appendix we present the details of the matrices we use in Chapter 6.

$$\underline{H}_0 = \begin{bmatrix} h_1 & 0 & 0 & 0 & 0 & h_2 & 0 & 0 & 0 & 0 & h_3 & 0 & 0 & 0 & 0 & h_4 & 0 & 0 & 0 & 0 & 0 & 0 \\ 0 & h_1 & 0 & 0 & 0 & 0 & h_2 & 0 & 0 & 0 & 0 & h_3 & 0 & 0 & 0 & 0 & h_4 & 0 & 0 & 0 & 0 & 0 \\ 0 & 0 & h_1 & 0 & 0 & 0 & 0 & h_2 & 0 & 0 & 0 & 0 & h_3 & 0 & 0 & 0 & 0 & h_4 & 0 & 0 & 0 & 0 \end{bmatrix} \tag{B.1}$$

Where h_i is the interpolation function for node i, being H_0 a (3x22) matrix.

$$\underline{V}_{12} = \begin{bmatrix}
0 & 0 & 0 & -V_{2x}^{1} & V_{1x}^{1} & 0 & 0 & 0 & 0 & 0 & 0 & 0 & 0 & 0 & 0 & 0 & 0 & 0 & 0 & 0 & 0 & 0 \\
0 & 0 & 0 & -V_{2y}^{1} & V_{1y}^{1} & 0 & 0 & 0 & 0 & 0 & 0 & 0 & 0 & 0 & 0 & 0 & 0 & 0 & 0 & 0 & 0 & 0 \\
0 & 0 & 0 & -V_{2z}^{1} & V_{1z}^{1} & 0 & 0 & 0 & 0 & 0 & 0 & 0 & 0 & 0 & 0 & 0 & 0 & 0 & 0 & 0 & 0 & 0 \\
0 & 0 & 0 & 0 & 0 & 0 & 0 & 0 & 0 & 0 & 0 & 0 & 0 & 0 & 0 & 0 & 0 & 0 & 0 & 0 & 0 & 0 \\
0 & 0 & 0 & 0 & 0 & 0 & 0 & 0 & 0 & 0 & 0 & 0 & 0 & 0 & 0 & 0 & 0 & 0 & 0 & 0 & 0 & 0 \\
0 & 0 & 0 & 0 & 0 & 0 & 0 & 0 & -V_{2x}^{2} & V_{1x}^{2} & 0 & 0 & 0 & 0 & 0 & 0 & 0 & 0 & 0 & 0 & 0 & 0 \\
0 & 0 & 0 & 0 & 0 & 0 & 0 & 0 & -V_{2y}^{2} & V_{1y}^{2} & 0 & 0 & 0 & 0 & 0 & 0 & 0 & 0 & 0 & 0 & 0 & 0 \\
0 & 0 & 0 & 0 & 0 & 0 & 0 & 0 & -V_{2z}^{2} & V_{1z}^{2} & 0 & 0 & 0 & 0 & 0 & 0 & 0 & 0 & 0 & 0 & 0 & 0 \\
0 & 0 & 0 & 0 & 0 & 0 & 0 & 0 & 0 & 0 & 0 & 0 & 0 & 0 & 0 & 0 & 0 & 0 & 0 & 0 & 0 & 0 \\
0 & 0 & 0 & 0 & 0 & 0 & 0 & 0 & 0 & 0 & 0 & 0 & 0 & 0 & 0 & 0 & 0 & 0 & 0 & 0 & 0 & 0 \\
0 & 0 & 0 & 0 & 0 & 0 & 0 & 0 & 0 & 0 & 0 & 0 & 0 & -V_{2x}^{3} & V_{1x}^{3} & 0 & 0 & 0 & 0 & 0 & 0 & 0 \\
0 & 0 & 0 & 0 & 0 & 0 & 0 & 0 & 0 & 0 & 0 & 0 & 0 & -V_{2y}^{3} & V_{1y}^{3} & 0 & 0 & 0 & 0 & 0 & 0 & 0 \\
0 & 0 & 0 & 0 & 0 & 0 & 0 & 0 & 0 & 0 & 0 & 0 & 0 & -V_{2z}^{3} & V_{1z}^{3} & 0 & 0 & 0 & 0 & 0 & 0 & 0 \\
0 & 0 & 0 & 0 & 0 & 0 & 0 & 0 & 0 & 0 & 0 & 0 & 0 & 0 & 0 & 0 & 0 & 0 & 0 & 0 & 0 & 0 \\
0 & 0 & 0 & 0 & 0 & 0 & 0 & 0 & 0 & 0 & 0 & 0 & 0 & 0 & 0 & 0 & 0 & 0 & 0 & 0 & 0 & 0 \\
0 & 0 & 0 & 0 & 0 & 0 & 0 & 0 & 0 & 0 & 0 & 0 & 0 & 0 & 0 & 0 & 0 & 0 & -V_{2x}^{4} & V_{1x}^{4} & 0 & 0 \\
0 & 0 & 0 & 0 & 0 & 0 & 0 & 0 & 0 & 0 & 0 & 0 & 0 & 0 & 0 & 0 & 0 & 0 & -V_{2y}^{4} & V_{1y}^{4} & 0 & 0 \\
0 & 0 & 0 & 0 & 0 & 0 & 0 & 0 & 0 & 0 & 0 & 0 & 0 & 0 & 0 & 0 & 0 & 0 & -V_{2z}^{4} & V_{1z}^{4} & 0 & 0 \\
0 & 0 & 0 & 0 & 0 & 0 & 0 & 0 & 0 & 0 & 0 & 0 & 0 & 0 & 0 & 0 & 0 & 0 & 0 & 0 & 0 & 0 \\
0 & 0 & 0 & 0 & 0 & 0 & 0 & 0 & 0 & 0 & 0 & 0 & 0 & 0 & 0 & 0 & 0 & 0 & 0 & 0 & 0 & 0 \\
0 & 0 & 0 & 0 & 0 & 0 & 0 & 0 & 0 & 0 & 0 & 0 & 0 & 0 & 0 & 0 & 0 & 0 & 0 & 0 & 0 & 0 \\
0 & 0 & 0 & 0 & 0 & 0 & 0 & 0 & 0 & 0 & 0 & 0 & 0 & 0 & 0 & 0 & 0 & 0 & 0 & 0 & 0 & 0
\end{bmatrix}$$

Where V_{1j}^{i} and V_{2j}^{i} are the components j of the versors $\underline{V}_1$and $\underline{V}_2$, node i. $\underline{V}_{12}$ is a (22x22) matrix.

$$\underline{MV}_n = \begin{bmatrix}
0 & 0 & 0 & 0 & 0 & 0 & 0 & 0 & 0 & 0 & 0 & 0 & 0 & 0 & 0 & 0 & 0 & 0 & 0 & 0 & V_{nx}^1 & V_{nx}^1\ t \\
0 & 0 & 0 & 0 & 0 & 0 & 0 & 0 & 0 & 0 & 0 & 0 & 0 & 0 & 0 & 0 & 0 & 0 & 0 & 0 & V_{ny}^1 & V_{ny}^1\ t \\
0 & 0 & 0 & 0 & 0 & 0 & 0 & 0 & 0 & 0 & 0 & 0 & 0 & 0 & 0 & 0 & 0 & 0 & 0 & 0 & V_{nz}^1 & V_{nz}^1\ t \\
0 & 0 & 0 & 0 & 0 & 0 & 0 & 0 & 0 & 0 & 0 & 0 & 0 & 0 & 0 & 0 & 0 & 0 & 0 & 0 & 0 & 0 \\
0 & 0 & 0 & 0 & 0 & 0 & 0 & 0 & 0 & 0 & 0 & 0 & 0 & 0 & 0 & 0 & 0 & 0 & 0 & 0 & 0 & 0 \\
0 & 0 & 0 & 0 & 0 & 0 & 0 & 0 & 0 & 0 & 0 & 0 & 0 & 0 & 0 & 0 & 0 & 0 & 0 & 0 & V_{nx}^2 & V_{nx}^2\ t \\
0 & 0 & 0 & 0 & 0 & 0 & 0 & 0 & 0 & 0 & 0 & 0 & 0 & 0 & 0 & 0 & 0 & 0 & 0 & 0 & V_{ny}^2 & V_{ny}^2\ t \\
0 & 0 & 0 & 0 & 0 & 0 & 0 & 0 & 0 & 0 & 0 & 0 & 0 & 0 & 0 & 0 & 0 & 0 & 0 & 0 & V_{nz}^2 & V_{nz}^2\ t \\
0 & 0 & 0 & 0 & 0 & 0 & 0 & 0 & 0 & 0 & 0 & 0 & 0 & 0 & 0 & 0 & 0 & 0 & 0 & 0 & 0 & 0 \\
0 & 0 & 0 & 0 & 0 & 0 & 0 & 0 & 0 & 0 & 0 & 0 & 0 & 0 & 0 & 0 & 0 & 0 & 0 & 0 & 0 & 0 \\
0 & 0 & 0 & 0 & 0 & 0 & 0 & 0 & 0 & 0 & 0 & 0 & 0 & 0 & 0 & 0 & 0 & 0 & 0 & 0 & V_{nx}^3 & V_{nx}^3\ t \\
0 & 0 & 0 & 0 & 0 & 0 & 0 & 0 & 0 & 0 & 0 & 0 & 0 & 0 & 0 & 0 & 0 & 0 & 0 & 0 & V_{ny}^3 & V_{ny}^3\ t \\
0 & 0 & 0 & 0 & 0 & 0 & 0 & 0 & 0 & 0 & 0 & 0 & 0 & 0 & 0 & 0 & 0 & 0 & 0 & 0 & V_{nz}^3 & V_{nz}^3\ t \\
0 & 0 & 0 & 0 & 0 & 0 & 0 & 0 & 0 & 0 & 0 & 0 & 0 & 0 & 0 & 0 & 0 & 0 & 0 & 0 & 0 & 0 \\
0 & 0 & 0 & 0 & 0 & 0 & 0 & 0 & 0 & 0 & 0 & 0 & 0 & 0 & 0 & 0 & 0 & 0 & 0 & 0 & 0 & 0 \\
0 & 0 & 0 & 0 & 0 & 0 & 0 & 0 & 0 & 0 & 0 & 0 & 0 & 0 & 0 & 0 & 0 & 0 & 0 & 0 & V_{nx}^4 & V_{nx}^4\ t \\
0 & 0 & 0 & 0 & 0 & 0 & 0 & 0 & 0 & 0 & 0 & 0 & 0 & 0 & 0 & 0 & 0 & 0 & 0 & 0 & V_{ny}^4 & V_{ny}^4\ t \\
0 & 0 & 0 & 0 & 0 & 0 & 0 & 0 & 0 & 0 & 0 & 0 & 0 & 0 & 0 & 0 & 0 & 0 & 0 & 0 & V_{nz}^4 & V_{nz}^4\ t \\
0 & 0 & 0 & 0 & 0 & 0 & 0 & 0 & 0 & 0 & 0 & 0 & 0 & 0 & 0 & 0 & 0 & 0 & 0 & 0 & 0 & 0 \\
0 & 0 & 0 & 0 & 0 & 0 & 0 & 0 & 0 & 0 & 0 & 0 & 0 & 0 & 0 & 0 & 0 & 0 & 0 & 0 & 0 & 0 \\
0 & 0 & 0 & 0 & 0 & 0 & 0 & 0 & 0 & 0 & 0 & 0 & 0 & 0 & 0 & 0 & 0 & 0 & 0 & 0 & 0 & 0 \\
0 & 0 & 0 & 0 & 0 & 0 & 0 & 0 & 0 & 0 & 0 & 0 & 0 & 0 & 0 & 0 & 0 & 0 & 0 & 0 & 0 & 0
\end{bmatrix} \tag{B.2}$$

V_{nj}^i : component j of versor $\underline{V}n$, node i. Dimension of $\underline{MV}_n$: (22x22).

$$\underline{MV}_{n_t} = \begin{bmatrix}
0&0&0&0&0&0&0&0&0&0&0&0&0&0&0&0&0&0&0&0&0&0 & V_{nx}^1 & 2\,t\,V_{nx}^1 \\
0&0&0&0&0&0&0&0&0&0&0&0&0&0&0&0&0&0&0&0&0&0 & V_{ny}^1 & 2\,t\,V_{ny}^1 \\
0&0&0&0&0&0&0&0&0&0&0&0&0&0&0&0&0&0&0&0&0&0 & V_{nz}^1 & 2\,t\,V_{nz}^1 \\
0&0&0&0&0&0&0&0&0&0&0&0&0&0&0&0&0&0&0&0&0&0 & 0 & \\
0&0&0&0&0&0&0&0&0&0&0&0&0&0&0&0&0&0&0&0&0&0 & 0 & \\
0&0&0&0&0&0&0&0&0&0&0&0&0&0&0&0&0&0&0&0&0&0 & V_{nx}^2 & 2\,t\,V_{nx}^2 \\
0&0&0&0&0&0&0&0&0&0&0&0&0&0&0&0&0&0&0&0&0&0 & V_{ny}^2 & 2\,t\,V_{ny}^2 \\
0&0&0&0&0&0&0&0&0&0&0&0&0&0&0&0&0&0&0&0&0&0 & V_{nz}^2 & 2\,t\,V_{nz}^2 \\
0&0&0&0&0&0&0&0&0&0&0&0&0&0&0&0&0&0&0&0&0&0 & 0 & \\
0&0&0&0&0&0&0&0&0&0&0&0&0&0&0&0&0&0&0&0&0&0 & 0 & \\
0&0&0&0&0&0&0&0&0&0&0&0&0&0&0&0&0&0&0&0&0&0 & V_{nx}^3 & 2\,t\,V_{nx}^3 \\
0&0&0&0&0&0&0&0&0&0&0&0&0&0&0&0&0&0&0&0&0&0 & V_{ny}^3 & 2\,t\,V_{ny}^3 \\
0&0&0&0&0&0&0&0&0&0&0&0&0&0&0&0&0&0&0&0&0&0 & V_{nz}^3 & 2\,t\,V_{nz}^3 \\
0&0&0&0&0&0&0&0&0&0&0&0&0&0&0&0&0&0&0&0&0&0 & 0 & \\
0&0&0&0&0&0&0&0&0&0&0&0&0&0&0&0&0&0&0&0&0&0 & 0 & \\
0&0&0&0&0&0&0&0&0&0&0&0&0&0&0&0&0&0&0&0&0&0 & V_{nx}^4 & 2\,t\,V_{nx}^4 \\
0&0&0&0&0&0&0&0&0&0&0&0&0&0&0&0&0&0&0&0&0&0 & V_{ny}^4 & 2\,t\,V_{ny}^4 \\
0&0&0&0&0&0&0&0&0&0&0&0&0&0&0&0&0&0&0&0&0&0 & V_{nz}^4 & 2\,t\,V_{nz}^4 \\
0&0&0&0&0&0&0&0&0&0&0&0&0&0&0&0&0&0&0&0&0&0 & 0 & \\
0&0&0&0&0&0&0&0&0&0&0&0&0&0&0&0&0&0&0&0&0&0 & 0 & \\
0&0&0&0&0&0&0&0&0&0&0&0&0&0&0&0&0&0&0&0&0&0 & 0 & \\
0&0&0&0&0&0&0&0&0&0&0&0&0&0&0&0&0&0&0&0&0&0 & 0 &
\end{bmatrix} \tag{B.3}$$

V_{nj}^i : component j of versor $\underline{V}n$, node i. Dimension of $\underline{MV}_{n\_t}$: (22x22).

B.2 Second case: compressible neo-Hookean model

In what follows we calculate each term of the Eq.(6.74) :$\frac{\partial\,\lambda_I}{\partial\,C_{PQ}}|_0^\tau$, $\frac{\partial\,S^I}{\partial\,C_{PQ}}|_0^\tau$ and $\frac{\partial\,f\,(C_{LM},\lambda_I)}{\partial\,C_{PQ}}|_0^\tau$.

B.2.1 $\frac{\partial\,\lambda_I}{\partial\,C_{PQ}}|_0^\tau$

To calculate $\frac{\partial\,\lambda_I}{\partial\,C_{PQ}}|_0^\tau$ we use the characteristic polynomial of the Green tensor [31] and calculate its derivative,

$$-\,{}^\tau\lambda_I^6\;+\;{}^\tau I_C^1\,{}^\tau\lambda_I^4\;-\;{}^\tau I_C^2\,{}^\tau\lambda_I^2\;+\;{}^\tau I_C^3=0\;\;. \tag{B.4}$$

$$\left(-6\,{}^\tau\lambda_I^5+4\,{}^\tau I_1^C\,{}^\tau\lambda_I^3-2\,I_2^C\,{}^\tau\lambda_I\right)\;\frac{\partial\,\lambda_I}{\partial\,C_{PQ}}|_0^\tau+\frac{\partial I_1^C}{\partial C_{PQ}}|_0^\tau\;\lambda_I^4\;-\;\frac{\partial I_2^C}{\partial C_{PQ}}|_0^\tau\;\lambda_I^2\;+\;\frac{\partial I_3^C}{\partial C_{PQ}}|_0^\tau\;=0$$

$$\frac{\partial\,\lambda_I}{\partial\,C_{PQ}}|_0^\tau=\frac{-\frac{\partial I_1^C}{\partial C_{PQ}}|_0^\tau\;\lambda_I^4\;+\;\frac{\partial I_2^C}{\partial C_{PQ}}|_0^\tau\;\lambda_I^2\;-\;\frac{\partial I_3^C}{\partial C_{PQ}}|_0^\tau}{-6\,{}^\tau\lambda_I^5\;+\;4\,{}^\tau I_1^C\,{}^\tau\lambda_I^3-2\,I_2^C\,{}^\tau\lambda_I}\;\;. \tag{B.5}$$

Multiple eigenvalues When we have multiple eigenvalues (for instance in the undeformed position) we introduce small perturbations, in order to avoid the denominators of Eqs. (6.64) and (B.5) to be zero [36].

Derivative of the first invariant ${}^\tau I_1^C$,

$${}^\tau I_1^C=tr\left({}^\tau_o\underline{\underline{C}}\right)={}^\tau_o C_{11}+{}^\tau_o C_{22}+{}^\tau_o C_{33} \tag{B.6}$$

$$\frac{\partial I_1^C}{\partial C_{PQ}}|_0^\tau=\delta_{PQ}\;\;. \tag{B.7}$$

Derivative of the second invariant ${}^\tau I_2^C$,

$$\begin{aligned}{}^\tau I_2^C\;&=\;\frac{1}{2}\;\left[\left({}^\tau I_1^C\right)^2-tr\left({}^\tau_o\underline{\underline{C^2}}\right)\right]\\ {}^\tau I_2^C\;&=\;{}^\tau_o C_{11}\,{}^\tau_o C_{22}+{}^\tau_o C_{11}\,{}^\tau_o C_{33}+{}^\tau_o C_{22}\,{}^\tau_o C_{33}-{}^\tau_o C_{12}\,{}^\tau_o C_{21}-\\ &\quad\;{}^\tau_o C_{13}\,{}^\tau_o C_{31}-{}^\tau_o C_{23}\,{}^\tau_o C_{32}\end{aligned} \tag{B.8a}$$

$$\frac{\partial I_2^C}{\partial C_{PQ}}|_0^\tau=\begin{bmatrix}{}^\tau_o C_{22}+{}^\tau_o C_{33} & -{}^\tau_o C_{21} & -{}^\tau_o C_{31}\\ -{}^\tau_o C_{12} & {}^\tau_o C_{11}+{}^\tau_o C_{33} & -{}^\tau_o C_{32}\\ -{}^\tau_o C_{13} & -{}^\tau_o C_{23} & {}^\tau_o C_{11}+{}^\tau_o C_{22}\end{bmatrix} \tag{B.9}$$

We are not imposing symmetry when we derivate.

Derivative of the third invariant ${}^{\tau}I_3^C$,

$$\begin{aligned} {}^{\tau}I_3^C &= \det\left({}^{\tau}_{o}\underline{\underline{C}}\right) \\ {}^{\tau}I_3^C &= {}^{\tau}_{o}C_{11}\,{}^{\tau}_{o}C_{22}\,{}^{\tau}_{o}C_{33} - {}^{\tau}_{o}C_{11}\,{}^{\tau}_{o}C_{32}\,{}^{\tau}_{o}C_{23} - {}^{\tau}_{o}C_{12}\,{}^{\tau}_{o}C_{21}\,{}^{\tau}_{o}C_{33} + \\ &\quad {}^{\tau}_{o}C_{12}\,{}^{\tau}_{o}C_{31}\,{}^{\tau}_{o}C_{23} + {}^{\tau}_{o}C_{13}\,{}^{\tau}_{o}C_{21}\,{}^{\tau}_{o}C_{32} - {}^{\tau}_{o}C_{13}\,{}^{\tau}_{o}C_{31}\,{}^{\tau}_{o}C_{22} \end{aligned} \tag{B.10}$$

$$\frac{\partial I_3^C}{\partial C_{PQ}}\Big|_0^{\tau} = \begin{bmatrix} {}^{\tau}_{o}C_{22}\,{}^{\tau}_{o}C_{33} - {}^{\tau}_{o}C_{32}\,{}^{\tau}_{o}C_{23} & -{}^{\tau}_{o}C_{21}\,{}^{\tau}_{o}C_{33} + {}^{\tau}_{o}C_{31}\,{}^{\tau}_{o}C_{23} & {}^{\tau}_{o}C_{21}\,{}^{\tau}_{o}C_{32} - {}^{\tau}_{o}C_{31}\,{}^{\tau}_{o}C_{22} \\ -{}^{\tau}_{o}C_{12}\,{}^{\tau}_{o}C_{33} + {}^{\tau}_{o}C_{13}\,{}^{\tau}_{o}C_{32} & {}^{\tau}_{o}C_{11}\,{}^{\tau}_{o}C_{33} - {}^{\tau}_{o}C_{13}\,{}^{\tau}_{o}C_{31} & -{}^{\tau}_{o}C_{11}\,{}^{\tau}_{o}C_{32} + {}^{\tau}_{o}C_{12}\,{}^{\tau}_{o}C_{31} \\ {}^{\tau}_{o}C_{12}\,{}^{\tau}_{o}C_{23} - {}^{\tau}_{o}C_{13}\,{}^{\tau}_{o}C_{22} & -{}^{\tau}_{o}C_{11}\,{}^{\tau}_{o}C_{23} + {}^{\tau}_{o}C_{13}\,{}^{\tau}_{o}C_{21} & {}^{\tau}_{o}C_{11}\,{}^{\tau}_{o}C_{22} - {}^{\tau}_{o}C_{12}\,{}^{\tau}_{o}C_{21} \end{bmatrix} . \tag{B.11}$$

Replacing the expressions of invariants and their derivatives (Eqns.B.6 to B.11) in (B.5), we obtain $\frac{\partial \lambda_I}{\partial C_{PQ}}\Big|_0^{\tau}$.

B.2.2 $\frac{\partial S^I}{\partial C_{PQ}}\Big|_0^{\tau}$

$$\frac{\partial S^I}{\partial C_{PQ}}\Big|_0^{\tau} = \frac{\partial S^I}{\partial \lambda_I}\Big|_0^{\tau}\,\frac{\partial\,\lambda_I}{\partial\,C_{PQ}}\Big|_0^{\tau} \ . \tag{B.12}$$

From Eqs.(6.68a) to (6.68c) we deduce the derivatives $\frac{\partial {}^{\tau}_{o}S^I}{\partial {}^{\tau}\lambda_I}$.

$$\begin{aligned} \frac{\partial S^I}{\partial \lambda_I}\Big|_0^{\tau} &= -\frac{2}{{}^{\tau}\lambda_I}\,{}^{\tau}_{o}S^I + \frac{1}{{}^{\tau}\lambda_I^2}\left[\begin{array}{c} \kappa\,{}^{\tau}J\,{}^{\tau}\lambda_{II}\,{}^{\tau}\lambda_{III} - \\ \frac{2}{3}\,G\,{}^{\tau}J^{\frac{-5}{3}}\,{}^{\tau}\lambda_{II}\,{}^{\tau}\lambda_{III}\left(\frac{2\,{}^{\tau}\lambda_I^2 - {}^{\tau}\lambda_{II}^2 - {}^{\tau}\lambda_{III}^2}{3}\right) + G\,{}^{\tau}J^{\frac{-2}{3}}\,\frac{4}{3}\,{}^{\tau}\lambda_I \end{array}\right] \\ \frac{\partial S^I}{\partial \lambda_{II}}\Big|_0^{\tau} &= \frac{1}{{}^{\tau}\lambda_I^2}\left[\begin{array}{c} \kappa\,{}^{\tau}J\,{}^{\tau}\lambda_I\,{}^{\tau}\lambda_{III} - \\ \frac{2}{3}\,G\,{}^{\tau}J^{\frac{-5}{3}}\,{}^{\tau}\lambda_I\,{}^{\tau}\lambda_{III}\left(\frac{2\,{}^{\tau}\lambda_I^2 - {}^{\tau}\lambda_{II}^2 - {}^{\tau}\lambda_{III}^2}{3}\right) - G\,{}^{\tau}J^{\frac{-2}{3}}\,\frac{2}{3}\,{}^{\tau}\lambda_{II} \end{array}\right] \\ \frac{\partial S^I}{\partial \lambda_{III}}\Big|_0^{\tau} &= \frac{1}{{}^{\tau}\lambda_I^2}\left[\begin{array}{c} \kappa\,{}^{\tau}J\,{}^{\tau}\lambda_I\,{}^{\tau}\lambda_{II} - \\ \frac{2}{3}\,G\,{}^{\tau}J^{\frac{-5}{3}}\,{}^{\tau}\lambda_I\,{}^{\tau}\lambda_{II}\left(\frac{2\,{}^{\tau}\lambda_I^2 - {}^{\tau}\lambda_{II}^2 - {}^{\tau}\lambda_{III}^2}{3}\right) - G\,{}^{\tau}J^{\frac{-2}{3}}\,\frac{2}{3}\,{}^{\tau}\lambda_{III} \end{array}\right] \end{aligned} \tag{B.13}$$

$$
\begin{aligned}
\frac{\partial S^{II}}{\partial \lambda_I}|_0^\tau &= \frac{1}{{}^\tau\lambda_{II}^2}\left[\begin{array}{c}\kappa\ {}^\tau J\ {}^\tau\lambda_{II}\ {}^\tau\lambda_{III} - \\ \frac{2}{3}\ G\ {}^\tau J^{\frac{-5}{3}}\ {}^\tau\lambda_{II}\ {}^\tau\lambda_{III}\ \left(\frac{2\ {}^\tau\lambda_{II}^2 - {}^\tau\lambda_I^2 - {}^\tau\lambda_{III}^2}{3}\right) - G\ {}^\tau J^{\frac{-2}{3}}\ \frac{2}{3}\ {}^\tau\lambda_I\end{array}\right] \\
\frac{\partial S^{II}}{\partial \lambda_{II}}|_0^\tau &= -\frac{2}{{}^\tau\lambda_{II}}\ {}^\tau_o S^{II} + \frac{1}{{}^\tau\lambda_{II}^2}\left[\begin{array}{c}\kappa\ {}^\tau J\ {}^\tau\lambda_I\ {}^\tau\lambda_{III} - \\ \frac{2}{3}\ G\ {}^\tau J^{\frac{-5}{3}}\ {}^\tau\lambda_I\ {}^\tau\lambda_{III}\ \left(\frac{2\ {}^\tau\lambda_{II}^2 - {}^\tau\lambda_I^2 - {}^\tau\lambda_{III}^2}{3}\right) + G\ {}^\tau J^{\frac{-2}{3}}\ \frac{4}{3}\ {}^\tau\lambda_{II}\end{array}\right] \\
\frac{\partial S^{II}}{\partial \lambda_{III}}|_0^\tau &= \frac{1}{{}^\tau\lambda_{II}^2}\left[\begin{array}{c}\kappa\ {}^\tau J\ {}^\tau\lambda_I\ {}^\tau\lambda_{II} - \\ \frac{2}{3}\ G\ {}^\tau J^{\frac{-5}{3}}\ {}^\tau\lambda_I\ {}^\tau\lambda_{II}\ \left(\frac{2\ {}^\tau\lambda_{II}^2 - {}^\tau\lambda_I^2 - {}^\tau\lambda_{III}^2}{3}\right) - G\ {}^\tau J^{\frac{-2}{3}}\ \frac{2}{3}\ {}^\tau\lambda_{III}\end{array}\right] \\
\frac{\partial S^{III}}{\partial \lambda_I}|_0^\tau &= \frac{1}{{}^\tau\lambda_{III}^2}\left[\begin{array}{c}\kappa\ {}^\tau J\ {}^\tau\lambda_{II}\ {}^\tau\lambda_{III} - \\ \frac{2}{3}\ G\ {}^\tau J^{\frac{-5}{3}}\ {}^\tau\lambda_{II}\ {}^\tau\lambda_{III}\ \left(\frac{2\ {}^\tau\lambda_{III}^2 - {}^\tau\lambda_I^2 - {}^\tau\lambda_{II}^2}{3}\right) - G\ {}^\tau J^{\frac{-2}{3}}\ \frac{2}{3}\ {}^\tau\lambda_I\end{array}\right] \\
\frac{\partial S^{III}}{\partial \lambda_{II}}|_0^\tau &= \frac{1}{{}^\tau\lambda_{III}^2}\left[\begin{array}{c}\kappa\ {}^\tau J\ {}^\tau\lambda_I\ {}^\tau\lambda_{III} - \\ \frac{2}{3}\ G\ {}^\tau J^{\frac{-5}{3}}\ {}^\tau\lambda_I\ {}^\tau\lambda_{III}\ \left(\frac{2\ {}^\tau\lambda_{III}^2 - {}^\tau\lambda_I^2 - {}^\tau\lambda_{II}^2}{3}\right) - G\ {}^\tau J^{\frac{-2}{3}}\ \frac{2}{3}\ {}^\tau\lambda_{II}\end{array}\right] \\
\frac{\partial S^{III}}{\partial \lambda_{III}}|_0^\tau &= -\frac{2}{{}^\tau\lambda_{III}}\ {}^\tau_o S^{II} + \frac{1}{{}^\tau\lambda_{III}^2}\left[\begin{array}{c}\kappa\ {}^\tau J\ {}^\tau\lambda_I\ {}^\tau\lambda_{II} - \\ \frac{2}{3}\ G\ {}^\tau J^{\frac{-5}{3}}\ {}^\tau\lambda_I\ {}^\tau\lambda_{II}\ \left(\frac{2\ {}^\tau\lambda_{III}^2 - {}^\tau\lambda_I^2 - {}^\tau\lambda_{II}^2}{3}\right) + G\ {}^\tau J^{\frac{-2}{3}}\ \frac{4}{3}\ {}^\tau\lambda_{III}\end{array}\right]
\end{aligned}
\tag{B.15}
$$

B.2.3 $\frac{\partial f\ (C_{LM},\ \lambda_I)}{\partial\ C_{PQ}}|_0^\tau$

From Eq. (6.72),

$$
f({}^\tau_o C_{LM}, {}^\tau\lambda_I) = \frac{{}^\tau_o C_{LM} - \left({}^\tau I_C^1 - {}^\tau\lambda_I^2\right)\ {}^o g_{LM} + {}^\tau I_C^3\ {}^\tau\lambda_I^{-2}\ {}^\tau_o C_{LM}^{-1}}{2\ {}^\tau\lambda_I^4 - {}^\tau I_C^1\ \lambda_I^2 + {}^\tau I_C^3\ {}^\tau\lambda_I^{-2}} = \frac{A}{B} \tag{B.16}
$$

applying the division derivatie rule we get,

$$
\frac{\partial\ f\ (C_{LM},\ \lambda_I)}{\partial C_{PQ}}|_0^\tau = \frac{\frac{\partial A}{\partial\ C_{PQ}}|_0^\tau\ B - A\ \frac{\partial B}{\partial\ C_{PQ}}|_0^\tau}{B^2} \tag{B.17}
$$

$$
\begin{aligned}
\frac{\partial A}{\partial C_{PQ}}|_0^\tau &= \frac{\partial C_{LM}}{\partial C_{PQ}}|_0^\tau - \left(\frac{\partial I_C^1}{\partial C_{PQ}}|_0^\tau - 2\ {}^\tau\lambda_I\ \frac{\partial \lambda_I}{\partial C_{PQ}}|_0^\tau\right)\ {}^o g_{LM} - \\
&\quad \left({}^\tau I_C^1 - {}^\tau\lambda_I^2\right)\ \frac{\partial^0 g_{LM}}{\partial C_{PQ}}|_0^\tau + \frac{\partial {}^\tau I_C^3}{\partial C_{PQ}}|_0^\tau\ {}^\tau\lambda_I^{-2}\ {}^\tau_o C_{LM}^{-1} - \\
&\quad 2\ {}^\tau I_C^3\ {}^\tau\lambda_I^{-3}\ {}^\tau_o C_{LM}^{-1}\ \frac{\partial \lambda_I}{\partial C_{PQ}}|_0^\tau + {}^\tau\ I_C^3\ {}^\tau\lambda_I^{-2}\ \frac{\partial C_{LM}^{-1}}{\partial C_{PQ}}|_0^\tau
\end{aligned}
$$

$$\begin{aligned}\frac{\partial B}{\partial C_{PQ}}|_0^\tau &= 8\ {}^\tau\lambda_I^3\ \frac{\partial \lambda_I}{\partial C_{PQ}}|_0^\tau - 2\ {}^\tau I_C^1\ {}^\tau\lambda_I\ \frac{\partial \lambda_I}{\partial C_{PQ}}|_0^\tau - \\ &\frac{\partial I_C^1}{\partial C_{PQ}}|_0^\tau\ {}^\tau\lambda_I^2 + \frac{\partial\ I_C^3}{\partial C_{PQ}}|_0^\tau\ {}^\tau\lambda_I^{-2} - 2\ {}^\tau I_C^3\ {}^\tau\lambda_I^{-3}\ \frac{\partial \lambda_I}{\partial C_{PQ}}|_0^\tau\ .\end{aligned}$$

Being,

$$\frac{\partial C_{LM}}{\partial C_{PQ}}|_0^\tau = \delta_{LP}\ \delta_{MQ}\ .$$

Replacing the last 3 equations into (B.17) we obtain the term $\frac{\partial f\ (C_{LM},\ \lambda_I)}{\partial\ C_{PQ}}|_0^\tau$.

B.2.4 $\frac{\partial C_{LM}^{-1}}{\partial C_{PQ}}|_0^\tau$

$$\begin{aligned}{}_o^\tau C_{LM}^{-1}\ {}_o^\tau C_{MN} &= \delta_{LN} \\ \frac{\partial C_{LM}^{-1}}{\partial C_{PQ}}|_0^\tau\ {}_o^\tau C_{MN} +{}_o^\tau C_{LM}^{-1}\ \frac{\partial C_{MN}}{\partial C_{PQ}}|_0^\tau &= 0 \\ \frac{\partial C_{LM}^{-1}}{\partial C_{PQ}}|_0^\tau\ {}_o^\tau C_{MN} +{}_o^\tau C_{LM}^{-1}\ \delta_{MP}\ \delta_{NQ} &= 0 \\ \frac{\partial C_{LM}^{-1}}{\partial C_{PQ}}|_0^\tau\ {}_o^\tau C_{MN}\ {}_o^\tau C_{NF}^{-1} &= -{}_o^\tau C_{LP}^{-1}\ \delta_{NQ}\ {}_o^\tau C_{NF}^{-1} \\ \frac{\partial C_{LM}^{-1}}{\partial C_{PQ}}|_0^\tau\ \delta_{MF} &= -{}_o^\tau C_{LP}^{-1}\ {}_o^\tau C_{QF}^{-1} \\ \frac{\partial C_{LF}^{-1}}{\partial C_{PQ}}|_0^\tau &= -{}_o^\tau C_{LP}^{-1}\ {}_o^\tau C_{QF}^{-1} \\ \frac{\partial C_{LM}^{-1}}{\partial C_{PQ}}|_0^\tau &= -{}_o^\tau C_{LP}^{-1}\ {}_o^\tau C_{QM}^{-1}\ . \end{aligned} \tag{B.18}$$

Please note that $\frac{\partial^0 g_{LM}}{\partial C_{PQ}}|_0^\tau = 0$.

B.3 Third case: linear relation between the Hencky strain tensor and its energy conjugate stress tensor

B.3.1 ${}^{\tau}_{0}\lambda^{MN}_{IJ}$

${}^{\tau}_{0}\lambda^{MN}_{IJ}$ are the components of a fourth order tensor, which is defined as,

$$ {}^{\tau}_{o}\lambda^{MN}_{IJ} = 2\,\frac{\partial H_{IJ}}{\partial C_{MN}}|^{\tau}_{0} \ . \tag{B.19} $$

Being ${}_{o}H_{IJ}$ the Hencky strain tensor increment,

$$ \begin{aligned} {}_{o}H_{IJ} &= \frac{\partial H_{IJ}}{\partial C_{MN}}|^{\tau}_{0}\ {}_{o}C_{MN} \ = 2\,\frac{\partial H_{IJ}}{\partial C_{MN}}|^{\tau}_{0}\ {}_{o}\varepsilon_{MN} \\ {}_{o}H_{IJ} &= {}^{\tau}_{o}\lambda^{MN}_{IJ}\ {}_{o}\varepsilon_{MN} \ . \end{aligned} \tag{B.20a} $$

We apply Serrin formula (6.64),

$$ \Phi_I \Phi_I = \ {}^{\tau}\lambda_I^2\ \frac{{}^{\tau}_{0}\underline{\underline{C}} - (I_1^C - {}^{\tau}\lambda_I^2)\ {}^{0}\underline{\underline{g}} + I_3^C\ {}^{\tau}\lambda_I^{-2}\ {}^{\tau}_{0}\underline{\underline{C}}^{-1}}{2\ {}^{\tau}\lambda_I^4 - I_1^C\ {}^{\tau}\lambda_I^2 + I_3^C\ {}^{\tau}\lambda_I^{-2}} \tag{B.21} $$

where ${}^{\tau}\lambda_I^2$ are the eigenvalues of the second order Green tensor. Therefore the components ${}^{\tau}_{o}C_{LM}$ are,

$$ {}^{\tau}_{o}C_{LM} = \ {}^{\tau}\lambda_I^2\ \left[{}^{\tau}\lambda_I^2\ \frac{{}^{\tau}_{o}C_{LM} - \left({}^{\tau}I_C^1\ -\ {}^{\tau}\lambda_I^2\right)\ {}^{o}g_{LM} + \ {}^{\tau}I_C^3\ {}^{\tau}\lambda_I^{-2}\ {}^{\tau}_{o}C^{-1}_{LM}}{2\ {}^{\tau}\lambda_I^4\ -\ {}^{\tau}I_C^1\ \lambda_I^2\ +\ {}^{\tau}I_C^3\ {}^{\tau}\lambda_I^{-2}} \right] \tag{B.22} $$

Taking into account the expression (6.72),

$$ {}^{\tau}_{o}C_{LM} = \ {}^{\tau}\lambda_I^2\ {}^{\tau}\lambda_I^2\ f({}^{\tau}_{o}C_{LM}, {}^{\tau}\lambda_I) $$

${}^{\tau}_{0}\underline{\underline{C}}$ and ${}^{\tau}_{0}\underline{\underline{H}}$ are colinear tensors, ${}^{\tau}_{0}\underline{\underline{H}} = \ln\sqrt{{}^{\tau}_{0}\underline{\underline{C}}}$ and the eigenvalues ${}^{\tau}\lambda_I^H$ of ${}^{\tau}_{0}\underline{\underline{H}}$ are ${}^{\tau}\lambda_I^H = \ln({}^{\tau}\lambda_I)$. Hence, we can write,

$$ {}^{\tau}_{o}H_{LM} = {}^{\tau}\lambda_I^H \, {}^{\tau}\lambda_I^2 \, f({}^{\tau}_{o}C_{LM}, {}^{\tau}\lambda_I) $$

$$ {}^{\tau}_{o}H_{LM} = \ln({}^{\tau}\lambda_I) \, {}^{\tau}\lambda_I^2 \, f({}^{\tau}_{o}C_{LM}, {}^{\tau}\lambda_I) $$

$$ \frac{\partial H_{LM}}{\partial C_{PQ}}|_0^{\tau} = (1 + 2 \, \ln({}^{\tau}\lambda_I)) \, {}^{\tau}\lambda_I \, \frac{\partial \lambda_I}{\partial C_{PQ}}|_0^{\tau} \; f({}^{\tau}C_{LM}, {}^{\tau}\lambda_I) + \ln({}^{\tau}\lambda_I) \, {}^{\tau}\lambda_I^2 \, \frac{\partial f(C_{LM}, \lambda_I)}{\partial C_{PQ}}|_0^{\tau} \tag{B.23} $$

The term $\frac{\partial \lambda_I}{\partial C_{PQ}}|_0^{\tau}$ was already calculated in Eqn.(B.5) while the term $\frac{\partial f(C_{LM}, \lambda_I)}{\partial C_{PQ}}|_0^{\tau}$ was calculated in Section B.2.3.

Appendix C

Elasto-plastic material

C.1 Fourth order tensor ${}^{\tau}_{0}\widehat{D}^{KL}_{IJ}$

$$ {}^{\tau}_{0}\widehat{D}^{KL}_{IJ}|^{(k-1)} = \frac{\partial \widehat{H}^{E}_{IJ}}{\partial H_{KL}}|^{(k-1)} = \frac{\partial \widehat{H}^{E}_{IJ}}{\partial \widehat{C}^{E}_{MN}}|^{(k-1)} \frac{\partial \widehat{C}^{E}_{MN}}{\partial C_{RS}}|^{(k-1)} \frac{\partial C_{RS}}{\partial H_{KL}}|^{(k-1)} \tag{C.1} $$

The first term of the previous equation, $\frac{\partial \widehat{H}^{E}_{IJ}}{\partial \widehat{C}^{E}_{MN}}|^{(k-1)}$, was already calculated in Appendix A.

C.1.1 $\frac{\partial \widehat{C}^{E}_{MN}}{\partial C_{RS}}|^{(k-1)}$

Taking into account Lee's multiplicative decomposition and the incremental step described in Figs. 6.4 and C.1 , the second order deformation gradient tensor is,

$$ {}^{\tau+\Delta\tau}_{0}\underline{\underline{X}}|^{(k-1)} = {}^{\tau+\Delta\tau}_{0}\underline{\underline{X}}_{E}|^{(k-1)} \cdot {}^{\tau+\Delta\tau}_{0}\underline{\underline{X}}_{p}|^{(k-1)} . $$

According to the Green tensor definition,

$$ {}^{\tau+\Delta\tau}_{0}\underline{\underline{C}}|^{(k-1)} = {}^{\tau+\Delta\tau}_{0}\underline{\underline{X}}^{T}|^{(k-1)} \cdot {}^{\tau+\Delta\tau}_{0}\underline{\underline{X}}|^{(k-1)} $$

operating,

$$ {}^{\tau+\Delta\tau}_{0}\underline{\underline{C}}|^{(k-1)} = ({}^{\tau+\Delta\tau}_{0}\underline{\underline{X}}_{p})^{T}|^{(k-1)} \cdot ({}^{\tau+\Delta\tau}_{0}\underline{\underline{X}}_{E})^{T}|^{(k-1)} \cdot {}^{\tau+\Delta\tau}_{0}\underline{\underline{X}}_{E}|^{(k-1)} \cdot {}^{\tau+\Delta\tau}_{0}\underline{\underline{X}}_{P}|^{(k-1)} . $$

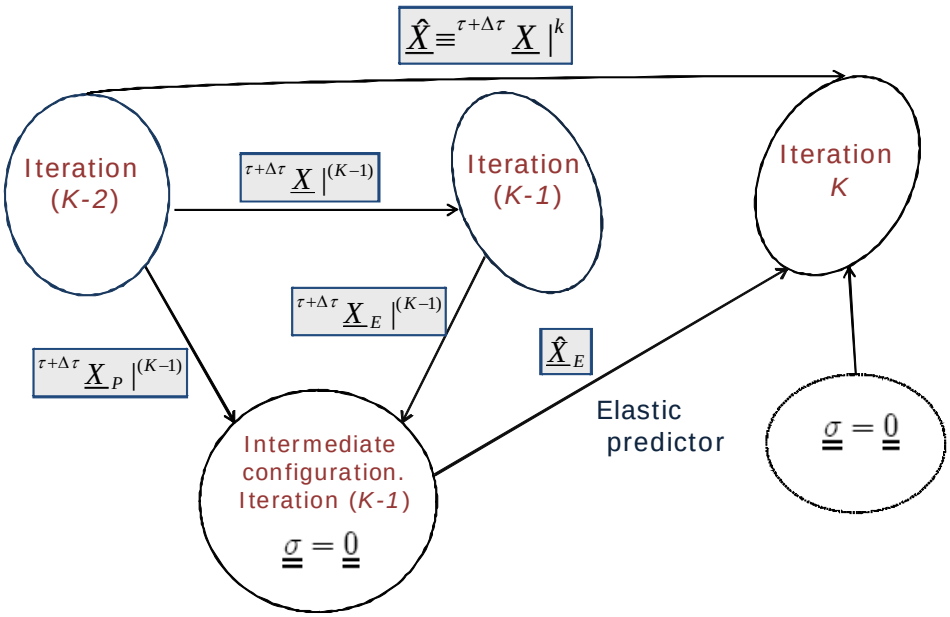

Figure C.1: Incremental step

Finally, we get,

$$ {}^{\tau+\Delta\tau}_{0}\underline{\underline{C}}|^{(k-1)} = ({}^{\tau+\Delta\tau}_{0}\underline{\underline{X}}_p)^T|^{(k-1)} \cdot {}^{\tau+\Delta\tau}_{0}\underline{\underline{C}}_E|^{(k-1)} \cdot {}^{\tau+\Delta\tau}_{0}\underline{\underline{X}}_P|^{(k-1)} $$

and the elastic Green tensor,

$$ {}^{\tau+\Delta\tau}_{0}\underline{\underline{C}}_E|^{(k-1)} = ({}^{\tau+\Delta\tau}_{0}\underline{\underline{X}}_p)^{-T}|^{(k-1)} \cdot {}^{\tau+\Delta\tau}_{0}\underline{\underline{C}}|^{(k-1)} \cdot \left({}^{\tau+\Delta\tau}_{0}\underline{\underline{X}}_P\right)^{-1}|^{(k-1)} $$

$$ {}^{\tau+\Delta\tau}_{0}C^E_{MN}|^{(k-1)} = ({}^{\tau+\Delta\tau}_{0}X_p)^{-T}_{MK}|^{(k-1)} \, {}^{\tau+\Delta\tau}_{0}C_{KL}|^{(k-1)} \, ({}^{\tau+\Delta\tau}_{0}X_p)^{-1}_{LN}|^{(k-1)} \quad . $$

Once the iteration $(k-1)$ is finished, to go to the following iteration k the trial step is elastic: the elastic predictor $\widehat{\underline{\underline{X}}}_E$.

The elastic predictor total deformation gradient tensor is,

$$ \widehat{\underline{\underline{X}}} = \widehat{\underline{\underline{X}}}_E \cdot {}^{\tau+\Delta\tau}_{0}\underline{\underline{X}}_P|^{(k-1)} $$

therefore, the trial Green tensor is,

$$ \widehat{\underline{\underline{C}}} = ({}^{\tau+\Delta\tau}_{0}\underline{\underline{X}}_p)^T|^{(k-1)} \cdot \widehat{\underline{\underline{C}}}^E \cdot ({}^{\tau+\Delta\tau}_{0}\underline{\underline{X}}_p)|^{(k-1)} $$

hence,

$$ \widehat{\underline{\underline{C}}}^E = ({}^{\tau+\Delta\tau}_{0}\underline{\underline{X}}_p)^{-T}|^{(k-1)} \cdot \widehat{\underline{\underline{C}}} \cdot ({}^{\tau+\Delta\tau}_{0}\underline{\underline{X}}_p)^{-1}|^{(k-1)} \quad . $$

But the elastic predictor total deformation gradient tensor $\widehat{\underline{\underline{X}}}$ is the actual one, ${}^{\tau+\Delta\tau}_{0}\underline{\underline{X}}\,|^{(k)}$. So, we can re-write the previous equation and get,

$$ \widehat{\underline{\underline{C}}}^E = ({}^{\tau+\Delta\tau}_{0}\underline{\underline{X}}_p)^{-T}|^{(k-1)} \cdot {}^{\tau+\Delta\tau}_{0}\underline{\underline{C}}|^{K} \cdot ({}^{\tau+\Delta\tau}_{0}\underline{\underline{X}}_p)^{-1}|^{(k-1)} $$

linearizing,

$$ \widehat{\underline{\underline{C}}}^E = ({}^{\tau+\Delta\tau}_{0}\underline{\underline{X}}_p)^{-T}|^{(k-1)} \cdot {}^{\tau+\Delta\tau}_{0}\underline{\underline{C}}|^{(k-1)} \cdot ({}^{\tau+\Delta\tau}_{0}\underline{\underline{X}}_p)^{-1}|^{(k-1)} $$

$$\widehat{C}^E_{MN} = ({}^{\tau+\Delta\tau}_{0}X_p)^{-T}_{MK}|^{(k-1)}\ {}^{\tau+\Delta\tau}_{0}C_{KL}|^{(k-1)}\ ({}^{\tau+\Delta\tau}_{0}X_p)^{-1}_{LN}|^{(k-1)}\ .$$

To derivate $\widehat{C}^E_{MN}$ is necessary to keep in mind that during the linearized step $({}^{\tau+\Delta\tau}_{0}\underline{\underline{X}}_p)|^{(k-1)}$ is constant,

$$\frac{\partial \widehat{C}^E_{MN}}{\partial C_{RS}}|^{(k-1)} = ({}^{\tau+\Delta\tau}_{0}X_p)^{-T}_{MK}|^{(k-1)}\ \delta_{KR}\ \delta_{LS}\ ({}^{\tau+\Delta\tau}_{0}X_p)^{-1}_{LN}|^{(k-1)}\ .$$

Finally,

$$\frac{\partial \widehat{C}^E_{MN}}{\partial C_{RS}}|^{(k-1)} = ({}^{\tau+\Delta\tau}_{0}X_p)^{-T}_{MR}|^{(k-1)}\ ({}^{\tau+\Delta\tau}_{0}X_p)^{-1}_{SN}|^{(k-1)}\ . \tag{C.2}$$

C.1.2 $\frac{\partial C_{RS}}{\partial H_{KL}}|^{(k-1)}$

The eigenvalues of the second order Hencky tensor ${}^{\tau}_{0}\underline{\underline{H}}$, ${}^{\tau}\lambda^H_I$, are the roots of the polynomial,

$$p(\lambda^H_I) = -\left({}^{\tau}\lambda^H_I\right)^3 + I^H_1\ {}^{\tau}\lambda^2_I - I^H_2\ {}^{\tau}\lambda^H_I + I^H_3 \tag{C.3}$$

while I^H_1, I^H_2 and I^H_3 are the invariants of ${}^{\tau}_{0}\underline{\underline{H}}$

$$I^H_1 = tr({}^{\tau}_{0}\underline{\underline{H}})$$

$$I^H_2 = \frac{1}{2}\ \left[\left(I^H_1\right)^2 - tr({}^{\tau}_{0}\underline{\underline{H}})^2\right]$$

$$I^H_3 = \det\left({}^{\tau}_{0}\underline{\underline{H}}\right)\ .$$

Applying Serrin formula, the igenvectors of ${}^{\tau}_{0}\underline{\underline{H}}$ are,

$$\Phi_I\Phi_I = \ {}^{t}\lambda^H_I\ \frac{{}^{\tau}_{0}\underline{\underline{H}} - (I^H_1\ -\ {}^{\tau}\lambda^H_I)\ {}^{0}\underline{\underline{g}} + I^H_3\ {}^{\tau}\lambda^{-2}_I\ {}^{\tau}_{0}\underline{\underline{H}}^{-1}}{2\ \left({}^{t}\lambda^H_I\right)^2 - I^H_1\ {}^{\tau}\lambda^H_I + I^H_3\ \left({}^{t}\lambda^H_I\right)^{-1}}\ . \tag{C.4}$$

The second order tensor ${}^{\tau}_{0}\underline{\underline{C}}$ and ${}^{\tau}_{0}\underline{\underline{H}}$ are colinear tensors, with eigenvalues ${}^{\tau}\lambda^{C}_{I} = {}^{\tau}\lambda^{2}_{I}$ and ${}^{\tau}\lambda^{H}_{I} = ln({}^{\tau}\lambda_{I})$, respectively. ${}^{\tau}\lambda_{I}$ are the eigenvalues of the second order right tensor ${}^{\tau}_{0}\underline{\underline{U}}$. Hence, we can write,

$$ {}^{\tau}_{0}C_{LM} = {}^{\tau}\lambda^{C}_{I}\ {}^{t}\lambda^{H}_{I}\ f({}^{\tau}_{0}H_{LM},\ {}^{\tau}\lambda^{H}_{I}) \tag{C.5} $$

with,

$$ f({}^{\tau}_{0}H_{LM},{}^{\tau}\lambda^{H}_{I}) = \frac{{}^{\tau}_{0}H_{LM} - (I^{H}_{1} - {}^{\tau}\lambda^{H}_{I})\ {}^{0}g_{LM} + I^{H}_{3}\ {}^{\tau}\lambda^{-2}_{I}\ {}^{\tau}_{0}H^{-1}_{LM}}{2\ \left({}^{t}\lambda^{H}_{I}\right)^{2} - I^{H}_{1}\ {}^{\tau}\lambda^{H}_{I} + I^{H}_{3}\ \left({}^{t}\lambda^{H}_{I}\right)^{-1}} . \tag{C.6} $$

Therefore, the derivative we are looking for, is,

$$ \begin{aligned} \frac{\partial C_{LM}}{\partial H_{PQ}}|^{\tau}_{0} \quad = \quad & \frac{\partial \lambda^{C}_{I}}{\partial \lambda^{H}_{I}}|^{\tau}_{0}\ \frac{\partial \lambda^{H}_{I}}{\partial H_{PQ}}|^{\tau}_{0}\ {}^{\tau}\lambda^{H}_{I}\ f({}^{\tau}_{0}H_{LM},\ {}^{\tau}\lambda^{H}_{I})\ + \\ & {}^{\tau}\lambda^{C}_{I}\ \frac{\partial \lambda^{H}_{I}}{\partial H_{PQ}}|^{\tau}_{0}\ f({}^{\tau}_{0}H_{LM},\ {}^{t}\lambda^{H}_{I})\ +\ {}^{\tau}\lambda^{C}_{I}\ {}^{\tau}\lambda^{H}_{I}\ \frac{\partial f(H_{LM},\ {}^{\tau}\lambda^{H}_{I})}{\partial H_{PQ}}|^{\tau}_{0}\ . \end{aligned} \tag{C.7} $$

In order to obtain the final expression of $\frac{\partial C_{LM}}{\partial H_{PQ}}|^{\tau}_{0}$, in what follows we calculate $\frac{\partial \lambda^{C}_{I}}{\partial \lambda^{H}_{I}}|^{\tau}_{0}$, $\frac{\partial \lambda^{H}_{I}}{\partial H_{PQ}}|^{\tau}_{0}$ and $\frac{\partial f(H_{LM},{}^{\tau}\lambda^{H}_{I})}{\partial H_{PQ}}|^{\tau}_{0}$.

Being,

$$ {}^{\tau}\lambda^{C}_{I} = {}^{\tau}\lambda^{C}_{I} = e^{2\ {}^{\tau}\lambda^{H}_{I}} \tag{C.8} $$

the first derivative of the previous expression is,

$$ \frac{\partial \lambda^{C}_{I}}{\partial \lambda^{H}_{I}}|^{\tau}_{0} = 2\ e^{2\ {}^{\tau}\lambda^{H}_{I}} = 2\ {}^{\tau}\lambda^{C}_{I} \ . \tag{C.9} $$

From C.3 we get the following expression,

$$ \frac{\partial \lambda^{H}_{I}}{\partial H_{PQ}}|^{\tau}_{0} = \frac{-\frac{\partial I^{H}_{1}}{\partial H_{PQ}}|^{\tau}_{0}\ ({}^{\tau}\lambda^{H}_{I})^{2} + \frac{\partial I^{H}_{2}}{\partial H_{PQ}}|^{\tau}_{0}\ {}^{t}\lambda^{H}_{I} - \frac{\partial I^{H}_{3}}{\partial H_{PQ}}|^{\tau}_{0}}{-3\ ({}^{\tau}\lambda^{H}_{I})^{2}\ +\ 2\ I^{H}_{1}\ {}^{\tau}\lambda_{I} - I^{H}_{2}} \tag{C.10} $$

Finally, to calculate $\frac{\partial f(H_{LM},\lambda^{H}_{I})}{\partial H_{PQ}}|^{\tau}_{0}$ we consider the following expression,

$$f({}^{\tau}_{0}H_{LM},\ {}^{\tau}\lambda^H_I) = \frac{{}^{\tau}_{0}H_{LM} - (I^H_1\ -\ {}^{\tau}\lambda^H_I)\ {}^{0}g_{LM} + I^H_3\ {}^{\tau}\lambda^{-2}_I\ {}^{\tau}_{0}H^{-1}_{LM}}{2\ \left({}^{\tau}\lambda^H_I\right)^2 - I^H_1\ {}^{\tau}\lambda^H_I + I^H_3\ \left(\lambda^H_I\right)^{-1}} = \frac{A}{B}\ .$$

This term is a division derivative, so,

$$\frac{\partial f(H_{LM},\lambda^H_I)}{\partial H_{PQ}}|^{\tau}_0 = \frac{\frac{\partial A}{\partial H_{PQ}}|^{\tau}_0\ B - A\ \frac{\partial B}{\partial H_{PQ}}|^{\tau}_0}{B^2} \tag{C.11}$$

$$\begin{aligned}\frac{\partial A}{\partial H_{PQ}}|^{\tau}_0 \quad = \quad & \frac{\partial H_{PQ}}{\partial H_{PQ}}|^{\tau}_0 - \left(\frac{\partial I^H_1}{\partial H_{PQ}}|^{\tau}_0 - \frac{\partial \lambda^H_I}{\partial H_{PQ}}|^{\tau}_0\right)\ {}^{0}g_{LM}\ +\ \frac{\partial I^H_3}{\partial H_{PQ}}|^{\tau}_0\ \frac{{}^{\tau}_{0}H^{-1}_{LM}}{{}^{t}\lambda^H_I}\ + \\ & \frac{\partial H^{-1}_{LM}}{\partial H_{PQ}}|^{\tau}_0\ \frac{I^H_3}{{}^{t}\lambda^H_I}\ -\ \frac{I^H_3\ {}^{\tau}_{0}H^{-1}_{LM}}{\left({}^{t}\lambda^H_I\right)^2}\ \frac{\partial \lambda^H_1}{\partial H_{PQ}}|^{\tau}_0\end{aligned}$$

$$\frac{\partial B}{\partial H_{PQ}}|^{\tau}_0 = \left(4\ {}^{\tau}\lambda^H_I - I^H_1 - \frac{I^H_3}{\left({}^{\tau}\lambda^H_I\right)^2}\right)\ \frac{\partial \lambda^H_I}{\partial H_{PQ}}|^{\tau}_0\ -\ \frac{\partial I^H_I}{\partial H_{PQ}}|^{\tau}_0\ {}^{\tau}\lambda^H_I\ +\ \frac{\partial I^H_3}{\partial H_{PQ}}|^{\tau}_0\ \frac{1}{{}^{\tau}\lambda^H_I}\ .$$

Finally, replacing the Eqs. (C.9), (C.10) and (C.11) into (C.7), we have completely defined $\frac{\partial C_{LM}}{\partial H_{PQ}}|^{\tau}_0$.

C.2 Sixth order tensor ${}^{\tau+\Delta\tau}_{0}\widehat{DD}^{KLRS}_{IJ}|^{(k-1)}$

$${}^{\tau+\Delta\tau}_{0}\widehat{DD}^{KLRS}_{IJ}|^{(k-1)} = \frac{\partial^2 \widehat{H}_{IJ}}{\partial H_{RS}\ \partial H_{KL}}|^{(k-1)}_0 = \frac{\partial}{\partial H_{RS}}\ \left(\frac{\partial \widehat{H}^E_{IJ}}{\partial H_{KL}}\right)|^{(k-1)} = \frac{\partial}{\partial H_{RS}}\ \left(\widehat{D}^{KL}_{IJ}\right)|^{(k-1)} \tag{C.12}$$

Replacing C.1 into the previous expression we get,

$${}^{\tau+\Delta\tau}_{0}\widehat{DD}^{KLPQ}_{IJ}|^{(k-1)} = \frac{\partial}{\partial H_{PQ}}\ \left(\frac{\partial \widehat{H}^E_{IJ}}{\partial H_{KL}}\right)|^{(k-1)} = \frac{\partial}{\partial H_{PQ}}\ \left(\frac{\partial \widehat{H}^E_{IJ}}{\partial \widehat{C}^E_{MN}}\ \frac{\partial \widehat{C}^E_{MN}}{\partial C_{RS}}\ \frac{\partial C_{RS}}{\partial H_{KL}}\right)|^{(k-1)}\ . \tag{C.13}$$

From Eq. C.2 we know that,

$$\frac{\partial}{\partial H_{PQ}}\ \left(\frac{\partial \widehat{C}^E_{MN}}{\partial C_{RS}}\right)|^{(k-1)} = 0 \tag{C.14}$$

hence, taking into account the product derivative rule,

$$ {}^{\tau+\Delta\tau}_{0}\widehat{DD}_{IJ}^{KLPQ}|^{(k-1)} = \frac{\partial}{\partial H_{PQ}} \left(\frac{\partial \widehat{H}_{IJ}^{E}}{\partial \widehat{C}_{MN}^{E}} \right)|^{(k-1)} \frac{\partial \widehat{C}_{MN}^{E}}{\partial C_{RS}}|^{(k-1)} \frac{\partial C_{RS}}{\partial H_{KL}}|^{(k-1)} + \frac{\partial \widehat{H}_{IJ}^{E}}{\partial \widehat{C}_{MN}^{E}}|^{(k-1)} \frac{\partial \widehat{C}_{MN}^{E}}{\partial C_{RS}}|^{(k-1)} \tag{C.15} $$

The terms between brackets have been already calculated in Eqs. (B.23) and (C.7). Therefore, from Eq. (C.15) we can get the final expression of the sixth order tensor components.

Bibliography

[1] Ahmad S., Irons B.M. and Zienkiewicz O.C. (1970), "Analysis of thick and thin shell structures by curved finite elements", Int. J. Numerical Methods in Engng., vol. 2, pp.419-451.

[2] Anand L. (1979), "On Hencky's approximate strain-energy function for moderate deformations", J. Appl. Mech., vol. 46, pp.78-82.M.M. Wolf, "Historical aspects and key technologies", The Making, Shaping and Treating of Steel (Ironmaking Volume, 11th. Edition), AISE Steel Foundation, (in press).

[3] Arbocz J. and Babcock C.D. (1969), "The effect of general imperfections on the buckling of cylindrical shell", ASME, J. Appl. Mechs., 36, pp. 28-38.

[4] Arbocz J. and Williams J.G. (1977), "Imperfection surveys of a 10-ft diameter shell structure", AIAA Journal, 15, pp. 949-956.

[5] Assanelli A.P. and López Turconi G. (2001), "Effect of measurement procedures on estimating geometrical parameters of pipes", 2001 Offshore Technology Conference, Paper OTC 13051, Houston, Texas.

[6] Assanelli A.P., Toscano R.G., Johnson D. and Dvorkin E.N. (2000), "Experimental / numerical analysis of the collapse behavior of steel pipes", Engng. Computations, Vol.17, pp. 459-486.

[7] Atluri, S.N. (1984), "Alternate stress and conjugate strain measures, and mixed variational formulation involvong rigid rotations for computational analysis of finitely

deformed solids, with applications to plate and shells. Part I", Comput. & Struct., 18, pp. 93-116.

[8] Bao Y. and Wierzbicki T. (2004), "A comparative study on various ductile crack formation criteria", *J. Engng. Materials and Technology ASME*, **126**, pp.314-324.

[9] Bathe K.J. (1996), Finite Element Procedures, Prentice Hall, Upper Saddle River,NJ.

[10] Bathe K.J. and Bolourchi S. (1980), "A geometric and material nonlinear plate and shell element", Computers & Struct., vol. 11, pp. 23-48.

[11] Bathe K.J. and Dvorkin E.N. (1983), "On the automatic solution of nonlinear finite element equations", Computers & Structures, Vol. 17, pp. 871-879.

[12] Bathe K.J. and Dvorkin E.N. (1985), "A four-node plate bending element based on Mindlin / Reissner plate theory and a mixed interpolation", Int. J. Numerical Methods in Engng., Vol. 21, pp. 367-383.

[13] Bathe K.J. and Dvorkin E.N. (1986), "A formulation of general shell elements - The use of mixed interpolation of tensorial components", Int. J. Numerical Methods in Engng., 22, pp. 697-722.

[14] Bathe K.J., Dvorkin E.N. and Ho L.W. (1983), "Our discrete-Kirchhoff and isoparametric shell elements for nonlinear analyses - an assessment", Computers & Struct., vol. 16, pp.89-98.

[15] Belytschko T., Stolarski H., Liu W.K., Carpenter N. and Ong J. (1985), "Stress projections for membrane and shear locking in shell finite elements", Comput. Meth. Appl. Mechs. Engng., vol. 51, pp. 221-258.

[16] Bischoff M. and Ramm E. (1997), "Shear deformable shell elements for large strains and rotations", Int. J. Numerical Methods in Engng., vol. 40, pp. 4427-4449.

[17] Brigham E.O. (1988), "The Fast Fourier Transform and its Applications", Prentice Hall, Englewood Cliffs, New Jersey.

[18] Brown R.J., King R., Lagner C. and Palmer A.C. (2001), "Structural Design of Pipelines", Marine Pipeline Engineering Course, Houston, TX.

[19] Brush D.O. and Almroth B.O. (1975), "Buckling of Bars, Plates and Shells", Mc Graw Hill, New York.

[20] Büchter N., Ramm E. and Roehl D. (1994), "Three-dimensional extension of non-linear shell formulation based on the enhanced assumed strain concept", Int. J. Numerical Methods in Engng., vol. 37, pp. 2551-2568.

[21] Chapelle D. and Bathe K.J. (2003), "The Finite Element Analysis of Shells - Fundamentals", Springer, Berlin.

[22] Clinedinst W.O. (1977), "Analysis of collapse test data and development of new collapse resistance formulas", Report to the API Task Group on Performance Properties.

[23] Corona E. and Kyriakides S. (1987), "An unusual mode of collapse of tubes under combined bending and pressure", ASME, J. Pressure Vessel Technol., 109, pp. 302-304.

[24] DeGeer D.D. and Cheng J.J. (2000), "Predicting Pipeline Collapse Resistance.", Proceedings of the International Pipeline Conference, Calgary, Alberta, Canada.

[25] De Winter P. E., Stark J. W. B. and Witteveen J. (1981), "Shell Structures - Stability and Strength", Chapter 7, (Ed. R. Narayan).

[26] DNV Rules - Offshore Standard OS-F101 - Submarine Pipeline Systems, Section 5, 2000.

[27] Dvorkin E.N. (1992), "On nonlinear analysis of shells using finite elements based on mixed interpolation of tensorial components", published in Nonlinear Analysis of Shells by Finite Elements, (Ed. F.G. Rammerstorfer), CISM Courses and Lectures No. 328, Springer - Verlag, Wien-New York.

[28] Dvorkin E.N. (1995), "Nonlinear analysis of shells using the MITC formulation", Archives Comput. Meth. Engng., vol. 2, pp.1-50.

[29] Dvorkin E.N. and Assanelli A.P. (1989), "Elasto-plastic analysis using a quadrilateral 2-D element based on mixed interpolation of tensorial components", Proc. Second International Conference on Computational Plasticity (Ed. D.R.J. Owen et al.), Pineridge Press, Swansea.

[30] Dvorkin E.N. and Bathe K.J. (1984), "A continuum mechanics based four-node shell element for general nonlinear analysis", Engng. Computations, vol. 1, pp. 77-88.

[31] Dvorkin E.N. and Goldschmit M.B. (2005), Nonlinear Continua, Springer, Berlin.

[32] Dvorkin E.N. and Toscano R.G. (2001), "Effects of external/internal pressure on the global buckling of pipelines", Computational Fluid and Solid Mechanics – Proceedings First MIT Conference on Computational Fluid and Solid Mechanics, (Ed. K.-J. Bathe), Elsevier.

[33] Dvorkin E.N. and Vassolo S.I. (1989), "A quadrilateral 2-D finite element based on mixed interpolation of tensorial components", Engng. Comput., 6, pp. 217-224.

[34] Dvorkin E.N., Assanelli A.P. and Toscano R.G. (1996), "Performance of the QMITC element in two-dimensional elasto-plastic analyses", Computers & Structures, 58, pp. 1099-1129.

[35] Dvorkin E.N., Oñate E. and Oliver J. (1988), "On a nonlinear formulation for curved Timoshenko beam elements considering large displacement/rotation increments", Int. J. Numerical Methods in Engng., vol. 26, pp. 1597-1613.

[36] Dvorkin E.N., Pantuso D. and Repetto E.A. (1995), "A formulation of the MITC4 shell element for finite strain elasto-plastic analysis", Comput. Meth. Appl. Mechs. Engng., vol. 125, pp.17-40.

[37] Fowler J.R., Hormberg B. and Katsounas A. (1990), "Large scale collapse testing", SES Report, prepared for the Offshore Supervisory Committee, American Gas Association.

[38] Fowler J.R., Klementich E.F. and Chappell J.F. (1983), "Analysis and testing of factors affecting collapse performance of casing", ASME, J. Energy Resources Technology, 105, pp. 574-579.

[39] Gebhardt H. and Schweizerhof K. (1993), "Interpolation of curved shell geometries by low order finite elements - Errors and modifications", Int. J. Numerical Methods in Engng., vol. 36, pp.287-302.

[40] Heise O. and Esztergar E.P. (1970), "Elasto-plastic collapse under external pressure", ASME, J. Engng. for Industry, 92, pp. 735-742.

[41] Herink M., Kyriakides S., Onoufriou A. and Yun H. (2006), "Effects of the UOE/UOC pipe manufacturing process on pipe collapse pressure", International Journal of Mechanical Sciences.

[42] Hill R. (1971), The Mathematical Theory of Plasticity, Oxford University Press, New York.

[43] Hughes T.J.R. and Carnoy E. (1983), "Nonlinear finite element shell formulation accounting for large membrane strains", Comput. Meth. Appl. Mechs. Engng., vol. 39, pp.69-82.

[44] Johns T.G., Mesloh R.E., Sorenson J.E. (1978), “Propagating buckle arrestors for offshore pipelines”. ASME Journal of Pressure Vessel Technology 1978; Vol. 100, pp. 206-214.

[45] Kanda M., Yazaki Y., Yamamoto K., Higashiyama H., Sato T., Inoue T., Murata T., Morikawa H. and Yanagimoto S. (1983), "Development of NT-series oil-country tubular good", Nippon Steel Technical Report, 21, pp. 247-262.

[46] Kråkeland B. (1978), "Nonlinear analysis of shells using degenerate isoparametric elements", Finite Elements in Nonlinear Mechanics (Eds. P.G. Bergan et al.), Tapir Publishers, Norwegian Institute of Technology, Trondheim, Norway.

[47] Krug G. (1983), "Testing of casing under extreme loads", Institute of Petroleum Engineering, Technische Universität, Clausthal.

[48] Kyriakides S. (1994), "Propagating instabilities in structures", Advances in Applied Mechanics, Vol. 30, pp.67-189.

[49] Kyriakides S. and Corona E. (), "Mechanics of offshore pipelines. Vol. I Buckling and collapse", Elsevier

[50] Kyriakides S., Park T.D. and Netto T.A. (1998), "On the design of Integral Buckle Arrestors for Offshore Pipelines", International Journal of Applied Ocean Research, Vol.20 pp.95-104.

[51] Langer C.G. (1999), "Buckle arrestors for Deepwater Pipelines", Proceedings of the Offshore Technology Conference, OTC 10711, Houston, TX, U.S.A.

[52] Malvern L. (1969), "Introduction to the mechanics of a continuous medium", Prentice-Hall, Inc., Englewood Cliffs, New Jersey.

[53] Marlow R.S. (1982), "Collapse performance of HC-95 casing", Report for the API PRAC Project No. 80-30.

[54] Mimura H., Tamano T. and Mimaki T. (1987), "Finite element analysis of collapse strength of casing", Nippon Steel Technical Report, 34, pp. 62-69.

[55] Netto T.A. and Estefen S. F. (1996), "Buckle Arrestors for Deepwater Pipelines", International Journal of Marine Structures, Vol.9 pp.873-883.

[56] Netto T.A. and Kyriakides S. (2000), "Dynamic performance of integral buckle arrestors for offshore pipelines. Part I: Experiments", International Journal of Mechanical Sciences, Vol.42 pp.1405-1423.

[57] Netto T.A. and Kyriakides S. (2000), "Dynamic performance of integral buckle arrestors for offshore pipelines. Part II: Analysis", International Journal of Mechanical Sciences, Vol.42 pp.1425-1452.

[58] Ogden R.W. (1997) , Non-linear Elastic Deformations, Dover.

[59] Palmer A.C. and J.H. Martin (1975), "Buckle propagation in submarine pipelines", Nature, Vol. 254, pp. 46-48.

[60] Palmer A.C. (1974), "Lateral Buckling of Axially Constrained Pipelines", JPT Forum.

[61] Palmer A.C. and King R. (2004), "Subsea pipeline engineering", PennWell.

[62] Park T.D. and Kyriakides S. (1997), "On the performance of Integral Buckle Arrestors for Offshore Pipelines", International Journal of Mechanical Sciences, Vol.39 pp.643-669.

[63] Press W.H., Flannery B.P., Teukolsky S.A. and Veherling W.T. (1986), Numerical Recipes, Cambridge University Press, Cambridge.

[64] Ramm E. (1977), "A plate/shell element for large deflections and rotations", Formulations and Computational Algorithms in Finite Element Analysis (Eds. K.J. Bathe et al.), MIT Press, Cambridge, MA.

[65] Roache P.J. (1998), Verification and Validation in Computational Science and Engineering, Hermosa Publishers.

[66] Rodal J.J.A. and Witmer E.A. (1979), "Finite-strain large-deflection elastic-viscoplastic finite-element transient analysis of structures", NASA CR 159874.

[67] Shunmugam M.S. (1991), "Criteria for computer-aided form evaluation", ASME, J. Engng. for Industry, 113, pp. 233-238.

[68] Simo J.C. , Fox D.D. and Rifai M.S. (1989), "On a stress resultant geometrically exact shell model. Part II: The linear theory; computational aspects", Comput. Meth. Appl. Mechs. Engng., vol. 73, pp.53-92.

[69] Simo J.C. , Fox D.D. and Rifai M.S. (1990), "On a stress resultant geometrically exact shell model. Part III: Computational aspects of the nonlinear theory", Comput. Meth. Appl. Mechs. Engng., vol. 79, pp.21-70.

[70] Simo J.C. and Fox D.D. (1989), "On a stress resultant geometrically exact shell model. Part I: Formulation and optimal parametrization", Comput. Meth. Appl. Mechs. Engng., vol. 72, pp.267-304.

[71] Simo J.C. and Hughes T.J.R. (1998), Computational Inelasticity, Springer, New York.

[72] Simo J.C. and Kennedy J.G. (1992), "On a stress resultant geometrically exact shell model. Part V: Nonlinear plasticity formulation and integration algorithms", Comput. Meth. Appl. Mechs. Engng., vol. 96, pp.133-171.

[73] Simo J.C., Fox D.D. and Rifai M.S. (1992), "On a stress resultant geometrically exact shell model. Part IV: Variable thickness shells with through-the-thickness stretching", Comput. Meth. Appl. Mechs. Engng., vol. 81, pp.91-126.

[74] Stark P. and McKeehan D. (1995), "Hydrostatic Collapse Research in Support of the Oman India Gas", Offshore Technology Conference, Paper OTC 7705.

[75] Tamano T., Mimaki T. and Yaganimoto S. (1983), "A new empirical formula for collapse resistance of commercial casing", ASME, Proc. 2nd Int. Offshore Mechanics and Arctic Engineering Symposium, Houston, pp. 489-495.

[76] The ADINA System, ADINA R&D, Watertown, MA, U.S.A.

[77] Timoshenko S.P. and Gere J.M. (1961), Theory of Elastic Stability, Mc Graw Hill.

[78] Tokimasa K. and Tanaka K., "FEM analysis of the collapse strength of a tube", ASME paper 84-PVP-104.

[79] Toscano R.G., Amenta P.M. and Dvorkin E.N. (2002), "Enhancement of the Collapse Resistance of Tubular Products for Deepwater pipeline Applications", IBC'S Offshore Pipeline Technology, Conference documentation.

[80] Toscano R.G. and Dvorkin E.N. (2008), "A new shell element for elasto–plastic finite strain analyzes. Application to the collapse and post-collapse analysis of marine pipelines", Proceedings 6th International Conference on Computation of Shell & Spatial Structures, Spanning Nano to Mega (Eds. John F. Abel and J. Robert Cooke), Ithaca, New York, USA.

[81] Toscano R.G. and Dvorkin E.N. (2006), "A shell element for finite strain analyses. Hyperelastic material models", Proceedings 7th World Congress on Computational Mechanics, Los Angeles, California.

[82] Toscano R.G. and Dvorkin E.N. (2007), "A Shell Element for Finite Strain Analyses. Hyperelastic Material Models", Engineering Computations, Vol.24, N° 5, pp.514-535.

[83] Toscano R.G., Gonzalez M. and Dvorkin E.N. (2003), "Validation of a finite element model that simulates the behavior of steel pipes under external pressure", The Journal of Pipeline Integrity, 2, pp.74-84.

[84] Toscano R.G., Mantovano L.,Amenta P., Charreau R., Johnson D., Assanelli A.P. and Dvorkin E.N. (2008), "Collapse arrestors for deepwater pipelines. Cross-over mechanisms", Computers&Structures, Vol. 86, pp. 782-743.

[85] Toscano R.G., Mantovano L.O. and Dvorkin E.N. (2004), "On the numerical calculation of collapse and collapse propagation pressure of steel deep-water pipelines under external pressure and bending: Experimental verification of the finite element results", Proceedings 4th International Conference on Pipeline Technology, pp. 1417-1428, Ostend, Belgium.

[86] Toscano R.G., Mantovano L.O., Amenta P., Charreau R., D. Johnson, A. Assanelli and Dvorkin E.N. (2006), " Collapse arrestors for deepwater pipelines: finite element models and experimental validations for different cross-over mechanisms", Proceedings OMAE 2006 - 25nd. International Conference on Offshore Mechanics and Arctic Engineering, Hamburg, Germany.

[87] Toscano R.G., Raffo J.L., Fritz M., Silva R., Hines J. and Timms C. (2008), "Modeling the UOE Pipe Manufacturing Process", Proceedings OMAE 2008 – OMAE2008-57605, 27nd. International Conference on Offshore Mechanics and Arctic Engineering, Estoril, Portugal,.

[88] Toscano R.G., Timms C., Dvorkin E.N. and DeGeer D. (2003), "Determination of the collapse and propagation pressure of ultra-deepwater pipelines", Proceedings OMAE 2003 - 22nd. International Conference on Offshore Mechanics and Arctic Engineering.

[89] Yeh M.K. and Kyriakides S. (1988), "Collapse of deepwater pipelines", ASME, J. Energy Res. Tech., 110, pp. 1-11.

[90] Zienkiewicz O.C. and Taylor R.L. (2000), The Finite Element Method, Vol. 2, 5^{th} Edition, Butterworth-Heinemann.

[91] Zienkiewicz O.C., Taylor R.L. and Too J.M. (1971), "Reduced integration technique in general analysis of plates and shells", Int. J. Numerical Methods in Engng., vol. 3, pp. 275-290.

[92] Zimmerman, T. and DeGeer D. (1999), "Large Pressure Chamber Tests Ultra-deepwater Pipe Samples", World Oil Deepwater Supplement.